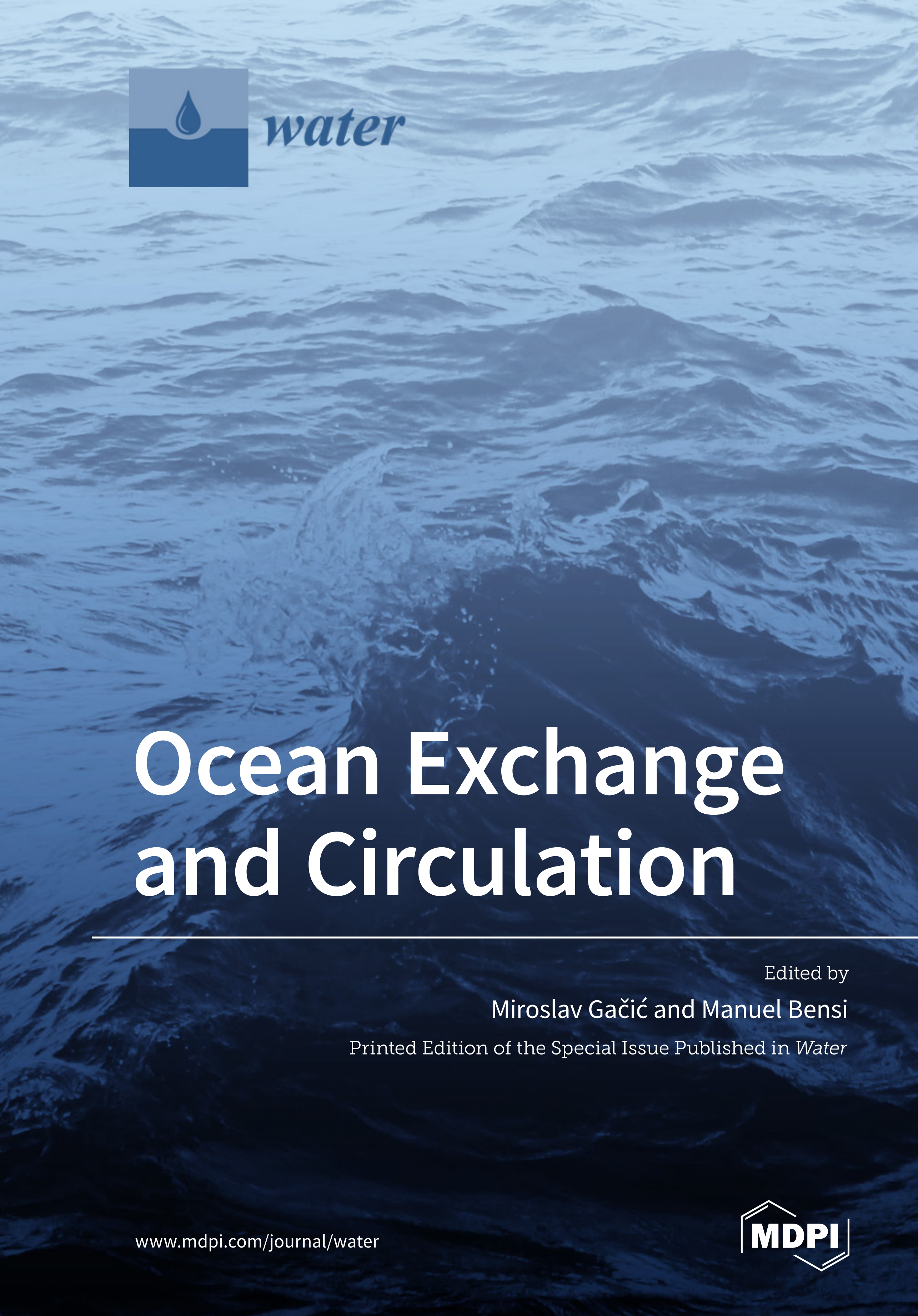

Ocean Exchange and Circulation

Edited by

Miroslav Gačić and Manuel Bensi

Printed Edition of the Special Issue Published in *Water*

www.mdpi.com/journal/water

Ocean Exchange and Circulation

Ocean Exchange and Circulation

Special Issue Editors

Miroslav Gačić
Manuel Bensi

MDPI • Basel • Beijing • Wuhan • Barcelona • Belgrade • Manchester • Tokyo • Cluj • Tianjin

Special Issue Editors
Miroslav Gačić
National Institute of Oceanography and Experimental Geophysics
Italy

Manuel Bensi
National Institute of Oceanography and Experimental Geophysics
Italy

Editorial Office
MDPI
St. Alban-Anlage 66
4052 Basel, Switzerland

This is a reprint of articles from the Special Issue published online in the open access journal *Water* (ISSN 2073-4441) (available at: https://www.mdpi.com/journal/water/special_issues/Ocean_Exchange_and_Circulation).

For citation purposes, cite each article independently as indicated on the article page online and as indicated below:

LastName, A.A.; LastName, B.B.; LastName, C.C. Article Title. *Journal Name* **Year**, *Article Number*, Page Range.

ISBN 978-3-03936-152-6 (Hbk)
ISBN 978-3-03936-153-3 (PDF)

Cover image courtesy of Manuel Bensi.

Contents

About the Special Issue Editors

Miroslav Gačić is a physical oceanographer at the National Institute of Oceanography and Applied Geophysics, Trieste (Italy), and was, until 2015, Head of the Oceanography Group for about 20 years. His main research interests and activities have been focused on the Adriatic and Mediterranean Seas, and have been related to: a) deep-water formation processes and their influence on the nutrient input into the euphotic zone, b) thermohaline circulation inside the basin and its interannual variability, c) the response of the basin to atmospheric forcing on various time scales, d) coastal circulation and response to local forcing and remote forcing and e) water exchange between semi-enclosed bays and seas and adjacent basins. Within coastal studies, he has been working on the analysis and interpretation of surface current measurements in the Northern Adriatic, in the Venice lagoon inlets. Special attention has been paid to understanding the water exchange dynamics between the lagoon and the open sea, and to quantify the relative contribution of tides and meteorological forcing. Within open-sea studies, he has worked on the winter convection and water exchange through the Strait of Otranto, and longitudinal water fluxes in the Adriatic Sea. An important aspect of his activity has been oriented towards the interannual and decadal variability of the Adriatic thermohaline properties and interaction with the Ionian Sea. One of the most important scientific results he has achieved is his contribution to the understanding of the decadal variability of the Ionian circulation and the feedback with the Adriatic Sea (Adriatic–Ionian bi-modal oscillating system—BiOS). He is the author of about 150 scientific papers in international journals and chapters in books.

Manuel Bensi, Ph.D., a researcher at the National Institute of Oceanography and Applied Geophysics, Trieste (Italy), is a marine scientist in the field of physical oceanography, with extensive experience in ocean data acquisition and analysis. His scientific activity focuses on thermohaline deep sea and large-scale circulation processes, dense water formation, and climate change in the Mediterranean Sea and Polar regions. He is the author and co-author of more than 80 scientific publications, including articles in journals, book chapters, and conference proceedings. Since 2003, he has participated in more than 25 oceanographic cruises (in the Mediterranean Sea, Atlantic and Arctic Ocean). He is the coordinator and task leader of several national and international projects. He is also a supervisor of doctoral students, and he constantly participates in scientific dissemination activities. He serves as a reviewer and guest editor for several ISI journals. He speaks three languages (Italian, English, Portuguese).

water

MDPI

Editorial

Ocean Exchange and Circulation

Miroslav Gačić and Manuel Bensi *

National Institute of Oceanography and Experimental Geophysics, Borgo Grotta Gigante 42-C, I-34010 Trieste, Italy; mgacic@inogs.it

* Correspondence: mbensi@inogs.it

Received: 12 March 2020; Accepted: 18 March 2020; Published: 20 March 2020

Abstract: The great spatial and temporal variability, which characterizes the marine environment, requires a huge effort to be observed and studied properly since changes in circulation and mixing processes directly influence the variability of the physical and biogeochemical properties. A multi-platform approach and a collaborative effort, in addition to optimizing both data collection and quality, is needed to bring the scientific community to more efficient monitoring and predicting of the world ocean processes. This Special Issue consists of nine original scientific articles that address oceanic circulation and water mass exchange. Most of them deal with mean circulation, basin and sub-basin-scale flows, mesoscale eddies, and internal processes (e.g., mixing and internal waves) that contribute to the redistribution of oceanic properties and energy within the ocean. One paper deals with numerical modelling application finalized to evaluate the capacity of coastal vegetated areas to mitigate the impact of a tsunami. The study areas in which these topics are developed include both oceanic areas and semi-enclosed seas such as the Mediterranean Sea, the Norwegian Sea and the Fram Strait, the South China Sea, and the Northwest Pacific. Scientific findings presented in this Special Issue highlight how a combination of various modern observation techniques can improve our understanding of the complex physical and biogeochemical processes in the ocean.

Keywords: mesoscale eddies; deep-sea thermohaline variability; dense-water formation; picoplankton distribution; glider; floats; high-frequency radar; moorings; tsunami; Kuroshio bifurcation; internal waves

1. Introduction

The oceanic circulation shows great spatial and temporal variability that requires a huge effort to be observed and studied properly [1]. Satellites, autonomous platforms, fixed point observatories located in key regions of the world ocean, and repeated hydrographic surveys are a means to collect new data. However, when the spatial and temporal resolution is not adequately resolved, numerical models can complement or compensate for the lack of information needed for the observation of the most complex oceanic dynamics and processes.

This Special Issue collects a series of scientific articles (Table 1) that address oceanic circulation and water mass exchange. The study areas in which these topics are developed are the Mediterranean Sea, the Norwegian Sea and the Fram Strait, the South China Sea, and the Northwest Pacific. The papers deal with the oceanic circulation generated by wind and/or density gradients, which contributes to the exchange of water between different parts of the ocean or between marginal seas and adjacent ocean areas. These processes develop at different spatial and temporal scales. Other than mean circulation, basin and sub-basin-scale flows, mesoscale eddies and internal processes (e.g., mixing induced by bottom roughness, internal waves) also contribute to the redistribution of oceanic properties and energy within the ocean, but they are not always correctly taken into consideration. Thermohaline ocean circulation is driven by winter convection and dense water formation processes, which are directly influenced by weather conditions. Subsequently, long-term and climatic changes in circulation and vertical mixing processes directly influence the variability of the ocean biogeochemical properties.

A special role in trapping and/or transporting the biogeochemical properties of seawater is played by travelling eddies; however, this is yet to be quantified. The scientific papers included in this Special Issue try to provide new evidence related to the processes associated with the circulation and mixing in both oceanic areas and semi-enclosed seas.

Table 1. Summary of the nine papers published in the Special Issue "Ocean Exchange and Circulation" in the *Water* Journal (https://www.mdpi.com/journal/water/special_issues/Ocean_Exchange_and_Circulation).

Keywords	Authors	Title	Study Area
remote sensing; high-frequency radar; Malta–Sicily Channel; Malta Sicily Gyre; surface circulation	Reyes–Suarez, N.; Cook, M.; Gačić, M.; Paduan, J.; Drago, A.; Cardin, V.	Sea Surface Circulation Structures in the Malta-Sicily Channel from Remote Sensing Data.	Mediterranean Sea, Malta-Sicily Channel
picoplankton community; deep-sea; Southern Adriatic; Mediterranean Sea	Šantić, D.; Kovačević, V.; Bensi, M.; Giani, M.; Vrdoljak Tomaš, A.; Ordulj, M.; Santinelli, C.; Šestanović, S.; Šolić, M.; Grbec, B.	Picoplankton Distribution and Activity in the Deep Waters of the Southern Adriatic Sea. Water 2019	Mediterranean Sea, Adriatic Sea
Mediterranean Sea; drifters; sub-basin-scale eddies; gliders	Mauri, E.; Sitz, L.; Gerin, R.; Poulain, P.; Hayes, D.; Gildor, H.	On the Variability of the Circulation and Water Mass Properties in the Eastern Levantine Sea between September 2016–August 2017	Mediterranean Sea, Levantine Sea
Sicily Channel; spatial and temporal variability; mesoscale eddies	Menna, M.; Poulain, P.; Ciani, D.; Doglioli, A.; Notarstefano, G.; Gerin, R.; Rio, M.; Santoleri, R.; Gauci, A.; Drago, A.	New Insights of the Sicily Channel and Southern Tyrrhenian Sea Variability.	Mediterranean Sea, Sicily Channel and the Tyrrhenian Sea
Levantine intermediate water formation; Levantine deep water formation; Rhodes Gyre; boundary currents; heat fluxes; Argo floats; dense water formation	Kubin, E.; Poulain, P.; Mauri, E.; Menna, M.; Notarstefano, G.	Levantine Intermediate and Levantine Deep Water Formation: An Argo Float Study from 2001 to 2017	Mediterranean Sea, Levantine Sea
Fram Strait; deep-sea thermohaline variability; slope currents; wind-induced processes; shelf-slope dynamics	Bensi, M.; Kovačević, V.; Langone, L.; Aliani, S.; Ursella, L.; Goszczko, I.; Soltwedel, T.; Skogseth, R.; Nilsen, F.; Deponte, D.; Mansutti, P.; Laterza, R.; Rebesco, M.; Rui, L.; Lucchi, R.; Wåhlin, A.; Viola, A.; Beszczynska-Möller, A.; Rubino, A.	Deep Flow Variability Offshore South-West Svalbard (Fram Strait)	Fram Strait; Greenland Sea; Barents Sea
Kuroshio bifurcation; Luzon Strait; SOM; temporal and spatial variation; sea surface temperature; mesoscale eddy	Sun, R.; Zhai, F.; Gu, Y.	The Four Patterns of the East Branch of the Kuroshio Bifurcation in the Luzon Strait.	Northwest Pacific, Luzon Strait
complex processes; eddies; mobility indicators; splitting and merging; community division; South China Sea	Wang, H.; Du, Y.; Liang, F.; Sun, Y.; Yi, J	A Census of the 1993–2016 Complex Mesoscale Eddy Processes in the South China Sea. Water 2019	South China Sea
tsunami waves; numerical simulation; wave run-up; flow structure; coastal vegetation	Zhang, H.; Zhang, M.; Xu, T.; Tang, J.	Numerical Investigations of Tsunami Run-Up and Flow Structure on Coastal Vegetated Beaches	Theoretical study

2. Oceanic Circulation and Mesoscale Features: Experimental and Modelling Approaches

One paper in this Special Issue represents an example of numerical modelling application, displayed by Zhang et al. [2], where the authors study the interaction of the ocean with the coastal area: in fact, coastal areas are the most densely populated and urbanized, but they are also complex and delicate environments. In coastal areas, waves have a strong impact that can be devastating and produce great damage as well as the loss of human lives. In this case, prevention, through the application of numerical models for case studies, e.g., the impact of tsunami waves, is very important. A depth-integrated numerical model was established to simulate wave propagation in a coastal region with and without forest cover, which could be considered buffer zones able to mitigate the impacts from tsunami waves over coastal areas. Overall, these findings provide cost-effective natural strategies to improve the effectiveness of vegetated bioshields against tsunami hazards.

Other papers in this Special Issue reflect the large interest and importance of mesoscale eddies in a number of semi-enclosed seas of the world ocean. A detailed census of mesoscale eddies and their generation and migration within the South China Sea is presented by Wang et al. [3]. A combined use of satellite measurement data and Hybrid Coordinate Ocean Model (HYCOM) reanalysis data, together with the self-organizing map (SOM) method, was used to investigate the east branch of the Kuroshio bifurcation where four coherent patterns associated with mesoscale eddies in the Pacific Ocean were found [4]. On the other hand, generation mechanisms like wind curl and dense water flow of the mesoscale eddies in the Ionian Sea (central Mediterranean) were addressed and some comparisons between the two forcing mechanisms were discussed in the paper by Menna et al. [5]. The Sicily Channel, in between the eastern and western Mediterranean basins, is another area characterized by large mesoscale variability and water mass exchanges that was analyzed in the paper by Reyez–Suarez et al. [6]. In this paper, data obtained by the High Frequency (HF) radar enabled authors to identify semi-permanent gyres, which were clearly evident from altimetry data also. By using satellite chlorophyll data, authors showed the signal present in the phytoplankton coinciding with altimetry or HF circulation data. Geostrophic flow obtained from the altimetry data fits very well with the HF radar data averaged over a few weeks. The paper presented by Menna et al. [5] deals with such variability more or less in the same area using a combination of long-term, time-series altimetry data, Sea Surface Temperature (SST), and remotely sensed wind data in order to study the seasonal and multiannual variability of mesoscale structures. Wind data allowed the authors to discuss in detail the generation mechanism of mesoscale eddies and the importance of wind stress and wind stress vorticity fields on their seasonal variability.

The role of mesoscale eddies in enhancing the primary production both at the open ocean [7,8] and in semi-enclosed seas (e.g., [9,10]) has been extensively addressed in oceanographic literature ever since the mid-1990s. There is also an important interaction between mesoscale eddies and plankton spatial patterns, and thus the biological features in the ocean are, to a large degree, conditioned by these circulation features [11]. In this issue, picoplankton biomass, distribution, and activity were addressed in the paper by Šantić et al. [12], where the authors used data collected during two Eurofleets2 cruises gathered in the Adriatic Sea (eastern Mediterranean) to compare pre- and post-winter convection phases. The Adriatic Sea is, in fact, one of the main dense water formation sites in the Mediterranean Sea [13], where long-term variability and climatic shifts can produce important effects on the overall circulation of this marginal sea, with possible repercussions on the global thermohaline circulation also [14]. Indeed, despite being a marginal sea, the large-scale dynamical effects linked to the interaction between the Mediterranean water outflow from the Strait of Gibraltar and the Atlantic Ocean has always been the subject of study [15]. The so-called "Meddies", for example, are lenses of warm and salty Mediterranean Water that travel through the North Atlantic at depths between ~500 and 1500 m. They are typically 40–100 km in diameter with their core being 500–1000 m thick [16]. Signatures of the timing of Mediterranean outflow water activity are recorded in the depositional sediment, revealing how the addition of the warm saline water to the cooler less-salty waters of the Atlantic was related to climate change, deep ocean circulation, and plate tectonics [17].

Furthermore, the deep flow variability and the dynamics related to internal waves are analyzed in the paper published by Bensi et al. [18], where the authors take into account the bottom current flows and thermohaline variability in the eastern part of the Fram Strait, which is a crossroad of waters between the North Atlantic and the Arctic Ocean. Starting from a detailed analysis of time series data collected through deep-sea oceanographic moorings, the authors discuss the ocean–atmosphere interactions in a region where they are particularly intense, and where they lead to multiple oceanographic processes, like shelf-slope dynamics, deep water variability through the mixing of Polar and Atlantic waters, as well as sea ice and dense water formation. A strong eddy activity was observed at 1000 m depth in the Fram Strait, associated with the passage of topographically trapped waves enhanced by the atmospheric events particularly intense in the winter season.

A multiplatform approach is an efficient experimental tool to study oceanic features and their evolution in time and space, and this is illustrated successfully in a series of papers in this issue. Based on the analyses of drifters, floats, altimetry, and glider data, the paper by Mauri et al. [19] focuses on quasi-permanent features, i.e., meandering structures and eddies/gyres, in the easternmost part of the Mediterranean Sea [19], which is also a region where the Levantine intermediate water originates from and starts its travel westwards, contributing to the generation of the necessary pre-conditions for the dense water formation in the Aegean, Adriatic, and West Mediterranean basins [20]. In particular, by the visual inspection of more than 800 vertical profiles of temperature, salinity, and potential density gathered from ARGO floats, Kubin et al. [20] detected the timing and evolution, of the Levantine intermediate and deep waters, revealing that, in some conditions, the algorithm used for the detection of the mixed layer depth can underestimate it during winter convection events.

3. Conclusions

This Special Issue contributes to highlight and discuss topics related to the oceanography of semi-enclosed seas and the open ocean. An important number of articles address the theme of mesoscale eddies and their generation/variability by external or internal forcing. In this Special Issue, the effects of mesoscale circulation on biological processes are also covered. The approach to these studies used a broad spectrum of modern measurement techniques that allow for a high temporal and spatial resolution; in this context, fixed-point observations, remote sensing techniques, data from gliders, floats, and drifters are used to a large extent. The characteristics of the circulation on larger spatial scales were also addressed and some important aspects, such as the thermohaline variability of deep layers or the formation of dense water, have been discussed. Future works should be more oriented towards an increasingly enhanced combination of numerical modelling data assimilation techniques and experimental data. Particularly promising results could be obtained from the assimilation of high-frequency radar data, which can also be used very efficiently in submesoscale vortex studies. A multi-platform approach, in addition to optimizing data collection—in terms of quality, also—will bring the scientific community to more efficient monitoring and better predictions of the world ocean processes. This must be a collaborative effort, useful to optimize and integrate ocean observing systems, sensor deployment, and usage [21]. Only with this approach can the scientific community take a step forward in the understanding of climate variability and the anthropogenic effect.

Author Contributions: the two authors contributed equally to the preparation of the article. Conceptualization, M.G. and M.B.; writing—original draft preparation, M.G. and M.B.; writing—review and editing, M.G. and M.B; All authors have read and agreed to the published version of the manuscript.

Funding: This research received no external funding.

Acknowledgments: Thanks are due to the editors of the journal, as well as to the authors who contributed with their articles to the Special Issue. Finally, special thanks go to the anonymous reviewers, who have contributed efficiently to improve the quality of the articles.

Conflicts of Interest: The authors declare no conflict of interest.

References

1. Stammer, D.; Wunsch, C.; Giering, R.; Eckert, C.; Heimbach, P.; Marotzke, J.; Adcroft, A.; Hill, C.N.; Marshall, J. Global ocean circulation during 1992–1997, estimated from ocean observations and a general circulation model. *J. Geophys. Res. Oceans* **2002**, *107*, 1-1-1-27. [CrossRef]
2. Zhang, H.; Zhang, M.; Xu, T.; Tang, J. Numerical Investigations of Tsunami Run-Up and Flow Structure on Coastal Vegetated Beaches. *Water* **2018**, *10*, 1776. [CrossRef]
3. Wang, H.; Du, Y.; Liang, F.; Sun, Y.; Yi, J. A Census of the 1993–2016 Complex Mesoscale Eddy Processes in the South China Sea. *Water* **2019**, *11*, 1208. [CrossRef]

4. Sun, R.; Zhai, F.; Gu, Y. The Four Patterns of the East Branch of the Kuroshio Bifurcation in the Luzon Strait. *Water* **2018**, *10*, 1822. [CrossRef]
5. Menna, M.; Poulain, P.-M.; Ciani, D.; Doglioli, A.; Notarstefano, G.; Gerin, R.; Rio, M.-H.; Santoleri, R.; Gauci, A.; Drago, A. New Insights of the Sicily Channel and Southern Tyrrhenian Sea Variability. *Water* **2019**, *11*, 1355. [CrossRef]
6. Reyes Suarez, N.C.; Cook, M.S.; Gačić, M.; Paduan, J.D.; Drago, A.; Cardin, V. Sea Surface Circulation Structures in the Malta-Sicily Channel from Remote Sensing Data. *Water* **2019**, *11*, 1589. [CrossRef]
7. Falkowski, P.G.; Ziemann, D.; Kolber, Z.; Bienfang, P.K. Role of eddy pumping in enhancing primary production in the ocean. *Nature* **1991**, *352*, 55–58. [CrossRef]
8. McGillicuddy, D.J.; Anderson, L.A.; Bates, N.R.; Bibby, T.; Buesseler, K.O.; Carlson, C.A.; Davis, C.S.; Ewart, C.; Falkowski, P.G.; Goldthwait, S.A.; et al. Eddy/Wind Interactions Stimulate Extraordinary Mid-Ocean Plankton Blooms. *Science* **2007**, *316*, 1021–1026. [CrossRef] [PubMed]
9. Crawford, W.R.; Brickley, P.J.; Thomas, A.C. Mesoscale eddies dominate surface phytoplankton in northern Gulf of Alaska. *Prog. Oceanogr.* **2007**, *75*, 287–303. [CrossRef]
10. Lin, I.-I.; Lien, C.-C.; Wu, C.-R.; Wong, G.T.F.; Huang, C.-W.; Chiang, T.-L. Enhanced primary production in the oligotrophic South China Sea by eddy injection in spring. *Geophys. Res. Lett.* **2010**, *37*. [CrossRef]
11. McGillicuddy, D.J. Mechanisms of Physical-Biological-Biogeochemical Interaction at the Oceanic Mesoscale. *Annu. Rev. Mar. Sci.* **2016**, *8*, 125–159. [CrossRef] [PubMed]
12. Šantić, D.; Kovačević, V.; Bensi, M.; Giani, M.; Vrdoljak Tomaš, A.; Ordulj, M.; Santinelli, C.; Šestanović, S.; Šolić, M.; Grbec, B. Picoplankton Distribution and Activity in the Deep Waters of the Southern Adriatic Sea. *Water* **2019**, *11*, 1655. [CrossRef]
13. Malanotte-Rizzoli, P.; Artale, V.; Borzelli-Eusebi, G.L.; Brenner, S.; Crise, A.; Gacic, M.; Kress, N.; Marullo, S.; Ribera d'Alcalà, M.; Sofianos, S.; et al. Physical forcing and physical/biochemical variability of the Mediterranean Sea: a review of unresolved issues and directions for future research. *Ocean Sci.* **2014**, *10*, 281–322. [CrossRef]
14. Robinson, A.R.; Leslie, W.G.; Theocharis, A.; Lascaratos, A. Mediterranean Sea Circulation. In *Encyclopedia of Ocean Sciences*; Elsevier: Amsterdam, The Netherlands, 2001; pp. 1689–1705. ISBN 978-0-12-227430-5.
15. Özgökmen, T.M.; Chassignet, E.P.; Rooth, C.G.H. On the Connection between the Mediterranean Outflow and the Azores Current. *J. Phys. Oceanogr.* **2001**, *31*, 461–480. [CrossRef]
16. Richardson, P.L.; Bower, A.S.; Zenk, W. A census of Meddies tracked by floats. *Prog. Oceanogr.* **2000**, *45*, 209–250. [CrossRef]
17. Hernández-Molina, F.J.; Stow, D.A.V.; Alvarez-Zarikian, C.A.; Acton, G.; Bahr, A.; Balestra, B.; Ducassou, E.; Flood, R.; Flores, J.-A.; Furota, S.; et al. Onset of Mediterranean outflow into the North Atlantic. *Science* **2014**, *344*, 1244–1250. [CrossRef] [PubMed]
18. Bensi, M.; Kovačević, V.; Langone, L.; Aliani, S.; Ursella, L.; Goszczko, I.; Soltwedel, T.; Skogseth, R.; Nilsen, F.; Deponte, D.; et al. Deep Flow Variability Offshore South-West Svalbard (Fram Strait). *Water* **2019**, *11*, 683. [CrossRef]
19. Mauri, E.; Sitz, L.; Gerin, R.; Poulain, P.-M.; Hayes, D.; Gildor, H. On the Variability of the Circulation and Water Mass Properties in the Eastern Levantine Sea between September 2016–August 2017. *Water* **2019**, *11*, 1741. [CrossRef]
20. Kubin, E.; Poulain, P.-M.; Mauri, E.; Menna, M.; Notarstefano, G. Levantine Intermediate and Levantine Deep Water Formation: An Argo Float Study from 2001 to 2017. *Water* **2019**, *11*, 1781. [CrossRef]
21. Pearlman, J.; Bushnell, M.; Coppola, L.; Karstensen, J.; Buttigieg, P.L.; Pearlman, F.; Simpson, P.; Barbier, M.; Muller-Karger, F.E.; Munoz-Mas, C.; et al. Evolving and Sustaining Ocean Best Practices and Standards for the Next Decade. *Front. Mar. Sci.* **2019**, *6*, 277. [CrossRef]

water

MDPI

Article

Levantine Intermediate and Levantine Deep Water Formation: An Argo Float Study from 2001 to 2017

Elisabeth Kubin [1,*], Pierre-Marie Poulain [1,2], Elena Mauri [1], Milena Menna [1] and Giulio Notarstefano [1]

[1] National Institute of Oceanography and Experimental Geophysics, OGS, 34010 Sgonico (TS), Italy
[2] Centre for Maritime Research and Experimentation, CMRE, 19126 La Spezia, Italy
* Correspondence: ekubin@inogs.it

Received: 12 July 2019; Accepted: 23 August 2019; Published: 27 August 2019

Abstract: Levantine intermediate water (LIW) is formed in the Levantine Sea (Eastern Mediterranean) and spreads throughout the Mediterranean at intermediate depths, following the general circulation. The LIW, characterized by high salinity and relatively high temperatures, is one of the main contributors of the Mediterranean Overturning Circulation and influences the mechanisms of deep water formation in the Western and Eastern Mediterranean sub-basins. In this study, the LIW and Levantine deep water (LDW) formation processes are investigated using Argo float data from 2001 to 2017 in the Northwestern Levantine Sea (NWLS), the larger area around Rhodes Gyre (RG). To find pronounced events of LIW and LDW formation, more than 800 Argo profiles were analyzed visually. Events of LIW and LDW formation captured by the Argo float data are compared to buoyancy, heat and freshwater fluxes, sea surface height (SSH), and sea surface temperature (SST). All pronounced events (with a mixed layer depth (MLD) deeper than 250 m) of dense water formation were characterized by low surface temperatures and strongly negative SSH. The formation of intermediate water with typical LIW characteristics (potential temperature > 15 °C, salinity > 39 psu) occurred mainly along the Northern coastline, while LDW formation (13.7 °C < potential temperature < 14.5 °C, 38.8 psu < salinity < 38.9 psu) occurred during strong convection events within temporary and strongly depressed mesoscale eddies in the center of RG. This study reveals and confirms the important contribution of boundary currents in ventilating the interior ocean and therefore underlines the need to rethink the drivers and contributors of the thermohaline circulation of the Mediterranean Sea.

Keywords: Levantine intermediate water formation; Levantine deep water formation; Rhodes Gyre; boundary currents; heat fluxes; Argo floats; dense water formation

---

1. Introduction

The Mediterranean Sea (Figure 1) is composed of two basins of nearly equal size, the Western and the Eastern Mediterranean Sea, connected by the Sicily Channel. The general circulation of the Mediterranean Sea can be divided into three dominant scales of motion: the basin scale including the thermohaline circulation, the sub-basin scale including permanent and quasipermanent cyclonic and anticyclonic gyres, and the mesoscale with small but energetic temporary eddies [1,2]. All these scales are interacting.

Through the Strait of Gibraltar, the relatively fresh Atlantic water (AW) enters the Western Mediterranean Sea within the upper 100 to 200 m. It is modified flowing eastward, passes the Sicily Channel and the Ionian Sea and enters the easternmost part of the Mediterranean, the Levantine Sea. The salinity of the AW in the Levantine Sea depends on the circulation patterns during its path, mainly influenced by the variability of the circulation of the North Ionian Gyre (NIG) which varies significantly at seasonal and decadal scales ([3–5]; Figure 1a).

Due to evaporation and air–sea exchanges, the AW is becoming saltier and warmer when reaching the Levantine Sea. The AW that enters the Levantine Sea is identified by a subsurface minimum of $S < 38.6$ psu and by a temperature of 14–15 °C. The Levantine intermediate water's (LIW) properties are defined by salinity values greater than 39 psu, potential temperature values greater than 15 °C and potential density values between 29 and 29.05 kgm^{-3} while typical ranges for Levantine deep water (LDW) are 13.7–14.5 °C and 38.8–38.9 psu [6].

The strong advective surface salinity preconditioning [7] and buoyancy losses due to heat and freshwater fluxes in winter lead to dense water formation, sinking takes place, and the LIW is formed (Figure 1a). The LIW is characterized by a subsurface salinity maximum and occupies and moves in the intermediate layers between 200 and 600 m throughout the Mediterranean Sea until it reaches the Atlantic Ocean through the Strait of Gibraltar. Therefore, the LIW contributes as an important driver to the thermohaline circulation of the Mediterranean Sea. The specific pathways of the thermohaline circulation depend strongly on where and when the LIW is formed.

According to the prevailing view, the LIW formation takes place within the cyclonic Rhodes Gyre (RG) during the winter months ([1,8], Figure 1a). However, experimental studies showed that the RG is also a place of LDW formation and that the Levantine basin is a site of multiple and different water mass formation processes [6,9,10]. Furthermore, recent theoretical models revealed that no net mean sinking takes place within Mediterranean convection sites such as the RG, while boundary currents undergo net intense sinking ([11–16]; mean from 1980 to 2013 for all seasons; Figure 1c). This is due to vorticity dynamics: Only dissipation at the boundary (and bottom friction) can balance the vortex stretching that arises from vertical motions induced by net sinking.

The focus of this study is on the Northwestern Levantine Sea (NWLS; latitude: 33°–37°, longitude: 26°–32°; red rectangle in Figure 1b), the larger area around the RG, including also the area along the Northern coast. The NWLS is characterized by a general cyclonic surface circulation and the presence of the permanent RG, cyclonic and anticyclonic structures (such as Ierapetra (IG) and Mersa-Matruh Eddy (MME)), intense jets (such as the Mid Mediterranean Jet (MMJ); with minimum subsurface salinity values), a strong coastal current along the Northern coastline (the Asia Minor Current (AMC)), and the passage from the Cretan to the Levantine Sea ([17], Figure 1b).

This study aims to describe where and when LIW and LDW formation take place within the NWLS, using Lagrangian Argo float data over a period of 16 years. The results were compared to heat and freshwater fluxes and satellite data (SSH, SST).

Dense water formation processes occur on daily scales and are linked to temperature and salinity extrema which are not represented using climatological data sets or mixed layer depth (MLD) detection algorithms. Therefore, more than 800 Argo float profiles from 2001 to 2017 were analyzed visually to investigate LIW and LDW formation during winter months.

The paper is organized as follows: In Section 2, the data sets and analysis methods are presented. In Section 3, the time evolution of the heat and freshwater fluxes from 2001 to 2017 for the center of the RG are shown to identify periods of extreme heat losses due to outbreaks of strong cold and dry winds leading to dense water formation. Section 3 gives two examples of the LDW formation within the RG and one example of the typical LIW formation along the Northern coastline and characterizes the newly formed water masses. Section 4 gives an overall discussion and summarizes the major results of this work.

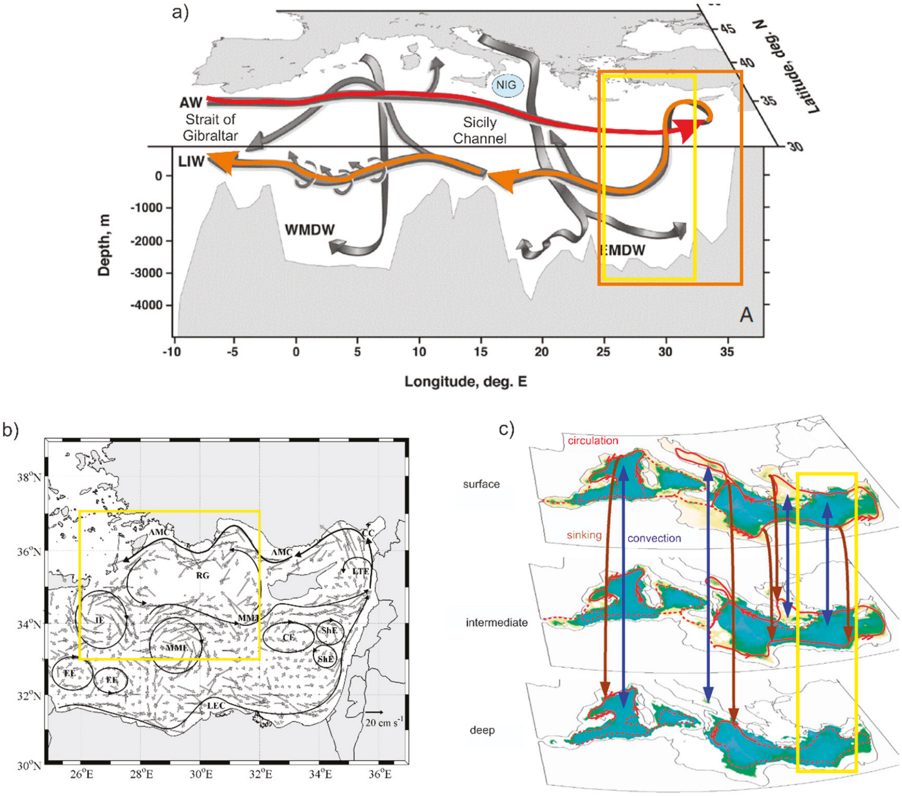

Figure 1. (**a**) General concept of the thermohaline circulation which, according to the prevailing view, is driven by a few convection sites within the Mediterranean Sea, adapted from [1]. The red arrow shows the entering Atlantic water (AW) while the orange arrow shows the Levantine intermediate water (LIW), which travels throughout the Mediterranean and flows into the Atlantic Ocean. The orange and yellow frames highlight the area of the Levantine Sea and of the Northwestern Levantine Sea (NWLS), respectively. The blue circle indicates the position of the North Ionian Gyre (NIG) the circulation of which is important for the advective salinity preconditioning. (**b**) Mean surface geostrophic circulation in the Levantine Sea from 1992 to 2010 derived from drifter data. The yellow rectangle indicates the area of study, the NWLS (latitude: 33–37°, longitude: 26–32°). Adapted from [17]. AMC—Asia Minor Current; CC—Cilician Current; CE—Cyprus Eddy; EE—Egyptian Eddies; IE—Ierapetra Eddy; LEC—Libyo-Egyptian Current; LTE—Latakia Eddy; MME—Mersa-Matruh Eddy; MMJ—Mid Mediterranean Jet; ShE—Shikmona Eddy. (**c**) A model run from 1980 to 2013 [15] showed that little to no net sinking takes place at convection sites (blue arrows; from left to right: Gulf of Lion, South Adriatic, Aegean Sea, Rhodes Gyre (RG)) while boundary layer currents undergo net intense sinking (brown arrows). The yellow rectangle indicates the area of study. Adapted from [15].

2. Datasets and Methods

The datasets used for this study are Argo floats vertical profiles of temperature and salinity (T/S) collected in the NWLS during winter months (January, February, March—JFM) between 2001 and 2017. In total 879 T/S profiles from 20 floats were analyzed visually. Figure 2 shows the position of the Argo float profiles and the annual distribution of profiles for JFM between 2001 and 2017 for the area of study.

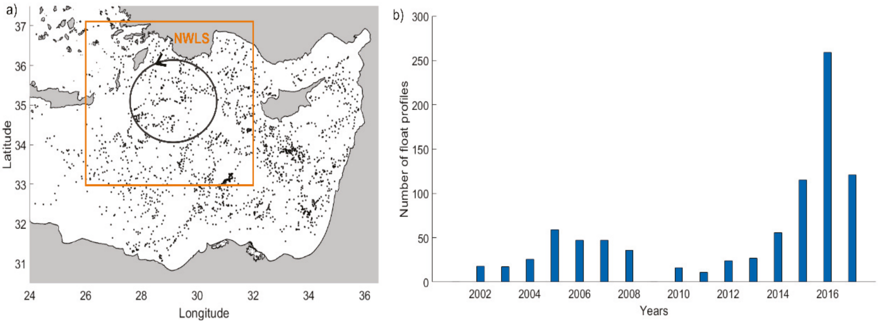

Figure 2. (**a**) Position of the 879 analyzed float profiles for January, February, and March (JFM) 2001–2017; Orange rectangle defines the area of study (the NWLS), the black ellipse describes the center of RG. (**b**) Annual distribution of float profiles in the NWLS: JFM 2001–2017.

With the help of an external bladder, the Lagrangian floats descend to a programmed parking depth (350 or 1000 m) where they stay for a specified period (1–10 days, mainly 5 days [18]). Then, they descend to greater depths (up to 2000 m). During their ascent back to the surface, they measure temperature and salinity throughout the water column. At the surface they transmit the data to satellites and descend again. The transmitted data are stored at data assembly centers (DAC) which apply a quality control and provide open access to real time and delayed mode quality controlled data.

Quality controlled Argo float data were downloaded from the Ifremer Data Assembly Center (DAC; ftp://ftp.ifremer.fr/ifremer/argo/dac/coriolis/). For this study, only data with the best quality control (qc=1) were taken into account. Downloaded parameters included float number, position, time, pressure, temperature, and salinity.

Hydrographic properties were expressed as potential temperature, potential density, and salinity according to the practical salinity scale (PSU).

The visual inspection of the Argo float profiles is important due to the fact that the Argo floats may pass an area not exactly during the event of mixing or convection. They can instead sample days or weeks later when the recapping (i.e., a newly formed shallow MLD) already occurred. In such a case, MLD detection algorithms indicate a shallow MLD, but do not give any information about mixing or convection events before the recapping. While at the top, there can be already a newly formed MLD and the convection event can still be visible deeper in the water column. MLD detection statistics rarely give information about deep mixing events while the visual inspection of the form of the profile (potential temperature, salinity, and potential density) reveals clearly such events. Figure 3a shows the climatology of the winter maximum MLD derived from Argo float data and downloaded from [19] in the period 2000 to 2018. The maximum MLD is 225 m along the coastline of the NWLS (Figure 3a). The visual inspection of the Argo profiles in the same region reveals deeper dense water formation events. For example, in winter 2007, the float WMO 6900098 (Figure 3b), moving along the northern coastline of the NWLS, shows the deepening of the winter MLD from 100 m (Figure 3c) to 200 m (Figure 3d) in January. In March, when the maximum MLD is about 550 m, the recapping occurred (due to surface warming) with a newly formed MLD of about 50 m (Figure 3e). In this case, the MLD detention algorithm can fail, indicating the depth of 50 m as maximum MLD.

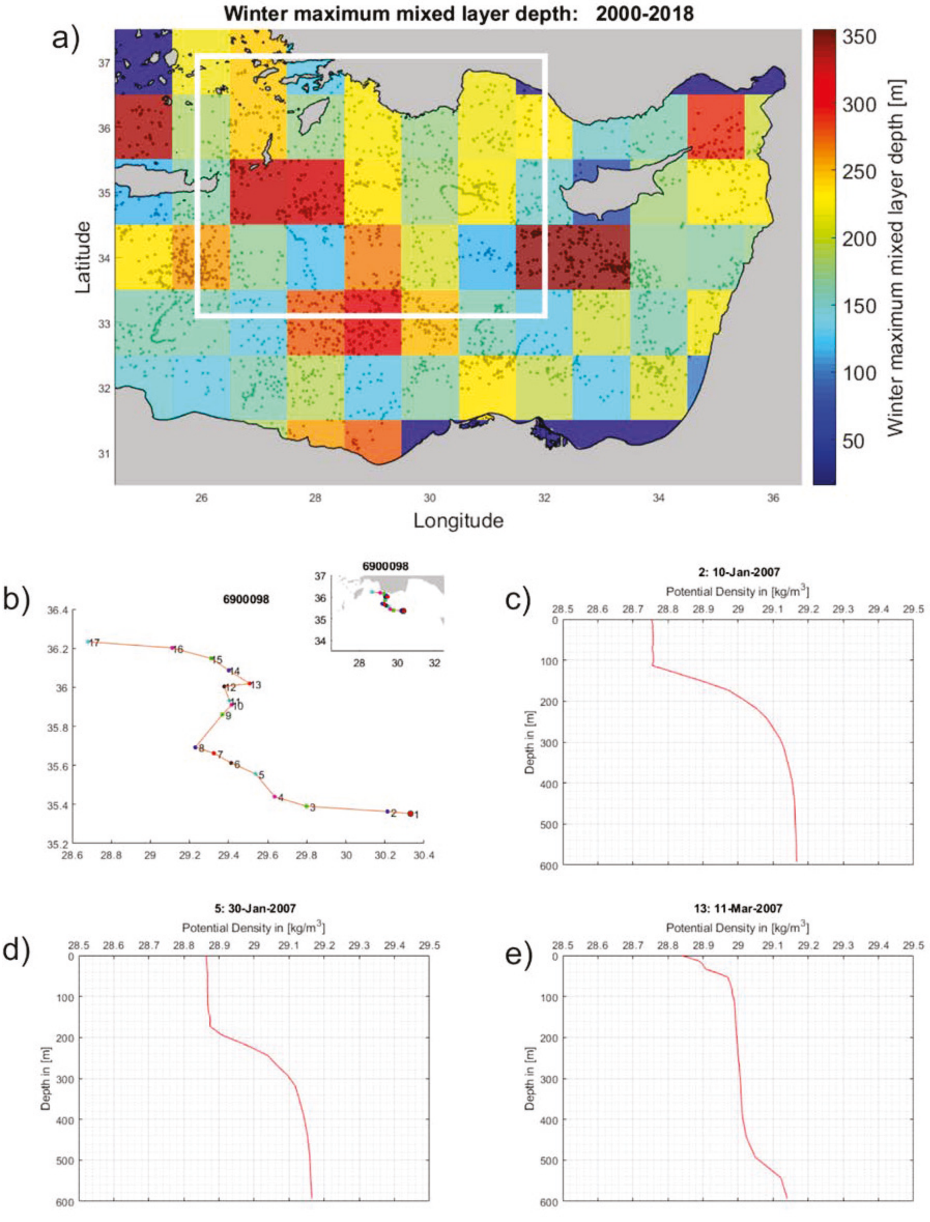

Figure 3. (**a**) Climatology of the winter maximum mixed layer depth (colors) and location of float profiles (grey dots) from 2000 to 2018. The white rectangle indicates the area of study, the NWLS. (**b**) Trajectory of the float WMO 6900098 during JFM 2007; the numbers along the trajectory show the locations of float profiles. Float potential density profiles at cycle 2 (**c**), 5 (**d**), and 13 (**e**).

The SST and sea surface height (SSH) data were downloaded from Copernicus (marine.copernicus.eu). The interpolated SST product (SST_MED_SST_L4_NRT_OBSERVATIONS_010_004_c_V2) has a daily temporal resolution and a spatial resolution of 0.04° × 0.04°. The interpolated SSH product

(SST_MED_SST_L4_REP_OBSERVATIONS_010_021) has a daily temporal resolution and a spatial resolution of 0.125° × 0.125°. Monthly means of SST superimposed with the geostrophic currents from SSH were used to describe the negative slope of eddies within the RG during intense convection events.

The freshwater fluxes were derived from ERA-INTERIM (daily) data. The downloaded parameters are evaporation (E) and total precipitation (P). The downloaded data have a time step of 12 hours, i.e., daily data at 00:00:00 and at 12:00:00 and a spatial resolution of 0.25° × 0.25°. The daily freshwater fluxes (FWF) were calculated as the subtraction of the daily means of E and P: FWF=E−P.

The air–sea heat fluxes were derived from ERA-INTERIM (daily) data. The downloaded parameters are: Surface net solar radiation (Q_{sw}), surface net thermal radiation (Q_{lw}), surface sensible heat flux (Q_s), and surface latent heat flux (Q_l). The heat budget can be expressed as the difference between the net shortwave solar radiation (incoming minus reflected) absorbed by the sea surface, the sum of the longwave back radiation, the sensible, the latent, and the advective heat flux. The advective heat flux (Q_{adv}) was not available at ERA-INTERIM and therefore not considered. The downloaded data have a time step of 12 hours, i.e., daily data at 00:00:00 and at 12:00:00 and a spatial resolution of 0.25° × 0.25°. The daily mean of each parameter as well as the daily net heat fluxes were calculated as the sum of the daily means of each parameter: $Q_{net} = Q_{sw} + Q_{lw} + Q_l + Q_s$. The surface buoyancy flux B, composed by thermal (B_T) and haline (B_S) components, was calculated according to [20]:

$$B = \alpha \times g \times (Cp \times \rho_0)^{-1} \times Qnet - \beta \times S_0 \times g \times (\rho_0)^{-1} \times (E-P)$$

where α is the thermal expansion coefficient, $g = 9.8\ ms^{-2}$ is the gravity acceleration, $Cp = 3.9715 \times 10^{-3}\ Jkg^{-1}K^{-1}$ is the specific heat capacity of sea water, $\rho_0 = 1029\ kgm^{-3}$ is a reference sea water density, β is the haline contraction coefficient and $S_0 = 38.9$ is a reference salinity. α and β were calculated at surface pressure, using monthly mean surface salinity and monthly mean surface temperature, downloaded from Copernicus (MEDSEA_REANALYSIS_PHYS_006_004). B is positive when surface water gets lighter and negative when surface water becomes denser (river inputs as well as horizontal and vertical advection also contribute to density changes, but were not considered due to lack of data).

The Turner angle (Tu) was computed to evaluate the relative roles of temperature and salinity gradients on the density gradients. Tu is defined as the four-quadrant arctangent [21], which units are degrees of rotation and was calculated with the Gibbs-SeaWater (GSW) Oceanographic Toolbox [22]. Argo float salinity and temperature were converted to absolute salinity and to conservative temperature, respectively. The conservative temperature represents more accurately the heat content [22].

$Tu = 45°$ indicates that temperature is the only contributor, while $Tu = -45°$ indicates that salinity is the only contributor to density changes; $|Tu| < 45°$ indicates stable stratification and in this condition both temperature and salinity contribute to the density change ; $45° < Tu < 90°$ shows that salinity is working against temperature and is also called the 'salt finger regime' with the strongest activity near 90°; $-90° < Tu < -45°$ is called the 'diffusive regime' and shows that temperature is working against salinity, reaching the strongest activity near −90°; $|Tu| > 90°$ characterizes a statically unstable water column (where the Brunt–Vaisalaa frequency $N_2 < 0$).

3. Results

3.1. Heat and Freshwater Fluxes within the Northwestern Levantine Sea

The intensity of the mixing and convection events depends mainly on the surface buoyancy fluxes B, which in turn depend on the heat fluxes through the air–sea interface, scaled by the thermal expansion coefficient α, and the freshwater fluxes, scaled by the haline contraction coefficient β. Monthly surface buoyancy fluxes and their thermal and haline (freshwater) components, integrated over the center of RG (longitude: 28–31°E, latitude: 34–36°N), are shown in Figure 4.

Table 1. Pronounced (mixed layer depth (MLD) >250 m) dense water formation events within the center of RG and along the Northern coastline: Area of formation, float WMO, time period, watermass characteristics, and maximum depth during the dense water formation events.

Area of Formation	Float WMO	Time Period	Water Mass Characteristics	Maximum Depth
RG	6900098	FM 2004	LDW	At least 600 m, probably 1000 m [1]
RG	6900098	FM 2005	LDW	At least 600 m, probably 1000 m [1]
RG	6900098	JF 2006	LDW	At least 600 m, probably 1000 m [1]
RG	6900098	FM 2008	LDW	At least 600 m, probably 1000 m [1]
COAST	6900098	M 2007	LIW	About 550 m
COAST	6900843	FM 2012	LIW	About 350 m
COAST	6901824	FM 2015	LIW	About 350 m
COAST	6901868	FM 2016	LIW	About 300 m

[1] T/S plots show the formation of dense water with a potential density that corresponds to the density of the upper deep boundary layer which is found at approximately 1000 m depth [23].

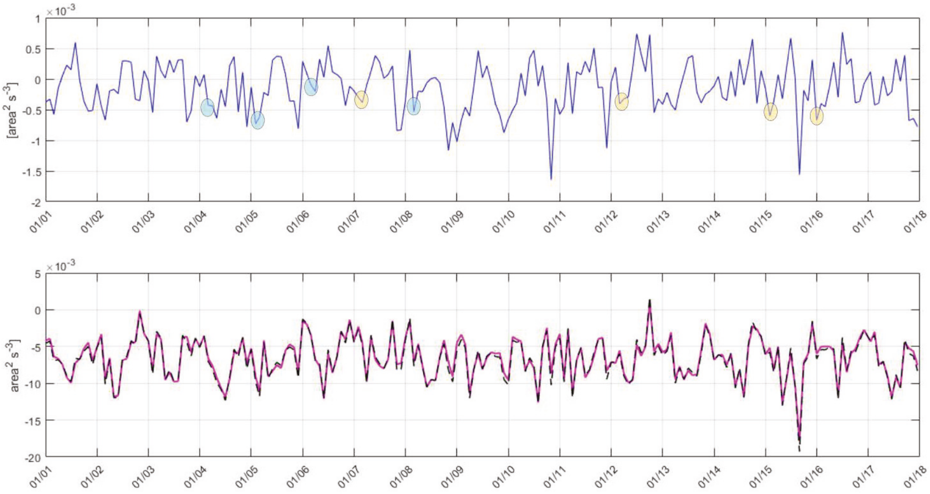

Figure 4. Upper panel: Time series of the monthly thermal component (B_T) from 2001 to 2017, integrated over the center of RG (longitude: 28–31°E, latitude: 34–36°N). Blue and yellow circles indicate events of pronounced dense water formation detected by the Argo floats within RG and along the coastline, respectively (Table 1). **Lower panel:** Time series of the monthly haline component (B_S; magenta line) and buoyancy fluxes (B; black dotted line).

The haline components (B_S) dominate the surface buoyancy fluxes (Figure4, Lower Panel), i.e., that intense evaporation, especially during the preconditioning phase (e.g., Figure 8 for winter 2006), controls the surface buoyancy loss. Detected events of pronounced (i.e., with a MLD deeper than 250 m) dense water formation by the Argo float data, are indicated with blue (RG) and yellow (coastline) circles (Table 1).

The climatology of monthly heat fluxes Qnet for the center of RG from 2001 to 2017 shows that the largest heat losses which induce the preconditioning phase occurred mainly in November and in December (Figure 5). The subsequent heat losses in JFM induce the formation of dense water and therefore lead to convection and mixing.

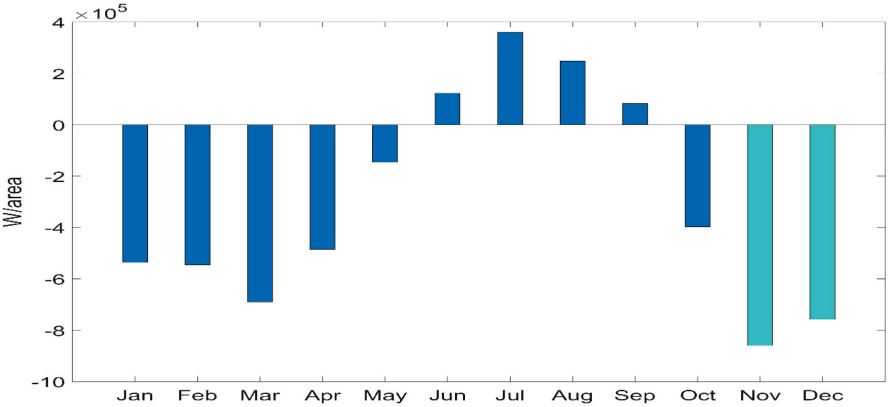

Figure 5. Climatology of monthly integrated heat fluxes for the center of RG from 2001 to 2017. Main heat losses generally occur in November and December (turquoise bars) and initiate the preconditioning phase. Subsequent heat losses in January, February, and March induce dense water formation.

3.2. LIW and LDW Formation within the Northwestern Levantine Sea

Intermediate and deep water formation events in the NWLS (latitude: 33–37°N, longitude: 26–32°E) were analyzed during the winter months (JFM) from 2001 to 2017 (879 T/S profiles from 20 floats). Most of the float profiles within the NWLS showed 'regular' winter MLDs, i.e., MLDs between 100 and 200 m. Pronounced dense water formation, i.e., with a MLD deeper than 250 m, occurred only within the center of RG, along the Northern coastline and along the Cretan Arch passage. Events of pronounced LDW (13.7 °C < potential temperature < 14.5 °C, 38.8 psu < salinity < 38.9 psu) and 'lower range' LIW (potential temperature around 15 °C and salinity around 39 psu) formation were detected within the center of RG in winter 2004, 2005, 2006, and 2008 and events of pronounced LIW formation (potential temperature > 15 °C and salinity > 39 psu) were detected along the Northern coastline in winter 2007, 2012, 2015. and 2016 (Table 1). More than 800 profiles of 20 floats were analyzed, but only four floats (Tables 1 and 2) captured pronounced dense water formation, being at the right place at the right time. To document the dense water formation events the float had to be either inside or pass later through the area of dense water formation. Float WMO 6900098 had an exceptionally long lifetime of nearly 6 years and therefore it was able to capture one event of pronounced LIW formation along the Northern coastline and four events of pronounced DWF. Unfortunately, it stopped measuring at 600 m depth. The WMO numbers of the Argo floats that found pronounced dense water formation events within the center of RG and along the coastline are listed in Table 2.

Table 2. Argo floats capturing pronounced (MLD >250 m) dense water formation events.

Float Number	Float Description
WMO 6900098	Apex Profiling Float, Naval Oceanographic Office (NAVO) Alive from 20.07.2003 to 19.04.2009, lifetime approximately 5 years Parking depth (PD)=1000 m; 5 day cycle;
WMO 6900843	Apex Profiling Float, Argomed, Euro-Argo Alive from 03.10.2011 to 31.5.2014, PD=350 m; 5 day cycle;
WMO 6901824	Arvor Profiling Float, Argo Italy, Argomed, Euro-Argo Alive from 04.11.2013 to 03.02.2018, PD=350 m; 5 day cycle;
WMO 6901868	Apex Profiling Float, Argo Italy, Euro-Argo Alive from 01.12.2014 to 29.07.2017. PD=350 m; 5 day cycle;

3.2.1. LDW formation within the Rhodes Gyre

Two examples of LDW formation within RG are given in this subsection.

(1) In JFM 2006, float WMO 6900098 was entrapped in the center of RG (Figure 6a). Hoevmueller plots of salinity, potential temperature, and potential density describe two pronounced events of mixing and convection during this winter (Figure 6b–d). The first event occurred by the end of January until mid-February and led to LDW formation (13.7 °C < potential temperature < 14.5 °C, 38.8 psu < salinity < 38.9 psu) while the second event around mid-March led to LDW and 'lower range' LIW (temperature about 15°C and salinity about 39 psu) formation.

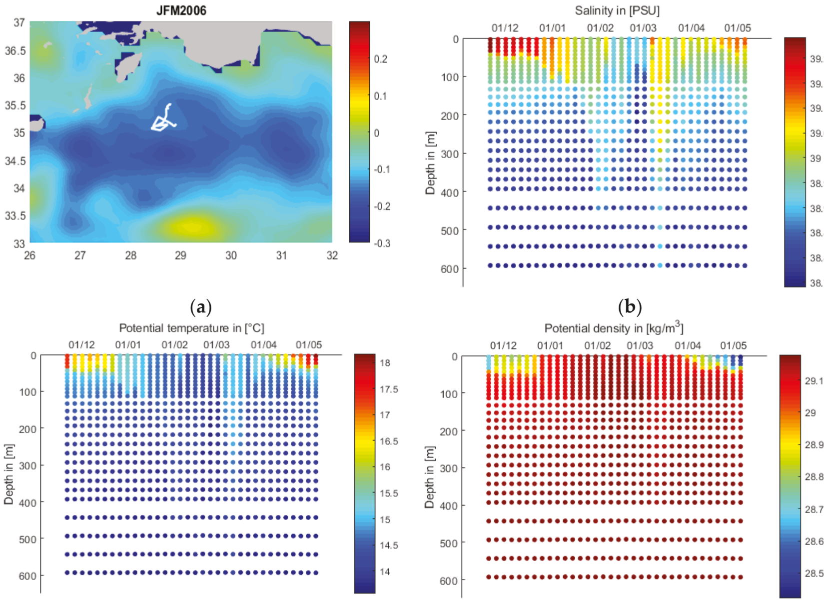

(**a**) (**b**) (**c**) (**d**)

Figure 6. (**a**) Mean sea surface height (SSH, m) and float trajectory of float WMO 6900098 for JFM 2006. (**b**) Salinity (PSU), (**c**) potential temperature (°C) and (**d**) potential density (kg/m^3) from December 2005 to April 2006.

In December, very high surface salinity values (S > 39.15 psu) were detected in the upper 50 m (Figure 6b). However, mixing and convection is still prevented by relatively high surface temperatures during December. The surface temperature has a decreasing trend from 17.5 °C by the beginning of

December to 15.5 °C in early January and reached a minimum of about 14 °C from the end of January to the end of February. From the beginning of March, the surface temperature gradually increased, reaching 15.5 °C during March with a successive increase to 17.5 °C by the end of April.

The MLD deepens from 50 m within December to about 100 m in the beginning of January and the high surface salinity is mixed to intermediate layers.

By the end of January, when lowest surface temperatures (T = 14–14.5 °C) are reached, dense water formation starts to occur. Potential density reaches its highest values (29.1 kg/m^3) by the end of January until mid-February and the examination of single profiles shows that deep convection takes place down to at least 600 m during this period.

The Hoevmueller plot of the Turner angle (Figure 7) reveals statically unstable conditions (|Tu|> 90°; dark blue and dark red points) from mid-January to the end of March and indicates the deep dense water formation events down to at least 600 m in February and March 2006. The deep dense water formation events are characterized by a stronger contribution of temperature (−45° < Tu < −90°; blue points), while the main contributor to the stable stratification in December and April is mainly the salinity (45° < Tu < 90°; yellow and light orange points).

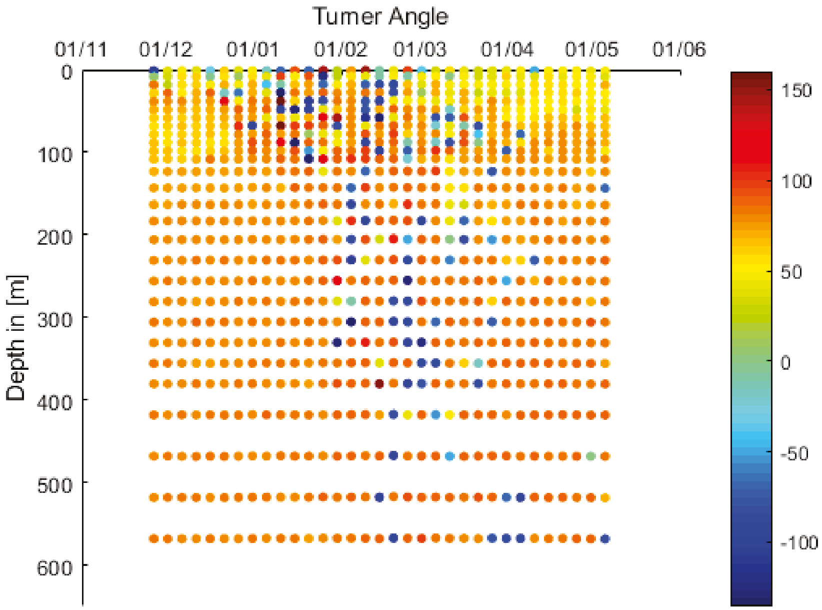

Figure 7. The Turner angle (°) of float WMO 6900098 describes the contribution of salinity and temperature gradients to the density gradient.

The heat and freshwater fluxes integrated over the center of RG show an intense preconditioning phase during December 2005, due to strong dry and cold winter winds which led to heat losses (Figure 8a) and evaporation (Figure 8b) and consequently to high surface salinity values. Additional heat losses by the end of January and the beginning of February coincide with the LDW formation event within the RG described above. The heat losses in mid-March coincide with the second dense water formation event within RG which led to a mixture of LDW and 'lower range' LIW formation.

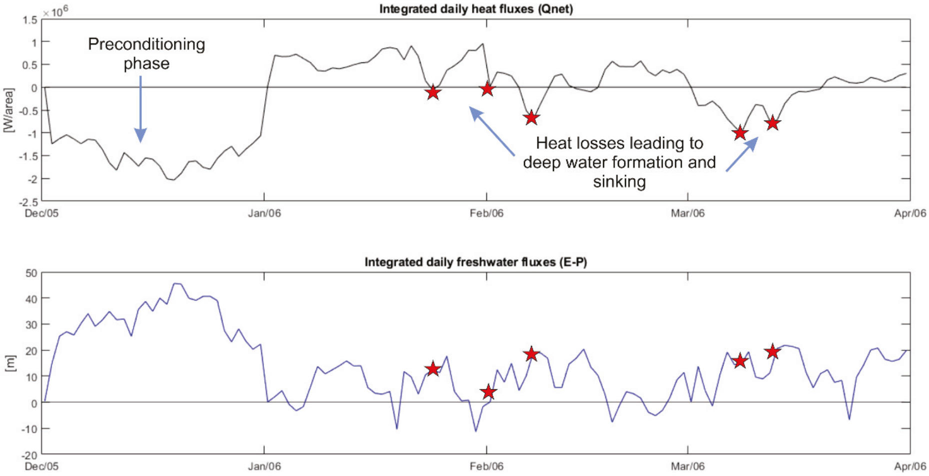

Figure 8. Upper panel: Time series of integrated daily surface heat fluxes from December 2005 to April 2006 for the center of Rhodes Gyre. The heat losses by the end of January and mid-February induced deep convection and formation of Levantine deep water (LDW) while the heat losses in March induced mixing and formation of LDW and 'lower range' LIW (see also Figure 6). **Lower panel:** Time series of integrated daily freshwater fluxes for the same time period as the above panel. The freshwater fluxes in December show a strong evaporation which led to increased surface salinity as shown by the Argo float data (Figure 6b).

This deep convection event from the end of January until mid-February coincides with a strong depression of SSH within the RG area during that time, overlapping the exact position of the float (longitude: 28.5–29°E, latitude: 35–35.5°N; Figure 9). Figure 9a shows the float trajectory and mean SSH of January, February, and March 2006 while Figure 9b,c,d show the negative daily SSH and geostrophic currents for three specific days during the period of deep convection event from the end of January to mid-February. The eddy in which the float was trapped, represents the strongest depression (SSH < −0.3 m; about 20 cm below the seasonal mean (Figure 9a)) during winter months reaching a negative maximum during the days of deep water formation (Figure 6b–d).

The mesoscale eddy during that time shows a diameter of about 60 km which is within the typical mesoscale eddy diameter within the Levantine Sea (40–80 km).

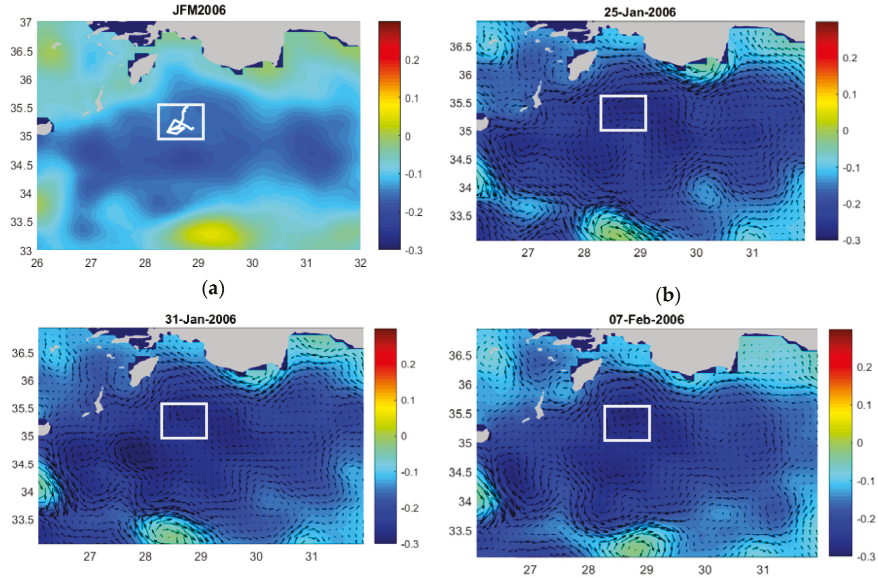

(**a**) (**b**) (**c**) (**d**)

Figure 9. (**a**) Trajectory of float WMO 6900098 depicted within white rectangle overlaid on mean SSH (m) for JFM 2006 for the NWLS. (**b–d**) daily SSH (m) during the LDW convection events (from 25 January to 7 February 2006). The mesoscale eddy within the white box has a diameter of about 60 km.

Figure 10 shows the monthly means of satellite SST superimposed on the geostrophic currents derived from SSH. The deep convection event occurred by the end of January until mid-February 2006 when the sea surface temperature was lowest. The lowest surface temperatures measured by the Argo float, evidenced within the Hoevmueller plots (Figure 6c), coincide with lowest temperatures by daily satellite SST (Figure 10e,f) and with the strongest depression of SSH (Figure 9b–d) by the end of January until mid-February.

Figure 11 shows the T/S plots for the two events of dense water formation during JFM 2006. Water masses above 100 m were not taken into account for the T/S plot to exclude shallow MLDs and recapping and to capture the events of pronounced intermediate and deep water formation. Water masses from 100 to 500 m are plotted with a green dot while water masses under 500 m are plotted with blue dots.

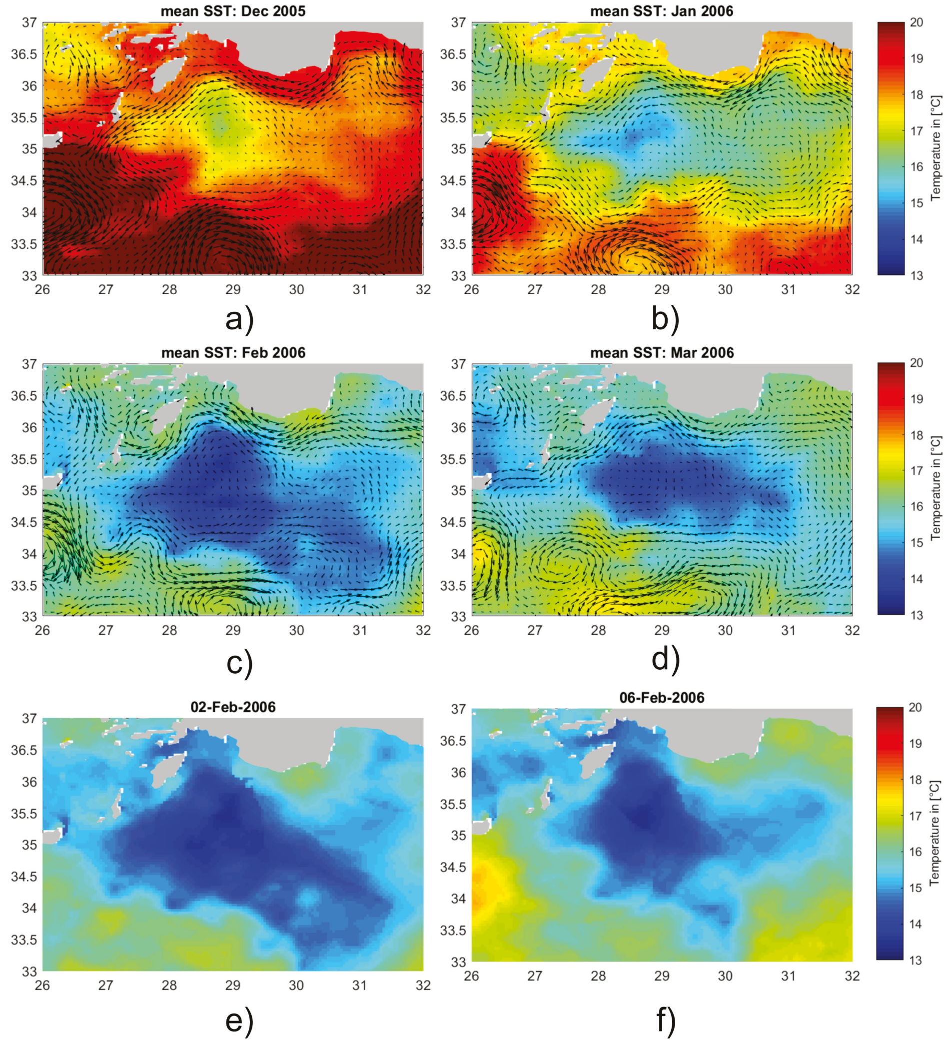

Figure 10. Monthly means of sea surface temperature (SST, °C) and geostrophic currents for (**a**) December 2005, (**b**) January, (**c**) February, and (**d**) March 2006. Daily SST (°C) of (**e**) 2 February 2006 and (**f**) 6 February 2006. Dense water formation and the deep convection event occurred by the end of January until mid-February when SST was lowest.

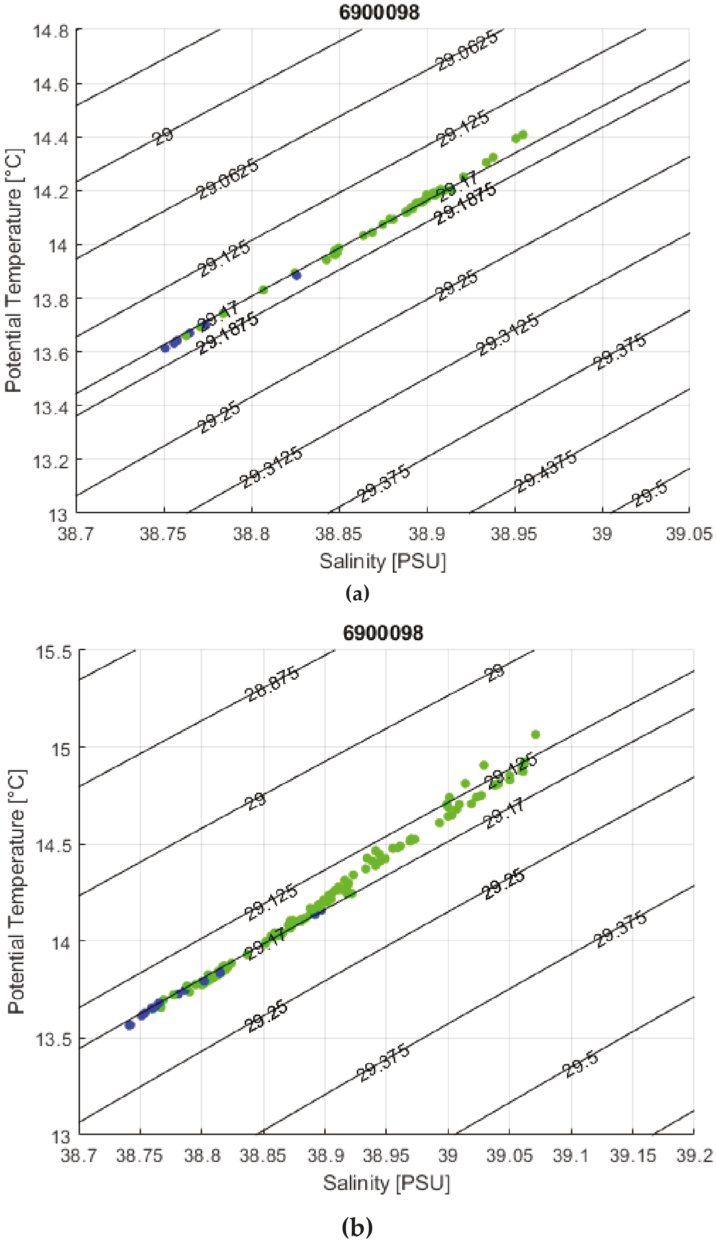

Figure 11. (**a**) The temperature and salinity (T/S) plot for float WMO 6900098 from 20 January to 20 February 2006 indicates LDW formation. The additional density line with a potential density value of 29.17 kgm^{-3} shows the upper deep-water boundary density which corresponds to approximately 1000 m depth for the NWLS [23]. (**b**) T/S plot for float WMO 6900098 for March 2006 indicates a mixture of LDW and 'lower range' LIW formation. Green dots represent depths from 100 to 500 m while blue dots represent depths from 500 to 600 m.

Figure 11a shows the T/S plot for the first dense water formation event: The potential temperature exhibits values smaller than 14.5 °C, the salinity shows values smaller than 39 psu, and the potential density shows a constant value of about 29.17 kg/m^3. The typical ranges for LDW for potential temperature are between 13.7 °C and 14.5 °C and for salinity between 38.8 to 38.9 psu [6,9,10]. The potential density line of 29.17 kgm^{-3} represents the upper deep-water boundary density for the NWLS, corresponding to approximately 1000 m depth [23]. All potential temperatures and salinity values lay on the line of constant potential density of 29.17 kgm^{-3}, i.e., that the formed water masses sank to at least 1000 m, until the same potential density was reached. Therefore, the T/S plot confirms that LDW took place during the first event by late January until mid-February (Figure 11a).

For the dense water formation event in March 2006, the T/S plot shows potential temperatures smaller than 15 °C, salinities smaller than 39.1 psu, and potential densities between 29.125 kg/m^3 and 29.17 kg/m^3. By nearly reaching 15 °C and with some salinity values above 39 psu, a part of the water mass reaches the lower range of LIW water mass characteristics (Figure 11b). This indicates a mixture of LDW and 'lower range' LIW formation during the second dense water formation event within RG.

(2) LDW formation took also place from the end of February until mid-March 2004 within another cyclonic mesoscale eddy located in the western part of the RG. Hoevmueller plots for DJFMA for salinity, potential temperature, and potential density are shown in Figure 12. During January and February, the MLD deepens constantly and the event of LDW formation occurs by the end of February until mid of March when the minimum surface temperature was reached. The examination of single profiles shows convection down to at least 600 m.

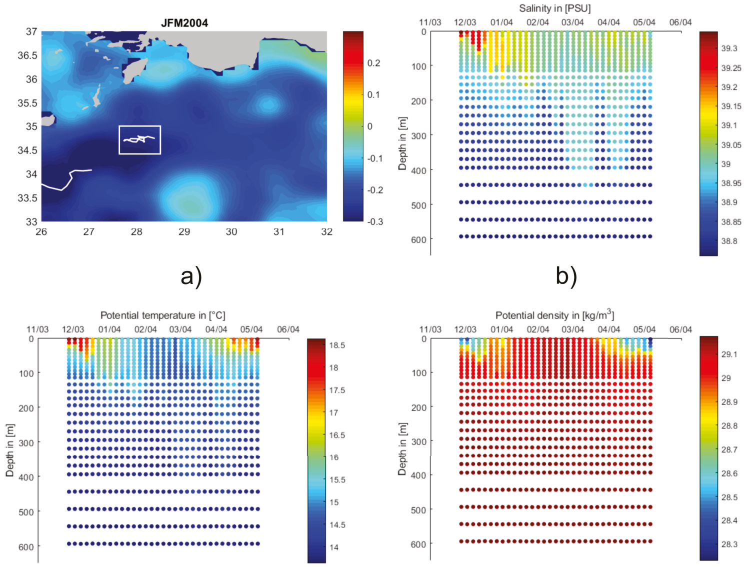

a) b)

c) d)

Figure 12. (**a**) Mean SSH (m) of the Northwestern Levantine Sea and float trajectory of float WMO 6900098 for JFM 2004. (**b**) Salinity (PSU), (**c**) potential temperature (°C), and (**d**) potential density (kgm^{-3}) from December 2003 to April 2004.

The Hoevmueller plot of the Turner angle (Figure 13) reveals statically unstable conditions ($|Tu| > 90°$; dark blue and dark red points) and therefore a continuous deepening of the MLD from mid-January to mid-March 2004 and indicates the deep dense water formation events down to 400 m by the end of February and mid-March. The main contributor to the stable stratification in December and April is the salinity ($45° < Tu < 90°$; yellow and light orange points), while the deep dense water formation events are also characterized by a stronger contribution of temperature gradients (−45° < Tu < −90°; blue points). 'Salt-fingering' (45° < Tu < 90°; yellow points) can be noticed at a depth of about 350 m.

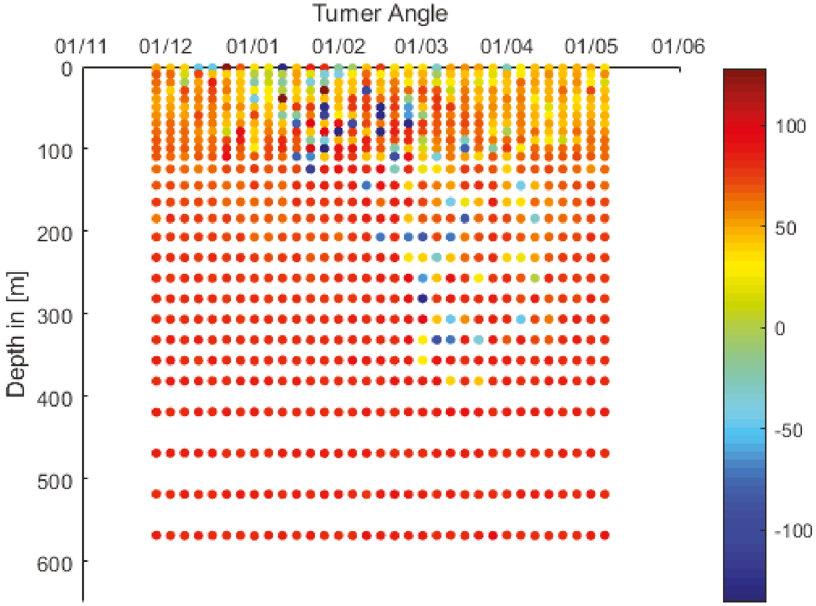

Figure 13. The Turner angle (°) of float WMO 6900098 shows the contribution of salinity and temperature gradients to the density gradient.

The T/S plot of JFM2004 shows mainly LDW formation (Figure 14). Green dots represent water masses between 100 and 500 m while blue dots represent water masses between 500 and 600 m. The water mass characteristics show LDW and 'lower range' LIW (potential temperature around 15 °C and 39 psu < salinity < 39.1 psu) formation.

Figure 15 shows: (a) the mean SSH for JFM 2004 and the float trajectory (longitude: 27.5° E–28.5° E, latitude: 34.5° N–35° N) during this period and daily SSH (b) before; (c) during; and (d) after the convection event. A strong powerful structure develops by mid-February with a negative SSH of more than −0.3 m. Analysis of single profiles shows that on 8 March 2004, a MLD down to about 450 m was formed while on the surface recapping already took place (newly formed MLD of about 80 m).

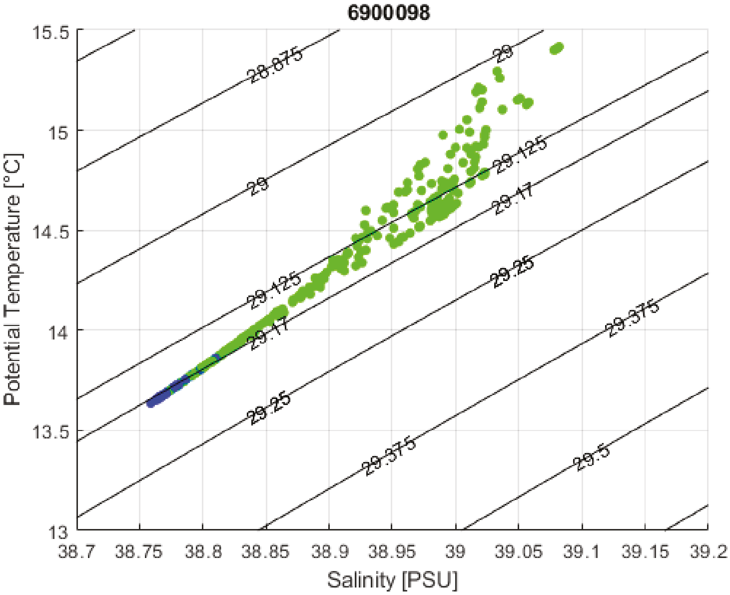

Figure 14. The T/S plot for float WMO 6900098 for JFM 2004 shows LDW and 'lower range' LIW formation. Green dots represent depths from 100 to 500 m while blue dots represent depths from 500 to 600 m.

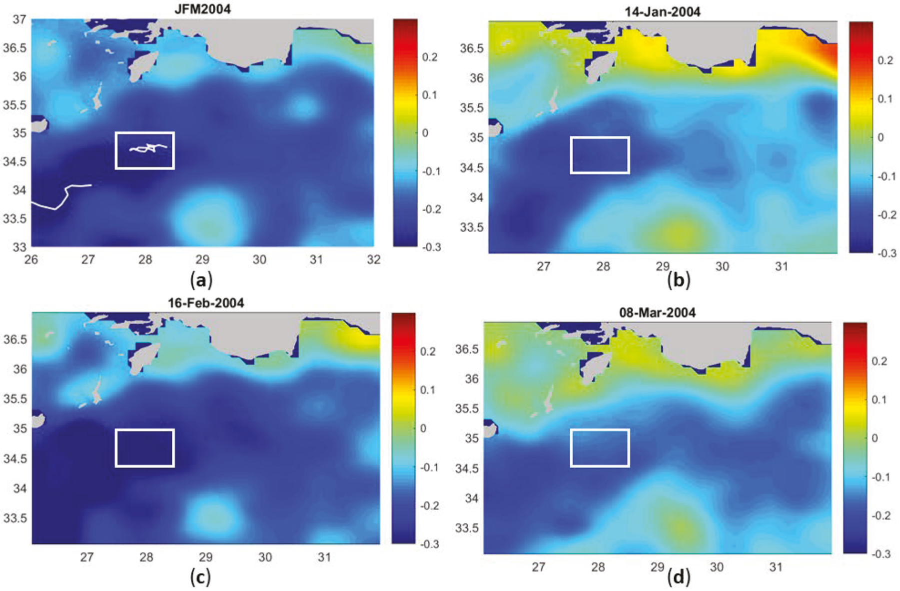

Figure 15. (**a**) mean SSH (m) for JFM 2004 and float trajectory of float WMO 6900098 (white rectangle). (**b**) SSH (m) for the 14 January 2004; float profiles show 'regular' winter MLDs around 150 m. (**c**) SSH (m) for the 16 February 2004; float profiles reveal dense water formation to about 350 m; (**d**) SSH (m) for 8 March 2004; recapping with a newly formed MLD of about 80 m occurred, while the dense water formation event down to 450 m is still captured by the float profile.

Monthly means of satellite SST are shown in Figure 16. The satellite SST reached a minimum between mid-February and mid-March, i.e., during the event of deep water formation, and coincides with the surface potential temperature measured by the Argo float (Figure 12).

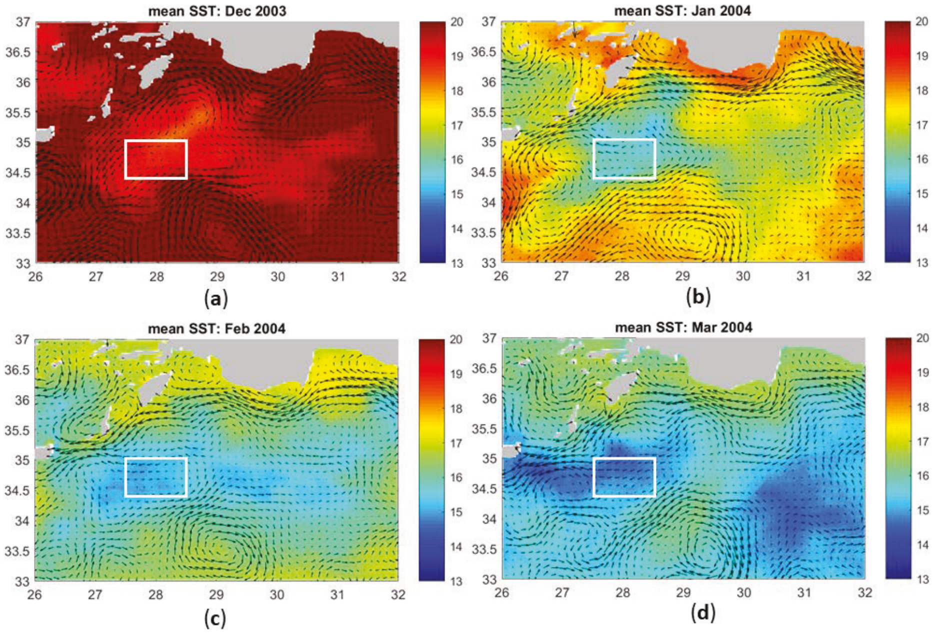

Figure 16. Monthly means of the satellite SST (°C) and absolute geostrophic currents from December 2003 to March 2004. The deep convection event occurred by the end of February and beginning of March 2004 when SST was lowest. The white rectangle shows the position of float WMO 6900098 during JFM 2004.

3.2.2. LIW Formation along the Coastline

One example of LIW formation along the coastline is given in this subsection.

While LDW was formed inside RG, typical LIW was instead formed along the Northern Turkish coastline, i.e., along the AMC. The salinity, potential temperature, and potential density values characterize a typical LIW formation event by the end of March (Figure 17).

In December and January, very high surface salinity values (S > 39.3 psu) can be seen in the upper 50 to 100 m (Figure 17b). However, deep mixing and convection is still prevented by relatively high surface temperatures (T > 17 °C) during this period. Surface temperature has a decreasing trend from about 20 °C by the very beginning of December to about 17 °C in March when deep convection occurs. By the end of April, the surface temperature gradually increases reaching 17.5 °C. The observed surface water temperature along the coastline is about 1 °C to 3 °C warmer than in the open sea (Figures 6 and 12).

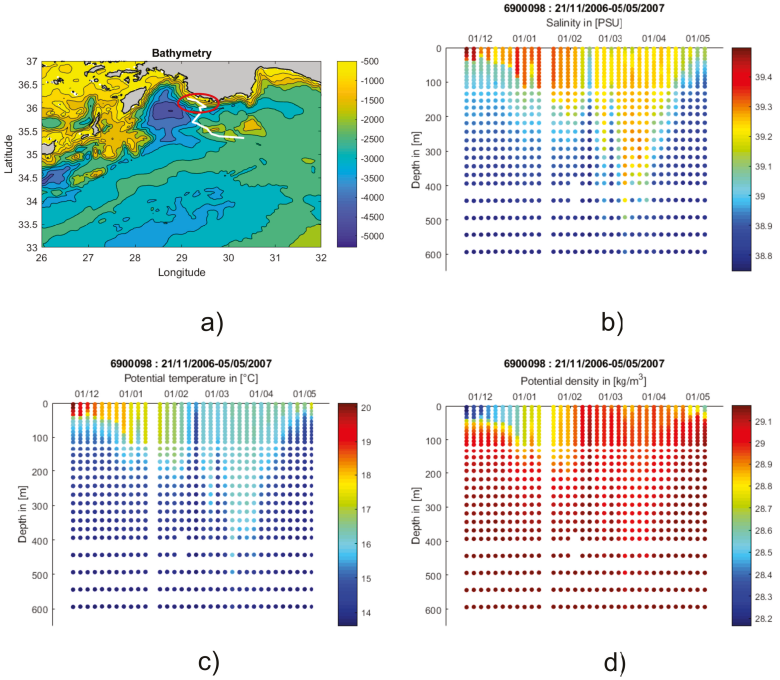

a) b)

c) d)

Figure 17. (**a**) Bathymetry of the Northwestern Levantine Sea (m) and float trajectory for float WMO 6900096 during JFM 2007. The red circle indicates the position of the float during March when the deep convection event occurred. Hoevmueller plots of (**b**) salinity (PSU), (**c**) potential temperature (°C), and (**d**) potential density (kgm^{-3}).

The MLD deepens gradually from about 50 m within December to about 250 m during February; therefore, the high surface salinity is mixed throughout intermediate layers (Figure 17b).

By the end of March, when lowest surface temperatures are reached (Figure 17c), dense water formation starts to occur. Surface potential density reaches values between 29 and 29.1 kg/m^3 during this period. The examination of single profiles shows that the mixing event takes place down to about 550 m.

The Hoevmueller plot of the Turner angle (Figure 18) reveals statically unstable conditions ($|Tu| > 90°$; dark blue and dark red points) and therefore a continuous deepening of the MLD in January and February 2007. The main contributors to the stratification in December are both temperature and salinity ($-45° < Tu < 45°$), while in April the main contributor is the salinity ($45° < Tu < 90°$; yellow and light orange points). The Turner angle indicates the deep LIW formation event down to 550 m in March, which is also characterized by a stronger contribution of temperature gradients ($-45° < Tu < -90°$; blue points).

The evolution of monthly mean SST from December 2007 to March 2007 is shown in Figure 19a–d. This deep convection event that was detected by the Argo float by the end of March 2007 coincides with the strongest depression of SSH and lowest surface temperatures along the coastline during winter 2007 (Figure 19a–c).

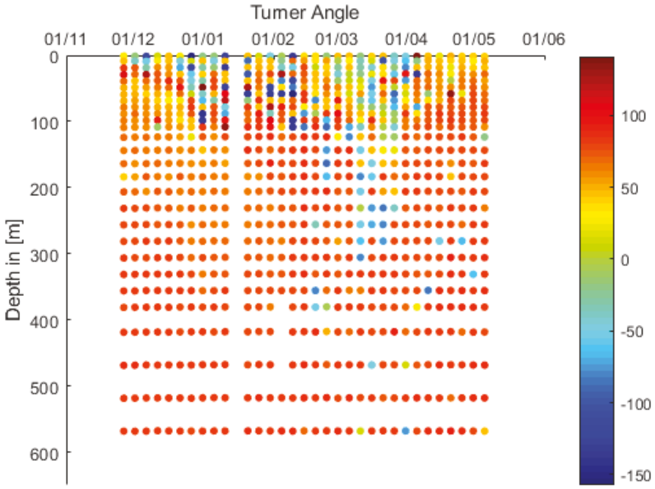

Figure 18. The Turner angle (°) of float WMO 6900098 shows the contribution of salinity and temperature to density change.

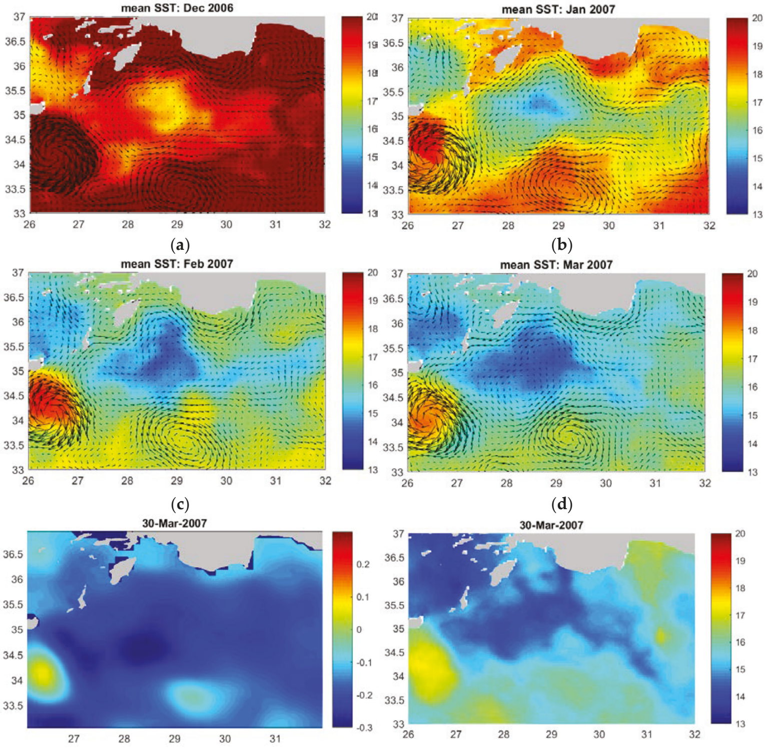

(a) (b)

(c) (d)

(e) (f)

Figure 19. (**a**–**d**) Monthly mean of satellite SST (°C) from December 2006 to March 2007. (**e**) SSH (m) and (**f**) SST (°C) on 30 March 2007, exhibiting strongest depression of SSH and lowest SST within this area during the whole winter period, coinciding with the deep dense water formation event. The white circle indicates the float position during March 2007.

The T/S plot for March 2007 reveals the formation of typical LIW, i.e., potential temperature above 15 °C and salinities higher than 39 psu (Figure 20). The potential density lines of 29–29.06 × kgm^{-3} represent the potential density range of typical LIW ([6]; Figure 20).

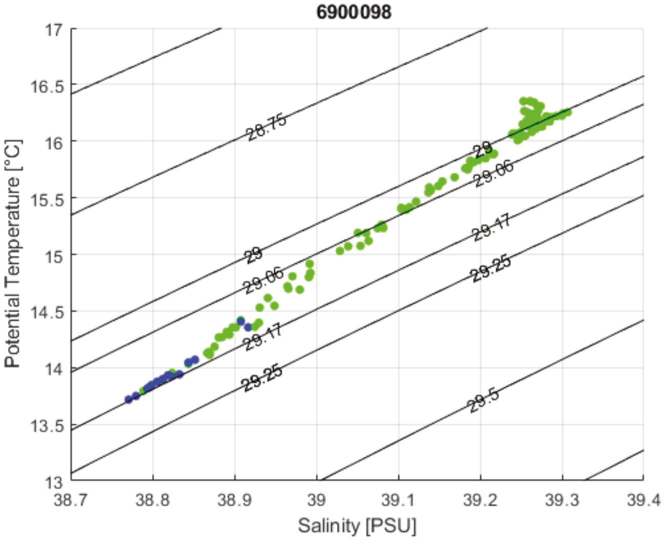

Figure 20. T/S plot for float WMO 6900098 for March 2007. Green points indicate depths from 100 to 500 m while blue points indicate depths from 500 to 600 m. The additional density line with a potential density value of 29.17 kgm^{-3} shows the upper deep-water boundary density while the potential density lines of 29–29.06 × kgm^{-3} represent the potential density range of typical LIW [6].

3.3. Climatology of Winter Mean MLD from 2000 to 2018

The climatology of the winter (JFM) mean MLD from 2000 to 2018 for the Levantine Sea is shown in Figure 21. Within the cyclonic RG, the mean winter MLD is quite shallow (around 70 m). Deeper mean winter MLDs are found within anticyclonic eddies (IE, MME, CE, ShE; see Figure 1b for position of eddies) and along the coastlines, indicating dense water formation along boundary currents.

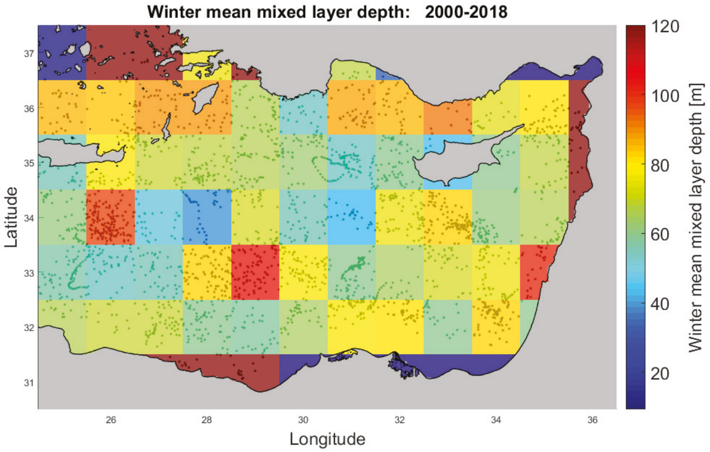

Figure 21. Climatology of the winter (JFM) mean MLD from 2000 to 2018 for the Levantine Sea.

4. Discussion and Conclusions

The present study is focused on the LIW and LDW formation events in the NWLS (Figure 22a) as detected by Argo float data from 2001 to 2017. The new and most interesting result is that the typical LIW (potential temperature > 15 °C and salinity > 39 psu) formation mainly occurred along the Northern coastline (Figure 18), while 'lower range' LIW (potential temperature about 15 °C and salinity about 39 psu) and LDW (13.7 °C < potential temperature < 14.5 °C, 38.8 psu < salinity < 38.9 psu) formation took place within mesoscale eddies located within the center of RG (Figure 22a; Figure 11a, Table 1).

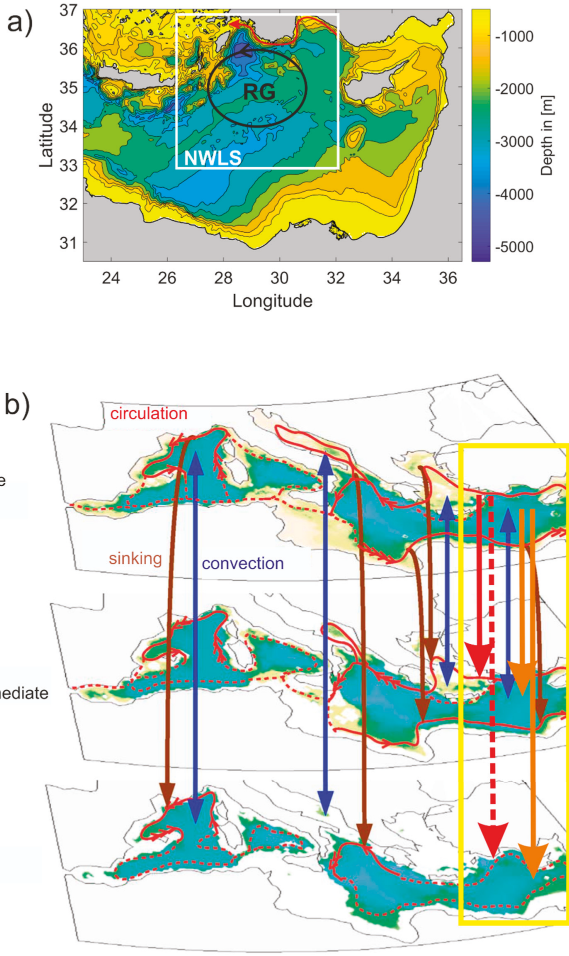

Figure 22. (**a**) The white rectangle confines the area of study, the NWLS. Typical LIW formation was found along the Northern coastline (red arrow), while 'lower range' LIW and LDW formation was found within submesoscale eddies within the center of RG (black ellipse). (**b**) This figure, adapted from [15], summarizes the obtained results for winter seasons in the NWLS (yellow rectangle): Dense water formation along the Northern coastline reached intermediate (200–500 m; red line) and deeper layers (500–600 m; dashed red line), while LDW formation within the center of RG reached intermediate and deep layers (at least 1000 m; orange lines).

The schematic summary of the results for the winter seasons from 2001 to 2017 is evident in Figure 22b. Blue and brown arrows describe the convection and net sinking areas of the Mediterranean Sea as derived from theoretical models by [15,16]. Red and orange arrows are derived from the results of the present work. Red solid and dashed lines represent the formation of intermediate (200–500 m) and deeper waters (500–600 m) along the Northern coastline. Orange arrows represent the formation of intermediate (200–500 m) and deep waters (about 1000 m) within the RG, respectively. The examination of individual profiles showed dense water formation events reaching down to 550 m depth along the coastline and down to 1000 m depth within the center of RG (Figure 22b).

The specific event of LIW formation, captured by the Argo float data in March 2007 along the coastline, reached a depth of about 550 m. The T/S plot (Figure 20) showed typical LIW formation during this event and the observed surface water temperature along the coastline was about 1°C to 3°C warmer than in the open sea (Figures 6, 12 and 17), in agreement with the results of [24,25]. In January–February 2006, the Argo float data detected the LDW formation in the core of a cyclonic mesoscale structure located in the center of RG. This structure (diameter of about 60 km) shows the typical horizontal scale of convective chimneys. The T/S plot in Figure 11a reveals the LDW characteristics of the convection event. All potential temperatures and salinity values lay on the line of constant potential density of 29.17 kgm^{-3}, revealing the sinking of the formed water masses to at least 1000 m as previously observed [6,9,10].

The intensity of the mixing and convection events depends mainly on the surface buoyancy flux B, which in turn depends on its thermal (B_T) and haline (B_S) components. The calculation and plot of the surface buoyancy flux and its components revealed that the haline component dominates over the thermal component (Figure 4, lower panel), i.e., intense evaporation ($B_S < 0$) controls the surface buoyancy loss, especially during the preconditioning phase (e.g., Figure 8 for winter 2006). Therefore, the area of the RG is an area of net buoyancy loss, driven by the haline component, as shown by [26].

The influence of salinity and temperature gradients to the density gradients are described in the Hoevmueller diagrams of the Turner angle (Figures 7, 13 and 18). During the preconditioning phase (November, December) and the constant deepening of the MLD in the beginning of January, the influence of the salinity gradient was dominant, while during strong unstable conditions and consequently dense water formation, also the temperature gradient was influential. The Turner angle also approximately indicated the depth of the convection events.

The deep dense water formation events within the area of the RG can be described by the following phases: The whole process is influenced by the cyclonic rotation of the RG leading to the upwelling of cooler waters to the surface. In November and December, the preconditioning phase starts (Figures 4 and 5): the heat losses due to cold and dry winds lead to increased surface salinity (Figures 6, 12 and 17) through the evaporation and to a steady deepening of the MLD. Additional, temporarily outbreaks of strong winds during January, February, or March cause strong heat losses (Figures 5 and 8), which cause further cooling of surface waters. When lowest surface temperatures are reached (Figures 10, 16 and 19), dense water formation starts to occur. Within hours, the newly formed dense water sinks down rapidly to a depth of equal density where it spreads horizontally, forming an anticyclonic circulation due to the influence of the Coriolis force.The convection event also implicates a stretching of the water column leading to a change in vorticity, an increased geostrophic velocity, and a depression of the SSH. In fact, all pronounced dense water formation events documented by the Argo floats were indicated by a strong depression of satellite SSH (Figures 9, 15 and 19) and by lowest SSTs (Figures 10, 16 and 19).

The Argo float data revealed that LDW formation took place within the RG during winter months and showed the key role of the boundary currents for the LIW formation. The climatology of the mean MLDs of the Levantine Sea (Figure 21) reveals that, despite the deep convection events, little to net mean sinking takes place within the center of RG, while the deeper MLDs along the coastline indicate dense water formation occurring along boundary currents. Therefore, the drivers, sources, and main contributors of the Mediterranean thermohaline circulation have to be rethought not only within the Levantine, but also within the Mediterranean Sea. Deployments of additional Argo floats to survey boundary currents and deployment of deep Argo floats within the main Mediterranean convection sites, i.e., the Gulf of Lion, the South Adriatic, and the RG area, will contribute to further understanding of dense water formation processes.

A better understanding of the Mediterranean thermohaline circulation is needed not only for a wider knowledge of the effects of climate change, but also for the impact on the ecology. Newly formed intermediate or deep waters can be polluted (with oil, microplastics, nutrients from extensive agriculture, heat due to global warming etc.), e.g., the Northern Levantine coastline, where pronounced dense water formation occurs, has the highest coastline plastic pollution within the Mediterranean Sea [27]. The newly formed water masses with the above-mentioned water properties and pollutants are transported throughout the Mediterranean to finally reach the Atlantic Ocean. The full impact (in terms of pollution and different water mass characteristics) will only be seen by future generations when these water masses emerge after decades or even centuries at different places within the Mediterranean Sea.

Therefore, it is obvious and evident that scientists and policy makers are obliged to join forces now to support and make commitments towards a real sustainable world that is not threatening, but protecting our ecosystems and lives.

Author Contributions: Conceptualization, E.K., P.-M.P. and E.M.; methodology, E.K., G.N. and M.M.; writing—original draft preparation, E.K.; writing—review and editing, M.M., E.M., P.-M.P. and G.N.; investigation, E.K.; data curation, E.K. and G.N.; supervision, P.-M.P. and E.M.; funding acquisition, P.-M.P.

Funding: The float data were collected and made freely available by the International Argo Program and the national programs that contribute to it (http://argo.jcommops.org). The Argo Program is part of the Global Ocean Observing System.

Acknowledgments: The authors would like to thank the two anonymous reviewers for their constructive comments and all the people who have deployed Argo floats in the Mediterranean Sea. We acknowledge Antonio Bussani and Massimo Pacciaroni for their technical support with the dataset and floats programming. In addition, we thank Vedrana Kovacevic for her suggestions and fruitful discussions.

Conflicts of Interest: The authors declare no conflict of interest.

References

1. Tsimplis, M.N.; Zervakis, V.; Josey, S.A.; Peneva, E.L.; Struglia, M.V.; Stanev, E.V.; Theocharis, A.; Lionello, P.; Malanotte-Rizzoli, P.; Artale, V.; et al. Changes in the Oceanography of the Mediterranean Sea and their Link to Climate Variability, in Mediterranean Climate Variability. In *Developments in Earth & Environmental Sciences*; Lionello, P., Malanotte-Rizzoli, P., Boscolo, R., Eds.; Elsevier: Amsterdam, The Netherlands, 2006; Volume 4, pp. 227–282.
2. Bergamasco, A.; Malanotte-Rizzoli, P. The circulation of the Mediterranean Sea: A historical review of experimental investigations. *Adv. Oceanogr. Limnol.* **2010**, *1*, 11–28. [CrossRef]
3. Gacic, M.; Civitarese, G.; Eusebi Borzelli, G.L.; Kovacevic, V.; Poulain, P.-M.; Theocharis, A.; Menna, M.; Catucci, A.; Zarokanellos, N. On the relationship between the decadal oscillations of the Northern Ionian Sea and the salinity distributions in the Eastern Mediterranean. *J. Geophys. Res. (Ocean.)* **2011**, *116*. [CrossRef]
4. Gacic, M.; Schroeder, K.; Civitarese, G.; Vetrano, A.; Eusebi Borzelli, G.L. On the relationship among the Adriatic-Ionian Bimodal Oscillating System (BiOS), the Eastern Mediterranean salinity variations and the Western Mediterranean thermohaline cell. *Ocean Sci. Discuss.* **2012**, *9*, 2561–2580. [CrossRef]
5. Menna, M.; Suarez, C.; Civitarese, G.; Gacic, M.; Poulain, P.-M.; Rubino, A. Decadal variations of circulation in the Central Mediterranean and its interactions with mesoscale gyres. *Deep Sea Res. Part II Top. Stud. Oceanogr.* **2019**. [CrossRef]
6. Malanotte-Rizzoli, P.; Manca, B.; Marullo, S.; Ribera d'Alcala, M.; Roether, W.; Theocharis, A.; Bergamasco, A.; Budillon, G.; Sansone, E.; Civitarese, G.; et al. The Levantine Intermediate Water Experiment (LIWEX) Group: Levantine basin—A laboratory for multiple water mass formation processes. *J. Geophys. Res.* **2003**, *108*, 8101. [CrossRef]

7. Theocharis, A.; Krokos, G.; Velaoras, D.; Korres, G. An Internal Mechanism Driving the Alternation of the Eastern Mediterranean Dense/DeepWater Sources. The Mediterranean Sea: Temporal Variability and Spatial Patterns. In *The Mediterranean Sea: Temporal Variability and Spatial Patterns*, 1st ed.; Eusebi Borzelli, G.L., Gagic, M., Lionello, P., Malanotte-Rizzoli, P., American Geophysical Union, Eds.; Geophysical Monograph 202; John Wiley & Sons: Hoboken, NJ, USA, 2014; Volume 10, pp. 113–137.
8. Lionello, P.; Malanotte-Rizzoli, P.; Boscolo, R.; Alpert, P.; Artale, V.; Li, L.; Luterbacher, J.; May, W.; Trigo, R.; Tsimplis, M.; et al. The Mediterranean Climate: An Overview of the Main Characteristics and Issues. *Dev. Earth Environ. Sci.* **2006**, *4*, 1–26.
9. Sur, H.I.; Özsoy, E.; Unluata, U. Simultaneous deep and intermediate depth convection in the Northern Levantine Sea, winter 1992. *Oceanol. Acta* **1993**, *16*, 33–43.
10. Gertman, I.F.; Ovchinnikov, I.M.; Popov, Y.I. Deep convection in the eastern basin of the Medi-terranean Sea. *Oceanology* **1994**, *34*, 19–25.
11. Spall, M.A.; Pickart, R.S. Where does dense water sink? A subpolar gyre example. *J. Phys. Oceanogr.* **2001**, *31*, 810–826. [CrossRef]
12. Spall, M.A. Boundary currents and water mass transformation in marginal seas. *J. Phys. Oceanogr.* **2004**, *34*, 1197–1213. [CrossRef]
13. Spall, M.A. Buoyancy-forced downwelling in boundary currents. *J. Phys. Oceanogr.* **2008**, *38*, 2704–2721. [CrossRef]
14. Spall, M.A. Dynamics of downwelling in an eddy-resolving convective basin. *J. Phys. Oceanogr.* **2010**, *40*, 2341–2347. [CrossRef]
15. Waldman, R.; Brüggemann, N.; Bosse, A.; Spall, M.; Somot, S.; Sevault, F. Overturning the Mediterranean Thermohaline Circulation. *Geophys. Res. Lett.* **2018**. [CrossRef]
16. Pinardi, N.; Cessi, P.; Borile, F.; Wolfe, C. The Mediterranean Sea Overturning Circulation. *J. Phys. Oceanogr.* **2019**. [CrossRef]
17. Menna, M.; Poulain, P.-M.; Zodiatis, G.; Gertman, I. On the surface circulation of the Levantine sub-basin derived from Lagrangian drifters and satellite altimetry data. *Deep Sea Res. Part I Oceanogr. Res. Pap.* **2012**, *65*, 46–58. [CrossRef]
18. Poulain, P.-M.; Barbanti, R.; Font, J.; Cruzado, A.; Millot, C.; Gertman, I.; Griffa, A.; Molcard, A.; Rupolo, V.; Le Bras, S.; et al. MedArgo: A drifting profiler program in the Mediterranean Sea. *Ocean Sci.* **2007**, *3*, 379–395. [CrossRef]
19. Holte, J.; Talley, L.D.; Gilson, J.; Roemmich, D. An Argo mixed layer climatology and database. *Geophys. Res. Lett.* **2017**, *44*, 5618–5626. [CrossRef]
20. Zahariev, K.; Garrett, C. An Apparent Surface Buoyancy Flux Associated with the Nonlinearity of the Equation of State. *J. Phys. Oceanogr.* **1997**, *27*, 362–368. [CrossRef]
21. Ruddick, B.R. A practical indicator of the stability of the water column to double-diffusivity activity. *Deep Sea Res. Part A* **1983**, *30*, 1105–1107. [CrossRef]
22. IOC; SCOR; IAPSO. *The International Thermodynamic Equation of Seawater—2010: Calculation and Use of Thermodynamic Properties*; Intergovernmental Oceanographic Commission, UNESCO (English): Paris, France, 2010; p. 196.
23. Roether, W.; Klein, B.; Manca, B.B.; Theocharis, A.; Kioroglou, S. Transient Eastern Mediterranean deep waters in response to the massive dense-water output of the Aegean Sea in the 1990's. *Prog. Oceanogr.* **2007**, *74*, 540–571. [CrossRef]
24. Feliks, Y. Downwelling along the Northeastern Coasts of the Eastern Mediterranean. *J. Phys. Oceanogr.* **1991**, *21*, 511–526. [CrossRef]
25. Feliks, Y.; Ghil, M. Downwelling-front instability and eddy formation in the Eastern Mediterranean. *J. Phys. Oceanogr.* **1993**, *23*, 61–78. [CrossRef]
26. Karstensen, J.; Lorbacher, K. A practical indicator for surface ocean heat and freshwater buoyancy fluxes and its application to the NCEP reanalysis data. *Tellus* **2011**, *63*, 338–347. [CrossRef]

27. WWF Mediterranean Marine Initiative Report. Stop the Flood of Plastic: How Mediterranean Countries Can Save Their Sea. 2019. Available online: http://awsassets.panda.org/downloads/a4_plastics_reg_low.pdf (accessed on 25 June 2019).

water

MDPI

Article

On the Variability of the Circulation and Water Mass Properties in the Eastern Levantine Sea between September 2016–August 2017

Elena Mauri [1,*], Lina Sitz [1], Riccardo Gerin [1], Pierre-Marie Poulain [1,2], Daniel Hayes [3] and Hezi Gildor [4]

1 Istituto Nazionale di Oceanografia e di Geofisica Sperimentale, OGS, Borgo Grotta Gigante, 42/c, 34010 Sgonico, Italy
2 Centre for Maritime Research and Experimentation, CMRE, 19126 La Spezia, Italy
3 Oceanography Center, University of Cyprus, P.O. Box 20537, 1678 Nicosia, Cyprus
4 The Hebrew University Institute of Earth Sciences, Edmond J. Safra Campus, Givat Ram, 91904 Jerusalem, Israel
* Correspondence: emauri@inogs.it; Tel.: +39-040-2140-203

Received: 18 July 2019; Accepted: 15 August 2019; Published: 21 August 2019

Abstract: The surface circulation and the thermohaline properties of the water masses of the eastern Levantine Sea (Mediterranean Sea) were monitored with mobile autonomous systems (surface drifters and gliders) during the period September 2016–August 2017. The drifters provided data for more than a year and revealed complex circulation features at scales ranging from the basin scale to the sub-mesoscale. Three drifters were captured in a semi-permanent gyre (Cyprus Eddy) allowing a quantitative study of its kinematics. During the experiment, three gliders were operated, in two different periods: September to December 2016 and February to March 2017. The autonomous instruments crossed the prevailing sub-basin structures several times. The collected in-situ observations were analyzed and interpreted in concert with remote sensing products (sea surface temperature and altimetry). The evolution of some of the prevailing features confirmed the complexity of the circulation of the basin. The Cyprus Eddy is the most persistent anticyclone, moving its geographical position and sometimes merging with the North Shikmona Eddy in a bigger structure. The gliders sampled this wide anticyclonic feature revealing its vertical structure in the two different periods. In fall, in stratified conditions, a high salinity core is evident below the thermocline. The isopycnals are characterized by an upward bending over the high salinity lens and a downward bending below it, typical of an anticyclonic modewater eddy. In winter, the core disappears following the vertical mixing that, homogenizes the upper Cyprus Eddy water down to 300 m.

Keywords: Mediterranean Sea; drifters; sub-basin-scale eddies; gliders

1. Introduction

The Levantine Sea (LS) is a complex multiscale system [1–3]. The basin-scale mean circulation, mesoscale and sub-basin scale eddies interact in a non-linear way producing a highly variable current field [4]. Despite many studies focusing on the LS, the basin has not been extensively sampled due to its high complexity and variability and to logistical or political issues.

Studies of the LS surface current started over a hundred years ago based on hydrographic data [5–11], revealing a basin-wide cyclonic circulation and the most persistent sub-basin scale features. A more detailed and complex circulation became evident only after the analysis of longtime series of satellite measurements, such as the Sea Surface Temperature (SST) [12,13] and the Absolute Dynamic Topography (ADT) [4,14–16] and numerical simulations [2,17–19]. Starting in 2005, as part of the Eddies and GYres Paths Tracking (EGITTO) [20] and North East MEDiterranean (NEMED) [4] projects, numerous drifters were deployed in the region, allowing to calculate pseudo-Eulerian velocity statistics for different time periods. In particular, the use of the ADT for the period 1993–2010 allowed to describe the inter-annual variability of the Eddy Kinetic Energy (EKE) of the prevailing mesoscale features in the LS. The basin surface circulation map resulting from this study shows an along-slope cyclonic coastal circulation named the Libyo-Egyptian Current [12,20,21] extending as a northward current along the Middle-East coast. The other dominant feature is a central eastward cross-basin meandering current named Mid-Mediterranean Jet (MMJ) between 24° E and the longitude of Cyprus [22–24], and a series of mesoscale features, including some eddies such as the Cyprus (CE), the Shikmona (ShE) and the Latakia Eddy (LE). The CE is described as a persistent anticyclonic eddy characterized by seasonal variability in shape, dimension and position with an average diameter of 250–300 km [4,25]. The ShE instead, represents a complex system, composed of several cyclonic and anticyclonic eddies off the Israeli coast, in which the positions, sizes and intensities vary markedly [4,26–28]. The LE can be present as a cyclone or an anticyclone and the change in rotation is induced by the interaction of the MMJ with the northward meandering coastal current [4].

The thermohaline structure of the eastern LS is well-defined in the warm season and it is characterized at surface by the Levantine Surface Water (LSW), with temperature values between 22 and 28 °C and salinity of 39 to 39.6 PSU. The Atlantic Water (AW) with temperature values of 18 to 22 °C and salinity between 38.6 and 39.2 PSU, is positioned below the LSW and it is advected from the western Mediterranean Sea. The Levantine Intermediate Water (LIW) formed when LSW cools down and sinks along isopycnals to intermediate depths (ca. $130 \text{ m} < z < 350 \text{ m}$), it presents typical values of 15 to 17.5 °C and 38.95 to 39.3 PSU [29]. Finally, the Levantine Deep Water (LDW) with its nearly constant values of temperature and salinity (13.8 °C and 38.7 PSU) is found below 750 m [30].

In the framework of the CINEL (CIrculation and water mass properties in the North Eastern Levantine) project drifters and gliders were operated in the eastern part of the LS for more than a year, starting in September 2016, to gain more insights on the variability of the physical and biochemical properties in the region and in particular, to study the major sub-basin scale and mesoscale eddies governing the dynamics of the eastern LS. The in situ observations provided by the drifters and gliders were used in concert with satellite products of SST and ADT to describe the spatial structure and the temporal evolution of the main eddies.

The use of satellite images in past studies to track mesoscale and sub-mesoscale features has been widely used. In the Mediterranean Sea, SST, chlorophyll and altimetry imagery were utilized in different studies [4,16,31–34], some of them the eddies were sampled by gliders [35–38].

In this study, we concentrate on the eastern LS, located between 30° E and 36° E, and 31° N and 37° N in the period between September 2016 and August 2017. The main focus of the analysis is on the detection and monitoring of strong sub-basin scale features and on their motion and evolution during the period of the experiment.

The paper is organized as follows. Information on the in-situ platforms (drifters and gliders) and the data they provided, as well as on the remotely sensed data (SST and ADT), is provided in Section 2. The methods applied to process all the data are also explained. In Section 3, the features highlighted by the SST anomaly and ADT images are interpreted in concert with the drifter tracks and the surface geostrophic currents computed from the satellite altimetry data. The vertical description of some sub-basin scale features using glider observations is also included in this section. Discussion and conclusions are found in Section 4.

2. Data and Methods

2.1. Glider Data

Three Seagliders (sg149 and sg150 of University of Cyprus—UCY; sg554 of National institute of Oceanography and Applied Geophysics—OGS) were operated in the eastern LS between 1 September 2016 and 16 March 2017 (See Table 1). The glider dataset includes five glider campaigns (Figure 1), which covered two different seasons: fall 2016 and winter 2016–2017. During the first period, three glider campaigns were organized; the first one was performed in September 2016 (C1) and the other two (C2 and C3) were almost concomitant and covered the month of November and the beginning of December 2016. The winter sampling comprised two simultaneous campaigns (C4 and C5) starting at the beginning of February and ending in mid-March 2017.

Table 1. Dates of glider campaigns in the two periods, conventional name of the missions used in the paper and number of recorded profiles.

Glider ID	Fall 2016	Name	Casts	Winter 2016–2017	Name	Casts
OC-UCY (sg150)	1 September–17 October	C1	203			
OGS (sg554)	19 October–7 December	C2	333	10 February–16 March	C5	127
OC-UCY (sg149)	4 November–6 December	C3	143	10 February–12 March	C4	168

The OGS sg554 glider is equipped with a pumped CTD (GPCTD) while the UCY gliders have a regular un-pumped CTD. The un-pumped data were corrected for the thermal lag using Kongsberg routines. Temperature and salinity data were collected in the top 950 m of the water column in all the five campaigns. Oxygen concentration was recorded by an Aanderaa optode 4330 and 3835 (for the OGS and UCY glider, respectively) and set to record data down to 600 m depth. All the gliders were also fitted with a Wetlab FLNTU sensor to collect chlorophyll and turbidity data at two wavelengths (470 and 700 nm) down to 300, 400 m or 600 m while crossing specific structures. The glider traveled along a ~26° inclined path with respect to the water surface. During the up casts, the glider collected high vertical resolution data (about 0.1 Hz, corresponding to about one sample every 2 m). The top 20 m CTD data of the OGS campaigns are missing. This behavior is common in Seabird GPCTD and is due to the incomplete download of the GPCTD buffer when the glider reaches the surface (SeaBird, 2013). The horizontal speed of the instrument spanned between 0.7 and 1.4 km/h depending on the sea currents. A glider took about 4–5 h to conclude a 950 m dive, therefore, the horizontal resolution was about 4 km. The data were transmitted via satellite Iridium links at each surfacing. In total, 974 casts were collected during the five missions.

During fall 2016 (campaigns C2 and C3), the OGS and UCY gliders were operated simultaneously. On 3 December, they were close by and the two profiles (one per glider) recorded at that particular moment (separated by about 1.5 km and 1 h) were used to intercompare the CTD data. Temperature and salinity profiles showed a good agreement (offset of 0.02 °C and 0.01 PSU, RMSD of 0.07 °C and 0.01 PSU). Oxygen data were not inter-compared because the oxygen factory calibration for the UCY gliders resulted too old and a sensor degradation (shift over times) was suspected. Therefore, only the relative values of the oxygen concentration are used in this paper. Chlorophyll and turbidity data were corrected using the dark counts computed from deep dives performed at the beginning and at the end of each glider campaigns. After a first quality control to eliminate obvious spikes [39], the data were averaged in 2-m non-overlapped bins. In this paper, the temperature, salinity, density and dissolved oxygen data are described while other parameters are only occasionally considered.

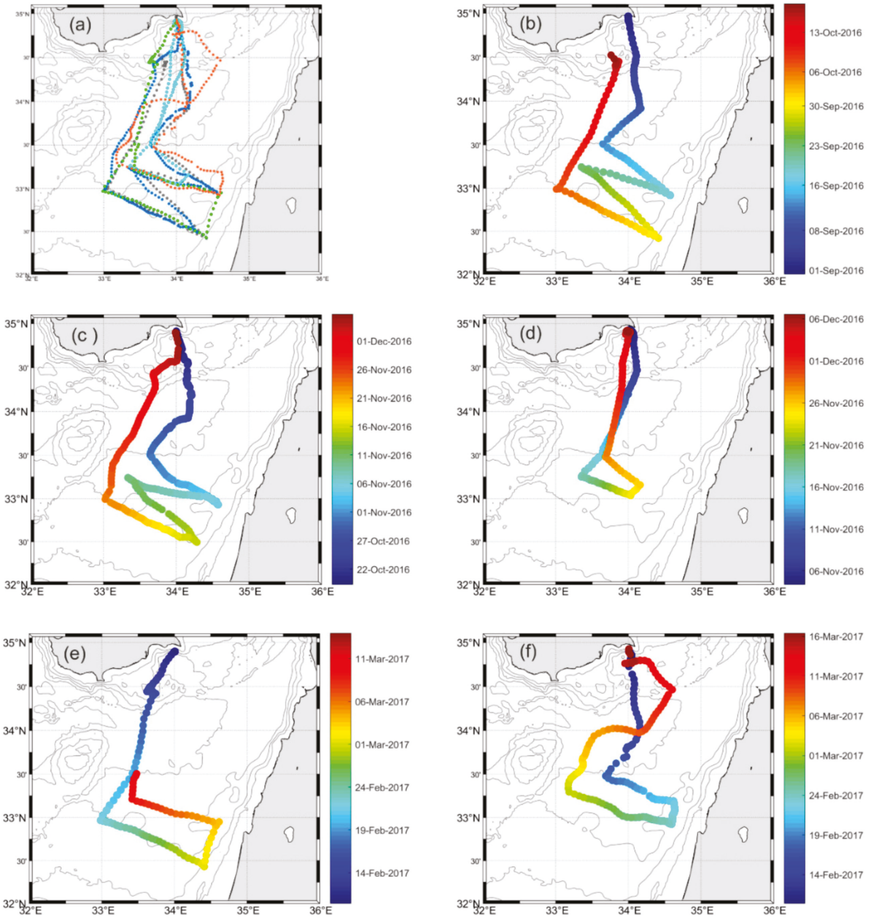

Figure 1. (**a**) Glider tracks during the CINEL experiment, (**b**) C1 mission performed by units SG150 glider during fall; (**c**) C2 by unit SG554 in fall, (**d**) C3 by unit SG149 in fall; (**e**) C4 by SG149 in winter; (**f**) C5 by SG554 in winter. Colors represent the evolution in time of each trajectory, with blue colors indicating the initial measurements and red colors showing the final observations. The actual dates for each mission are reported in Table 1.

2.2. Drifter Data

The CINEL drifter dataset includes the tracks provided by 16 drifters launched in 3 episodes: 4 drifters on 20–21 October 2016 along a meridional transect south of Cyprus and 8 drifters off the central coast of Israel on 7 February 2017 and 4 drifters again south of Cyprus (same positions as in October 2016) on 25 February 2017. One drifter stranded near Larnaca in Cyprus on 14 March 2017. It was recovered and redeployed south of Cyprus on 29 March. The drifters used during the experiment were the Surface Velocity Programme SVP drifter design [40] with a drogue centered at 15 m depth, equipped with a sensor for the SST and a tension sensor to monitor the drogue presence. They were manufactured by METOCEAN. Each drifter provides its location through the global positioning system (GPS) and transmits the data on land via Iridium satellite link. The drifter data were first edited from spikes and outliers [39], then the data of position, temperature, voltage and drogue presence were interpolated at 30-min uniform intervals using a kriging optimal interpolation method [41,42].

The velocities were then calculated as finite differences of the interpolated position. The interpolated positions were also subsampled at 2-h regular interval and low-pass filtered using a Hamming filter with a cut-off period at 36 h in order to remove high frequency current components (tidal and inertial currents) and then sub-sampled every 6 h. A composite diagram with all the low-pass filtered drifter trajectories between 20 October 2016 and 31 August 2017 is shown in Figure 2.

Drifter trajectory segments were superimposed on SST anomaly and ADT images to describe specific snapshots of surface circulation. A quantitative analysis of the drifter trajectories was also performed to characterize the CE, when some drifters were caught in its core for several months. To estimate the motion of the eddy center, loops in the drifter tracks were identified by considering the drifter positions bounded by two successive longitude maxima [43]. Then, the center of each loop was computed by averaging the longitudes and latitudes corresponding to each loop. A regression line was fitted through the center estimates to estimate the mean displacement of the eddy. The size and strength of the eddy were determined by considering the drifter speeds as a function of distance with respect to the eddy center.

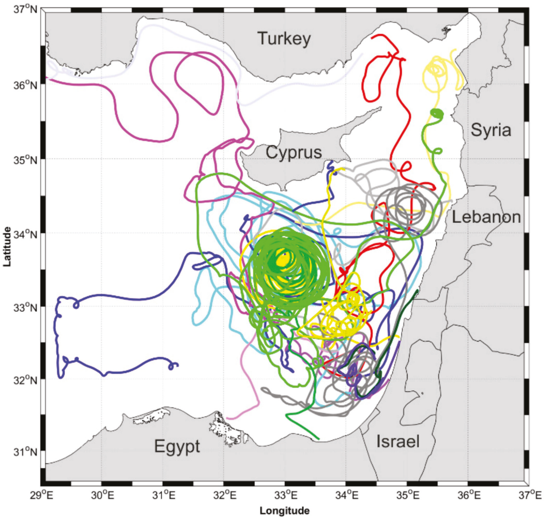

Figure 2. Tracks of drifters operated during the CINEL experiment from September 2016 to August 2017.

2.3. Sea Surface Temperature

The satellite SST products considered in this study are daily gap-free maps (L4) at high (HR 0.0625°) spatial resolution over the Mediterranean Sea. These products are based on night-time images collected by the infrared sensors mounted on different satellite platforms and cover the Southern European Seas. Remotely-sensed L4 SST datasets are operationally produced by the Consiglio Nazionale delle Ricerche-Gruppo di Oceanografia da Satellite (CNR-GOS). The basic design and the main algorithms used are described in [44]. The products are distributed by the Copernicus programme (http://marine.copernicus.eu). In this study, we generated SST anomaly maps for the east LS (30–36° E and 31–37° N) with a constant colorscale (between −2 and +2 °C) in order to enhance the features present in the area. In particular, each image was generated after subtracting the mean SST of the area and dividing the result by the standard deviation.

2.4. Absolute Dynamic Topography

The altimetry data are processed by the DUACS multi-mission altimeter data processing system and provided by Copernicus. Satellite gridded Sea Level Anomaly (SLA) are computed with respect to a twenty-year mean and is estimated by Optimal Interpolation [45], merging the measurement from all the available altimeter missions (Jason-3, Sentinel-3A, HY-2A, Saral/AltiKa, Cryosat-2, Jason-2, Jason-1, T/P, ENVISAT, GFO, ERS1/2) (see QUID document or http://duacs.cls.fr pages for processing details). The SLA data resolution is 0.125° by 0.125°; to derive the ADT, the SLA is added to the Synthetic Mean Dynamic Topography (SMDT). The geostrophic currents are then derived by finite differencing and normalizing the ADT.

3. Results

3.1. *Surface Circulation and Sub-Basin Features*

The analysis of the drifter trajectories (Figure 2), and the SST anomaly/ADT daily images confirm the eastern LS as a very dynamical area, characterized by a number of permanent eddies and other features that are intermittent, eventually disappearing or merging with other eddies, creating wider structures. The ADT averaged throughout the whole period of study (September 2016–August 2017; Figure 3) and the drifter tracks (Figure 2) show the CE as the most persistent feature present in the area, covering a broad area south of Cyprus. Other relevant anticyclones are the North Shikmona Eddy (NSE), which is the easternmost feature off the Lebanese coast and another eddy located more to the south in front of the Israeli coast, hereafter called E1. In between these two anticyclones, a cyclone is evident. It is referred to as the South Shikmona Eddy (SSE) hereafter. Finally, another two cyclones, evidenced in the mean ADT, can be seen: one south of the CE, named E2 and the second one east of Cyprus island called the Latakia Eddy (LE). The above-mentioned features with the exception of the CE, are not permanent throughout the year, they can disappear for short periods or move slightly their geographical position or sometimes change their shape merging with other eddies. A qualitative analysis of the most salient features during a 1-year period starting from September 2016 was performed using SST anomaly and satellite altimetry maps. To analyze the mesoscale circulation, geostrophic currents computed from the altimetry data of the same day were superimposed on the daily SST anomaly images. Drifter tracks were also integrated to study the dynamics of the area.

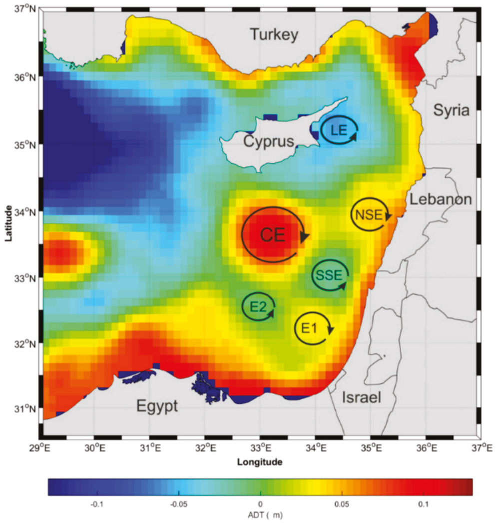

Figure 3. Mean Absolute Dynamic Topography (ADT) for the period September 2016 to August 2017, evidencing the Cyprus eddy (CE), the north Shikmona Eddy (NSE), the south Shikmona Eddy (SSE), the anticyclone E1 in front of the Israeli coast, a cyclone south of CE called E2 and the Latakia Eddy (LE). The colorscale unit is m.

3.1.1. Qualitative Description

Mid Mediterranean Jet and Thermal Front between Cyprus and Syria

From the beginning of September 2016 a strong jet (Figure 4a), crossing from west to east the eastern LS south of Cyprus, was evidenced by low temperature and by strong geostrophic currents. The wind over the whole basin blew from the west starting from June 2016 and becoming stronger and more stable at the beginning of August and lasting until 25 September 2016 (https://winds.jpl.nasa.gov/missions/quikscat/). The jet, called from now on the Mid Mediterranean Jet (MMJ), bended toward Cyprus skimming the CE to the north, and proceeding toward the Syrian coast. Before reaching, the coast, it flowed to the north between two eddies: the LE to the north and the NSE to the south (Figure 4b). The cold water of the MMJ (1.5–2 °C lower than the surrounding water), intruded from the west, joining the coastal upwelled water along the southern coast of Cyprus. In early October, the cold MMJ faded away (Figure 4c) and the warmer waters of the CE, intruded to the north, confining the cold upwelled water to the southeastern part of Cyprus (Figure 4c–i). The cold water, together with the general cooling of the area northeast of Cyprus, generated a zonal thermal front (Figure 4e–i). From September to November 2016 (Figure 4a–f) the strong geostrophic currents flowing from south of Cyprus toward the Syrian coast, were mainly located south of the front (in warmer waters). Three of the four drifters deployed along the meridional section of the CE in October 2016, clearly highlighted the zonal jet associated with the front. The northern drifter was immediately captured by the jet (Figure 4d) and reached the Syrian coast after about a week, then it veered to the north (not shown). The drifter deployed in the CE more to the south, after being involved for 10 days in a small eddy southwest of CE, was first caught by the CE, then it moved to the north and entered in the jet (Figure 4e). On 21 November, it reached the Syrian coast. Another drifter reached this area on 25 November and then both instruments moved southward along the Lebanese coast (Figure 4f). The geostrophic current in front of the Lebanon/Syrian coast, computed by the altimetry, show for this period a current flowing against the drifter tracks (not shown). One drifter was caught in the SSE, while the other one proceeded to the south along the coast until 11 December when it changed direction and moved northward to reach the SSE, in agreement with the geostrophic currents (not shown).

The zonal thermal front northeast of Cyprus persisted until March 2017 changing its shape and orientation. After a first phase in September 2016 during which the front appears jagged and not well defined in the SST anomaly (Figure 4c), in October and November it became sharper with a surface temperature gradient of 1.5–2 °C (Figure 4f). Two gliders were operated in November and both crossed the front simultaneously a few km apart. During this period, the zonally oriented front persisted until 15 December when a cyclonic eddy located around 34° E, intruded in the warmer side bringing colder water to the south (not shown). The wide cold bulge expanded more than 1 degree of latitude to the south in 1 December (Figure 4g) and the intrusion became narrow due to the weakening of the cyclone by 11 January 2017 (Figure 4h). A small feature of cold water, which detached from the above-mentioned bulge, remained at 33.5° E 34.3° N in mid-January (Figure 4i) and was included in a small cyclonic eddy (probably the SSE). On 23 February, two cold intrusions of 10 km size propagated to the east along the front moving more than 40 km in 4 days (Figure 4j,k). In early March the jet decreased in intensity and more meanders and filaments developed. Some of them were also identified by the drifter tracks (Figure 4l).

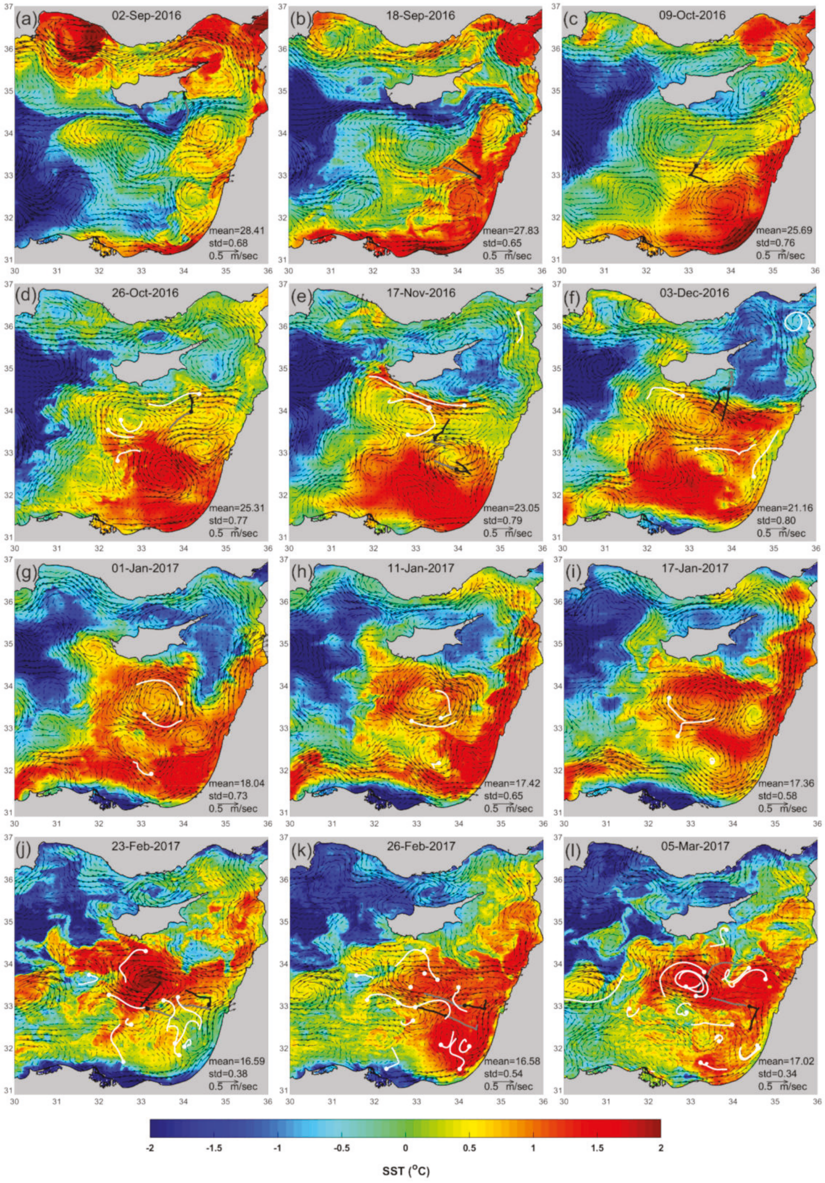

Figure 4. Geostrophic currents overlaid on the Sea Surface Temperature (SST) anomaly images, near the bottom the right corner of the sub-plots, mean, and standard deviation of the image are reported as well as the speed scale of the currents. Black (gray) lines indicate the glider track 4 days before (4 days after) the date reported on top of the image (black dot). White lines represent the drifter tracks 4 days before the reported date (white dot). Mid-Mediterranean Jet (MMJ) and the upwelling south of Cyprus, marked by cold water (**a**); the fading of MMJ with instabilities along the edge (**b**); cold front south east of Cyprus (**c**); cold front highlighted by a drifter (**d**); a second drifter evidences the fast geostrophic current north of Cyprus (**e**); drifters proceeding south along the Lebanon coast (**f**); north intrusion in the front (**g**); evolution of the intrusion (**h**); creation of a separate cyclonic eddy (**i**); intrusions (**j**); evolution of the intrusions (**k**) and cold front weakening (**l**).

Cyprus Eddy and North Shikmona Eddy

Even though the CE prevailed throughout the period of study from September 2016 to the end of August 2017, its shape and position changed significantly with time as revealed by the analysis of the ADT maps. At the beginning of September, the CE and NSE were present as two separate anticyclones (Figure 5a), then, on 4 October, three small eddies developed (Figure 5b) and in a few days, a wide zonally-elongated anticyclonic structure formed (Figure 5c). This broad feature persisted (Figure 5d) until the beginning of December, when the two eddies eventually detached from each other (Figure 5e) and the CE moved back to its original location, while the NSE completely disappeared (Figure 5f).

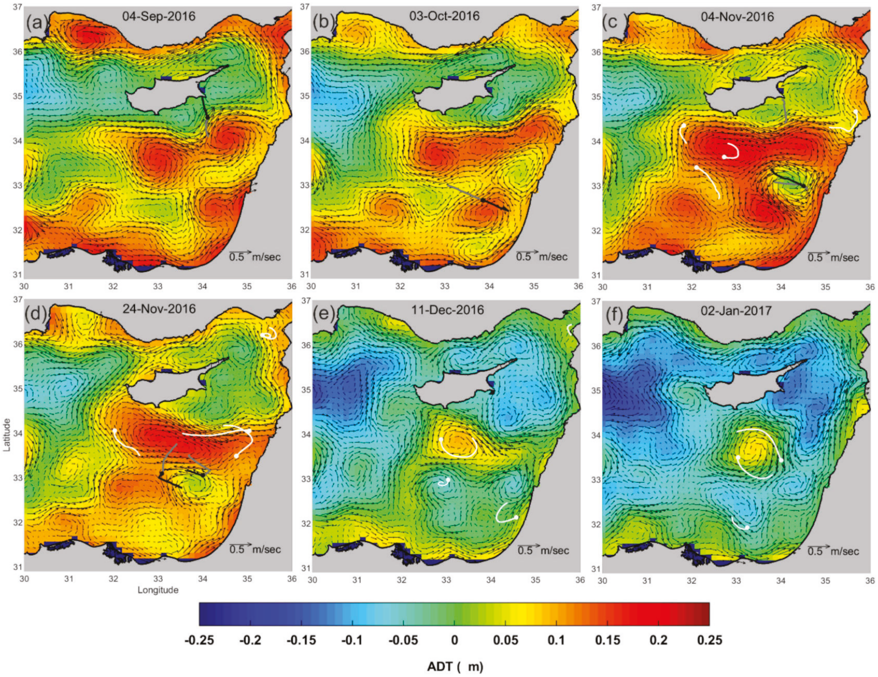

Figure 5. Selected maps of ADT with overlaid geostrophic currents with black, gray and white lines and dots as in Figure 4. CE and NSE evolution; anticyclones as separated eddies (**a**); presence of 3 small eddies in the same area (**b**); wide zonally-elongated anticyclonic structure (**c**); persistence of the CE-NSE anticyclone (**d**); weakening of the elongated anticyclone eddies (**e**) and disappearance of NSE (**f**).

To better show the time evolution of the two eddies and their geographical position, two Hovmoeller diagrams using as reference the altimetry data at 33.81° N (Figure 6a) and 34.2° E (Figure 6b) were produced. The latitude and longitude of the CE were selected based on the mean ADT for the period September 2016 to August 2017 (see Figure 3). As mentioned before, from October to December 2016 a large zonally-expanded anticyclone structure characterized the area. In November, this feature covered zonally the broadest area from 32° E to 35° E (Figure 6a) and in the meridional direction from 33.4° N to 34.7° N (Figure 6b). Starting from December, the CE was evident again as a single anticyclone with a lower signature in ADT and a smaller extension of about one degree in both longitude and latitude.

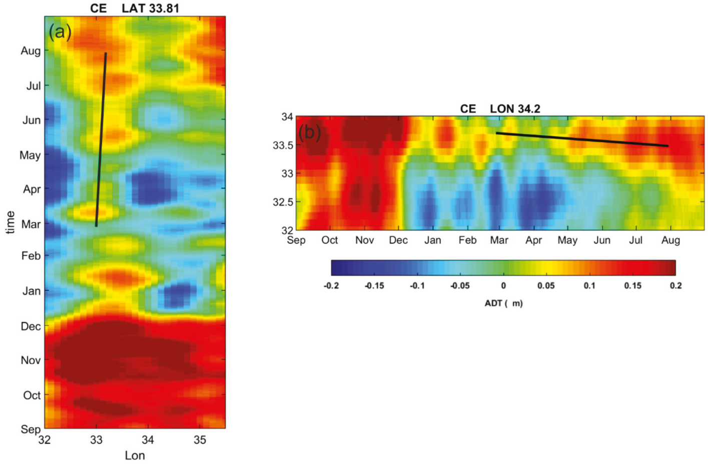

Figure 6. Hovmoeller diagram of ADT (**a**) along latitude 33.81° N and (**b**) longitude 33.19° E. Position of the CE determined from the annual ADT image. The black line shows the eddy displacement derived from the drifter data.

In September the gliders sampled the water column in the CE while in October-November 2016 they captured the CE-NSE merging event (refer to paragraph 3.2.).

In stratified conditions, from May until August 2017, the anticyclone was evidenced by a core of cold water (Figure 7). The area south of Cyprus was characterized by a strong upwelling with cold waters advected southward by the CE (Figure 7a–c). Starting from May, the eastern part of the basin becomes increasingly cooler. In July, cold filaments were advected toward the north, tracing the external edge of the CE (Figure 7b). By mid of August 2017, the cold western water was not entering as MMJ as in the previous year (Figure 7c). From June until August the NSE moved more than $\frac{1}{2}$ degree north, despairing for 2 weeks in mid-July.

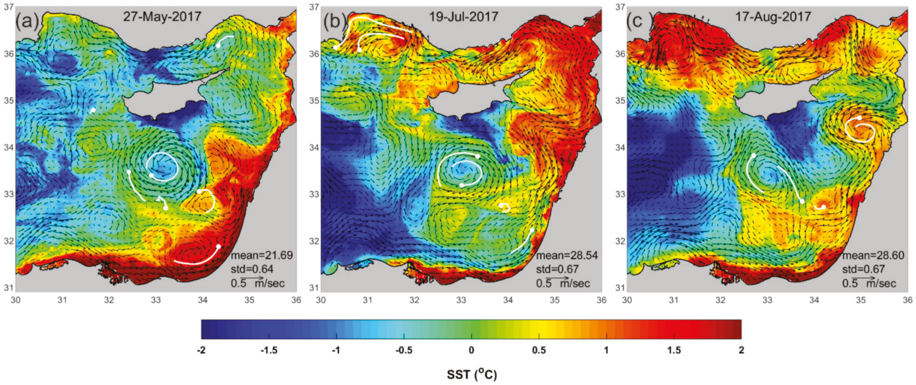

Figure 7. SST anomaly images with overlaid geostrophic current with white lines and dots as in Figure 4. CE marked by a cold core from May to August 2017; cold core and upwelled water south of Cyprus advected by the CE (**a**); CE cold core and a westward filament tracing the external edge of the CE (**b**); CE extending to the Cyprus coast, upwelling south of Cyprus, absence of the MMJ (**c**).

Upwelling off Israel and South Shikmona Eddy

In late November 2016, an event of upwelling took place along the Israeli coast and lasted for about 7 days. The phenomenon, induced by eastern wind blowing for 10 consecutive days over 3 m/sec, was visible from 26 November to 2 December 2016. The upwelled water showed a temperature decrease of 2 °C close to the coast. The SSE and other smaller eddies to the south probably advected the cold water in the open sea and the offshore flowing filaments maintained a difference in temperature while moving away from the coast (Figure 8). The two gliders sampled the area during the same period, but they did not capture the upwelling signature. The cold layer, advected away from the coast, probably affected only the top surface layer, which was not sampled by the gliders.

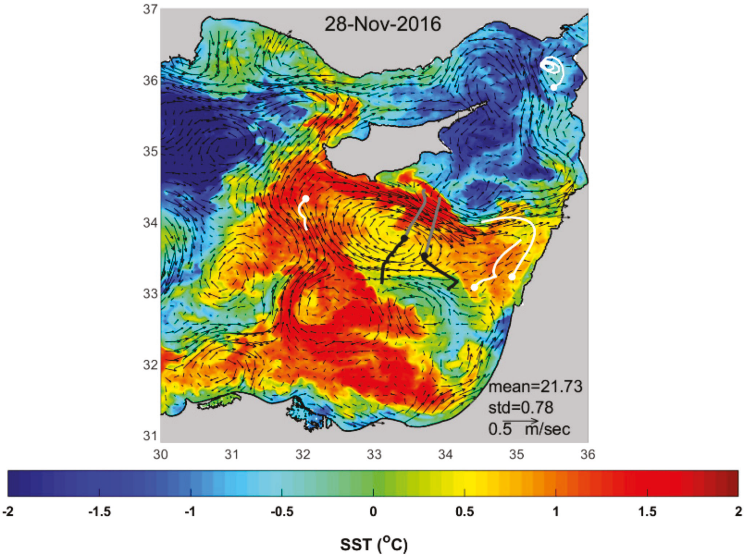

Figure 8. SST anomaly image with overlaid geostrophic currents with black, gray and white lines and dots as in Figure 4. Event of upwelling in front of the Israeli coast at the end of November 2017.

During fall and winter, the ADT maps show a distinct motion of the SSE. In order to have a better description of the 1-year eddy evolution Hovmoeller diagrams of the ADT were constructed (Figure 9). The reference position (latitude 33.06° N–longitude 34.31° E) of the eddy was identified from the mean ADT map (Figure 3). In September during the first glider campaign the eddy was weakly detected in ADT, then from October to the end of November during the second and the third glider campaigns the eddy became well defined (Figure 5c) and moved southwestward ($\frac{1}{2}$ degree south and 1 degree west; Figure 9a,b). In early December, the SSE moved farther west and a new SSE appeared at the usual position. From mid-December to the beginning of May, the SSE alternated periods when the eddy was well defined and periods in which it merged with another cyclone intruded to the south; sometimes the south tongue was close to the Lebanon coast (Figure 10a), other times the presence of NSE pushed the intrusion farther offshore (Figure 10b). The SSE finally splits in two cyclones at the end of May 2017 as shown in Figure 10c. During the summer months the eddy was weak or disappeared for weeks while in August it moved $\frac{1}{2}$ degree north (Figure 7c).

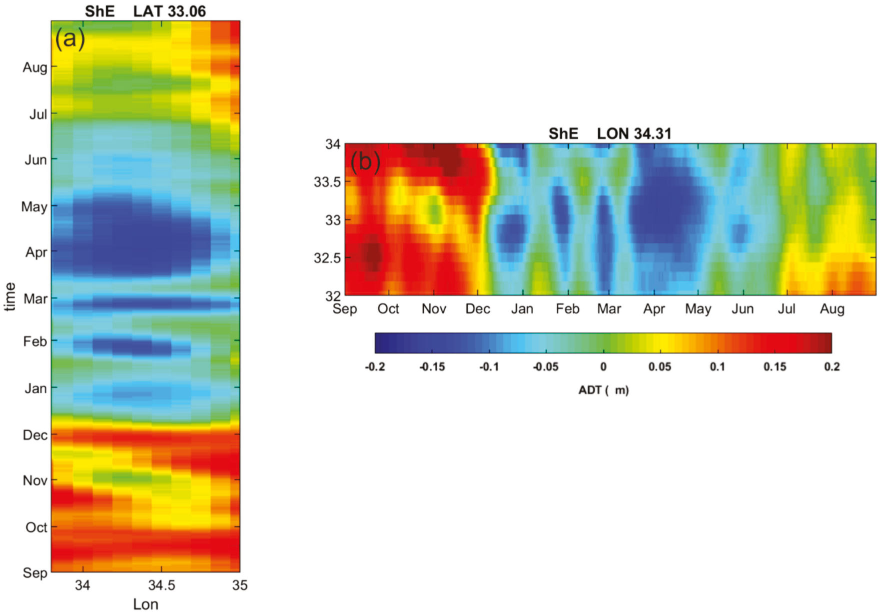

Figure 9. Hovmoeller diagram of ADT (**a**) along latitude 33.06° N and (**b**) longitude 34.31° E.

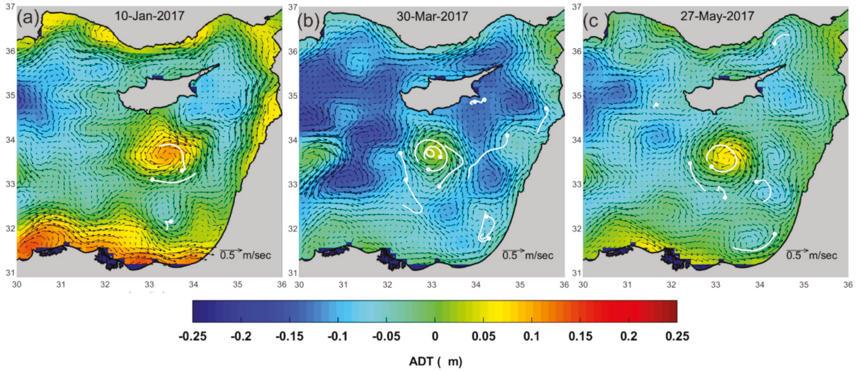

Figure 10. ADT with overlaid geostrophic currents with white lines and dots as in Figure 4. SSE merged with a cyclone intruded from the north: sometimes the intrusion was close to the Lebanon coast (**a**); the presence of NSE pushed the northern intrusion father offshore (**b**); SSE splits in two cyclones (**c**).

3.1.2. Quantitative Description of CE Using Drifter Data

Three drifters moved in and around the CE from February to May 2017, while two of them remained trapped in the eddy until August 2017. From the analysis of the data of the 3 drifters it was found that the eddy can be considered to be in quasi-solid body rotation up to a radius of 40–50 km, where the maximum drifter speed of 50 cm/s occurred [43]. In the 4 months period, the radius ranged between <10 km to about 100 km with some oscillations, due to the fat that the eddy might not be perfectly circular and also due to possible variations in rotation strength. From the estimation of the eddy center position, it was found that the anticyclone moved toward the southeast at a speed of about 150 m/day (see more details in [43]). This displacement is in good agreement with the ADT maps.

The black line depicted using the coefficients computed by the drifter data follows the motion of the CE displayed by Hovmoeller diagrams (Figure 6).

3.2. Qualitative Vertical Description of Some Sub-Basin Features Using Glider Surveys

In Fall 2016, the three glider campaigns were designed to sample the vertical structure of some sub-basin scale features between September and the beginning of December. The data of the second campaign (see track in Figure 1c) were plotted as a function of time (Figure 11). The eastern LS area appears strongly influenced by the presence of sub-basin eddies and mesoscale features. The thermohaline structure throughout the mission, shows a strong vertical stratification, with the presence of warm and salty LSW near the surface down to 40 m (Figure 11a), which gradually deepens, cooling and freshening (Figure 11b). The temperature (salinity) parameter between 20 m to 40 m reaches a maximum value of 26.24 °C (39.57 PSU). By the end of the mission, the mixed layer has deepened to 90 m and the maximum temperature has decreased to 20.38 °C (39.36 PSU). The AW is found at depths just below the LSW, under the thermocline (at about 50 m in October and 100 m depth at the end of November), revealed as a local minimum in salinity (about 38.8 PSU; Figure 11b), which slowly disappeared as the season comes to the end. Furthermore, a 70 m thick layer with relative salinity maximum is observed between 100 and 400 m corresponding to the thermohaline characteristics of the LIW. Below that depth in the LDW, the salinity gradually decreases with depth (not shown).

The contour plots of the second campaign (Figure 11) reveal the downward bending of the isolines of the water mass properties in correspondence to the CE anticyclone at the beginning and at the end of the mission. In between these anticyclones, a sequence of 4 transects, marked by individual upward domings, depicts different parts of the SSE area. The data after the second SSE transect (10–11 November) corresponds to the CE only partially sampled. After the fourth transect (22–25 November) data describe an anticyclone south of CE. The anticyclonic and cyclonic features are identified by acronyms and vertical black lines in Figure 11. The isopycnal curves overlaid on the temperature field show a homogeneous top layer and a highly stratified layer in correspondence to the AW below the thermocline.

The contour lines, representing the oxygen concentration (overlaid in Figure 11b) show a subsurface maximum between 65–100 m, diminishing gradually along the water column, while the top layer is quite homogeneous. The oxygen stratification is evident throughout the mission with the exception of the CE, where the isolines between 150 m depth and the LIW show a less stratified field. Some mesoscale structures visible in temperature, salinity and oxygen are present inside the CE (see description in the following section). The chlorophyll concentration (Figure 11c) displays a Deep Chlorophyll Maximum (DCM) at around 50 and 150 m depth. Its spatial structure (thickness and patchiness) is strongly influenced by the presence of the eddies. In the anticyclone, the DCM is deeper than in the cyclone, where the chlorophyll concentration is slightly higher. Maximum values are around 0.8 µg/L while the minimum is around 0.2 µg/L. Some filaments detach from the DCM in particular along the edges of the anticyclone, reaching 200–250 m depth. The backscattering (Figure 11d) exhibits different vertical distributions in the anticyclones and cyclones. In the CE backscattering is relatively high between 50 and 150 m, while inside the eddy below 150 m it is extremely low. This feature is present not only in the two CE transects but also in the area where two anticyclones were partially sampled (10–11 and 22–25 November). The extremely low backscattering values in the CE (the absolute minimum of the mission) also corresponds to the region of lower stratification in oxygen concentration. In the deeper layer down to 600 m (not shown, because sampled in mission C3) the backscattering is low, but the recorded absolute minimum is still between 150 and 300 m depth. The cyclone exhibits higher values of backscattering in the upper layer in the first 2 crossings of the SSE, then when the winter mixing starts, the values are lower even in the upper part of the SSE. There are relatively higher backscattering values below 200 m in the SSE area.

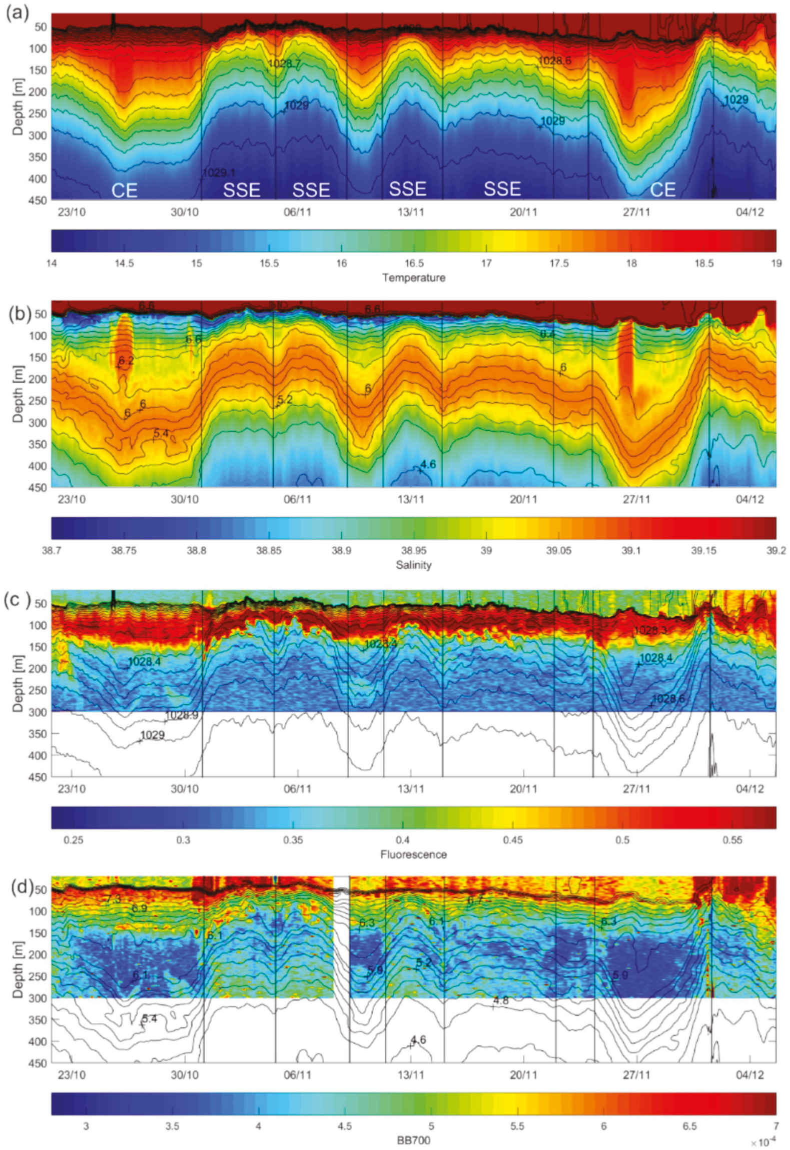

Figure 11. Glider data collected during the second campaign as a function of time and depth (20–450 m). Temperature field (°C) with isopycnal (intervals of 0.1 kg/m^3) overlaid (**a**), salinity field with oxygen (intervals of 0.2 mL/L) overlaid (**b**), fluorescence field (µg/L) with isopycnal overlaid (**c**), backscattering at 700 (m^{-1}) with oxygen overlaid (**d**).

The Cyprus Eddy and North Shikmona Eddy

During fall 2016, the area of the CE formation was sampled five times (see Table 2 for timing and other details). Since the gliders crossed the anticyclones along almost meridional transects (in both directions), the data were plotted in Figure 12 as a function of latitude for a better description and comparison. Each crossing transect was completed in 5 to 10 days from the beginning of October to the beginning of December 2016.

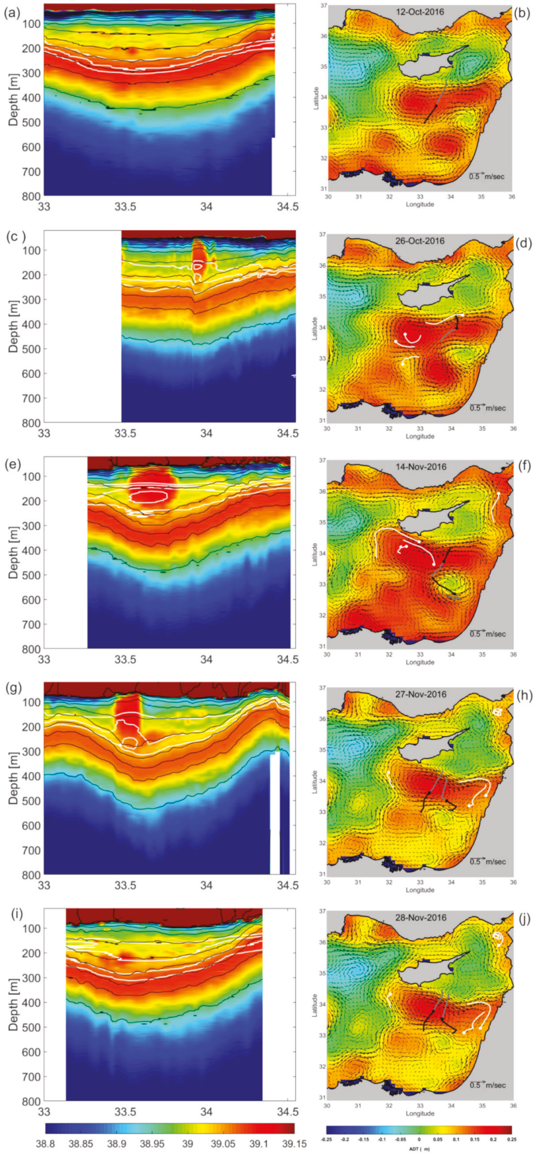

Figure 12. Fall salinity fields of the anticyclonic structures in the region of the CE (**left**). Transects are ordered chronologically and dates are reported in Table 2. Isopycnal (intervals of 0.1 kg/m^3) and isolines of oxygen concentration (intervals of 0.2 mL/L) are respectively shown with black and white lines. On the right, the ADT field and geostrophic currents. Black, grey, white lines and dots as in Figure 4. Salinity sections depicted in panels (**e**,**g**,**i**) correspond to the northern, western and eastern glider tracks in panels (**f**,**h**,**j**), respectively.

Table 2. Season (F—fall and W—winter), numbers assigned to the transect crossing the CE, mission name, period and approximate direction of sampling.

Season	Transect	Mission	Glider ID	Date	Glider Direction
F	1	C1	sg150	07 October 2016–15 October 2016	Northward
F	2	C2	sg554	21 October 2016–30 October 2016	Southward
F	3	C3	sg149	7 November 2016–17 November 2016	Southward
F	4	C2	sg554	23 November 2016–02 December 2016	Northward
F	5	C3	sg149	27 November 2016–02 December 2016	Northward
W	6	C4	sg149	17 February 2017–21 February 2017	Southward
W	7	C5	sg554	02 March 2017–06 March 2017	Northward

All five salinity fields collected during fall are displayed in chronological order in Figure 12. The ADT fields, with the associated geostrophic currents and glider/drifter tracks overlaid, (Figure 12, right column), give additional information of the surface dynamics during the sampling interval. The dates of the selected ADT maps correspond to the times when the gliders sampled the center of the isolines deepening. The black dot on the glider track corresponds to its position on that date. From the analysis of the ADT the first transect (Figure 12b) crosses a zonally elongated anticyclone corresponding to the merging of the CE and NSE, described in paragraph 3.1.1. Transect 2 (Figure 12d), one week later, crosses the wide formed structure close to the NSE usual position. As time passes the anticyclone becomes larger with strong geostrophic currents as observed during the third glider crossing (Figure 12f). Approximately one week later (Figure 12g–j), the same structure is captured almost simultaneously along transects 4 and 5. The transect 4 evidences the eddy in its central part, while the transect 5 is relative to its easternmost portion.

On the left side of Figure 12 the salinity vertical structure with density (black curves) and oxygen (white curves) overlaid, describes the five sampled transects of the anticyclone in the CE area between October and the beginning of December 2016. The water masses of the CE are typical of the eastern LS but the thermohaline vertical structure is strongly influenced by the deepening of the isolines extending down to 950 m. It is noticeable that all the transects exhibit an asymmetry in all parameters that does not seem to be related to the sampling method, since it is present both in the transects sampled from north to south (Figure 12c,e) and in those sampled in the opposite direction (Figure 12a,g,i).

A high salinity subsurface core of different shape and size is present in all transects. The homogeneous salinity core or lens is around 39.1 PSU and mainly enclosed within an isohaline of 39.05 PSU. The vertical extension of the core in transects 2, 3, 4 is between 50 and 250 m and laterally from 33.4 to 34° E (more specifically 33.4–33.6° E in transect 2, 33.5–33.8° E in transect 3 and 33.9–34° E in transect 4). This core is marked also in temperature (not shown): the 18 and 18.5 °C isotherms are bended downward, surrounding the lower part of the lens (e.g., Figure 11a). The core in its upper part evidences an upward doming in salinity, density and oxygen concentration.

The isopycnals highlight a strong vertical stratification in density in the upper part of the core while the lower part is rather homogeneous. A minimum of oxygen is clearly visible in the lower part of the lens (white lines in Figure 12c,e,g). The high salinity core evident in transects 1 and 5 (Figure 12a,i) have smaller vertical extension spanning between 250 and 300 m and laterally from 33.3 to 33.5° E in transect 5, while it is barely visible in transect 1.

In the attempt to have a better perception of the high salinity core geographical position, the five glider pathways, crossing the CE, were overlaid on the bathymetry of the area (Figure 13). The dots correspond to the salinity at 150 m and they are color-coded according to the salinity values. The transects are numbered following a chronological order. During the first and fifth transect a small high salinity core is barely visible because the lens is located deeper (Figure 12a), while in transect 2, 3, 4 the core is well captured. Figure 13 shows that the salty core was sampled first to the west during transect 2, then it was captured $\frac{1}{2}$ degree to the east in transect 3 and again $\frac{1}{2}$ degree to east during transect 4. Transect 5 was almost concomitant to the fourth transect but did not capture the salty core at 150 m. High salinity is also evident in the northern part of the transects, where the bathymetry is shallower than in the southern part, but this is another feature different from the signature of the high salinity core.

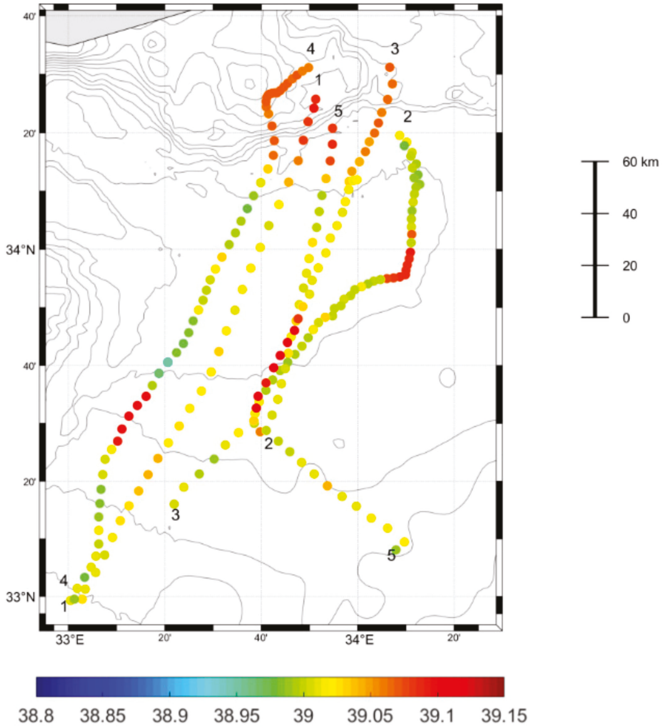

Figure 13. The fall 2016 glider pathways corresponding to the transects shown in Figure 12. The color-coded dots are the salinity sampled at 150 m depth. Transects are numbered chronologically according to Table 2.

In winter, the gliders crossed the CE twice (see transects 6 and 7 in Table 2) and only transect 6 is described as an example. The deepening of the water mass properties is evident. The salinity field is displayed in Figure 14a, while its geographical position is shown on the ADT image in Figure 14b. The CE appears like a body of homogeneous salty water (39.2 PSU) down to 400 m depth, included in the downward doming of the LIW. The temperature in the surface layer (not shown) is homogeneous only to 100 m depth in the northern edge and 200 m in the southern edge, confirmed by the isopycnals (black lines in Figure 14a). The AW is no longer visible as a local minimum in salinity, having been mixed with the layers below and above during the winter in the previous weeks. The LIW is also no longer identifiable as a relative maximum in salinity but it still conserves the thermohaline properties found during fall (Figure 15). In the winter structures, both chlorophyll and turbidity fields (not shown) are vertically homogeneous reaching 300 m depth.

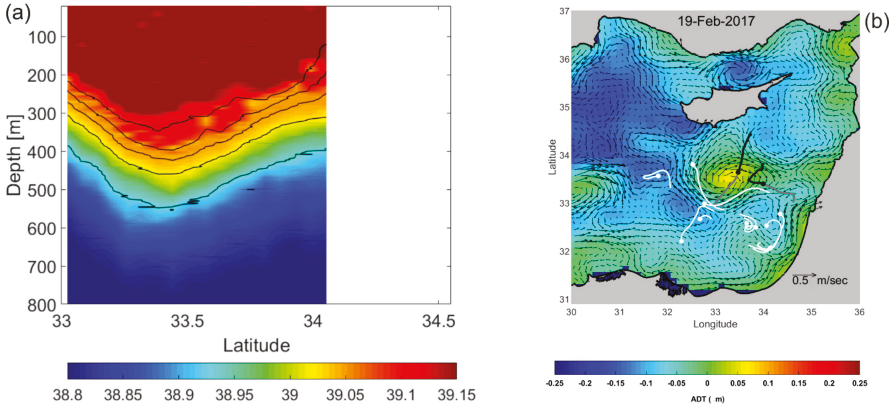

Figure 14. Winter salinity field of transect 6 (dates in Table 2) isopycnals (black lines, intervals of 0.1 kg/m^3) overlaid (**a**); ADT image of the day when the glider crossed the center of the eddy (**b**). The transect is relative to the glider track depicted to the left, the dot is the position of the glider on the same day of the image, the black line is relative to 4 days before and the gray line is relative to 4 days after. White curves are 4-day trajectory segments of drifters (shown with white dots).

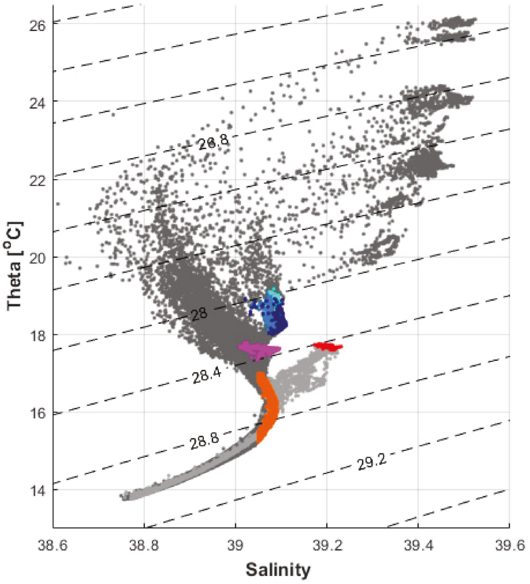

Figure 15. Theta-S diagram in the CE region obtained from the fall (winter) glider data in dark gray (light gray), the dashed lines are isopycnals. Turquoise, light blue, dark blue and magenta dots correspond to the high salinity core found in the transects 2, 3, 4 and 5 respectively. Red dots are relative to values between 20–200 m in winter transect, while orange dots correspond to the salinity maximum associated to the LIW, both for fall and winter missions.

To analyze further the thermohaline properties of the high salinity core a Theta-Salinity (TS) diagram of the CE region is depicted in Figure 15. All the glider temperature and salinity data of transects 1 to 6 (see Table 2 and Figures 12 and 14) are represented during fall (dark grey) and winter (in light grey). The high salinity core data, found in transects 2, 3, 4 and 5 are respectively plotted in turquoise, light blue, dark blue and magenta. The red is used to distinguish the homogeneous salty water mass present in the upper layer (20–200 m) inside the CE during winter (Figure 14a), while orange corresponds to the salinity maximum associated with the LIW, in both seasons. All the high salinity cores present the salinity of the LIW, with exception of a few values of the core in transect 5. The density of each core ranges between 28 and 28.34 kg/m^3 and the vertical structure inside the core is mainly driven by temperature (as visible from the isopycnals in Figure 12). The core in transect 5 has a lower temperature in comparison with the others resulting in a higher density (28.36–28.4 kg/m^3).

4. Discussion and Conclusions

The use of satellite altimetry and SST anomaly in concert with drifter data allowed us to analyze the surface evolution of some of the major sub-basin and mesoscale circulation structures in the eastern LS in two different seasons between September 2016 and August 2017. The eastern LS appears very variable over time: the geostrophic position, the size and the shape of most eddies change in a few weeks due to their interaction or their complete disappearance.

The anticyclonic CE is the most persistent feature in the above-mentioned period covering a broad geographical region south of Cyprus. It evolves while changing in shape, merging with other eddies like the NSE during fall 2016. Drifters were captured by it between February and May 2017 allowing a quantitative study of its kinematics. The mean radius of the eddy is about 40–50 km and the maximum speed of about 50 cm/s is reached at 40 km from the eddy center. The CE moves 150 m/day to the southeast. The NSE is present mainly during fall until the beginning of December, when it becomes partially merged with the CE. Then, it disappears until July when it reappears and it moves $\frac{1}{2}$ degree more to the north. The cyclonic SSE in some periods moves far from the coast to the southwest, merging with other cyclones and disappearing from its most probable position for weeks. Other eddies are present in the area like E1, E2 and LE (Figure 3), but their presence and position during the year of the study seems to be very variable and difficult to easily describe.

Besides eddies, the eastern LS is also characterized by a strong upwelling south of Cyprus in the summer months (September 2016 and May–August 2017), and other features occasionally present like the MMJ and the cold front east of Cyprus. The MMJ is present during the whole month of September 2017, crossing the basin from west to east, clearly traced by the cold water in the SST anomaly images, by the drifter tracks and by the geostrophic currents computed from the ADT fields. The jet skims the southern coast of Cyprus and flows toward the Syria/Lebanon coast, where it decreases in strength and it turns north along the coast. The disappearance of the jet corresponds to a wider extension of the CE to the north. The thermal zonal front, spanning from the southeast coast of Cyprus to the Syria/Lebanon coast represents a persistent feature from October to the beginning of March, concomitant with the cooling of the northern part of the basin. The front with a prevailing zonal orientation is first jagged and undefined, then it becomes sharper characterized by a strong current in the warmer side and finally, when the currents weaken, the north intrusions start to degrade the front. The upwelling in front of Israel at the end of November 2016 represents another sporadic event.

The glider campaigns sampled the vertical structures present in the area allowing a general description of a few circulation features in fall 2016 and in winter 2016–2017. The CE is the most sampled eddy during the fall season; it shows the usual thermohaline structure of the area, modulated below the mixed layer (50–100 m), by the downward bending of all the physical parameters measured. However above it, the isopycnals bend upward (Figure 12c,e,g) and in between the up and downward isopycnals, a homogeneous volume of water is present. This kind of eddies has been described as anticyclonic modewater eddies or submesoscale coherent vortices in different basins of the world [46–50]. The CE has a strong signature in ADT, but usually these eddies are also characterized by a negative SST anomaly, that was not seen at least during fall and winter. In summer, instead, the signature in SST anomaly was evident for three full months, but it was not supported by any glider measurement.

The existence of a high salinity core in the CE area was previously reported in studies implying CTD and XCTS surveys [3,25,30,51–53]. More recently, this lens was also described in glider missions, which took place in late fall and at the beginning of winter during the years 2009, 2010 and 2011–2012 [54]. However, in these earlier glider observations, the maximum of the salinity (around 39.3 PSU) showed higher values and lower temperature (around 17 °C) with respect to the LIW. In the present study, the core has the same salinity and a higher temperature (around 18.5 °C) than the LIW. A minimum in oxygen is evident in the lower part of the core; it is probably related to biological processes as those indicated in the Tropical North Atlantic by [48,55] and in the Mediterranean Sea by [56].

The CE shows a north-south asymmetry with steeper isolines in the north, where the bathymetry is shallower (Figure 13). This can be due to an interaction between the CE and the bathymetry as already shown in previous studies [13,30,36,57]. The shallow bathymetry is probably responsible for the strengthening of the geostrophic currents in the northern part of the CE, also underlined by the ADT maps analyzed in this study and the results described in [4].

Based on the obtained results, it is difficult to identify a specific process involved in the generation of the high salinity core found in the CE region. We can only speculate on the possible generation mechanisms. The shallower bathymetry in the northern part of the CE region, leads to a rising of the high salinity maximum of the LIW during summer or fall. The interaction of this layer with the bathymetry could generate instabilities that induces the creation of a nucleus of high salinity. Another origin of the core thermohaline properties could be related to the water mass created during winter mixing, as mentioned in [25,56]. This is consistent with the results of [58,59], who showed that the CE is able to maintain its core temperature and salinity characteristics for periods of up to two years. However further understanding of the local mechanisms of water mass exchanges and mixing processes is needed. This will be the subject of future studies.

Author Contributions: Conceptualization, E.M. and P.-M.P.; Data curation, L.S., R.G. and D.H.; Formal analysis, E.M. and L.S.; Funding acquisition, P.-M.P.; Investigation, D.H. and H.G.; Validation, L.S. and R.G.; Writing—original draft, E.M., L.S.; Writing—review & editing, L.S., R.G. and P.-M.P.

Funding: This study is part of the CINEL project sponsored by the U.S. Office of Naval Research (ONR) under grant N000141512459.

Acknowledgments: We thank the following persons who have helped with the sea-going operations and the processing of the data: Antonio Bussani, Milena Menna, Piero Zupelli, Massimo Pacciaroni, Stefano Kuchler and Aya Hozumi.

Conflicts of Interest: The authors declare no conflict of interest.

References

1. Ozsoy, E.; Hecht, A.; Unluata, U.; Brenner, S.; Oguz, T.; Bishop, J.; Latif, M.A.; Rozentraub, Z. A review of Levantine Basin circulation and variability during 1985–1988. *Dyn. Atmos. Oceans* **1991**, *15*, 421–456. [CrossRef]
2. Pinardi, N.; Masetti, E. Variability of the large-scale general circulation of the Mediterranean Sea from observations and modelling: A review. *Palaeogeogr. Palaeoclimatol. Palaeoecol.* **2000**, *158*, 153–173. [CrossRef]
3. Fusco, G.; Manzella, G.M.R.; Cruzado, A.; Gacic, M.; Gasparini, G.P.; Kovacevic, V.; Millot, C.; Tziavos, C.; Velasquez, Z.R.; Walne, A.; et al. Variability of mesoscale features in the Mediterranean Sea from XBT data analysis. *Ann. Geophys.* **2003**, *21*, 21–32. [CrossRef]
4. Menna, M.; Poulain, P.-M.; Zodiatis, G.; Gertman, I. On the surface circulation of the Levantine sub-basin derived from Lagrangian drifters and satellite altimetry data. *Deep-Sea Res. Part I* **2012**, *65*, 46–58. [CrossRef]
5. Nielsen, J.N. Hydrography of the Mediterranean and adjacent waters. *Rep. Dan. Oceanogr. Exp. Medit.* **1912**, *1*, 77–192.
6. Ovchinnikov, I.M. Circulation in the surface and intermediate layer of the Mediterranean. *Oceanology* **1966**, *6*, 48–59.
7. Ovchinnikov, I.M.; Plakhin, E.A.; Moskalenko, L.V.; Negliad, K.V.; Osadchii, A.S.; Fedoseev, A.F.; Krivoscheya, V.G.; Voitova, K.V. *Hydrology of the Mediterranean Sea*; Gidrometeoizdat: Leningrad (URSS), Russia, 1976; p. 375.

8. Robinson, A.R.; Golnaraghi, M.; Leslie, W.G.; Artegiani, A.; Hecht, A.; Lazzoni, E.; Michelato, A.; Sansone, E.; Theocharis, A.; Unluata, U. The Easte rn Mediterranean general circulation: Features, structure and variability. *Dyn. Atmos. Oceans* **1991**, *15*, 215–240. [CrossRef]
9. Ozsoy, E.; Hecht, A.; Unluata, U.; Brenner, S.; Sur, H.I.; Bishop, J.; Latif, M.A.; Rozentraub, Z.; Oguz, T. A synthesis of the Levantine Basin circulation and hydrography, 1985–1990. *Deep-Sea Res.* **1993**, *40*, 1075–1119.
10. Robinson, A.R.; Golnaraghi, M. Circulation and dynamics of the Eastern Mediterranean Sea; Quasi-Synoptic data-driven simulations. *Deep Sea Res.* **1993**, *40*, 1207–1246. [CrossRef]
11. Malanotte-Rizzoli, P.; Manca, B.; Ribera D'Alcala, M.; Theocharis, A.; Bergamasco, A.; Bregant, D.; Budillon, G.; Civitarese, G.; Georgopoulos, D.; Michelato, A.; et al. A synthesis of the Ionian Sea hydrography, circulation and water masses pathway during POEM-Phase I. *Prog. Oceanogr.* **1997**, *39*, 153–204. [CrossRef]
12. Millot, C.; Taupier-Letage, I. Circulation in the Mediterranean Sea. *Handb. Environ. Chem.* **2005**, *5*, 29–66.
13. Hamad, N.; Millot, C.; Taupier-Letage, I. The surface circulation in the eastern basin of Mediterranean Sea. *Sci. Mar.* **2006**, *70*, 457–503.
14. Pascual, A.; Pujol, M.; Larnicol, G.; Le Traon, P.Y.; Rio, M. Mesoscale mapping capabilities of multisatellite altimeter missions: First results with real data in the Mediterranean Sea. *J. Mar. Syst.* **2007**, *65*, 190–211. [CrossRef]
15. Rio, M.-H.; Poulain, P.-M.; Pascual, A.; Mauri, E.; Larnicol, G.; Santoleri, R. A mean dynamic topography of the Mediterranean Sea computed from altimetric data, in-situ measurements and a general circulation model. *J. Mar. Syst.* **2007**, *65*, 484–508. [CrossRef]
16. Amitai, I.; Lehahn, Y.; Lazar, A.; Heifetz, E. Surface circulation of the eastern Mediterranean Levantine basin: Insights from analyzing 14 years of satellite altimetry data. *J. Geophys. Res.* **2010**, *115*, C10058. [CrossRef]
17. Tziperman, E.; Malanotte-Rizzoli, P. The climatological seasonal circulation of the Mediterranean Sea. *J. Mar. Res.* **1991**, *49*, 411–434. [CrossRef]
18. Lascaratos, A.; Williams, R.G.; Tragou, E. A Mixed-layer study of the formation of levantine intermediate water. *J. Geophys. Res.* **1993**, *98*, 739–749. [CrossRef]
19. Alhammoud, B.; Branger, K.; Mortier, L.; Crepon, M.; Dekeyser, I. Surface circulation of the Levantine basin: Comparison of model results with observation. *Prog. Oceanogr.* **2005**, *66*, 299–320. [CrossRef]
20. Gerin, R.; Poulain, P.-M.; Taupier-Letage, I.; Millot, C.; Ben Ismail, S.; Sammari, C. Surface circulation in the Eastern Mediterranean using Lagrangian drifters (2005–2007). *Ocean Sci.* **2009**, *5*, 559–574. [CrossRef]
21. Millot, C.; Gerin, R. The Mid-Mediterranean Jet Artefact. *Geophys. Res. Lett.* **2010**, *37*, L12602. [CrossRef]
22. Pinardi, N.; Zavatarelli, M.; Arneri, E.; Crise, A.; Ravaioli, M. The physical, sedimentary and ecological structure and variability of shelf areas in the Mediterranean Sea. In *The Sea*; Robinson, A.R., Brink, K., Eds.; Harvard University Press: Cambridge, MA, USA, 2006; Volume 14, pp. 1245–1330.
23. Zodiatis, G.; Hayes, D.; Gertman, I.; Samuel-Rhoads, Y. The Cyprus warm Eddy and the Atlantic water during the CYBO cruises (1995–2009). Generation Shikmona anticyclonic eddy from long shore current. *Rapp. Commun. Int. Mer. Medit.* **2010**, *39*, 202.
24. Pinardi, N.; Bonazzi, A.; Dobricic, S.; Milliff, R.F.; Wikle, C.K.; Berliner, L.M. Ocean ensemble forecasting. Part II: Mediterranean forecast system response. *Q. J. R. Meteorol. Soc.* **2011**, *137*, 879–893. [CrossRef]
25. Zodiatis, G.; Drakopoulos, P.; Brenner, S.; Groom, S. Variability of Cyprus warm core eddy during the CYCLOPS project. *Deep-Sea Res.* **2005**, *52*, 2897–2910. [CrossRef]
26. Ayoub, N.; Le Traon, P.; De Mey, P. A description of the Mediterranean surface variable circulation from combined ERS-1 and TOPEX/POSEIDON altimetric data. *J. Mar. Syst.* **1998**, *18*, 3–40. [CrossRef]
27. Zodiatis, G.; Theodorou, A.; Demetropulos, A. Hydrography and circulation south of Cyprus in late summer 1995 and in spring 1996. *Oceanol. Acta* **1998**, *21*, 447–458. [CrossRef]
28. Gertman, I.; Zodiatis, G.; Murashkovsky, A.; Hayes, D.; Brenner, S. Determination of the locations of southeastern Levantine anticyclonic eddies from CTD data. *Rapp. Commun. Int. Mer. Medit.* **2007**, *38*, 151.
29. Ozer, T.; Gertman, I.; Kress, N.; Silverman, J.; Herut, B. Interannual thermohaline (1979–2014) and nutrient (2002–2014) dynamics in the Levantine surface and intermediate water masses, SE Mediterranean Sea. *Glob. Planet. Chang.* **2017**, *151*, 60–67. [CrossRef]
30. Brenner, S. Structure and evolution of warm core eddies in the eastern Mediterranean Levantine Basin. *J. Geophys. Res.* **1989**, *94*, 12593–12602. [CrossRef]

31. Aulicino, G.; Cotroneo, Y.; Ruiz, S.; Sanchez Roman, A.; Pascual, A.; Fusco, G.; Tintore, J.; Budillon, G. Monitoring the Algerian Basin through glider observations, satellite altimetry and numerical simulations along a SARAL/AltiKa track. *J. Mar. Syst.* **2018**, *179*, 55–71. [CrossRef]
32. Olita, A.; Ribotti, A.; Sorgente, R.; Fazioli, L.; Perilli, A. SLA-chlorophyll-a variability and covariability in the Algero-Provençal Basin (1997–2007) through combined use of EOF and wavelet analysis of satellite data. *Ocean Dyn.* **2011**, *61*, 89–102. [CrossRef]
33. Pujol, M.I.; Larnicol, G. Mediterranean Sea eddy kinetic energy variability from 11 years of altimetric data. *J. Mar. Syst.* **2005**, *58*, 121–142. [CrossRef]
34. Font, J.; Isern-Fontanet, J.; Salas, J.J. Tracking a big anticyclonic eddy in the Western Mediterranean Sea. *Sci. Mar.* **2004**, *68*, 331–342. [CrossRef]
35. Bosse, A.; Testor, P.; Mayot, N.; Prieur, L.; d'Ortenzio, F.; Mortier, L.; Le Goff, H.; Gourcuff, C.; Coppola, L.; Lavigne, H.; et al. A submesoscale coherent vortex in the Ligurian Sea: From dynamical barriers to biological implications. *J. Geophys. Res. Oceans* **2017**, *122*, 6196–6217. [CrossRef]
36. Cotroneo, Y.; Aulicino, G.; Ruiz, S.; Pascual, A.; Budillon, G.; Fusco, G.; Tintore, J. Glider and satellite high resolution monitoring of a mesoscale eddy in the Algerian basin: Effects on the mixed layer depth and biochemistry. *J. Mar. Syst.* **2016**, *162*, 73–88. [CrossRef]
37. Troupin, C.; Pascual, A.; Ruiz, S.; Olita, A.; Casas, B.; Margirier, F.; Poulain, P.M.; Notarstefano, G.; Torner, M.; Fernández, J.G.; et al. The AlborEX dataset: Sampling of sub-mesoscale features in the Alboran Sea. *Earth Syst. Sci. Data* **2019**, *11*, 129–145. [CrossRef]
38. Liblik, T.; Karstensen, J.; Testor, P.; Mortier, L.; Alenius, P.; Ruiz, S.; Pouliquen, S.; Hayes, D.; Mauri, E.; Heywood, K. Potential for an underwater glider component as part of the Global Ocean Observing System. *Meth. Oceanogr.* **2016**, *17*, 50–82. [CrossRef]
39. Menna, M.; Gerin, R.; Bussani, A.; Poulain, P.-M. *The OGS Mediterranean Drifter Dataset: 1986–2016*; Rel. OGS 2017/92 OCE 28 MAOS; Istituto Nazionale di Oceanografia e di Geofisica Sperimentale: Trieste, Italy, 2017; p. 34.
40. Lumpkin, R.; Pazos, M. Measuring surface currents with SVP drifters: The instrument, its data and some results. In *Lagrangian Analysis and Prediction of Coastal and Ocean Dynamics*; Griffa, A., Kirwan, A.D., Jr., Mariano, A.J., Özgökmen, T., Rossby, H.T., Eds.; Cambridge University Press: Cambridge, UK, 2007; pp. 39–67.
41. Hansen, D.V.; Poulain, P.-M. Processing of WOCE/TOGA drifter data. *J. Atmos. Ocean. Technol.* **1996**, *13*, 900–909. [CrossRef]
42. Poulain, P.-M.; Barbanti, R.; Cecco, R.; Fayes, C.; Mauri, E.; Ursella, L.; Zanasca, P. *Mediterranean Surface Drifter Database: 2 June 1986 to 11 November 1999*; Rel. 75/2004/OGA/31; CDRom; OGS: Trieste, Italy, 2004.
43. Prigent, A.; Poulain, P.-M. *On the Cyprus Eddy Kinematics*; Rel. 2017/77 sez. OCE 19 MAOS; OGS: Trieste, Italy, 2017; p. 11.
44. Buongiorno Nardelli, B.; Tronconi, C.; Pisano, A.; Santoleri, R. High and Ultra-High resolution processing of satellite Sea Surface Temperature data over Southern European Seas in the framework of MyOcean project. *Remote Sens. Environ.* **2013**, *129*, 1–16. [CrossRef]
45. Pujol, M.-I.; Faugère, Y.; Taburet, G.; Dupuy, S.; Pelloquin, C.; Ablain, M.; Picot, N. DUACS DT14: The new multi-mission altimeter data set reprocessed over 20 years. *Ocean Sci.* **2016**, *12*, 1067–1090. [CrossRef]
46. McWilliams, J.C. Submesoscale, coherent vortices in the ocean. *Rev. Geophys.* **1985**, *23*, 165–182. [CrossRef]
47. D'Asaro, E.A. Generation of submesoscale vortices: A new mechanism. *J. Geophys. Res.* **1988**, *93*, 6685–6693. [CrossRef]
48. Karstensen, J.; Schütte, F.; Pietri, A.; Krahmann, G.; Fiedler, B.; Grundle, D.; Hauss, H.; Körtzinger, A.; Löscher, C.R.; Testor, P.; et al. Upwelling and isolation in oxygen-depleted anticyclonic modewater eddies and implications for nitrate cycling. *Biogeosciences* **2017**, *14*, 2167–2181. [CrossRef]
49. Testor, P.; Bosse, A.; Houpert, L.; Margirier, F.; Mortier, L.; Legoff, H.; Conan, P. Multiscale observations of deep convection in the northwestern Mediterranean Sea During winter 2012–2013 using multiple platforms. *J. Geophys. Res. Oceans* **2018**, *123*, 1745–1776. [CrossRef]
50. Meunier, T.; Pallàs-Sanz, E.; Tenreiro, M.; Portela, E.; Ochoa, J.; Ruiz-Angulo, A.; Cusí, S. The Vertical Structure of a Loop Current Eddy. *J. Geophys. Res. Oceans* **2018**, *123*, 6070–6090. [CrossRef]
51. Zodiatis, G.; Manca, B.; Balopoulos, E. Synoptic, seasonal and interannual variability of the warm core Eddy south of Cyprus. SE Levantine Basin. *Rapp. Comm. Int. Mer. Medit.* **2001**, *36*, 89–90.

52. Zodiatis, G.; Drakopoulos, P.; Brenner, S.; Groom, S. CYCLOPS project: The hydrodynamics of the warm core eddy south of Cyprus. In *Oceanography of the Eastern*; Yilmaz, A., Ed.; Tubitak Publishers: Ankara, Turkey, 2003; pp. 18–23.
53. Manzella, G.M.R.; Cardin, V.; Cruzado, A.; Fusco, G.; Gacic, M.; Galli, C.; Gasparini, G.P.; Gervais, T.; Kovacevic, V.; Millot, C.; et al. EU sponsored effort improves monitoring of circulation variability in the Mediterranean. *EOS Trans. AGU* **2001**, *82*, 497–504. [CrossRef]
54. Hayes, D.R.; Zodiatis, G.; Konnaris, G.; Hannides, A.; Solovyov, D.; Testor, P. Glider transects in the Levantine Sea: Characteristics of the warm core Cyprus eddy. In Proceedings of the Oceans 2011 IEEE-Spain, Santander, Spain, 6–9 June 2011; pp. 1–9. [CrossRef]
55. Karstensen, J.; Fiedler, B.; Schütte, F.; Brandt, P.; Körtzinger, A.; Fischer, G.; Zantopp, R.; Hahn, J.; Visbeck, M.; Wallace, D. Open ocean dead zones in the tropical North Atlantic Ocean. *Biogeosciences* **2015**, *12*, 2597–2605. [CrossRef]
56. Moutin, T.; Prieur, L. Influence of anticyclonic eddies on the Biogeochemistry from the Oligotrophic to the Ultraoligotrophic Mediterranean (BOUM cruise). *Biogeosciences* **2012**, *9*, 3827–3855. [CrossRef]
57. Hamad, N.; Millot, C.; Taupier-Letage, I. A new hypothesis about the surface circulation in the eastern basin of the Mediterranean Sea. *Prog. Oceanogr.* **2005**, *66*, 287–298. [CrossRef]
58. Brenner, S. Long-term evolution and dynamics of a persistent warm core eddy in the Eastern Mediterranean Sea. *Deep-Sea Res. II* **1993**, *40*, 1193–1206. [CrossRef]
59. Brenner, S.; Rosentraub, Z.; Bishop, J.; Krom, M. The mixed layer/thermocline cycle of a persistent warm core Eddy in the Eastern Mediterranean. *Dyn. Atmos. Oceans* **1991**, *15*, 457–476. [CrossRef]

water

Article

Sea Surface Circulation Structures in the Malta-Sicily Channel from Remote Sensing Data

Nydia C. Reyes Suarez [1,2,*], Michael S. Cook [3], Miroslav Gačić [2], Jeffrey D. Paduan [3], Aldo Drago [4] and Vanessa Cardin [1]

[1] Istituto Nazionale di Oceanografia e di Geofisica Sperimentale—OGS, 34010 Sgonico (TS), Italy
[2] TRIL Programme, Abdus Salam International Center for Theoretical Physics—ICTP, 34151 Trieste, Italy
[3] Department of Oceanography, Naval Postgraduate School—NPS, Monterey, CA 93943, USA
[4] Physical Oceanography Research Group, Department of Geosciences, University of Malta, 2080 Msida, Malta
* Correspondence: nreyessuarez@inogs.it

Received: 20 June 2019; Accepted: 25 July 2019; Published: 31 July 2019

Abstract: The Malta-Sicily Channel is part of the Sicily Channel system where water and thermohaline properties between the Eastern and Western Mediterranean basins take place. Several mesoscales features are detached from the main circulation due to wind and bathymetric forcing. In this paper, surface circulation structures are studied using different remotely sensed datasets: satellite data (absolute dynamic topography, Cross-Calibrated Multi-Platform wind vector analysis, satellite chlorophyll and sea surface temperature) and high frequency radar data. We identified high frequency motions (at short time scales—hours to days), as well as mesoscale structures fundamental for the understanding of the Malta-Sicily Channel circulation dynamics. One of those is the Malta-Sicily Gyre; an anticyclonic structure trapped between the Sicilian and Maltese coasts, which is poorly studied in the literature and often confused with the Malta Channel Crest and the Ionian Shelf Break Vortex. In order to characterize this gyre, we calculated its kinetic properties taking advantage of the fine-scale temporal and spatial resolution of the high frequency radar data, and thus confirming its presence with an updated version of the surface circulation patterns in the area.

Keywords: remote sensing; high frequency radar; Malta-Sicily Channel; Malta Sicily Gyre; surface circulation

1. Introduction

Study Area

Although smaller than the synoptic scale, mesoscale to sub-mesoscale structures influence the stratification and contribute to the vertical and horizontal advection of sea water properties. Due to the small Rossby radius of deformation in the Mediterranean Sea (15–20 km) the typical mesoscale features are characterized by scales of the order of 10–100 km [1,2]. The circulation in the Sicily Channel (SC; defined as 11–16.5° E and 33—38° N in Figure 1 for our studies) is mainly driven by the Mediterranean thermohaline circulation together with its mesoscale and seasonal variability showing intra-annual and inter-annual variability [3–5]. This area is characterized by a complex bathymetry with a two-sill system at the Sicily Strait (SS) [6]. On the Italian side, the sill is very narrow with a maximum depth of ~430 m, while on the Tunisian side it is wider and shallower with a sill depth of ~360 m [7]. The exit to the Ionian Sea is bounded by the Malta Plateau and the Medina Bank (MP and MB in Figure 1). In the center of the SC three important depressions are present; the Pantelleria trough (PT; ~1300 m depth), the Linosa trough (LT; ~1500 m depth) and the Malta trough (MT; ~1700 m depth). These bathymetric features can strongly influence the current system in the SC.

Contrary to the SC, the Malta-Sicily Channel (hereafter referred as the channel) is a shelf in the mid Mediterranean Sea that separates the Malta island from the southern tip of Sicily. Topographically this shelf is characterized by a plateau in the middle (MP) with an average depth of 150 m as shown in Figure 1. On its northwestern side the shelf is bounded by the submarine ridges aforementioned with depressions reaching 1700 m deep where the Maltese islands represent the emerged part of the ridge [8]. On its southeastern side, the channel abruptly deepens into the Ionian Sea (~3000 m deep) due to the presence of the Sicily-Malta Escarpment (~2500 m deep) which is one of the largest and least explored underwater cliffs in the Mediterranean Sea [8]. The circulation on longer time scales (lower frequency) is mainly driven by the Atlantic Ionian Stream (AIS) and the Malta-Sicily Gyre (MSG), where the latter has been identified as a quasi-permanent structure with highest incidence in the winter period and related to the variability of the AIS [9,10]. In addition, the Malta-Sicily Gyre (MSG) has been poorly described in the literature, and is often confused with the Malta Channel Crest (MCC) and the Ionian Shelf Break Vortex (ISV) [9]. For the purpose of this work the channel has been defined as the area comprising 14–16° E and 35–37° N.

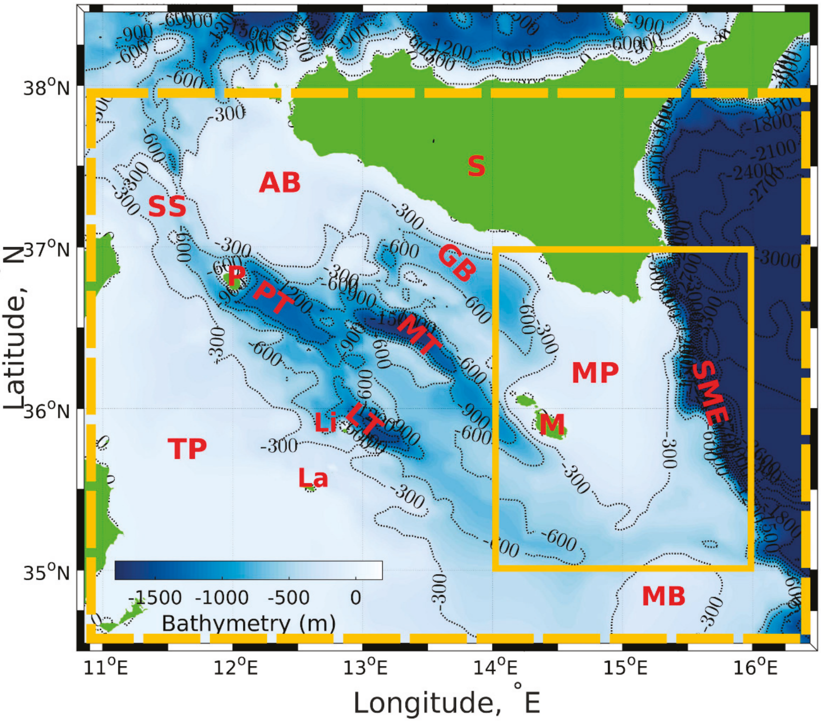

Figure 1. Bathymetric map of the Sicily Channel (SC) (dashed yellow box) and the channel (solid yellow box) and the surrounding area. Geographical places are indicated with red letters: Adventure Bank (AB), Gela Basin (GB), Lampedusa Island (La), Linosa Island (Li), Linosa Trough (LT), Maltese Islands (M), Malta Plateau (MP), Malta Trough (MT), Medina Bank (MB) Pantelleria Island (P), Pantelleria Trough (PT), Sicily Island (S), Sicily Strait (SS), Sicily-Malta Escarpment (SME), and Tunisia Plateau (TP). The colorbar represents depth in meters. Bathymetric data was obtained from https://topex.ucsd.edu/cgi-bin/get_data.cgi [11].

The AIS is a well-studied sea surface structure mainly composed of Atlantic Water (AW). During summer it strengthens and remains constrained towards Sicily where the flow behaves like a jet stream gaining positive vorticity due to westerly winds and the SC complex bathymetry [12]. As it reaches the shelf break east of Malta, it maintains an upwelling front along the southern coast of Sicily showing a seasonal behavior [13–16]. Its path starts at Adventure Bank where the AW enters the SC via the SS where complex circulation patterns are induced by the bathymetry and the shape of the coastline [1,17,18]. During summer, at the SS, the jet stream flows towards Malta following the bathymetry and ends its journey in the channel by emptying into the Ionian Sea. Depending on the phase of the North Ionian Gyre (NIG; [19–22]) the AIS can flow towards the North Ionian Sea or move as a zonal current crossing the Central Ionian Sea. In the latter case this flow is known as the Mid Ionian Jet, (MIJ; [1,4]) and connects the SC with the Cretan passage [4,19–21,23]. On its eastward propagation the stretching and squeezing of the AIS results in the formation of important mesoscales structures e.g., eddies, gyres or plumes like the MSG [14,24,25]. Additionally, local winds, tides and the Coriolis effect can introduce high frequency motions in the area.

The main focus of this paper is to study the surface circulation patterns in the channel with particular emphasis on a quantitative characterization of the MSG. This mesoscale feature appears to be important to and diagnostic of the circulation in the area under study but it has been poorly studied and often confused with other mesoscale structures. Our aim is to give an updated version of the sea surface circulation structures in the channel. This paper is divided in four parts besides the introduction. In Section 2, we introduce the data and methods used for this study. The data were selected due to their spatial and temporal availability and capability of being compared with high frequency radar data (HFR). A summary of the datasets used and their principal characteristics can be found in Table 1. Section 3 is devoted to results and discussion. We first describe the principal features that comprise the surface circulation in the channel and in the SC (solid and dashed yellow boxes in Figure 1) using surface geostrophic velocities (SGV) and absolute dynamic topography (ADT). Secondly, we identify the short time scales in the channel by analyzing the sea surface circulation and the dynamical processes in the area with available remote sensing data i.e., ADT, SGV, HFR velocities, wind stress fields, sea surface temperature (SST), and chlorophyll satellite images (CHL). Finally, we focus on the characterization of the MSG (identified using the aforementioned data) by calculating its kinematic properties. Section 4 is dedicated to conclusions.

Table 1. Main characteristics of the remote sensing datasets.

	HFR	Altimetry	MODIS	MODIS	CCMP
Variable	Sea surface velocities	ADT, geostrophic currents	SST	CHL-a	Wind stress
Frequency	Hourly	Daily	Monthly	Monthly	6-Hourly
Spatial resolution	1 km	1/8°	4.6 km	4.6 km	1/4°
Vertical integration	1 m	surface	surface	surface	10 m above sea level
Study period	1 Aug 2012–31 Jan 2015	1 Jan 1993–31 Dec 2015	Jan–Dec 2013	Jan–Dec 2013	1 Aug 2013–31 Jan 2015

2. Data and Methods

To describe the channel's main surface structures, we have analyzed the available remote sensing data summarized in Table 1.

2.1. Remote Sensing Data

- HFR data from three CODAR SeaSondes stations installed in Ta'Sopu (Gozo, Malta), Ta'Barkat (Malta) and Pozzallo Harbor (Sicily, Italy) shown in Figure 2, provided surface current maps in the channel from the period August 2012 to January 2015. These data correspond to a setup of two HFR stations initially installed at Ta'Sopu and Ta'Barkat in August 2012. The third station was added in August 2013 in Pozzallo improving the spatial coverage of the channel [26]. The data are organized in time series of hourly velocity vectors with u (zonal, East-West) and v (meridional, North-South) components of the total velocity. The datasets were based on CALYPSO HFR, compiled and processed by Dr. Simone Cosoli from the University of Western Australia, Perth [27]. The CALYPSO system operating set-up and resolution (13.5 MHz frequency, angular resolution 5°, range resolution 1.6 km, for more details see Drago et al. [10]) provides radar measurements that are representative of the first meter of the ocean with grid sizes from 0.3 to 8.3 km^2. The radars share the same transmit frequency using a GPS-synchronization module and operate with both the ideal and measured antenna beam patterns. Hourly sea surface current maps were derived on a Cartesian grid with 3×3 km^2 horizontal resolution by least-squares fitting of the radial components of the ocean currents from two or more radar stations in areas of common overlap. Grid points were included in the analysis only if they satisfied a minimum data return of 50% using an interpolation technique described in Cosoli et al. [27]. Validation of this array has been carried out in different studies since the installation of the system making this dataset a reliable product [27–29].

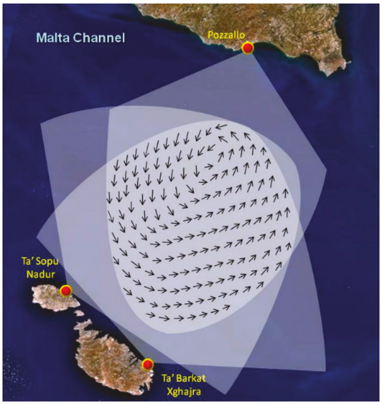

Figure 2. High frequency radar stations of three CODAR SeaSondes stations at Ta'Sopu (Gozo, Malta), Ta'Barkat (Malta) and Pozzallo Harbor (Sicily, Italy) from [30] showing the area of maximum coverage of the array.

- Ssalto/Duacs multi-mission L4 altimeter products in the period January 1993 to December 2015 containing daily multi-mission ADT on a 1/8° × 1/8° mercator projection grid, and distributed by the Copernicus Marine and Environment Monitoring Service (CMEMS) [4,5,31] were used to calculate SGV where,

$$u'_g = -\frac{g}{f}\frac{\partial \zeta}{\partial y}, \tag{1}$$

$$v'_g = \frac{g}{f}\frac{\partial \zeta}{\partial x}. \tag{2}$$

  are the zonal and meridional geostrophic velocities, and ζ, denotes the dynamic topography provided by the altimeter.
- Monthly Level-3 binned SST [doi: 10.5067/AQUA/MODIS/L3M/SST/2014] and CHL [doi: 10.5067/AQUA/MODIS/L3B/CHL/2018] datasets with a spatial resolution of 4.6 km were downloaded from January to December 2013 from the OceanColor web portal (https://oceandata.sci.gsfc.nasa.gov/MODIS-Aqua/Binned/Monthly/) under the NASA aqua-MODIS (Moderate Resolution Imaging Spectroradiometer) satellite mission.
- A sub-grid ranging from 35.8–36.8° N to 13.8–15.4° E from the six-hourly gridded Cross-Calibrated Multi-Platform (CCMP) V2.0, Remote Sensing Systems (RSS), Santa Rosa, California, USA. Level-3 wind vector analyses product was downloaded from Remote Sensing Systems (RSS) for the

period spanning August 2013 to January 2015 to analyze wind patterns in the channel [32]. The CCMP dataset combines cross-calibrated satellite microwave winds from scatterometers and radiometers with instrument observations using a variational analysis method to produce 1/4° gridded data [33]. Both radiometer and scatterometer data are validated against ocean moored buoys (in agreement within 0.8 m/s), where wind observations are referenced to a height of 10 m. For a complete description of the dataset see [32].

2.2. Complex Correlation and Veering Estimates

Average veering between two 2D time series can be obtained from the phase angle of the complex correlation coefficient [34]. Additionally, we used this method to determine if the wind and HFR velocities are in Ekman Balance.

Let,

$$w(t) = u(t) + iv(t), \tag{3}$$

be the complex representation of the velocity time series at time t. The complex correlation coefficient between the two vector time series 1 and 2 in terms of the east and west components is:

$$p = \frac{\langle u_1\, u_2 + v_1\, v_2 \rangle}{\langle u_1^2 + v_1^2 \rangle^{\frac{1}{2}}\, \langle u_2^2 + v_2^2 \rangle^{\frac{1}{2}}} + i \frac{\langle u_1\, v_2 - u_2\, v_1 \rangle}{\langle u_1^2 + v_1^2 \rangle^{\frac{1}{2}}\, \langle u_2^2 + v_2^2 \rangle^{\frac{1}{2}}}, \tag{4}$$

where the phase angle or average veering is,

$$\alpha_{av} = \frac{\langle u_1\, v_2 - u_2\, v_1 \rangle}{\langle u_1\, u_2 + v_1\, v_2 \rangle}. \tag{5}$$

2.3. Kinematic Properties of an Eddy

In order to describe the channel in terms of its kinematic properties, we applied the method described by Sanderson [35] using the lstranslate routine developed by the HFR group at the Naval Postgraduate School.

Assuming there is an eddy linearly translated in time with spatially uniform velocity gradients as follows:

$$g_{11} = \frac{\partial u}{\partial x} \tag{6}$$

$$g_{12} = \frac{\partial u}{\partial y} \tag{7}$$

$$g_{21} = \frac{\partial v}{\partial x} \tag{8}$$

$$g_{22} = \frac{\partial v}{\partial y} \tag{9}$$

From Equations (6)–(9), the divergence is defined as $d = g_{11} + g_{22}$, stretching deformation $a = g_{11} - g_{22}$, vorticity $c = g_{21} - g_{12}$ and the shearing deformation $b = g_{21} + g_{12}$, which are functions of the velocity gradients. The method assumes that the center of the eddy is located at X, Y and moves with constant velocity (U, V), whereas, at some distance from the center of the eddy, the flow velocity has an added component due to the velocity gradients. X_0, Y_0 is defined as the initial position of the eddy. Then the flow center position can be written as,

$$X = X_0 + U(t), \tag{10}$$

$$Y = Y_0 + V(t). \tag{11}$$

with,

$$\alpha = U - g_{11}X_0 - g_{12}Y_0, \tag{12}$$

$$\beta = V - g_{21}X_0 - g_{22}Y_0, \tag{13}$$

$$\alpha_1 = -g_{11}U - g_{12}V, \tag{14}$$

$$\beta_1 = -g_{21}U - g_{22}V. \tag{15}$$

and solving Equations (12)–(15) for U, V, X_0, Y_0 yields,

$$U = \frac{g_{22}\alpha_1 - g_{12}\beta_1}{g_{12}g_{21} - g_{11}g_{22}} \tag{16}$$

$$V = \frac{g_{11}\beta_1 - g_{21}\alpha_1}{g_{12}g_{21} - g_{11}g_{22}} \tag{17}$$

$$X_0 = \frac{g_{22}(\alpha - U) - g_{12}(\beta - V)}{g_{12}g_{21} - g_{11}g_{22}} \tag{18}$$

$$Y_0 = \frac{g_{11}(\beta - V) - g_{21}(\alpha - U)}{g_{12}g_{21} - g_{11}g_{22}} \tag{19}$$

For our studies, we focused on the vorticity component applied to the HFR data in order to quantitatively identify the mesoscale features within the study area.

3. Results and Discussion

3.1. Mean Surface Circulation, the Sicily Channel

Due to baroclinic instabilities, the Atlantic current (AC) regularly forms meanders that eventually detach from the current and become either cyclonic or anticyclonic eddies [36] like the ones observed by Jouini et al. [3] and Jebri et al. [37,38]. Figure 3 shows the SC inter-annual geostrophic circulation derived from the ADT data depicting some of the AC-born structures described in Jouini et al. [3] and Menna et al. [5] such as the cyclonic Medina Gyre (MG), the cyclonic Messina Rise Vortex (MRV), the anticyclonic Pantelleria Vortex (PV, which in the literature is mentioned as cyclonic), the anticyclonic MSG, the AIS, the Bifurcation Atlantic Current (BAC) and the Atlantic Tunisian Current (ATC). From ADT and SGV, the MSG shows a seasonal semi-permanent behavior and contributes to the channel's circulation along with the AIS. Due to its poor description in the literature its characterization is an important result of our studies. The complex bathymetry in the SC, with its longitudinal subdivision into two sills, influences the distribution of ADT leading to a difference in level between the two sides of the channel as seen in Figure 3. Towards the Italian side the sea level is lower than on the Tunisian side with a dipole like sea level shape, positive ADT close to Tunisia and negative towards Sicily.

The seasonal variability of the circulation in Figure 4 was obtained by averaging the ADT maps using the following groupings: Winter (December, January, February), Spring (March, April, May), Summer (June, July, August) and Autumn (September, October, November). In winter (Figure 4a) the mean geostrophic circulation shows the presence of the AC bifurcating at the SS in two branches due to the two-sill bathymetry of the strait. The BAC flows toward the northern tip of Sicily while the ATC to the Tunisian side. The MSG is observed as well with a radius of ~50 km and centered at 14.5°E–36.1°N. It is also prominent during the winter/spring season as seen in Figure 4b, dominating the circulation in the channel when the AIS is not present. This can be interpreted as a result of the conservation of potential vorticity [13–15] since the water depth abruptly changes from ~700 m at the Malta graben to shallow (~100 m) in the channel (see Figure 1). For this season, the MSG velocity ranges between 5–10 cm s^{-1}. Additionally, other structures observed for this season are the anticyclonic MCC, the cyclonic MG and MRV.

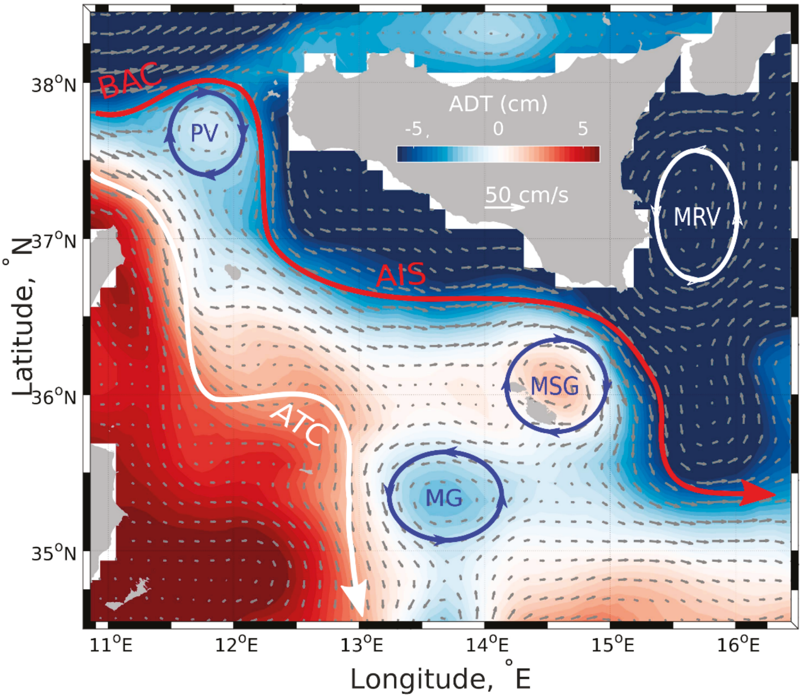

Figure 3. Inter-annual map of absolute dynamic topography (ADT) and mean surface geostrophic velocities (SGV) in the SC. Permanent structures in white, summer/autumn in red and winter/spring in blue. The colorbar represents the ADT variations over the study area while gray arrows are the SGV vectors.

In spring we identify some of the winter structures indicated in Jouini et al. [3] and Menna et al. [4,5] like the ATC, BAC, MCC, MG, MSG, MRV and the PV as shown in Figure 4b. The ATC flows towards Sicily where two gyres are detached, the cyclonic MG and the anticyclonic MCC circling around Linosa island, most likely due to the influence of the LT at 36°N. In addition, at the northern tip of Sicily there is a re-circulation of AW that enters into the SC where the PV is detached and the MSG is reinforced.

For the summer period we observe the strong influence of the AIS (Figure 4c) which behaves like a jet stream in the SC and the channel [13]. It is characterized by a velocity of ~25 cm s^{-1} and occasionally reaching values higher than 50 cm s^{-1}. This current consists mainly of AW and changes properties as it passes through the SS deepening and bifurcating into the Ionian Sea northwards or to the Central Ionian Sea depending on the NIG phase [19,21,23,38]. Additionally, the ADT and SGV also show another yet unidentified mesoscale structure close to the coast of Tunisia detached from the ATC, and a shift of the MG eastwards.

Figure 4d shows autumn mean geostrophic circulation which is driven by the AIS and reinforced by AW coming from the BAC and the ATC. The ATC bifurcates at the SS and then rejoins south of Pantelleria. We observed other mesoscale structures, like the cyclonic MRV and the anticyclonic MCC, as well as the formation of the anticyclonic MSG which has been undocumented in the literature.

Other permanent structures were found in the SC in disagreement with the current literature. For example, the anticyclonic PV at 37.5°N–11.5°E is in disagreement with the studies of Robinson et al. [12], Lermusiaux and Robinson. [15] and Jouini et al. [3]. In their case the PV is cyclonic and positioned at 37°N–12°E. Additionally, the MCC is described as a summer only pattern in the literature but in our studies is also present in winter and spring. The cyclonic Adventure Bank Vortex (ABV) and the ISV were summer only structures in the literature but were not found in our seasonal or inter-annual geostrophic decomposition. Furthermore, over the monthly mean analysis we were able to identify some of these structures, but they seemed to be temporary and appeared just in some years/months where they could have been triggered by rare and strong atmospheric events. An updated picture of the surface circulation structures in the whole SC where the discrepancies and the reasons why they are enhanced should be clarified and studied with more extent and detail. A new study of all these structures and the forcing mechanisms behind them can be found in Menna et al. [5], but again the MSG is not mentioned.

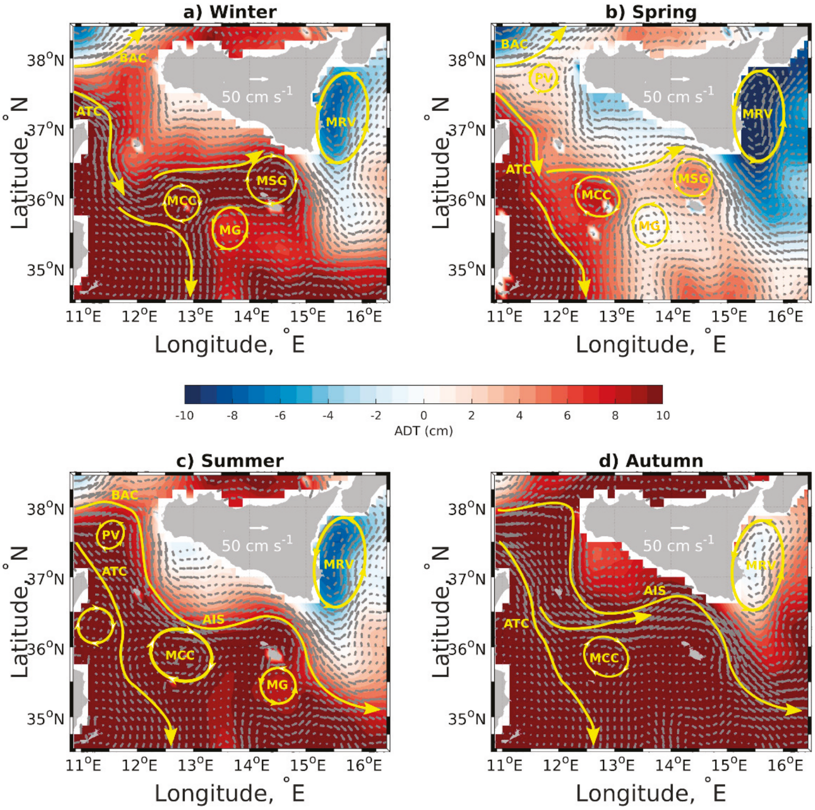

Figure 4. Mean seasonal maps of ADT and SGV in the SC. (**a**) winter, (**b**) spring, (**c**) summer and (**d**) Autumn. Yellow arrows represent the sea surface patterns found. Gray arrows represent the SGV in cm s^{-1}. The colorbar shows ADT in centimeters.

Wind stress curl and deseasonalized geostrophic eddy kinetic energy (EKE) studies in Menna et al. [4] revealed the influence of the wind and highlights the regions with high EKE in the Central Mediterranean Sea. Wind stress data (Figure 3c,d in Menna et al. [4]) shows that towards the southwestern side of the Sicilian coast northwesterly winds favor upwelling (+ wind stress) revealing persistent coastal Ekman pumping events [39,40]. Wind forcing imparts an indirect influence in the current field at longer time scales (weekly, monthly, and inter-annual), where even if neglected in the geostrophic approximation, helps to build up the sea level to generate a sufficiently large pressure gradient needed to balance the Coriolis force. On the other hand, deseasonalized geostrophic EKE studies (Figure 6 in Menna et al. [4]) highlight areas in the central Mediterranean Sea where the inter-annual variability is stronger with values of ~80 cm^2 s^{-2} in the channel. A broader EKE variability using altimetry and model datasets in the Mediterranean Sea can be found in Pujol and Larnicol [41] and Jordi and Wang [42].

3.2. Short Time Scales in the Malta Sicily Channel

3.2.1. Comparison among Available Spatial Data

Ocean currents can be described as a combination of geostrophic and ageostrophic terms, the latter being associated with wind driven features. HFRs offer good resolution in both time and space, and have the capability to measure near real-time complete currents [43,44], measuring both wind-driven and geostrophic components influencing the sea surface. Weekly, monthly, inter-annual and seasonal averages of SGV and HFR velocity field were compared. Figure 5 shows monthly means of both components correlate well geographically. This strong correlation was found at all-time scales greater than a day and thus identified the channel to be in geostrophic balance at these time scales. As expected, the stretching and squeezing of the anticyclonic MSG and the AIS jet stream were also observed from the HFR data as did the SGV and ADT. In addition, the MSG can occasionally have velocities as high as 40 cm s^{-1} as seen in Figure 5b.

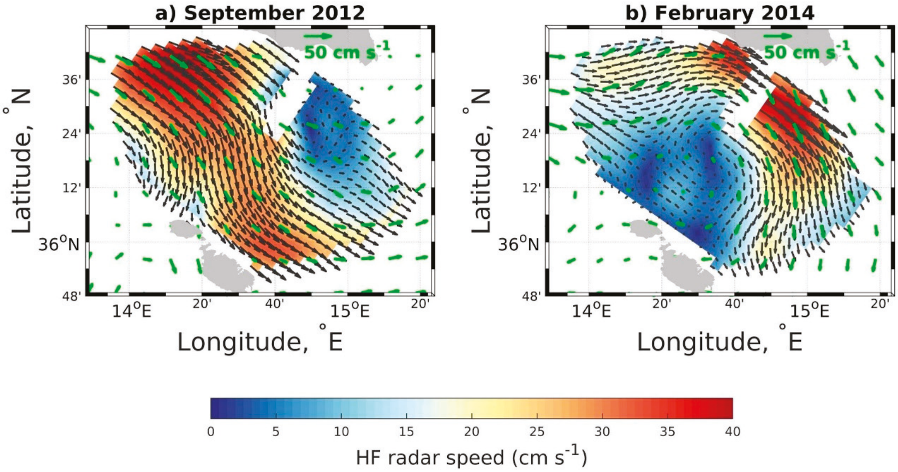

Figure 5. SGV calculated from ADT showing the pathway of Atlantic Ionian Stream (AIS) on September 2012 (left-hand panel) and the Malta-Sicily Gyre (MSG) identified on February 2014 (right-hand panel). Black lines represent monthly averaged current fields derived from high frequency radar data (HFR) data in cm s^{-1}. Green arrows represent SGV in cm s^{-1}. The colorbar gives the magnitude of each velocity vector in cm s^{-1}.

Other spatial observations available for this area include monthly satellite derived SST and CHL data, which were compared with HFR monthly averages for the period from January to December 2013. Since the prevailing signal in the HFR data at monthly time scales is geostrophic, it is expected that the advection of properties follows this flow. However, one should remember that SST and CHL are not conservative tracers but can be used in general to track currents, circulation, and water mass mixing among other properties. Figure 6a,c show SST and CHL maps in January 2013 respectively, revealing relatively higher temperatures and lower CHL occupying the channel and lower temperatures and higher CHL constrained towards the Sicilian coast. This behavior can be associated with the presence of the MSG, which for the winter season is the predominant pattern. Figure 6b,d illustrate that as the AIS flows towards the Ionian Sea it generates a well-defined front which advects properties in the channel along its path [12]. Additionally, the SST field varies from 17 °C to 26 °C while CHL from 0.5

to 0.05 mg m^{-3} through winter to the end of summer. A detailed statistical analysis of CHL and SST data is presented in Capodici et al. [26].

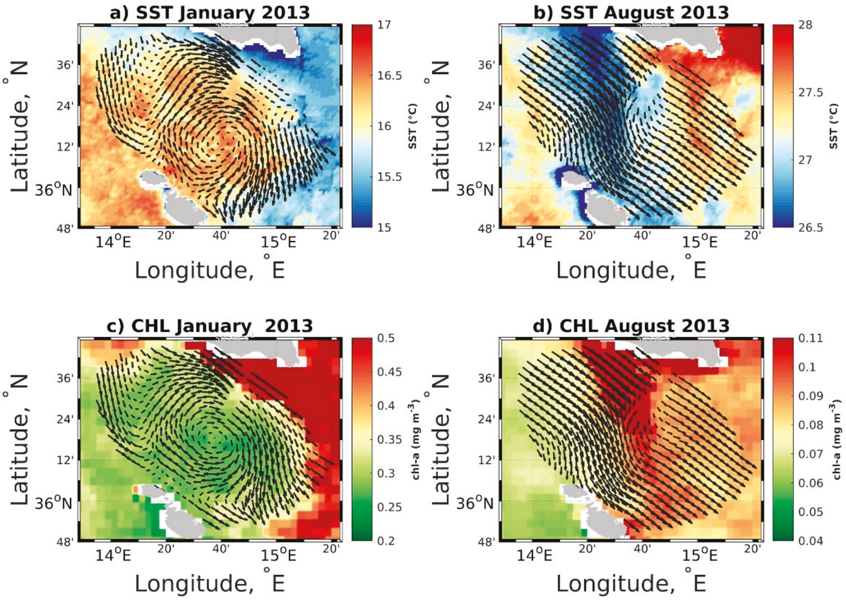

Figure 6. Sea surface temperature (SST) and chlorophyll satellite images (CHL) fields from Aqua-MODIS satellite mission showing the MSG on January 2013 (panel (**a**) and (**c**), respectively) and the AIS pathway August 2013 (panel (**b**) and (**d**), respectively). Gray lines represent monthly averaged surface currents from the HFR, whereas the colorbar represents the SST field in °C (upper panels) and chlorophyll concentration in mg pigment m^{-3} (lower panels).

3.2.2. Complex Correlation

We spatially averaged wind (1/4°), SGV (1/8°) and HFR (1 km) daily gridded data to match the 1/4° wind grid. Figure 7 shows the spatially averaged time series over the 1/4° grid for each dataset. The comparison of the three parameters in panels a and c of Figure 7 show that the geostrophic components (u,v_{SGV}) behave like a low-pass filter of the HFR time series because the geostrophic adjustment takes place on a longer time scale. Wind (u,v_{wind}) and HFR (u,v_{radar}) time series show most of the high frequency motions included at short time scales, where the wind plays an important role on the *channel* circulation. Additionally, panels b and d compare the wind speed time series with the residual velocity obtained by removing the geostrophic component from the HFR data, $u,v_{\mathrm{residual}} = u,v_{\mathrm{radar}} - u,v_{\mathrm{SGV}}$, where the residual is expected to be better correlated to the wind components than to the geostrophic current. Here the u component (panel b) shows good agreement with the residual as expected, except for some time intervals such as January to March 2013 where the wind is positive and the residual is negative and higher in magnitude. The residual meridional v component of the velocity (panel d) behaves differently from the wind signal in the first few months (until September 2013). This is probably due to data availability since for some grid cells the lack of HFR data could play an important role in the magnitude of the vectors and thus the averaging process.

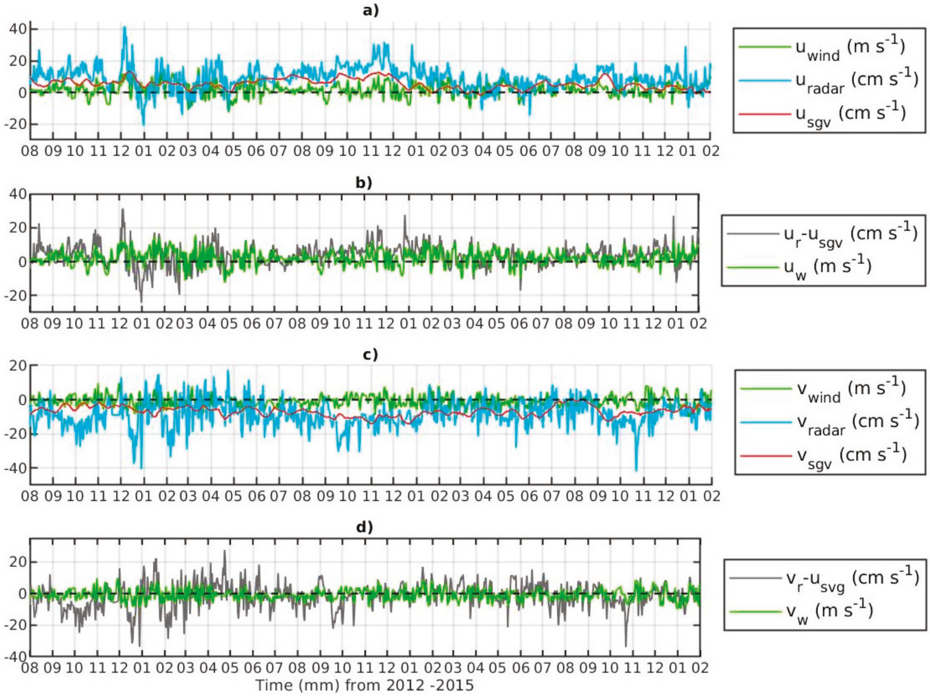

Figure 7. u and v components of daily wind, SGV and HFR speed time series spatially averaged over a 1/4° grid. Panels (**a**,**c**) compare u (zonal, East-West) and v (meridional, North-South) component of the wind (green), SGV (red) and HFR (blue) velocities respectively. Panels (**b**,**d**) compare the residual u and v speed ($u,v_{\mathrm{residual}} = u,v_{\mathrm{radar}} - u,v_{\mathrm{geostrophic}}$) with u and v components of the wind speed.

In order to look for the relationship between different variables, we compute the vector correlation between the interpolated time series in Figure 7 over the grid represented in Figure 8 where the boxes represent the 1/4° grid defined previously. HFR to the wind complex correlation (as seen in Table 2) shows the veering 43.5781 ± 8.238 degrees to the right, in a good agreement with theory. The angles of the velocity to the wind vector varies between 23 to 53 degrees with a range correlation between 0.24 to 0.35, showing the importance of the wind forcing at shorter time scales and in the set-up of the Ekman layer. The correlation between the residual current and the wind vector is higher than the radar to wind correlation. The angles between residual and wind are closer to 45 degrees, as a result of the removal of the geostrophic components from the time series (see Table 2). Finally, as expected the complex correlation between the geostrophic flow and the wind is very low since processes in both time series evolve at different time scales; the wind component at short time scales generate rapid and variable motions (i.e., inertial oscillations) in the ocean whereas the geostrophic field evolves at larger scales accounting for low frequency phenomena.

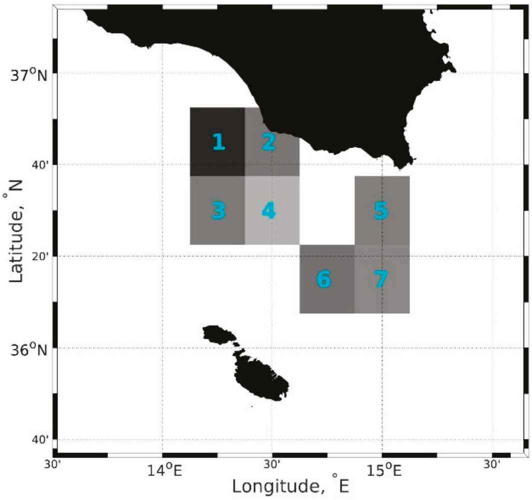

Figure 8. Grid cells where complex correlation is computed. The subscripts represent the corresponding grid cell for each set of parameters, e.g., p_1, θ_1 are the parameters corresponding to cell 1.

Table 2. Shows complex correlation coefficients and veering angles for each time series (high frequency radar data (HFR), surface geostrophic velocities (SGV) and residual) with the wind.

Time Series	Correlation Coefficient	Phase Angle
Radar to Wind	$p_1 = 0.3848$	$\theta_1 = 34.1950$
	$p_2 = 0.3586$	$\theta_2 = 38.9211$
	$p_3 = 0.3515$	$\theta_3 = 40.1103$
	$p_4 = 0.3554$	$\theta_4 = 23.1126$
	$p_5 = 0.3249$	$\theta_5 = 44.4289$
	$p_6 = 0.2475$	$\theta_6 = 53.4827$
	$p_7 = 0.2971$	$\theta_7 = 33.9368$
Residual to Wind	$p_1 = 0.4669$	$\theta_1 = 37.9316$
	$p_2 = 0.3749$	$\theta_2 = 38.9211$
	$p_3 = 0.4030$	$\theta_3 = 49.3575$
	$p_4 = 0.4424$	$\theta_4 = 31.4394$
	$p_5 = 0.3145$	$\theta_5 = 45.5068$
	$p_6 = 0.2920$	$\theta_6 = 59.7371$
	$p_7 = 0.3202$	$\theta_7 = 42.1535$
Geostrophic to Wind	$p_1 = 0.0566$	$\theta_1 = -101.4697$
	$p_2 = 0.0230$	$\theta_2 = -14.4575$
	$p_3 = 0.1082$	$\theta_3 = -86.2521$
	$p_4 = 0.0876$	$\theta_4 = -97.4430$
	$p_5 = 0.0511$	$\theta_5 = -34.6377$
	$p_6 = 0.0961$	$\theta_6 = -99.0749$
	$p_7 = 0.0712$	$\theta_7 = -91.4430$

3.3. The Malta Sicily Gyre

Evidence of mesoscale activity in the channel was highlighted by four datasets considered in this study: ADT, HFR, CHL and SST. To identify this mesoscale activity, we computed the vorticity using the method described in Sanderson [35] considering only a subset of the HFR time series, using the high resolution and continuity criteria. For the continuity criteria we defined the area in Figure 9e where data was available since the start of acquisition. This area also coincides with the place where the MSG was identified with the HFR velocities and geostrophic current analysis.

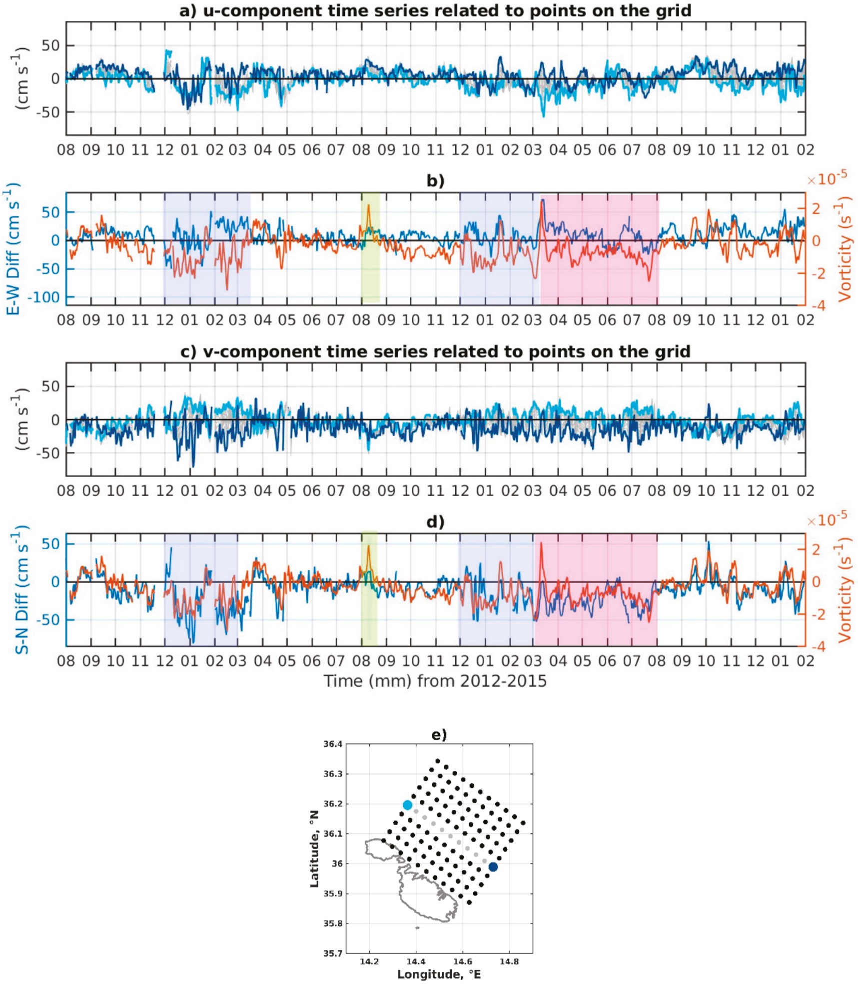

Figure 9. Subset time series of the original HFR grid. Panel (**a**) represents the *u* (east-west) while panel (**c**) the *v* (north-south) components of the HFR time series respectively. Blue and gray represent the time series respective to the dots on panel (**e**). Panels (**b**,**d**) represent the East-West and North-South differences calculated from the blue time series in panel (**a**,**c**) respectively. Vorticity is depicted in the right-hand side of panels (**b**,**d**) and was calculated using Sanderson's method [35]. Violet shaded areas show the months when the MSG was found. Pink shaded areas show the months where the Atlantic Ionian Stream (AIS) and Malta-Sicily Gyre (MSG) co-existed. Green shaded areas show the cyclonic mesoscale in Figure 10c.

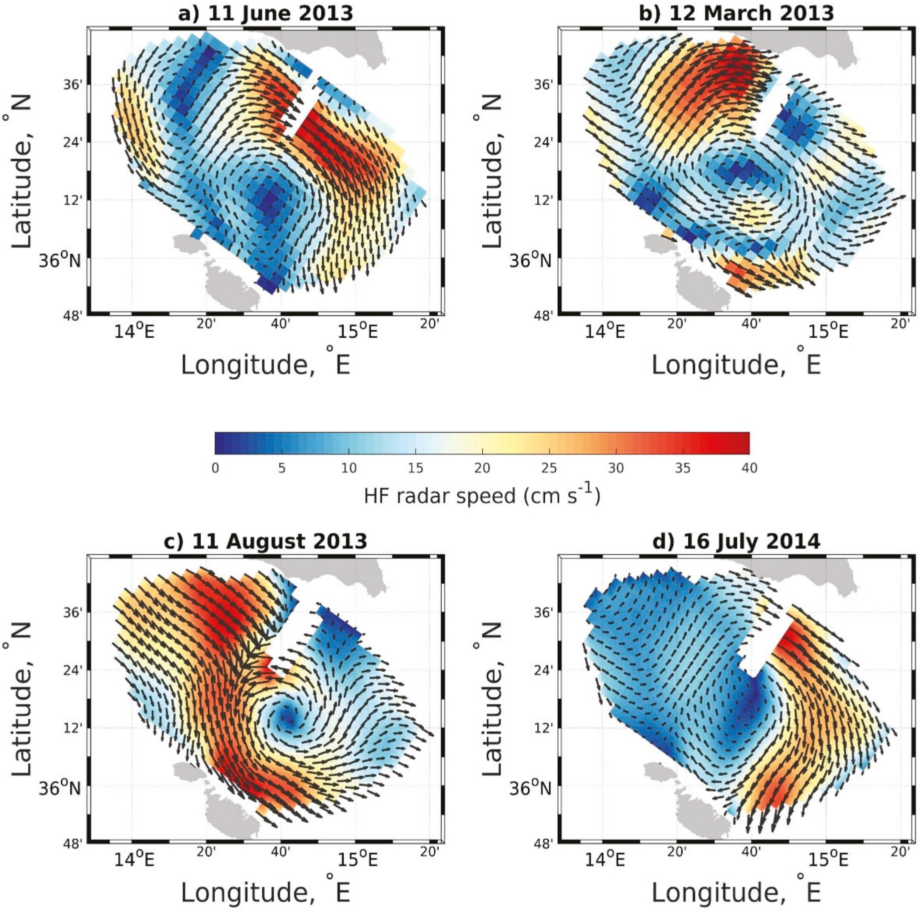

Figure 10. Daily HFR current maps showing anticyclonic (**a**,**b**,**d**) and cyclonic (**c**) mesoscale gyres in agreement with the vorticity calculated through Sanderson's method. The colorbar gives the magnitude of each velocity vector in cm s^{-1}. Please note that panel **c** depicts one of the cyclonic gyres corresponding to the green shaded areas in Figure 9. Panel **a** and **d** depict some of the anticyclonic gyres in the pink shaded areas of Figure 9 occurring alongside the AIS. Panel **b** shows a snapshot of the MSG in one of shaded violet areas of panels **b** and **d** of Figure 9.

Figure 9 (panel b and d) shows the presence of the anticyclonic MSG in winter between December-March 2013 and December-August 2014, corroborated by a vorticity of $c = -2 \times 10^{-5}$ s^{-1} using Sanderson's method (panel b and c). These results are in agreement with the winter/spring recurrence of the MSG identified with the ADT and SGV analysis. Here we also note that the MSG co-existed with the AIS from April to August 2014 (shaded areas in Figure 9). This provides a quantitative description of the gyre. Finally, with this method we were able to identify other mesoscales gyres that were either cyclonic (+vorticity) or anticyclonic (−vorticity). Some examples are depicted in Figure 10.

4. Summary and Conclusions

The main focus of this paper has been to characterize the channel circulation, which was done using satellite-derived geostrophic currents HFR-derived currents, and wind vector analyses on daily time scales in addition to SST and CHL on monthly time scales. Analyzing the available data, with particular emphasis on the higher spatial and temporal resolution of the HFR observations, the MSG is studied in more detail. This is an anticyclonic structure occupying a substantial portion of the channel that has been poorly studied and often confused with the ISV or the MCC. We believe that the standardization of the names and characteristics for these structures will benefit researchers and resource managers working in the region. Menna et al. [5] provides a good description of the main surface circulation structures in the SC but characterizes the MSG (or MCC as they called it) as a seasonal feature, occurring in the summer only. This creates some discrepancies since based on the lower frequency qualitative studies (i.e., SGV, SST and CHL maps), that agree with [10], the mesoscale feature is present mostly in the winter-spring period. This however is not always the case since in 2014 both the AIS and the MSG were present from January to August. Tracking the anticyclonic MSG was particularly well done using the vorticity analysis performed on the HFR observations. While the channel-scale MSG was dominant, other cyclones and anticyclones were identified at daily time scales in the HFR observations making Sanderson's method a good tool for identifying mesoscale features. A longer HFR time series with better spatial coverage can be useful to study the mesoscale.

Geostrophic balance was found to be a good approximation to describe the dynamics in the channel at weekly, monthly, seasonal and inter-annual time scales. At these time scales, wind forcing is important for creating the density gradients and the subsequent geostrophic velocities, but wind data are not essential in diagnosing the circulation patterns (wind stress curl as in Menna et al. [4], shows persistent coastal Ekman upwelling events along the coast of Sicily.) The geostrophic velocity field in the channel is reinforced by the wind, which is mostly northwest and is responsible for the advection of different properties in the area. At short time scales (hours to days) we were able to use the combination of HFR and geostrophic velocities to show that direct wind forcing must be accounted for. The vector complex correlation between the HFR and the wind time series allowed us to show that the high frequency components included an Ekman balance between wind and surface current. The analysis showed a veering angle for the currents of 43.5781 ± 8.238 degrees to the right of the wind forcing, which is in good agreement with Ekman theory. The agreement was even better when the geostrophic currents were subtracted from the HFR observations to produce a residual current. Hence, we conclude that HFR observations or a wind-based correction to the geostrophic currents, are recommended at daily time scales. This set of analyses using observations at larger time and space scales from satellites and observations of higher frequency, higher resolution features from HFR suggests that this suite of observations can provide effective monitoring of the circulation state for important regions, such as the area studied here.

Author Contributions: Writing—original draft, N.C.R.S.; Writing—review & editing, N.C.R.S., M.S.C., M.G., J.D.P., A.D. and V.C.; Conceptualization, N.C.R.S., M.S.C., M.G. and J.D.P.; Data curation, N.C.R.S. and M.S.C.; Formal analysis, N.C.R.S., M.S.C. and J.D.P.; Funding acquisition, A.D., M.G. and V.C.; Investigation, N.C.R.S. and M.G.; Methodology, N.C.R.S., M.G. and J.D.P.; Resources, M.G., A.D. and V.C.; Software, M.S.C. and J.D.P.; Supervision, M.S.C., M.G. and J.D.P; Visualization, N.C.R.S.

Funding: This research was financially supported through the award of the scholarship to N.C.R.S. by the Istituto Nazionale di Oceanografia e Geofisica Sperimentale—OGS, the University of Trieste—UNITS and the TRIL program of the Abdus Salam International Center for Theoretical Physics—ICTP. HF radar data were collected within the Italia-Malta program-Cohesion Policy 2007–2013, European Union regional Development Funds (ERDF) through the CALYPSO project.

Acknowledgments: The authors would like to thank Aldo Drago for providing the HFR data used in this study. We also acknowledged Simone Cosoli for providing the processed and QC dataset from the HFR array. Last but not least, we also thank to the two anonymous reviewers for their constructive observations.

Conflicts of Interest: The authors declare no conflict of interest.

Abbreviations

The following abbreviations are used in this manuscript:

Currents	
AC	Atlantic Current
ATC	Atlantic Tunisian Current
AIS	Atlantic Ionian Stream
BAC	Bifurcation Atlantic/Algerian current
MIJ	Mid-Ionian Jet
Water Masses	
AW	Atlantic Water
Geographical Names	
AB	Adventure Bank
MP	Malta Plateau
GB	Gela Basin
MT	Malta Trough
La	Lampedusa
P	Pantelleria
Li	Linosa
PT	Pantelleria Trough
LT	Linosa Trough
S	Sicily
M	Maltese Islands
SC	Sicily Channel
Channel	Malta-Sicily Channel
SME	Sicily-Malta Escarpment
MB	Medina Bank
SS	Sicily Strait
TP	Tunisia Plateau
Gyres	
ABV	Adventure Bank Vortex (Cyclonic)
MRV	Mesina Rise Vortex (Cyclonic)
ISV	Ionian Shelf Break Vortex (Cyclonic)
MSG	Malta-Sicily Gyre (Anticyclonic)
MCC	Malta Channel Crest (Anticyclonic)
MG	Medina Gyre (Cyclonic)
NIG	North Ionian Gyre (Cyclonic/Anticyclonic)
PV	Pantelleria vortex (Anticyclonic)
Datasets	
CCMP	Cross-Calibrated Multi-Platform wind vector analysis
CMEMS	Copernicus Marine and Environment Monitoring Service
CODAR	Coastal ocean dynamics applications radar
HFR	High Frequency Radar
MODIS	Moderate Resolution Imaging Spectroradiometer
NASA	National Aeronautics and Space Administration
NOAA	The National Oceanic and Atmospheric Administration
NSF	National Science Foundation
RSS	Remote sensing systems (scientific company)
Physical Properties	
ADT	Absolute Dynamic Topography
CHL	Satellite Sea surface chlorophyll concentrations
EKE	Eddy Kinetic Energy
SGV	Surface Geostrophic Velocity
SST	Satellite Sea Surface Temperature

References

1. Robinson, A.R.; Leslie, W.G.; Theocharis, A.; Lascaratos, A. *Encyclopedia of Ocean Sciences: Mediterranean Sea Circulation*, 2nd ed.; Academic London: London, UK, 2001; Volume 3, pp. 1689–1705. [CrossRef]
2. Malanotte-Rizzoli, P.M.; Robinson, A.R. *Ocean Processes in Climate Dynamics: Global and Mediterranean Examples*; Springer Science & Business Media: Berlin, Germany, 2012; Volume 419. [CrossRef]
3. Jouini, M.; Béranger, K.; Arsouze, T.; Beuvier, J.; Thiria, S.; Crépon, M.; Taupier-Letage, I. The Sicily Channel surface circulation revisited using a neural clustering analysis of a high-resolution simulation. *J. Geophys. Res. Oceans* **2016**, *121*, 4545–4567. [CrossRef]
4. Menna, M.; Reyes-Suarez, N.C.; Civitarese, G.; Gačić, M.; Poulain, P.-M.; Rubino, A. Decadal variations of circulation in the Central Mediterranean and its interactions with the mesoscale gyres. *Deep Sea Res. Part II Top. Stud. Oceanogr.* **2019**. [CrossRef]
5. Menna, M.; Poulain, P.-M.; Ciani, D.; Doglioli, A.; Notarstefano, G.; Gerin, R.; Rio, M.H.; Santoleri, R.; Gauci, A.; Drago, A. New insights of the Sicily Channel and southern Tyrrhenian Sea variability. *Water* **2019**, *11*, 1355. [CrossRef]
6. Würtz, M.; Rovere, M. *Atlas of the Mediterranean Seamounts and Seamount-Like Structures*; IUCN: Grand, Switzerland, 2015.
7. Ismail, S.B.; Schroeder, K.; Sammari, C.; Gasparini, G.P.; Borghini, M.; Aleya, L. Interannual variability of water mass properties in the Tunisia–Sicily Channel. *J. Mar. Syst.* **2014**, *135*, 14–28. [CrossRef]
8. Lodolo, E.; Ben-Avraham, Z. A submerged monolith in the Sicilian Channel (central Mediterranean Sea): Evidence for Mesolithic human activity. *J. Archaeol. Sci. Rep.* **2015**, *3*, 398–407. [CrossRef]
9. Drago, A.; Azzopardi, J.; Gauci, A.; Tarasova, R.; Ciraolo, G.; Capodici, F.; Gačić, M. Sea surface currents by HF radar in the Malta channel. *Rapp. Comm. Int. Mer Medit.* **2013**, *40*, 144.
10. Drago, A.; Ciraolo, G.; Capodici, F.; Cosoli, S.; Gačić, M.; Poulain, P.-M.; Tarasova, R.; Azzopardi, J.; Gauci, A.; Maltese, A.; et al. CALYPSO—An operational network of HF radars for the Malta-Sicily Channel. In Proceedings of the 7th International Conference on EuroGOOS, Lisbon, Portugal, 28–30 October 2014; Volume 30, pp. 28–30.
11. Smith, W.H.F.; Sandwell, D.T. Global seafloor topography from satellite altimetry and ship depth soundings. *Science* **1997**, *277*, 1957–1962. [CrossRef]
12. Robinson, A.R.; Sellschopp, J.; Warn-Varnas, A.; Leslie, W.G.; Lozano, C.J.; Haley, P.J., Jr.; Anderson, L.A.; Lermusiaux, P.F.J. The Atlantic Ionian Stream. *J. Mar. Syst.* **1999**, *20*, 129–156. [CrossRef]
13. Drago, A.; Sorgente, R.; Olita, A. *Sea Temperature, Salinity and Total Velocity Climatological Fields for the South-Central Mediterranean Sea*. MedSudMed Technical Documents Gcp/Rer/010/Ita/Msm-Td-14. 2010, 35. No. 14. Available online: http://www.faomedsudmed.org/html/doc/Publication_issue.asp?id=195 (accessed on 30 July 2019).
14. Lermusiaux, P.F.J. Estimation and study of mesoscale variability in the Strait of Sicily. *Dyn. Atmos. Oceans* **1999**, *29*, 255–303. [CrossRef]
15. Lermusiaux, P.F.J.; Robinson, A.R. Features of dominant mesoscale variability, circulation patterns and dynamics in the Strait of Sicily. *Deep Sea Res. Part I Oceanogr. Res. Pap.* **2001**, *48*, 1953–1997. [CrossRef]
16. Béranger, K.; Mortier, L.; Gasparini, G.P.; Gervasio, L.; Astraldi, M.; Crépon, M. The dynamics of the Sicily Strait: A comprehensive study from observations and models. *Deep Sea Res. Part II Top. Stud. Oceanogr.* **2004**, *51*, 411–440. [CrossRef]
17. Robinson, A.R.; Malanotte-Rizzoli, P.; Hecht, A.; Michelato, A.; Roether, W.; Theocharis, A.; Ünlüata, Ü; Pinardi, N.; Artegiani, A.; Bergamasco, A.; et al. General circulation of the Eastern Mediterranean. *Earth-Sci. Rev.* **1992**, *32*, 285–309. [CrossRef]
18. Pinardi, N.; Zavatarelli, M.; Adani, M.; Coppini, G.; Fratianni, C.; Oddo, P.; Simoncelli, S.; Tonani, M.; Lyubartsev, V.; Dobricic, S.; et al. Mediterranean Sea large-scale low-frequency ocean variability and water mass formation rates from 1987 to 2007: A retrospective analysis. *Prog. Oceanogr.* **2015**, *132*, 318–332. [CrossRef]
19. Gačić, M.; Borzelli, G.E.; Civitarese, G.; Cardin, V.; Yari, S. Can internal processes sustain reversals of the ocean upper circulation? The Ionian Sea example. *Geophys. Res. Lett.* **2010**, *37*. [CrossRef]

20. Gačić, M.; Civitarese, G.; Eusebi Borzelli, G.L.; Kovačević, V.; Poulain, P.M.; Theocharis, A.; Menna, M.; Catucci, A.; Zarokanellos, N. On the relationship between the decadal oscillations of the northern Ionian Sea and the salinity distributions in the eastern Mediterranean. *J. Geophys. Res. Oceans* **2011**, *116*. [CrossRef]
21. Gačić, M.; Schroeder, K.; Civitarese, G.; Cosoli, S.; Vetrano, A.; Eusebi Borzelli, G.L. Salinity in the Sicily Channel corroborates the role of the Adriatic–Ionian Bimodal Oscillating System (BiOS) in shaping the decadal variability of the Mediterranean overturning circulation. *Ocean Sci.* **2013**, *9*, 83–90. [CrossRef]
22. Civitarese, G.; Gačić, M.; Lipizer, M.; Eusebi Borzelli, G.L. On the impact of the Bimodal Oscillating System (BiOS) on the biogeochemistry and biology of the Adriatic and Ionian Seas (Eastern Mediterranean). *Biogeosciences* **2010**, *7*, 3987–3997. [CrossRef]
23. Bessières, L.; Rio, M.H.; Dufau, C.; Boone, C.; Pujol, M.I. Ocean state indicators from MyOcean altimeter products. *Ocean Sci.* **2013**, *9*. [CrossRef]
24. Sammari, C.; Millot, C.; Taupier-Letage, I.; Stefani, A.; Brahim, M. Hydrological characteristics in the Tunisia–Sardinia–Sicily area during spring 1995. *Deep Sea Res. Part I Oceanogr. Res. Pap.* **1999**, *46*, 1671–1703. [CrossRef]
25. Ciappa, A.C. Surface circulation patterns in the Sicily Channel and Ionian Sea as revealed by MODIS chlorophyll images from 2003 to 2007. *Cont. Shelf Res.* **2009**, *29*, 2099–2109. [CrossRef]
26. Capodici, F.; Ciraolo, G.; Cosoli, S.; Maltese, A.; Mallandrino, G. The synergy of water quality and sea surface currents data in determining the spatio-temporal evolution of large-scale circulation features. In *Remote Sensing for Agriculture, Ecosystems, and Hydrology XVI*; International Society for Optics and Photonics: Amsterdam, The Netherlands, 2014; Volume 9239, p. 923927. [CrossRef]
27. Cosoli, S.; Drago, A.; Ciraolo, G.; Capodici, F. Tidal currents in the Malta–Sicily Channel from high-frequency radar observations. *Cont. Shelf Res.* **2015**, *109*, 10–23. [CrossRef]
28. Gauci, A.; Drago, A.; Abela, J. Gap Filling of the CALYPSO HF Radar Sea Surface Current Data through Past Measurements and Satellite Wind Observations. *Int. J. Navig. Obs.* **2016**. [CrossRef]
29. Capodici, F.; Cosoli, S.; Ciraolo, G.; Nasello, C.; Maltese, A.; Poulain, P.M.; Drago, A.; Azzopardi, J.; Gauci, A. Validation of HF radar sea surface currents in the Malta-Sicily Channel. *Remote Sens. Environ.* **2019**, *225*, 65–76. [CrossRef]
30. CALYPSO: Real-Time Viewing of Sea Surface Currents in the Malta Channel. Available online: http://www.mongoos.eu/-/calypso-real-time-viewing-of-sea-surface-currents-in-the-malta-channel (accessed on 4 July 2018).
31. Rio, M.H.; Pascual, A.; Poulain, P.M.; Menna, M.; Barceló, B.; Tintoré, J. Computation of a new mean dynamic topography for the Mediterranean Sea from model outputs, altimeter measurements and oceanographic in situ data. *Ocean Sci.* **2014**, *10*, 731–744. [CrossRef]
32. Wentz, F.J.; Scott, J.; Hoffman, R.N.; Leidner, S.M.; Atlas, R.; Ardizzone, J. Remote Sensing Systems Cross-Calibrated Multi-Platform (CCMP) 6-Hourly Ocean Vector Wind Analysis Product on 0.25 deg Grid, Version 2.0, [Aug 2013–Jan 2015]. Remote Sensing Systems: Santa Rosa, CA. Available online: www.remss.com/measurements/ccmp (accessed on 5 December 2017).
33. Atlas, R.; Hoffman, R.N.; Ardizzone, J.; Leidner, S.M.; Jusem, J.C.; Smith, D.K.; Gombos, D. A cross-calibrated, multiplatform ocean surface wind velocity product for meteorological and oceanographic applications. *Bull. Am. Meteorol. Soc.* **2011**, *92*, 157–174. [CrossRef]
34. Kundu, P.K. Ekman veering observed near the ocean bottom. *J. Phys. Oceanogr.* **1976**, *6*, 238–242. [CrossRef]
35. Sanderson, B.G. Structure of an eddy measured with drifters. *J. Geophys. Res. Oceans* **1995**, *100*, 6761–6776. [CrossRef]
36. Malanotte-Rizzoli, P.; Artale, V.; Borzelli-Eusebi, G.L.; Brenner, S.; Crise, A.; Gačić, M.; Kress, N.; Marullo, S.; Ribera d'Alcalà, M.; Sofianos, S.; et al. Physical forcing and physical/biochemical variability of the Mediterranean Sea: A review of unresolved issues and directions for future research. *Ocean Sci.* **2014**, *10*, 281–322. [CrossRef]
37. Jebri, F.; Birol, F.; Zakardjian, B.; Bouffard, J.; Sammari, C. Exploiting coastal altimetry to improve the surface circulation scheme over the central Mediterranean Sea. *J. Geophys. Res. Oceans* **2016**, *121*, 4888–4909. [CrossRef]
38. Jebri, F.; Zakardjian, B.; Birol, F.; Bouffard, J.; Jullion, L.; Sammari, C. Interannual variations of surface currents and transports in the Sicily channel derived from coastal altimetry. *J. Geophys. Res. Oceans* **2017**, *122*, 8330–8353. [CrossRef]

39. Drago, A.; Sorgente, R.; Ribotti, A. A high resolution hydrodynamic 3-D model simulation of the Malta shelf area. *Ann. Geophys.* **2003**, *21*, 323–344. [CrossRef]
40. Manzella, G.M.; Gasparini, G.P.; Astraldi, M. Water exchange between the eastern and western Mediterranean through the Strait of Sicily. *Deep Sea Res. Part A Oceanogr. Res. Pap.* **1988**, *35*, 1021–1035. [CrossRef]
41. Pujol, M.I.; Larnicol, G. Mediterranean Sea eddy kinetic energy variability from 11 years of altimetric data. *J. Mar. Syst.* **2005**, *58*, 121–142. [CrossRef]
42. Jordi, A.; Wang, D.P. Mean dynamic topography and eddy kinetic energy in the Mediterranean Sea: Comparison between altimetry and a 1/16 degree ocean circulation model. *Ocean Model.* **2009**, *29*, 137–146. [CrossRef]
43. Paduan, J.D.; Washburn, L. High-frequency radar observations of ocean surface currents. *Annu. Rev. Mar. Sci.* **2013**, *5*, 115–136. [CrossRef]
44. Paduan, J.D.; Graber, H.C. Introduction to high-frequency radar: Reality and myth. *Oceanography* **1997**, *10*, 36–39. [CrossRef]

water

Article

New Insights of the Sicily Channel and Southern Tyrrhenian Sea Variability

Milena Menna [1,*], Pierre-Marie Poulain [1,2], Daniele Ciani [3], Andrea Doglioli [4], Giulio Notarstefano [1], Riccardo Gerin [1], Marie-Helene Rio [5], Rosalia Santoleri [3], Adam Gauci [6] and Aldo Drago [6]

[1] Istituto nazionale di Oceanografia e Geofisica Sperimentale, OGS, 34010 Sgonico (TS), Italy
[2] Centre for Maritime Research and Experimentation (CMRE), 19126 La Spezia, Italy
[3] Consiglio Nazionale delle Ricerche, Istituto di Scienze Marine, CNR-ISMAR, Via del Fosso del Cavaliere, 100, 00133 Rome, Italy
[4] Marseille Université, Université de Toulon, CNRS, IRD, MIO UM 110, Marseille, France, 13288 Marseilles, France
[5] European Space Research Institute, ESA-ESRIN, 00044 Frascati, Italy
[6] Physical Oceanography Research Group, Department of Geosciences, University of Malta, 2080 Msida, Malta
* Correspondence: mmenna@inogs.it; Tel.: +39-0402140302

Received: 31 May 2019; Accepted: 27 June 2019; Published: 29 June 2019

Abstract: The dynamics of the Sicily Channel and the southern Tyrrhenian Sea are highly influenced by the seasonal variability of the Mediterranean basin-wide circulation, by the interannual variability of the numerous mesoscale structures present in the Channel, and by the decadal variability of the adjacent Ionian Sea. In the present study, all these aspects are investigated using in-situ (Lagrangian drifter trajectories and Argo float profiles) and satellite data (Absolute Dynamic Topography, Sea Level Anomaly, Sea Surface Temperature, wind products) over the period from 1993 to 2018. The availability of long time series of data and high-resolution multi-sensor surface currents allow us to add new details on the circulation features and on their driving mechanisms and to detect new permanent eddies not yet described in literature. The structures prevailing in winter are mainly driven by wind, whereas those prevailing in summer are regulated by topographical forcing on surface currents. The strength of the surface structures located at the western entrance of the Ionian Sea and of the mesoscale activity along the northern Sicily coast is modulated by the large-scale internal variability. The vertical hydrological characteristics of these mesoscale eddies are delineated using the Argo float profiles inside these structures.

Keywords: Sicily Channel; spatial and temporal variability; mesoscale eddies

1. Introduction

Thanks to its location in the centre of the Mediterranean Basin, the Sicily Channel (SC) plays a crucial role in connecting the western and eastern Mediterranean basins and modulating their exchange of surface and intermediate waters [1,2]. The SC is characterized by a complex bottom topography, with submarine ridges and shallow banks, and it is delimited to the north by the Tyrrhenian Sea and the Sicily coast, to the south by the Libyan coast, to the west by the Tunisia coast, and to the east by the Ionian Sea (Figure 1a). Its circulation can be schematized on the vertical as a two-layer exchange with an eastward flow of Atlantic Water (AW) superposed to a westward flow of intermediate water, dominated by the Levantine Intermediate Water (LIW) [3]. Microstructure measurements taken in the SC show that it is a hotspot for turbulent mixing [4,5]. Consequently, the SC is a key area for the regulation of salt exchanges between Eastern and Western basins, with an impact on deep-water formation processes [6].

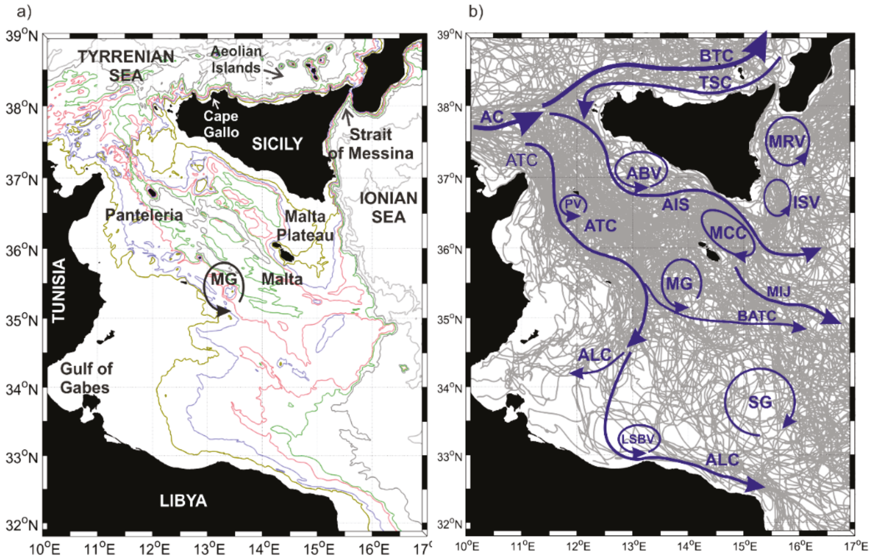

Figure 1. (**a**) Bathymetry of the SC (100 m, 200 m, 400 m, 600 m, 1000 m, 2000 m isobaths) and geographical references. (**b**) Low-pass filtered drifter trajectories in the SC between 1993 and 2018, superimposed with the schematic surface circulation adapted from [1,3]. Acronyms are listed in Table 1.

Circulation in the upper layer of the SC and in the southern Tyrrhenian Sea is mainly dictated by the large-scale Mediterranean thermohaline circulation, the wind-driven currents along the shelf, the upwelling events off Sicily, the sub-basin scale, and mesoscale permanent and quasi-permanent structures [1,3,7–9]. The recent results of AW circulation schemes, derived by numerical model simulation [1,3], are summarized in Figure 1b (both permanent and seasonal circulation structures are depicted with the same color in Figure 1b; more details on the time scales and variability of these structures are available in Section 3; acronyms are defined in Table 1). The sub-basin scale structures are characterized by a prominent seasonal variability [9–12] associated with large wind stress fluctuations [13]. The numerous mesoscale structures located in the SC are mainly driven by the instability of the large-scale circulation, by the interactions between currents and bathymetry, and by the direct wind forcing [1].

Presently, the availability of long time series of in-situ and satellite data and of sophisticated statistical techniques allow us to add new details on the mesoscale features and on their driving mechanisms. In this study, Lagrangian drifter trajectories, Argo float profiles, and satellite data (Absolute Dynamic Topography, Sea Level Anomaly, Sea Surface Temperature, wind products) are used to describe the surface circulation of the SC and the southern Tyrrhenian Sea over the period from 1993 to 2018. The simultaneous use of all these datasets leads to overcoming the intrinsic limitations of each of them, e.g., the accurate but discontinuous spatial and temporal drifter sampling and the low accuracy of altimetry gridded data in the identification of the mesoscale field [14]. Moreover, the knowledge of the mesoscale field is ameliorated using the multi-sensor currents (defined hereafter as 'optimal currents') derived from merging the satellite altimetry data and the Sea Surface Temperature (SST) fields [15]. This product enables the improvement of the description of eddy dynamics and non-geostrophic dynamical features [15]. The vertical structures and the hydrological characteristics of the mesoscale eddies are delineated using the Argo float profiles inside these structures. All these data and products enhance the knowledge on the temporal variability of the mesoscale structures, with detection of new features not yet described in the literature, and the addition of new insights on the formation mechanisms of these structures.

Table 1. List of acronyms used in this paper.

Geographical Names	
SC	Sicily Channel
Water Masses	
AW	Atlantic Water
LIW	Levantine Intermediate Water
Currents	
AC	Algerian Current
AIS	Atlantic Ionian Stream
ALC	Atlantic Libyan Current
ATC	Atlantic Tunisian Current
ATC	Atlantic Tunisian Current
MIJ	Mid-Ionian Jet
BTC	Bifurcation Tyrrhenian Current
BATC	Bifurcation Atlantic Tunisian Current
TSC	Tyrrhenian Sicilian Current
TSC	Tyrrhenian Sicilian Current
Gyres and Eddies	
ABV	Adventure Bank Vortex
ISV	Ionian Shelf break Vortex
LSBV	Libyan Shelf Break Vortex
MG	Medina Gyre
MCC	Maltese Channel Crest
MRV	Messina Rice Vortex
NSA	Northern Sicily Anticyclone
PV	Pantelleria Vortex
SCA	Sicily Channel Anticyclone
SG	Sidra Gyre
SISV	Southern Ionian Shelf break Vortex
SMG	Southern Medina Gyre
SMA	Southern Maltese Anticyclone
Physical Properties	
ADT	Absolute Dynamic Topography
AGV	Absolute Geostrophic Velocities

2. Materials and Methods

The datasets used for this study are as follows:

- The OGS Mediterranean drifter dataset in the SC and Southern Tyrrhenian Sea, composed of 377 drifter tracks collected between 1993 and 2018 (Figure 1b). Drifter data were retrieved from the OGS own projects, but also from databases collected by other research institutions and by international data centers (Global Drifter Program, SOCIB, CORIOLIS, MIO, etc.). These data were cleaned of potential outliers and elaborated with standard procedures (editing, manual editing, and interpolation [16,17]). In particular, we use the low-pass filtered and interpolated (6 h) drifter tracks, which represent the near-surface currents between 0 m and 15 m in depth.
- The daily (1/8° Mercator projection grid) Absolute Dynamic Topography (ADT) and correspondent Absolute Geostrophic Velocities (AGV) derived from altimeter and distributed by CMEMS in the period from 1993 to 2018 (product user manual CMEMS-SL-QUID_008-032-051). The ADT was obtained by the sum of the sea level anomaly and a 20 year synthetic mean estimated in Reference [18] over the 1993 to 2012 period.
- The Argo float vertical profiles of temperature and salinity from the upper 2000 m of the water column and the horizontal current displacements at the parking depth. In the Mediterranean Sea, the Argo floats are generally programmed to execute 5 day cycles with a drifting depth of 350 m (parking depth). Additionally, they alternate the profiling depth between 700 m and 2000 m

(see the MedArgo program in Reference [19]). When a float drifts in a shallow area and touches the ground, it can increase its buoyancy to get away from bottom, or can stay there until it is time to ascent (depending on how it is programmed). Information about grounding events is contained in the Argo float trajectory file. Among all the data available in the Mediterranean Sea, we selected from the part of the Argo floats trajectories which correspond to a float entrapped in the mesoscale structures of the SC and southern Tyrrhenian Sea. These data were used to define the vertical hydrographic peculiarities of the mesoscale features. Details about the missions of the seven floats selected for this work are listed in Table 2.

- The optimal currents, estimated by Reference [15] and presently available in the period from 2012 to 2016. This product was used to confirm the occurrence of the mesoscale structure derived from altimetry and to estimate their interannual variability. Indeed, the optimal currents are based on the synergy of the daily 1/8° Copernicus CMEMS altimeter-derived geostrophic velocities (data ID: SEALEVEL_MED_PHY_L4_REP_OBSERVATIONS_008_051) and the daily 1/24° CMEMS sea-surface temperatures for the Mediterranean Sea (data ID: SST_MED_SST_L4_REP_OBSERVATIONS_010_021). The optimal reconstruction method is based on the inversion of the ocean heat conservation equation in the mixed layer [15]. The principles of the optimal currents are thoroughly described in References [15,20,21]. Such a method takes advantage of the high-resolution spatial temporal gradients of the satellite-derived SST to improve the temporal (1 day) and spatial (1/24°) resolution of the altimeter derived geostrophic currents at the basin scale. The reconstruction method of the optimal currents yielded positive improvements for both the components of the motion in the SC [15].
- The Cross-Calibrated, Multi-Platform (CCMP) V2.0 ocean surface wind velocity data, which were downloaded from the NASA Physical Oceanography DAAC for the period from July 1993 to May 2016 [22]. These products were created using a variational analysis method to combine wind measurements derived from several satellite scatterometers and micro-wave radiometers. The temporal resolution of the CCMP product is six hours and the spatial resolution is 25 km (level 3.0, first-look version 1.1).

Table 2. List of selected Argo float profiles with dates and positions of the first and the last profile considered in this work, parking and profiling depths, and the cycle period of each instrument.

Float WMO	First Profile	Last Profile	Parking Depth (m)	Profile Depth (m)	Cycle Period (days)
6900981	23 April 2012 38.9° N, 13.6° E	3 January 2013 38.8° N, 14.9° E	350	600/2000	5
6901044	16 December 2012 36.3° N, 14.3° E	22 April 2013 36.7° N, 14.5° E	350	700	1
6903242	11 September 2018 35.4° N, 14.4° E	13 November 2018 35.2° N, 15.0° E	200	200	0.125
1900629	22 August 2007 33.7° N, 13.5° E	5 March 2008 34.5° N, 13.9° E	350	700/2000	5
1900948	19 July 2015 33.0° N, 15.6° E	28 February 2016 32.9° N, 15.0° E	1000	1500	4
1900954	16 October 2016 35.8° N, 15.6° E	5 March 2017 35.2° N, 14.8° E	1000	1500	4

Drifter velocities were divided in bins of 0.25° × 0.25° and pseudo-Eulerian statistics were computed over the period from 1993 to 2018 and qualitatively compared with the ADT derived from altimetry. The mean current field was also estimated in the period from 2012 to 2016, using the optimal currents. The seasonal variability of the drifter, altimetry, and optimal current fields was estimated by dividing the dataset in two extended seasons, the extended summer corresponding to May–October, and the extended winter to November–April, as suggested by Reference [9].

The CCMP six-hourly gridded analyses were used to quantify the wind stress and the vertical component of the wind stress curl, $[curl\ \tau]_z$, over the study area:

$$[curl\tau]_z = \frac{\partial \tau_y}{\partial x} - \frac{\partial \tau_x}{\partial y}; \left(\tau_y, \tau_x\right) = \rho C_D (u_w, v_w) U_{10} \tag{1}$$

where (τ_x, τ_y) are the wind stress components, ρ (1.22 Kg/m^3) is the density of air, (u_w, v_w) and U_{10} are the components and the magnitude of the wind speed at 10 m, respectively, and C_D is the drag coefficient already used in the Mediterranean Sea by References [23,24], as follows:

$$\begin{array}{ll} C_D = 10^{-3} & |U_{10}| \leq 3\frac{m}{s} \\ C_D = (0.29 + \frac{3.1}{U_{10}} + \frac{7.7}{U_{10}^2}) \times 10^{-3} & 3\frac{m}{s} \leq |U_{10}| \leq 6\frac{m}{s} \\ C_D = (0.6 + 0.07U_{10}) \times 10^{-3} & 6\frac{m}{s} \leq |U_{10}| \leq 26\frac{m}{s} \end{array} \tag{2}$$

Wind stress and wind stress vorticity fields were used to speculate on the link between the wind variations and the seasonal and/or interannual variability of mesoscale structures.

The monthly means of the AGV and optimal current fields were used to estimate the relative vorticity (ζ), defined as the vertical component of the velocity field curl, as follows:

$$\zeta = \frac{\partial V}{\partial x} - \frac{\partial U}{\partial y}; \tag{3}$$

where U and V are the velocity components. The resulting current vorticity fields were spatially averaged in the regions of the main mesoscale structures listed in Table 1 and filtered (13 month moving average) in order to remove the seasonal and intra-annual variations.

3. Results

3.1. Mean Currents and Wind Fields

The qualitative comparison between the ADT and drifter data shows that the two datasets fit rather well (Figure 2a) and allow us to update the pseudo-Eulerian current maps described in Reference [9] and to enhance the schematic circulation maps published by References [1,3] summarized in Figure 1b. The averages were made over different periods in accordance with the availability of data, 1993–2018 for the drifter and altimetry data (Figure 2a), 2012–2016 for the optimal currents (Figure 2b), and 1993–2016 for the wind (Figure 2c,d). The time periods are rather long and the statistics are rather robust to consider the average in Figure 2a comparable with those in Figure 2c,d and representative of the mean conditions in the SC. The optimal currents are available over a reduced period and are, therefore, not directly compared with the other datasets. Rather, they are used to bring out some aspects of the current field that are not obvious, using only drifters and altimetry data. The structures emphasized in white in Figure 2a,b, are described here for the first time or with different shapes and positions with respect to those schematized in Figure 1b.

The Atlantic Tunisian Current (ATC) originates from the branch of the Algerian Current (AC) that enters in the SC and flows southward between Pantelleria Island and the Tunisian coast [9]. It shows a complex pattern only partially described by the previous model studies. Indeed, the ATC splits in two branches at about 36.5° N (Figure 2a). One branch continues to move southward along the Tunisian coast (shown in white color), whereas another branch moves eastward south of Pantelleria Island. At about 35.5° N and 13° E, the ATC splits another time. A part of the current forms the Bifurcation Atlantic Tunisian Current (BATC) and the other part turns southward towards the Libyan coast at ~13° E. The latter branch describes the Atlantic Libyan Current (ALC [1,3]), which moves westward towards the Gulf of Gabes and eastward along the Libyan coast (Figures 1b and 2a).

Drifter and altimetry data confirm the well-known meandering pattern of the Atlantic Ionian Stream (AIS) and outline the edge of the Maltese Channel Crest (MCC), located on the Maltese Plateau.

The Medina Gyre (MG) is located on the west and/or southwest side of the Malta Island in agreement with the scheme of Reference [3]. The region where the ATC splits and forms the BATC is characterized by a sudden reduction of depth due to the shelf extension (see the location of MG in Figure 1a), which probably facilitates the cyclonic rotation of the surface currents around 35°–36° N and 13°–14.5° E. It is interesting to note that Reference [1] located the MG in a different position southeast of Malta (see Figure 2 of [1]). South of the MG, altimetry and drifter data detect another permanent cyclonic mesoscale structure that has never been described before in the literature; hereafter we will refer to this structure as the Southern Medina Gyre (SMG) (emphasized in white Figure 2a). The Libyan Shelf Break Vortex (LSBV) is well described only by altimetry data (Figure 2a) because of a scarce quantity of drifter tracks along the Libyan coast. This structure appears meridionally elongated and squeezed along the Libyan coast, showing a different shape and location with respect to Reference [1].

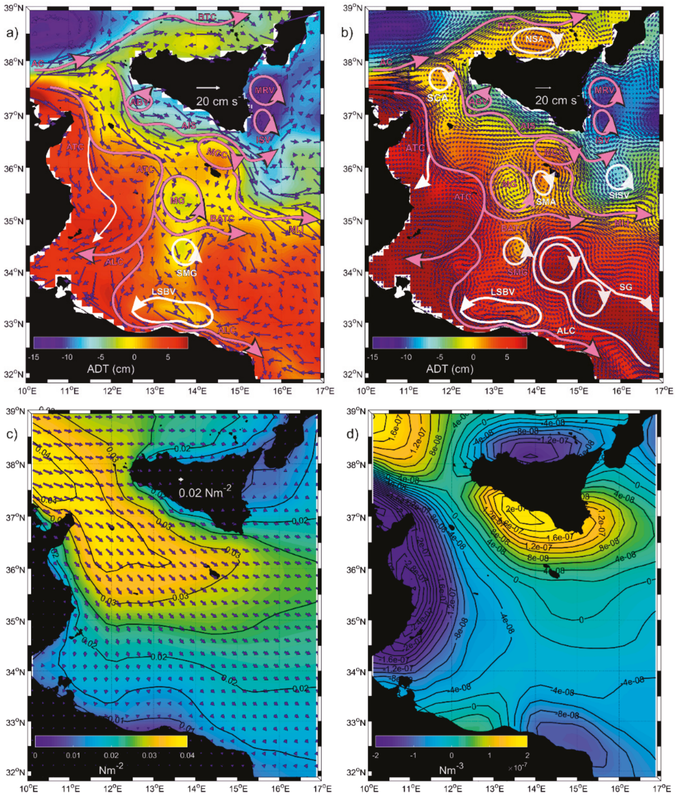

Figure 2. Mean drifter currents (**a**) in spatial bins of 0.25° × 0.25° (blue vectors) superimposed on mean maps of absolute dynamic topography (colors) during the period from 1993 to 2018. Mean optimal currents (**b**) in spatial bins of 1/12° (vectors; one vector every two grid points is plotted) superimposed on mean maps of absolute dynamic topography (colors) during the period from 2012 to 2016. The structures emphasized with white arrows in panels (**a**,**b**) are new or with different shapes and positions with respect to those described in Figure 1b. The structures already known are highlighted with pink arrows. (**c**) Mean map of the wind stress amplitude (colors) and direction (vectors) and (**d**) wind stress curl over the period from 1993 to 2016.

The higher spatial resolution of the mean circulation derived by optimal currents (2012–2016; Figure 2b) permits a more detailed description of the mesoscale structure of the SC and the southern

Tyrrhenian Sea. The anticyclonic structure, clearly visible along the northern coast of Sicily and located between the Aeolian Islands and Cape Gallo (38.1–38.5° N; 13.5–15° E), was observed by Reference [25] in September 2012, but it was not described by these authors; hereafter it will be defined as the Northern Sicily Anticyclone (NSA). Another mesoscale anticyclone is located at the entrance of the SC (37.5–38° N; 11.5–12° E) and represents a kind of watershed between the waters entering the Tyrrhenian Sea (Bifurcation Tyrrhenian Current—BTC) and those entering the SC; hereafter we will define it as the Sicily Channel Anticyclone (SCA). A third mesoscale anticyclone is squeezed between the MG and Malta Island (35.5°–36° N; 14°–14.5° E) and we will define it hereafter as the Southern Maltese Anticyclone (SMA). Similarly, southeast of the Ionian Shelf break Vortex (ISV), there is another steady cyclonic structure hereafter defined as the Southern Ionian Shelf break Vortex (SISV). In addition, the optimal currents reveal new information on the shape of the Sidra Gyre (SG), which appears as a large anticyclone that involves two smaller anticyclonic structures (Figure 2b) and confirms the existence of the SMG (Figure 2b). The cyclonic circulation in the region of the Adventure Bank Vortex (ABV; 37–37.5° N; 12–13° E) is detected by the three datasets (drifter, altimetry, and optimal currents) but the vortex is not well resolved by any of them. It appears more like a cyclonic meander rather than a vortex (Figure 2, upper panels).

In the study area the mean wind stress is oriented to the east in the southern Tyrrhenian Sea and to the southeast in the SC (Figure 2c) with amplitude (range of values between 0 and 0.04 Nm^{-2}) and directions in agreement with the results of Reference [12]. The regions mostly impacted by the wind stress are located in the band north of 35° N and south of the southern Sicily coast (Figure 2c). The rotating motion induced by the wind (wind stress curl Figure 2d) is cyclonic (positive) along the southern and eastern Sicily coasts and on the Malta plateau, whereas it is anticyclonic (negative) along the Tunisia coast and in the southern Tyrrhenian Sea (along the northern Sicily coast). We can speculate that the wind field plays an important role in shaping the sub-basin circulation (e.g., the branch of the ATC that moves southward along the Tunisia coast) and in defining the sense of rotation of the mesoscale structures located around the Sicily coast (e.g., the ABV, the Messina Rise Vortex (MRV), the ISV, and the NSA).

3.2. Seasonal Variability of Currents and Wind Fields

The seasonal variability of the drifter-derived and optimal current fields is shown in Figure 3, together with the altimetry data. Results substantially confirm the paths described in Reference [9], but add new insights. The BTC is a permanent feature, as shown by Reference [1], and it is stronger in winter (Figure 3b,d; winter speeds larger than 20 cm/s; mean summer speeds of ~10 cm/s), whereas the NSA is much more intense in summer (Figure 3a,c; mean winter speeds of ~5 cm/s; mean summer speeds of ~10 cm/s). Along the northern coast of Sicily, the drifter data describe a westward current during summer, with the consequent inflow of surface water in the SC (Figure 3a), whereas the coastal currents move eastward during winter (Figure 3b). This summer westward current (mean speeds of ~10 cm/s) was already described in Reference [3] and defined as the Tyrrhenian Sicilian Current (TSC). The TSC is not identified by the optimal currents (Figure 3c,d).

The ATC is part of the permanent pattern of the SC, in agreement with Reference [3], and it is more intense and more meandering in nature during the extended winter (Figure 3b,d; maxima winter speeds of ~30 cm/s; maximum summer speeds of ~20 cm/s). It is interesting to note that Reference [1] described it as a winter structure. The cyclonic Pantelleria Vortex (PV) is observed only during the extended winter (Figure 3b,d; speeds of 10–15 cm/s), in agreement with the optimal currents and with Reference [3] and in disagreement with Reference [1], which describes this as part of the permanent pattern. The MCC is stronger during the extended summer (speeds larger than 15 cm/s), as well as the AIS (Figure 3a,c; mean winter speed of ~5 cm/s; mean summer speeds of ~15 cm/s). The SG is stronger and larger in size during summer (Figure 3a,c; mean winter speeds of ~7 cm/s; mean summer speeds of ~12 cm/s; winter longitudinal extension of ~100 km; summer longitudinal extension larger than 250 km), in agreement with the results of Reference [26], which report the SG seasonal expansion in the summer and contraction in the winter. The ISV and the MRV are permanent structures, in agreement with Reference [1], and they are stronger in the winter (Figure 3b,d; mean winter speeds of ~9 cm/s; mean summer speeds of ~6 cm/s). In addition, the SISV is a permanent structure more intense in the winter, according to the optimal currents (Figure 3d; mean winter speeds of ~10 cm/s; mean summer speeds of ~5 cm/s). The BATC is predominant during winter south of the MG (Figure 3b,d; maxima winter speeds of ~20 cm/s; maxima summer speeds of ~10 cm/s), in agreement with Reference [1]. The ALC is stronger in the winter (Figure 3b,d; speeds larger than 15 cm/s), whereas the LSBV is stronger in the summer (Figure 3a,c; speeds larger than 25 cm/s).

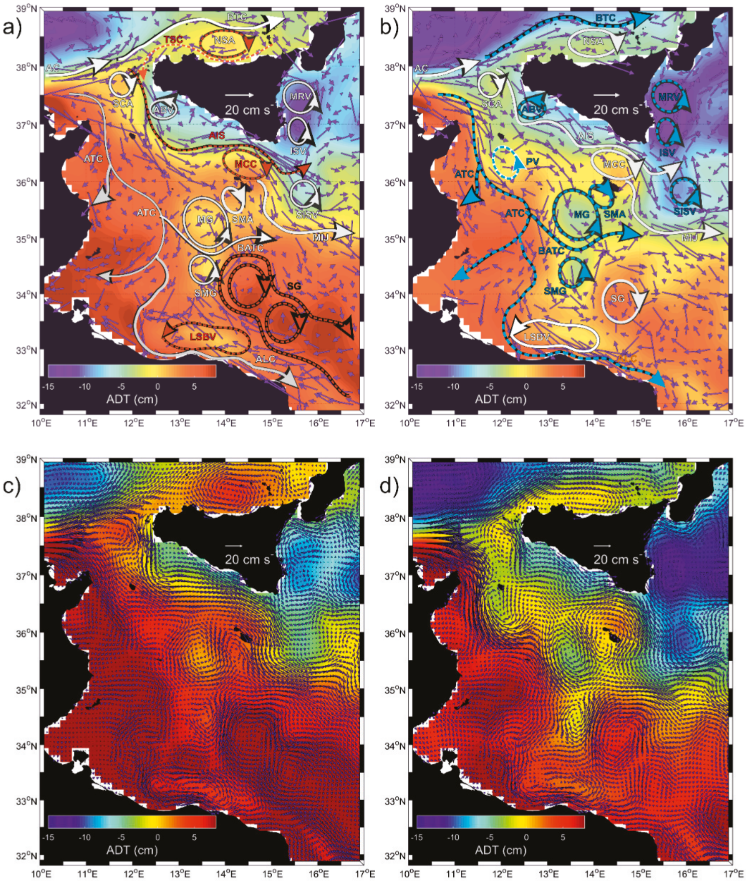

Figure 3. Pseudo-Eulerian drifter statistics (blue vectors) superimposed on mean maps of the absolute dynamic topography (colors) for the (**a**) extended summer and (**b**) extended winter. The schematic circulation structures superimposed on the current fields are colored with red arrows (**a**) when they are most intense in summer and with light blue arrows (**b**) when they are most intense in winter. Mean optimal currents in spatial bins of 1/12° (blue vectors: one vector every two grid points is plotted) superimposed on mean maps of absolute dynamic topography (colors) during the period from 20 12to 2016 for the (**c**) extended summer and (**d**) extended winter.

The wind stress and the wind stress curl are more intense in winter (Figure 4), influencing the seasonal variability of some sub-basin currents, such as the BTC, the ALC, the BATC. The winter intensification of the BATC and its interaction with the topography lead to an intensification of the MG.

The wind stress does not impact the circulation structures, which are more intense in summer (MCC, AIS, NSA, SG), when the wind stress and the wind stress curl are weakened. The seasonal variability of these structures is presumably related to other forcings, such as the instability of the surface currents and the interaction with the topography. The behaviour of the AIS and of the MCC confirms the following insight: The AIS is stronger in the summer (Figure 3a) when the wind stress is weaker (Figure 4a) and its meander on the Malta Plateau (the MCC) is anticyclonic, although the vorticity induced by the wind in this region is substantially cyclonic (Figure 4c). Along the northern coast of the Sicily, the amplitude of the wind stress and the anticyclonic vorticity induced by the wind are stronger in winter (Figure 4), whereas the strengthening of the NSA is observed in the summer (Figure 3a,c). This result suggests that the wind influences the sense of rotation of the surface circulation in the NSA, but other forcings modulate the strength of the seasonal and interannual variability of this circulation structure. The summer intensification of the LSBV appears to be instead related to the intensification of the cyclonic wind stress curl along the western Libyan coast (Figure 4c). The SG shows a pronounced longitudinal extension in summer (Figure 3a), when the wind stress is weaker but the vorticity induced by the wind is essentially anticyclonic in the southeastern region of the SC (Figure 4a). Its southern margin is oriented parallel to the Libyan coast following the 400 m isobath.

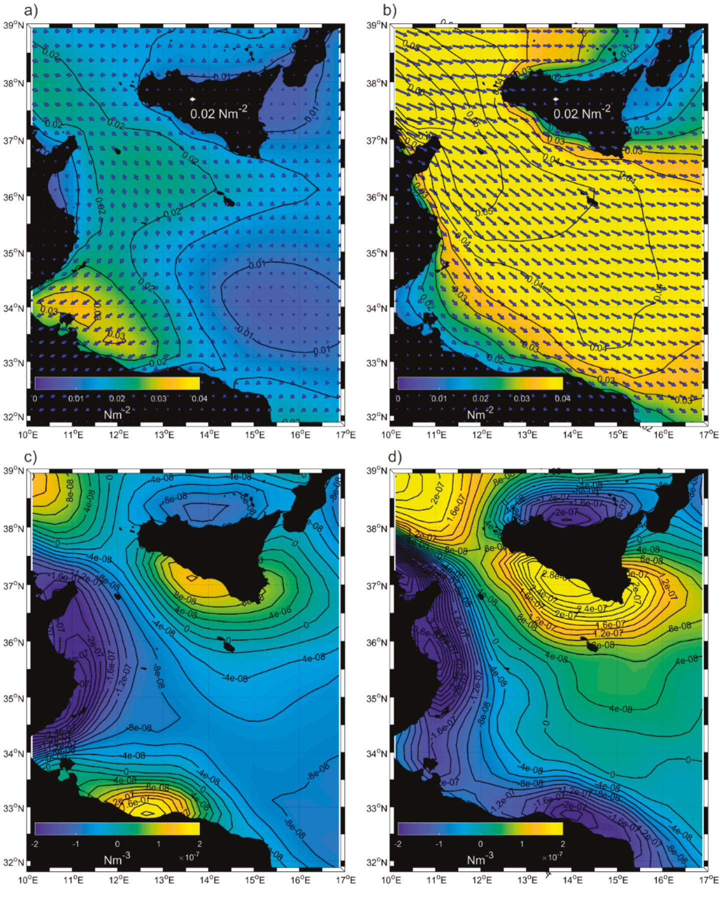

Figure 4. Mean map of the wind stress (upper panels) amplitude (colours) and direction (vectors) and (**d**) wind stress curl (lower panels) over the extended summer (**a**,**c**) and extended winter (**b**,**d**).

3.3. Decadal Variations

Decadal variations are emphasized by removing the mean ADT and AGV (1993–2018) fields from the interannual composite mean over the time periods characterized by the anticyclonic (1993–1996, 2006–2010, and 2016–2017) and cyclonic (1997–2005 and 2011–2016) circulation modes in the northern Ionian (Figure 5). In the region located between Pantelleria and Malta islands (35.5° N–37° N, 11° E–15° E), the surface currents are smaller than the mean field during the anticyclonic mode (Figure 5a; current anomalies are oriented in an opposite direction with respect to the mean field) and larger during the cyclonic mode (Figure 5b). Along the northern coast of the Sicily, the NSA is reduced in intensity, with respect to the mean field, during the anticyclonic mode (Figure 5a; the current anomalies are oriented cyclonically) and increased during the cyclonic mode.

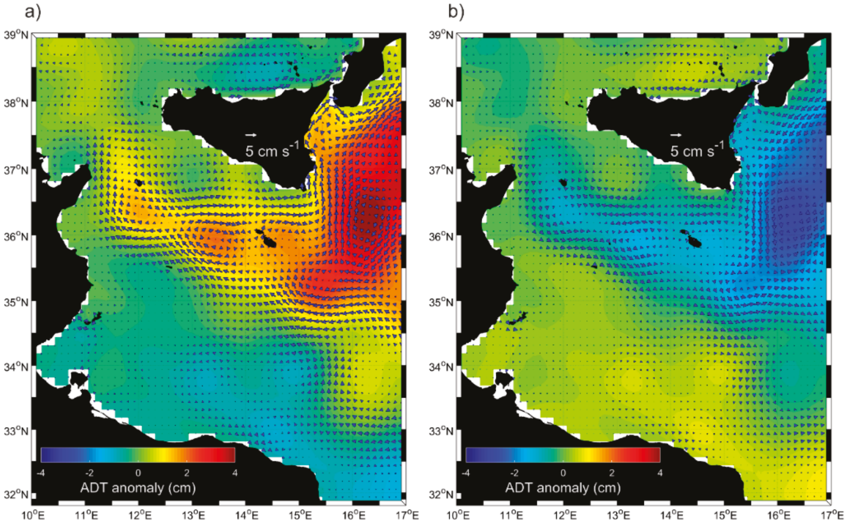

Figure 5. Mean maps of absolute geostrophic velocity anomalies (vectors) superimposed to the absolute dynamic topography anomalies (colours) during (**a**) anticyclonic (1993–1996, 2006–2010, 2017–2018) and (**b**) cyclonic (1997–2005 and 2011–2016) circulation modes in the northern Ionian.

The largest variations are observed east of 15° E, in agreement with the results of Reference [24]. The MRV and the SISV are less intense than the mean currents during the anticyclonic mode (Figure 5a) and slightly more intense during the cyclonic mode (Figure 5b). The AIS tends to be deflected towards the northern Ionian during the anticyclonic circulation mode (northeastward currents along the Sicily eastern coast) and the MIJ is reduced in intensity with respect to the mean currents (Figure 5a). During the cyclonic circulation mode, the AIS feeds the MIJ, which shows larger intensities with respect to the mean, and the currents are mainly directed southwestward along the western coasts of the Ionian Sea (Figure 5b).

3.4. Interannual Variability and Vertical Structure of the Quasi-Permanent Mesoscale Eddies in the Sicily Channel and Southern Tyrrhenian Sea

The main quasi-permanent mesoscale eddies of the SC and southern Tyrrhenian are analyzed in terms of their interannual variability, using the time series of spatially averaged vorticity fields derived both from altimetry and optimal currents data. In the period in which the optimal currents are available, the accuracy of the vorticity derived by the AGV is generally improved, showing larger complexity in the temporal variability of the signal (see Figure 6, Figure 8, and Figure 11). The thermohaline properties and the vertical extension in the water column of these mesoscale eddies is studied using the Argo float profiles.

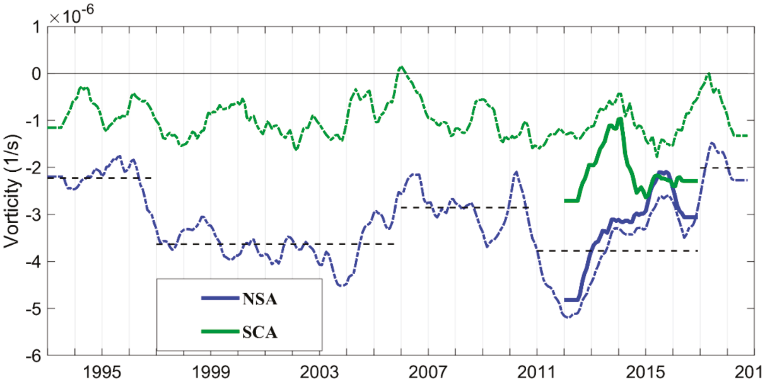

Figure 6. Time series of the spatially averaged, low pass filtered (13 month) vorticity field over the regions of the NSA and SCA. Dashed-dotted lines refer to the vorticity field derived from the AGV. The continuous lines are related to the vorticity field derived from optimal currents from 2012 to 2016. The dashed black lines show the average values of the vorticity over each anticyclonic/cyclonic period of the Northern Ionian Gyre.

3.4.1. Southern Tyrrhenian Sea and Sicily Channel Entrance

The analysis of the vorticity field in the areas of the NSA (38.1–38.5° N; 13.5–15° E) and SCA (37.5–38° N; 11.5–12° E) confirms that the anticyclonic nature of these regions persists with time (Figure 6). A more accurate analysis of the temporal evolution of the vorticity in the NSA shows quasi-decadal variations of the intensity of the vorticity field that coincide with the inversions of the surface circulation in the northern Ionian. The black dashed lines in Figure 6 give an indication of the mean vorticity values during each anticyclonic/cyclonic circulation mode. The anticyclonic vorticity of the NSA is reduced during the anticyclonic circulation modes of the northern Ionian (1993–1996, 2006–2010, 2017–2018), whereas it is enhanced during the cyclonic circulation modes (1997–2005, 2011–2016). This result supports the relationship between the large–scale interior ocean variability in the central Mediterranean Sea and the local dynamics, suggested by Reference [27]. More specifically, these authors suggest a link between the inversions of the surface circulation in the northern Ionian and the local tidal observations in the area of the Strait of Messina. The present work shows that not only the Strait of Messina, but all the coastal areas adjacent to the northern Sicily coast can be influenced by the variability attributed to the large-scale dynamics of the central Mediterranean.

The vertical structure of the NSA is defined by the profiles of the float WMO 6900981, which circulated on the border of the NSA between late April 2012 and early January 2013 (Figure 7a,b). This float shows that the NSA extends about 50 m in depth and confirms its anticyclonic nature with a reduction of density and the deepening of the isopycnal surfaces, in particular between the end of June 2012 and November 2012, when the float profiles were close to the core of the eddy. The trajectory of the float WMO 6900981 gives an indication of the intermediate current displacements at the parking depth (350 m; see Table 2). It is interesting to note that, during the period covered by the float WMO 6900981, the intermediate currents in the region of the NSA flowed in an opposite direction (cyclonic displacements; Figure 7a), with respect to the mean surface currents (Figure 2b). The diagram in Figure 7b shows a gap of the float profiles between 1 September 2012 and 20 October 2012. Despite this gap, the float remains confined to the eastern part of the NSA, from which it moves away only in December 2012. Unfortunately, we have no floats entrapped in the SCA.

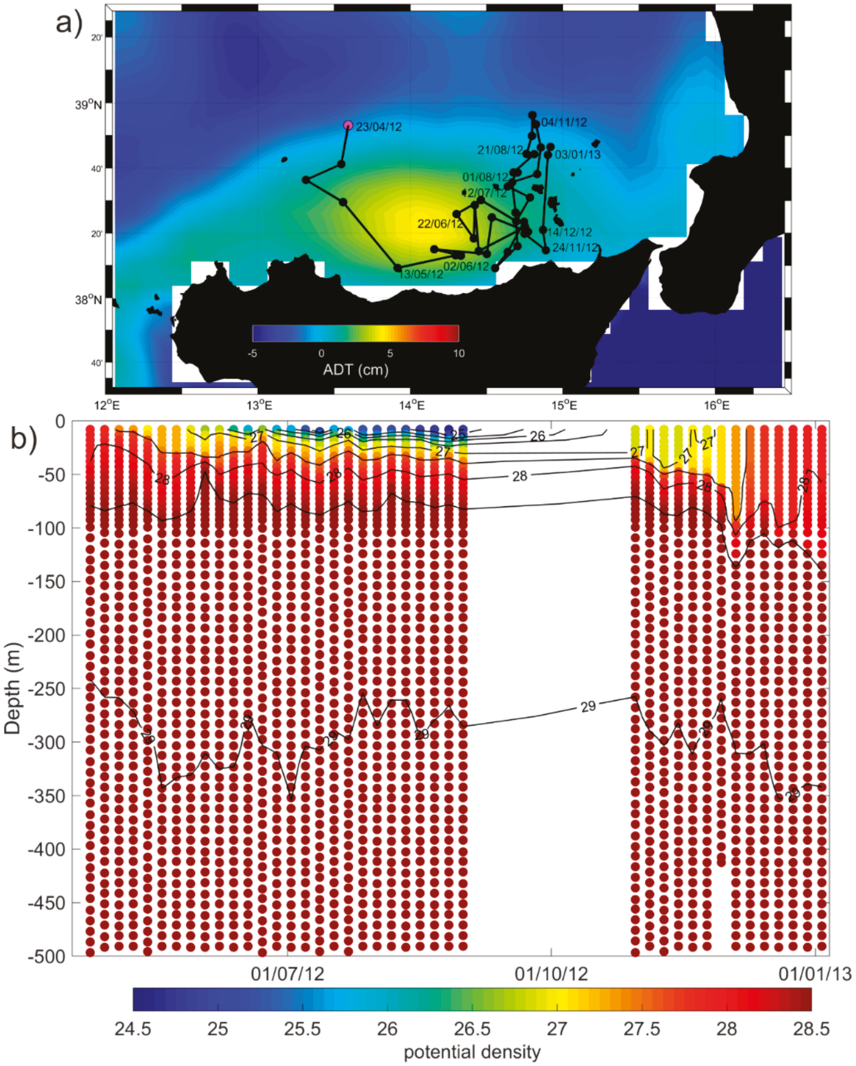

Figure 7. Map of the trajectory (black line) and profile positions (First profile: Magenta dot; Other profiles: Black dots) of the float WMO 6900981 superimposed on the mean map of the ADT (between 18 April 2012 and 3 January 2013) (**a**) and contour diagram of the potential density versus depth and time (**b**).

3.4.2. Malta Plateau

The surface circulation in the region of the Malta Plateau is strongly influenced by the flow of the AIS that forms a large anticyclonic meander defined as MCC. The permanent anticyclonic vorticity in this region (36.1–36.8° N; 14–15° E) is confirmed by the time series of the vorticity field (Figure 8). At local scale, this meander can sporadically create an anticyclonic gyre on the Malta plateau [28].

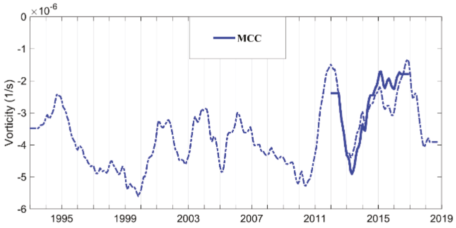

Figure 8. Time series of the spatially averaged, low pass filtered (13 month) vorticity field over the regions of the Malta plateau. Dashed-dotted lines are referred to the vorticity field derived from the AGV; continuous lines are related to the vorticity field derived from optimal currents from 2012 to 2016.

In the framework of the Italia-Malta Calypso Project [28], about 38 drifters were deployed on the Malta plateau between December 2012 and September 2016. These drifters were captured by the anticyclonic gyre on the plateau in two specific deployments, December 2012 and March 2014 (Figure 9). From December 2012 through January 2013, drifters were captured by the anticyclonic gyre for about four weeks (approximately between 14 December 2012 and 10 January 2013) before being transported out of the plateau (Figure 9a). This gyre is also confirmed by the trajectory of the float WMO 6901044 (Figure 10a) and by HF radar measurements [29,30]. On 22 March 2014, six drifters were deployed in the area and were trapped in the gyre for about 2 weeks (Figure 9b). Drifters allow for estimating the radius and the rotation period of the structure considering the centroids computed from all the closed loops of the drifter trajectories. The radius spanned between 11 and 27 km and the period increased from 4.1 to 8.4 days, coinciding with an increased distance from the centre.

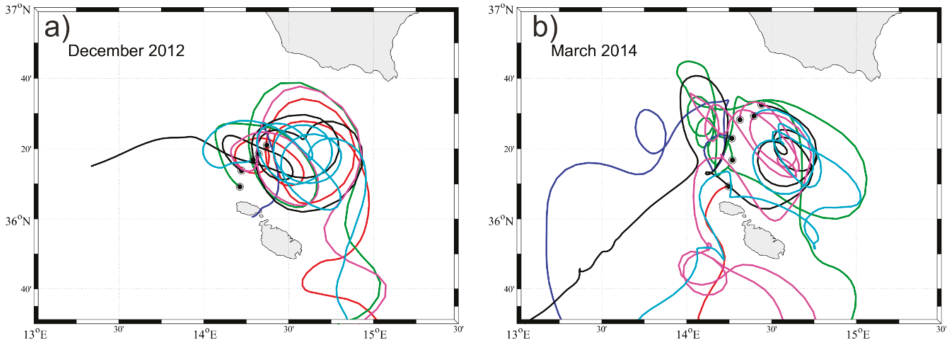

Figure 9. Trajectories and deployment positions (black dots) of the drifters deployed on the Malta Plateau in December 2012 (**a**) and March 2014 (**b**).

The float WMO 6901044 was entrapped in the MCC between 15 December 2012 and 17 February 2013, then it joined a cyclonic structure located north-west of the Malta Plateau (Figure 10a). It had a cycling period of 1 day, and its trajectory gives an indication of the 350 m displacements (see Table 2). In the first part of its tracks, the float sampled the interior of the anticyclonic MCC, showing a deepening of the isopycnal surfaces (December 2012–January 2013) and reduced densities. In February 2013, the float moved along the border of the MCC, then it was entrapped in the cyclonic structure located in the north-western proximities of the Malta plateau (Figure 10b). Both the MCC and the cyclonic structure show a similar vertical structure, extending to a depth of about 200–250 m (Figure 10b).

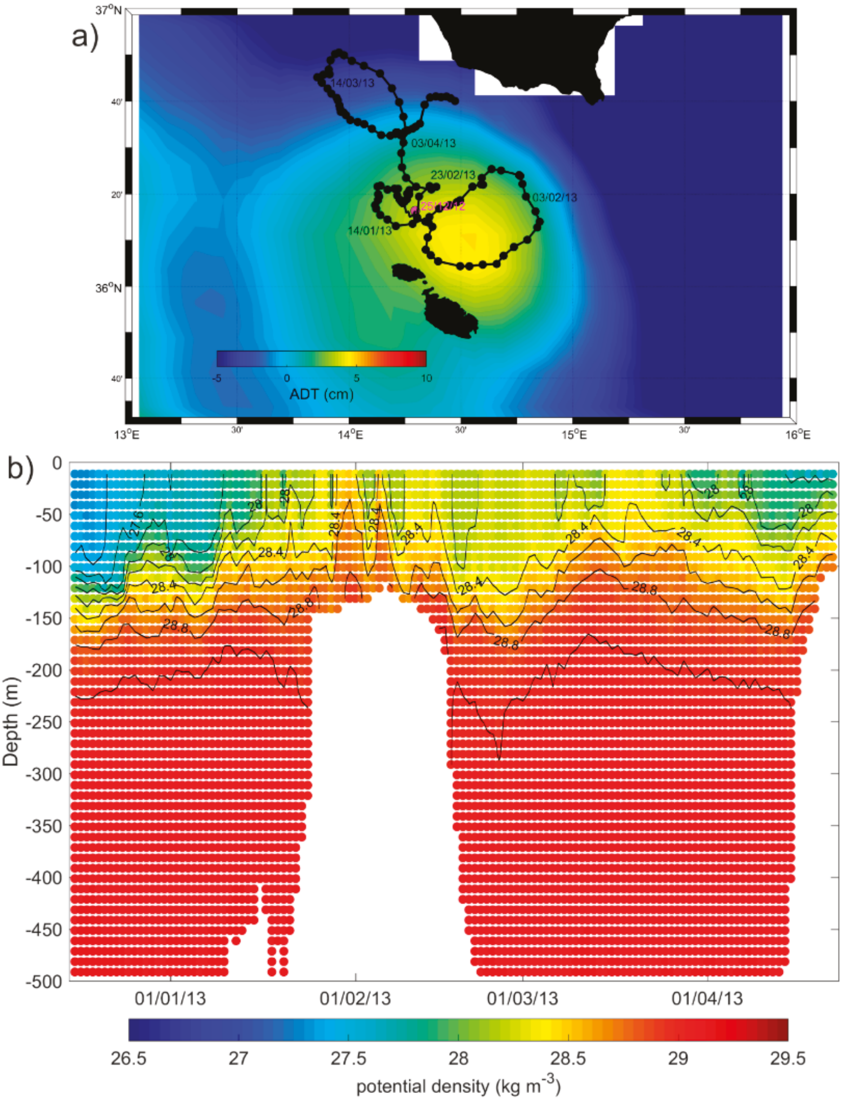

Figure 10. Map of the trajectory (black line) and profile positions (First profile: Magenta dot; Other profiles: Black dots) of the float WMO 6901044, superimposed on the mean map of the ADT (between 16 December 2012 and 30 April 2013) (**a**) and contour diagram of the potential density versus depth and time (**b**).

3.4.3. South of Malta

The time series of the vorticity fields obtained at the locations of the mesoscale eddies south and south-west of Malta are shown in Figure 11. The MG (35°–35.5° N; 13°–14° E) and the SMA (35.5°–36° N; 14°–14.5° E), two adjacent structures located south-west of the Maltese Islands, show larger variabilities of the vorticity field, with respect to the SMG (34°–35° N; 13°–14° E) and LSBV (33°–33.5° N; 12.5°–14° E). This behaviour is probably related to the wind-stress, which is more intense in the Malta region than in the southern SC (Figure 2c). The vorticity of SMA increased with time over the considered period.

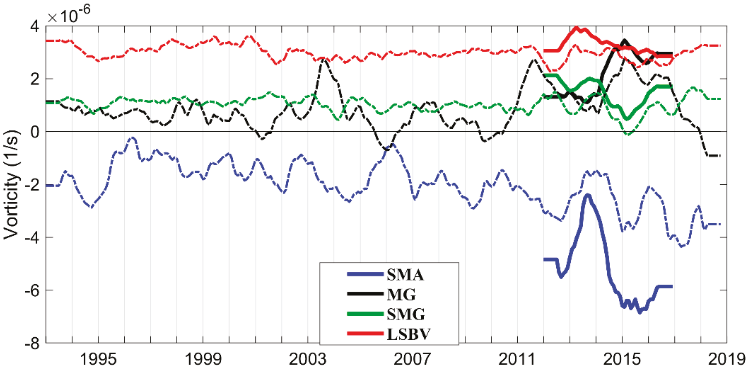

Figure 11. Time series of the spatially averaged, low pass filtered (13 month) vorticity field over the regions of MG, SMA, SMG, and LSBV. Dashed-dotted lines refer the vorticity field derived from the AGV. The continuous lines are related to the vorticity field derived from optimal currents from 2012 to 2016.

The float WMO 6903242, became entrapped in the anticyclonic SMA in mid-September 2018 and described five loops around the eddy core before being captured by the eastward BATC (Figure 12a). It had a short cycling period (see Table 2) and its trajectory indicates the mean near surface displacements (0–180 m). The subsurface density distribution clearly shows the net differences between the water masses located east (potential density smaller than 24.8 kg/m^3) and south (potential density larger than 26 kg/m^3) of the of SMA (Figure 12b). The SMA extends down to a depth of about 40 m (Figure 12c). At the end of October 2018, the float left the cyclonic structures and moved eastward, encountering surface waters of eastern origin and denser than 1026 kg/m^3.

The float WMO 1900629, coming from the Libyan coast, was entrapped in the cyclonic SMG at the end of 2007 (Figure 13a). This structure is denser than the surrounding waters (Figure 13b). Since, in the region of the SMG, the maximum depth of the sea bottom is about 400 m (Figure 1a), and since the cyclonic trajectory of the float WMO 1900629 (Figure 13a) represents the displacements of the currents at the parking depth of 350 m (see Table 2), we can conclude that the cyclonic structure affects the entire water column in this area.

The cyclonic LSBV is sampled by the float WMO 1900948 during the period from October 2015 to February 2016 is shown in Figure 14a. The entrance of this float in the LSBV is emphasized in Figure 14b by a higher density, compared to the surrounding waters, and by changes in the shape of the isopycnal surfaces. Even if float WMO 1900948 has a parking depth of 1000 m (see Table 2), its displacements represent the current at 350 m depth, due to the bathymetry of the LSBV region (see Figures 1a and 14b). We can conclude that the cyclonic structure affects the entire water column in this area (Figure 14b).

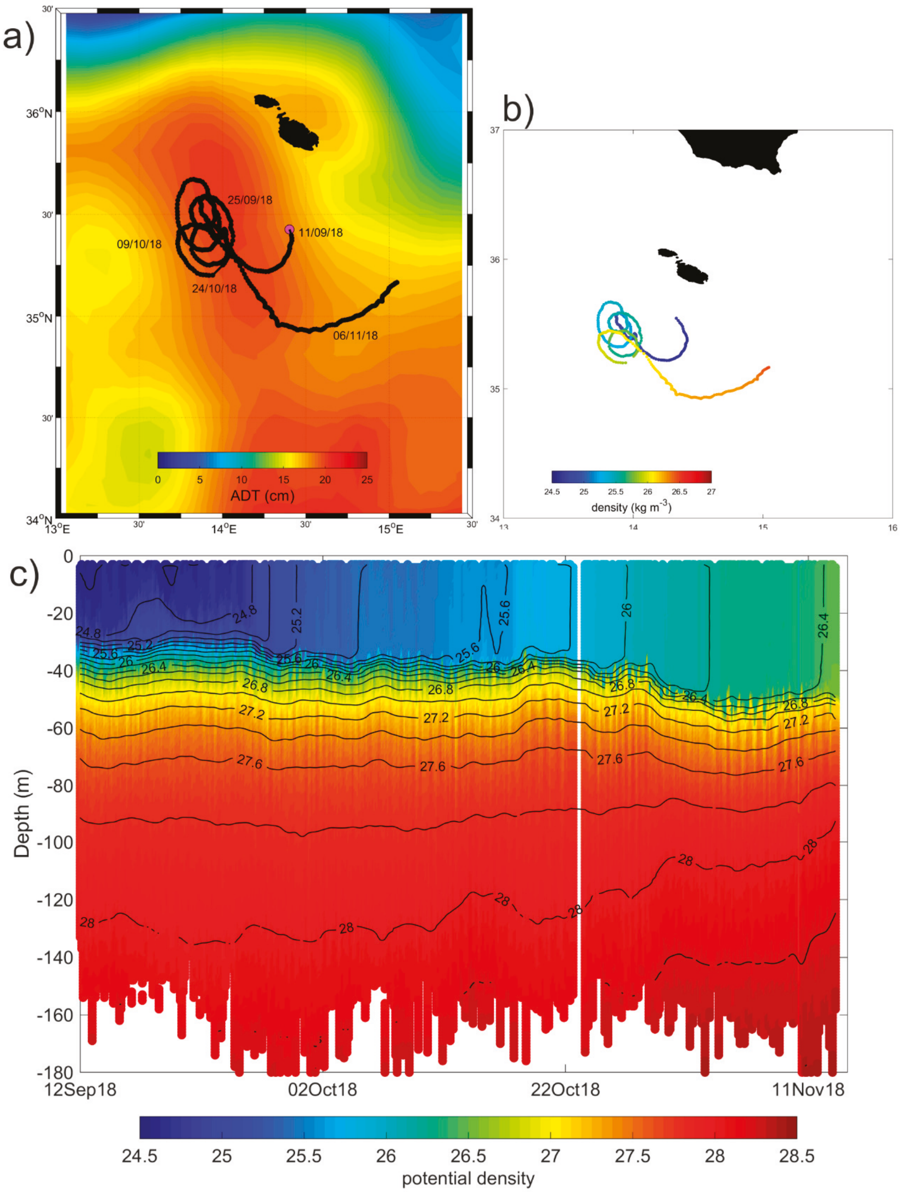

Figure 12. Map of the trajectory (black line) and profile positions (First profile: Magenta dot; Other profiles: Black dots) of the float WMO 6903242, superimposed on the mean map of the ADT (between 12 September 2018 and 11 November 2018) (**a**). Map of the potential density measured at 20 m depth (**b**) and contour diagram of the potential density versus depth and time (**c**).

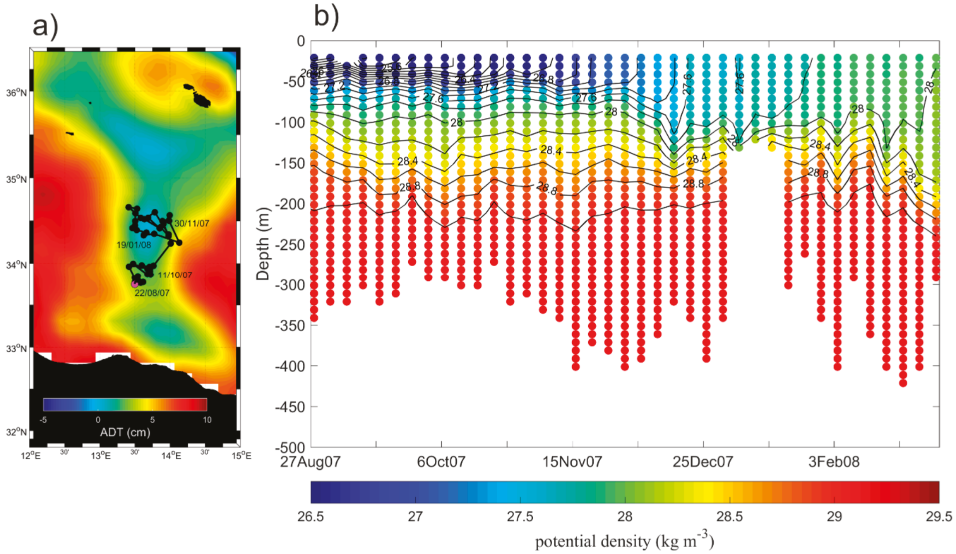

Figure 13. Map of the trajectory (black line) and profile positions (First profile: Magenta dot; Other profiles: Black dots) of the float WMO 1900629, superimposed on the mean map of the ADT (between 27 August 2007 and 23 February 2008) (**a**) and contour diagram of the potential density versus depth and time (**b**).

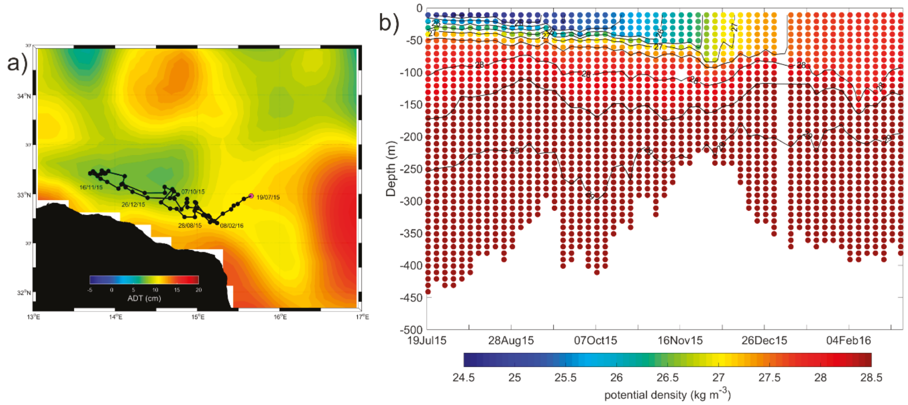

Figure 14. Map of the trajectory (black line) and profile positions (First profile: Magenta dot; Other profiles: Black dots) of the float WMO 1900948 superimposed on the mean map of the ADT (between 19 July 2015 and 28 February 2016) (**a**), and contour diagram of the potential density versus depth and time (**b**).

3.4.4. Ionian Cyclones

Figure 15a shows the time series of the vorticity field along the eastern coast of Sicily (MRV and ISV area—36.5°–38° N; 15°–16° E) and in the region of the SISV. Figure 15a shows an inconsistency between the vorticity derived from AGV and those derived from the optimal currents in the region of the SISV. From the optimal current validation carried out by Reference [15], this structure lies in an area where the method degrades the quality of the surface currents (in particular of the meridional component), when compared with the AGV (see Figure 10 of [15]). Therefore, the optimal currents could not be consistent in the description of SISV.

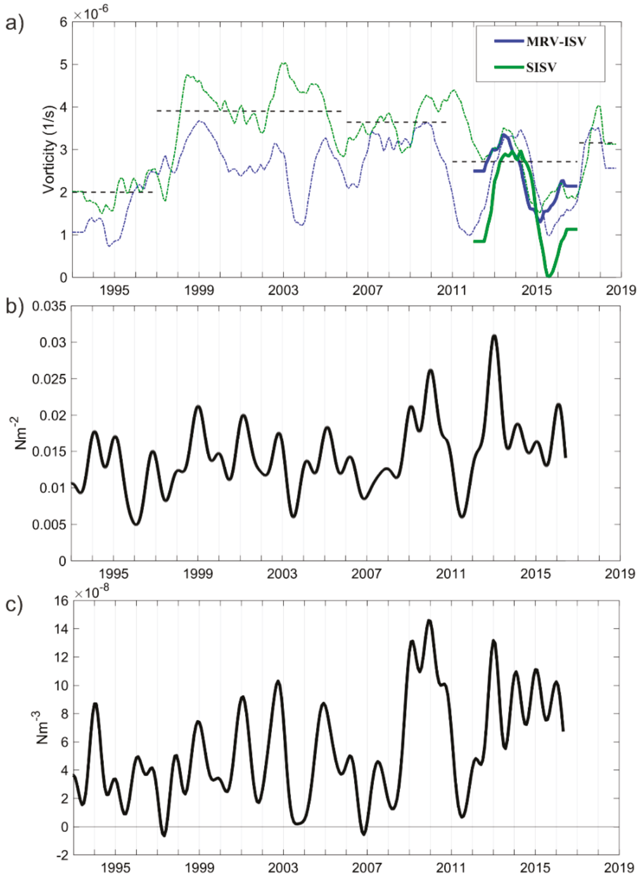

Figure 15. (**a**) Time series of the spatially averaged, low pass filtered (13 month) vorticity field over the regions of the MRV-ISV and SISV. Dashed-dotted lines refer to the vorticity field derived from the AGV. The continuous lines are related to the vorticity field derived from optimal currents from 2012 to 2016; (**b**) time series of the monthly, spatially averaged low-pass filtered (13 month) wind-stress and (**c**) wind stress vorticity in the MRV region.

The MRV and ISV are wind-driven structures [7,24] and their interannual variability is related to the wind-stress along the eastern coast of Sicily (Figure 15b,c), e.g., lower values of current vorticity in the MRV-ISV regions are related to lower wind-stress and lower wind stress curl. The SISV (35.5°–36.6° N; 15°–16° E) is not influenced by the wind-stress vorticity, whereas it appears to be influenced by the quasi-decadal reversal of the northern Ionian (see black dashed lines in Figure 15a that give an indication of the mean vorticity value during each anticyclonic/cyclonic circulation mode) in the period from 1993 to 2010. After 2010, the vorticity of the currents was no longer consistent with the decadal variability and, rather, seems to be linked to some other phenomena that are not currently detectable from our datasets.

The float WMO 1900954, coming from the eastern Ionian, was entrapped in the SISV in December 2017 (Figure 16a) and showed an increase of density with respect to the water located north of this mesoscale structure (Figure 16b). Even if the float WMO 1900954 has a parking depth of 1000 m (see Table 2), its displacement represents the current at about 500 m depth, due to the bathymetry of the SISV region (see Figures 1a and 16b). The vertical extension of the SISV is about 100 m (Figure 16b).

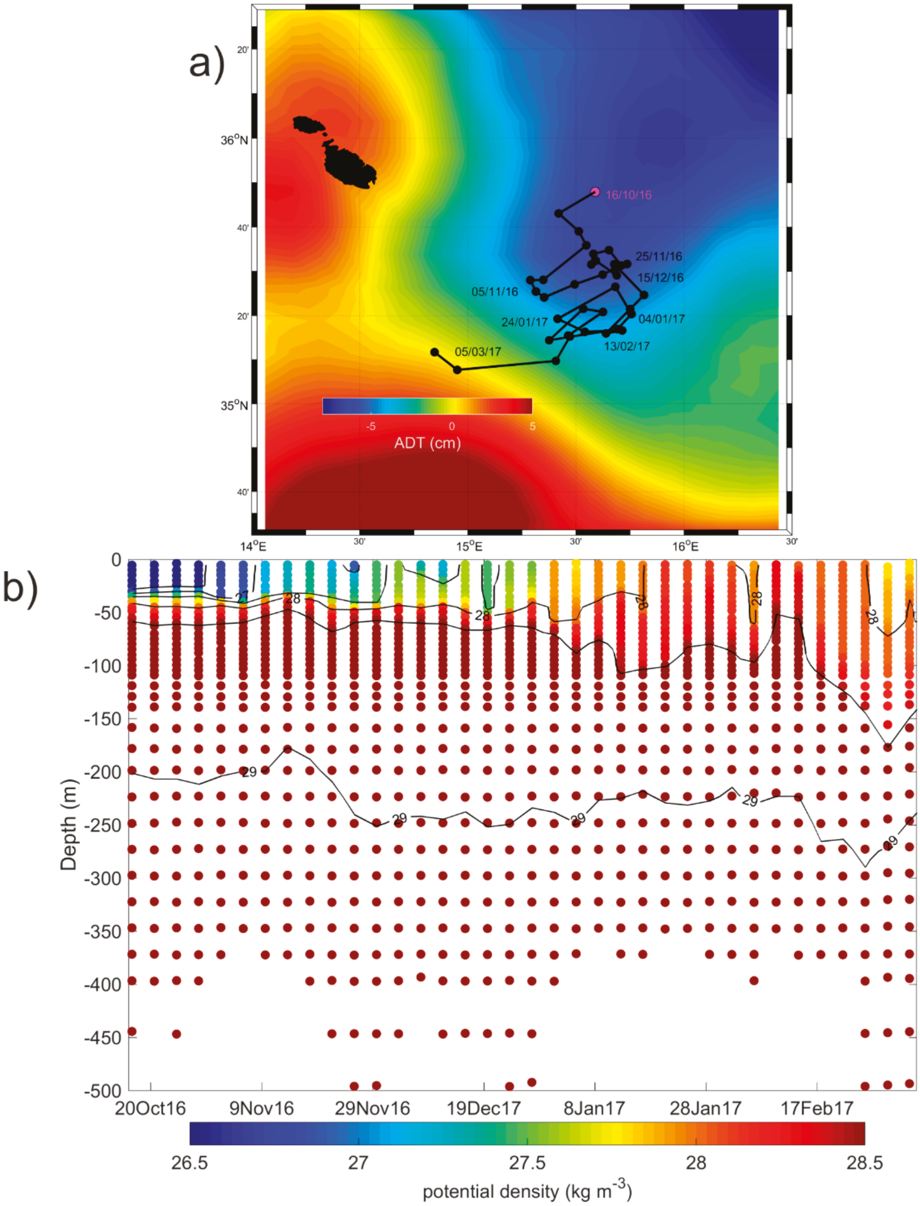

Figure 16. Map of the trajectory (black line) and profile positions (First profile: Magenta dot; Other profiles: Black dots) of the float WMO 1900954, superimposed on the mean map of the ADT (between 20 October 2016 and 7 March 2017) (**a**) and contour diagram of the potential density versus depth and time (**b**).

4. Discussion and Conclusions

The main findings of this work are summarized in Figure 17, where a schematic diagram of the surface circulation, based on the mean circulation map depicted in Figure 2b, is presented. In Figure 17a the main circulation structures are classified according to their seasonal variability, whereas in Figure 17b they are identified based on the main forcing factor that determines them.

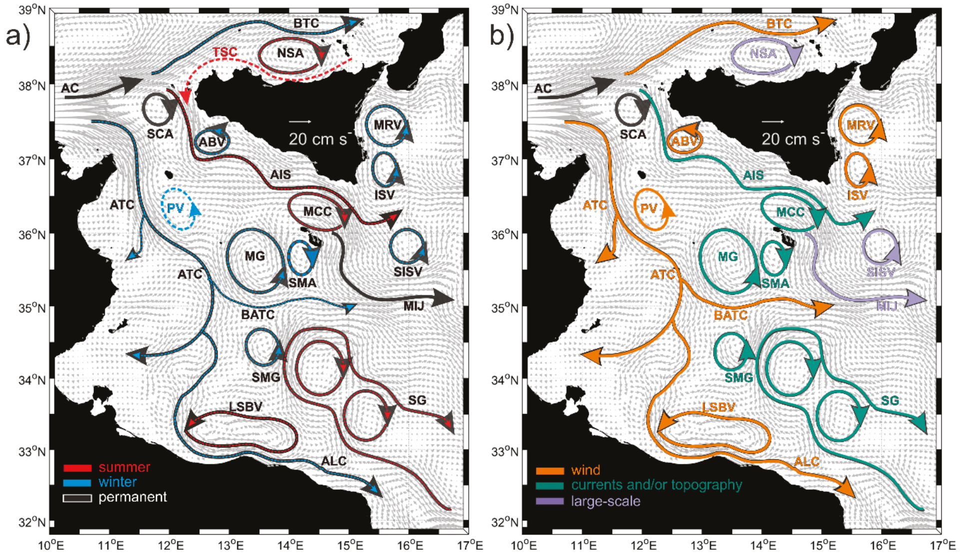

Figure 17. Schematized representation of the mean surface circulation in the Sicily Channel and Southern Tyrrhenian Sea (black arrows), based on the mean optimal current circulation map depicted in Figure 2b (bright grey vectors). (**a**) Black arrows emphasize the permanent sub-basin and mesoscale structures; dashed red/blue lines emphasize the seasonal summer/winter structures, respectively; red/blue arrows are superimposed on the black arrows when the structures are permanent but most intense in summer/winter, respectively. (**b**) Sub-basin and mesoscale structures are classified according to the mechanisms that drive them, wind forcing (orange arrows), the interaction between currents and topographical forcings (light green arrows), and large-scale internal processes (light purple arrows).

The basin scale circulation is essentially oriented according to the wind stress direction (northwest–southeast; Figure 2a,c and Figure 17). Most of the exclusively main sub-basin scale current systems and mesoscale structures are permanent but affected by a strong seasonal variability (Figure 17a). Only the TSC and the PV show a seasonal incidence and occur in summer and winter, respectively. The BTC, ATC, BATC, and ALC show a winter intensification (Figure 17a) concurrent with the intensification of the wind stress (Figures 3 and 4). For this reason, they are classified as wind-driven features in Figure 17b. The relationship between the sub-basin scale structures and the wind stress variability was already suggested by References [13,31]. Other sub-basin scale and mesoscale structures, e.g., the meandering AIS, the SG, and the MCC, are stronger in summer, when the wind stress is weaker. Hence, we exclude the direct impact of the wind on the variability of these structures. Rather, we suggest that they are influenced by other forcings, such as the instability of the surface currents and/or their interaction with the complex and relative shallow bottom topography (Figure 17b), characterized by continental shelves and channels.

The MG and SMA are located in a highly dynamic region (high level of Eddy Kinetic Energy, see Figure 6 of Reference [24] and Figure 9a of Reference [11]) characterized by the split of the ATC, whose eastward branch forms the BATC, and by a sudden reduction of depth (Figure 1a). These factors probably interact in facilitating the eddies formation and retention. From these considerations, the MG and SMA are influenced by the surface current dynamics and/or topography (Figure 17b). They are stronger in winter because the sub-basin currents, involved in their formation (ATC and BATC), are most intense and energetic in this season (Figure 17a).

The ABV, the MRV, and the ISV are located along the southern and the eastern coast of Sicily where the wind stress curl is steadily cyclonic (Figures 2d and 4c,d). Their strength and their interannual variability are influenced by the temporal evolution of the wind stress amplitude and vorticity (Figures 15 and 17b).

The SMG is located on the margins of the African shelf break (Figures 1a and 2a,b) and its vertical extension affects the entire water column (maximum depth of 400 m), as documented by float WMO 1900629 (Figure 13). The wind stress is weak and dimly cyclonic in this region (Figure 2 lower panels). Therefore, we define the SMG in Figure 17b as strongly influenced by the interaction between the surface currents and the topography.

The mesoscale structures located in regions where the influence of the wind stress is lower can be forced by the large-scale internal variability of the ocean. An example of this interaction is the SISV, whose interannual variability is connected to the decadal variability of the surface circulation in the northern Ionian (Figure 15a). However, the most representative example of the influence of internal forcing on the variability of a mesoscale structure is the NSA. This anticyclone, although located in the southern Tyrrhenian Sea, is affected by the decadal variability induced by the adjacent Ionian Sea (Figure 6). This result, as suggested by Reference [27], opens to a new interpretation of the link between different Mediterranean sub-basins and underlines the importance of internal processes on the variability of the mesoscale structures.

In summary, the surface circulation in the SC and southern Tyrrhenian Sea is characterized by multi-scale spatial and temporal variability. The main spatial scales involved are the basin, sub-basin, and mesoscale. The main temporal scales involved are the seasonal, interannual, and decadal scales. In this work, the complexity of the SC current system was investigated by combining different in-situ data and satellite products. Results provide an updated picture of the surface circulation, detecting new mesoscale features and describing their temporal variability and strength in relation to the main external and/or internal forcings. The winter strengthening of the wind stress directly influences most of the structures stronger in this season. The structures stronger in summer and/or located in high dynamical regions are mainly driven by the instability of the surface current and/or by their interaction with the bottom topography. In the regions where the influence of the external forcings is weaker, the large-scale internal variability of the adjacent Mediterranean basins can influence the local dynamics.

Author Contributions: Writing—original draft preparation, M.M.; writing—review and editing, P.-M.P., D.C., A.D. (Andrea Doglioli), G.N., and R.G.; investigation, M.M. and P.-M.P.; data curation, M.M., G.N., R.G., D.C., and M.-H.R.; formal analysis, M.M., G.N., and R.G.; resources, D.C., M.-H.R., A.G., and R.S.; funding acquisition, P.-M.P. and A.D. (Aldo Drago).

Funding: This research was mainly funded by the Italian Ministry of Education, University and Research as part of the Argo-Italy program, and partly funded by the Italia-Malta Programme—Cohesion Policy 2007–2013, European Union Regional Development Funds (ERDF) through the CALYPSO and CALYPSO FO projects. The program MISTRALS of CNRS funded the drifters deployed during the PEACETIME cruise (Guieu C., Desboeufs K., 2017, RV Pourquoi pas? https://doi.org/10.17600/17000300).

Acknowledgments: The authors would like to thanks all the people who have deployed drifters and made their data available in the Mediterranean Sea in the period 1993–2018. We acknowledge Antonio Bussani for his technical support and his work in the production of the Mediterranean drifter dataset, and Elena Mauri for her constructive comments. We thank the two anonymous reviewers for their constructive comments on the manuscript.

Conflicts of Interest: The authors declare no conflict of interest.

References

1. Sorgente, R.; Olita, A.; Oddo, P.; Fazioli, L.; Ribotti, A. Numerical simulation and decomposition of kinetic energy in the Central Mediterranean: insight on mesoscale circulation and energy conversion. *Ocean. Sci.* **2011**, *7*, 503–519. [CrossRef]
2. Schroeder, K.; Chiggiato, J.; Josey, S.A.; Borghini, M.; Aracri, S.; Sparnocchia, S. Rapid response to climate change in marginal sea. *Sci. Rep.* **2017**, *7*, 4065. [CrossRef] [PubMed]
3. Jouini, M.; Béranger, K.; Arsouze, T.J.; Beuvier, S.; Thiria, M.; Crepon, I.; Taupier-Letage, I. The Sicily Channel surface circulation revisited using a neural clustering analysis of a high-resolution simulation. *J. Geophys. Res. Ocean.* **2016**, *121*, 4545–4567. [CrossRef]
4. Ferron, B.; Bouruet Aubertot, P.; Cuypers, Y.; Schroeder, K.; Borghini, M. How important are diapycnal mixing and geothermal heating for the deep circulation of the Western Mediterranean? *Geophys. Res. Lett.* **2017**, *44*, 7845–7854. [CrossRef]
5. Vladoui, A.; Bouruet-Aubertot, P.; Cuypers, Y.; Ferron, B.; Schroeder, K.; Borghini, M.; Leizour, S.; Ben Ismail, S. Turbulence in the Sicily Channel from microstructure measurements. *Deep Sea Res. Part I Oceanogr. Res. Pap.* **2018**, *137*, 97–122. [CrossRef]
6. Millot, C.; Taupier-Letage, I. Circulation in the Mediterranean Sea. *Handb. Environ. Chem.* **2005**, *5*, 29–66.
7. Lermusiaux, P.F.J.; Robinson, A.R. Features of dominant mesoscale variability, circulation patterns and dynamics in the Strait of Sicily. *Deep Sea Res. Part I Oceanogr. Res. Pap.* **2001**, *48*, 1953–1997. [CrossRef]
8. Béranger, K.; Mortier, L.; Gasparini, G.-P.; Gervasio, L.; Astraldi, M.; Crepon, M. The dynamics of the Sicily Strait: A comprehensive study from observations and models. *Deep Sea Res. Part II Top. Stud. Oceanogr.* **2004**, *51*, 411–440. [CrossRef]
9. Poulain, P.M.; Zambianchi, E. Surface circulation in the central Mediterranean Sea as deduced from Lagrangian drifters in the 1990s. *Cont. Shelf Res.* **2007**, *27*, 981–1001. [CrossRef]
10. Astraldi, M.; Balopoulos, S.; Candela, J.; Font, J.; Gacic, M.; Gasparini, G.P.; Manca, B.; Theocharis, A.; Tintoré, J. The role of straits and channels in understanding the characteristics of Mediterranean circulation. *Prog. Oceanogr.* **1999**, *44*, 65–108. [CrossRef]
11. Poulain, P.-M.; Menna, M.; Mauri, E. Surface geostrophic circulation of the Mediterranean Sea derived from drifter and satellite altimeter data. *J. Phys. Oceanogr.* **2012**, *42*, 973–990. [CrossRef]
12. Pinardi, N.; Zavatarelli, M.; Adani, M.; Coppini, G.; Fratianni, C.; Oddo, P.; Simoncelli, S.; Tonani, M.; Lyubartsev, V.; Dobricic, S.; et al. Mediterranean Sea large-scale low-frequency ocean variability and water mass formation rates from 1987 to 2007: a retrospective analysis. *Prog. Oceanogr.* **2015**, *132*, 318–332. [CrossRef]
13. Molcard, A.; Gervasio, L.; Griffa, A.; Gasparini, G.P.; Mortier, L.; Ozgokmen, T.M. Numerical investigation of the Sicily Channel dynamics: density currents and water mass advection. *J. Mar. Syst.* **2002**, *36*, 219–238. [CrossRef]
14. Amores, A.; Jordà, G.; Arsouze, T.; Le Sommer, J. Up to what extent can we characterize ocean eddies using present day gridded altimetric products? *J. Geophys. Res.Ocean.* **2018**, *123*. [CrossRef]
15. Ciani, D.; Rio, M.-H.; Menna, M.; Santoleri, R. A synergetic approach for the space-based sea surface currents retrieval in the Mediterranean Sea. *Remote Sens.* **2019**, *11*, 1285. [CrossRef]
16. Menna, M.; Gerin, R.; Bussani, A.; Poulain, P.-M. *The OGS Mediterranean Drifter Database: 1986–2016*; Technical report 2017/92 Sez. OCE 28 MAOS; OGS: Trieste, Italy, 2017.
17. Menna, M.; Poulain, P.-M.; Bussani, A.; Gerin, R. Detecting the drogue presence of SVP drifters from wind slippage in the Mediterranean Sea. *Measurement* **2018**, *125*, 447–453. [CrossRef]
18. Rio, M.H.; Pascual, A.; Poulain, P.-M.; Menna, M.; Barcelò, B.; Tintorè, J. Computation of a new mean dynamic topography for the Mediterranean Sea from model outputs, altimeter measurements and oceanographic in situ data. *Ocean. Sci.* **2014**, *10*, 731–744. [CrossRef]
19. Poulain, P.-M.; Barbanti, R.; Font, J.; Cruzado, A.; Millot, C.; Gertman, I.; Griffa, A.; Molcard, A.; Rupolo, V.; Le Bras, S.; et al. MedArgo: a drifting profiler program in the Mediterranean Sea. *Ocean. Sci.* **2007**, *3*, 379–395. [CrossRef]
20. Rio, M.H.; Santoleri, R. Improved global surface currents from the merging of altimetry and Sea Surface Temperature data. *Remote Sens. Environ.* **2018**, *216*, 770–785. [CrossRef]

21. Piterbarg, L.I. A simple method for computing velocities from tracer observations and a model output. *Appl. Mat. Model.* **2009**, *33*, 3693–3704. [CrossRef]
22. Atlas, R.; Hoffman, R.N.; Ardizzone, J.; Leidner, S.M.; Jusem, J.C.; Smith, D.K.; Gombos, D. A cross-calibrated, multiplatform ocean surface wind velocity product for meteorological and oceanographic applications. *Bull. Am. Meteorol. Soc.* **2011**, *92*, 157–174. [CrossRef]
23. Shabrang, L.; Menna, M.; Pizzi, C.; Lavigne, H.; Civitarese, G.; Gačić, M. Long-term variability of the southern Adriatic circulation in relation to North Atlantic Oscillation. *Ocean. Sci.* **2016**, *12*, 233–241. [CrossRef]
24. Menna, M.; Reyes Suarez, N.C.; Civitarese, G.; Gacic, M.; Poulain, P.-M.; Rubino, A. Decadal variations of circulation in the Central Mediterranean and its interactions with the mesoscale gyres. *Deep Sea Res. Part II: Top. Stud. Oceanogr.* **2019**, in press. [CrossRef]
25. Aulicino, G.; Cotroneo, Y.; Lacava, T.; Sileo, G.; Fusco, G.; Carlon, R.; Satriano, V.; Tramutoli, V.; Budillon, G. Results of the first wave glider experiment in the southern Tyrrhenian Sea. *Adv. Oceanogr. Limnol.* **2016**, *7*, 16–35. [CrossRef]
26. Ciappa, A.C. Surface circulation patterns in the Sicily Channel and Ionian Sea as revealed by MODIS chlorophyll images from 2003 to 2007. *Contin. Shelf Res.* **2009**, *29*, 2099–2109. [CrossRef]
27. Rubino, A.; Zanchettin, D.; Androsov, A.; Voltzinger, N.-E. Tidal record as liquid climate archives for large-scale interior Mediterranean variability. *Sci. Rep.* **2018**, *8*, 12586. [CrossRef]
28. Drago, A.; Ciraolo, G.; Capodici, F.; Cosoli, S.; Gacic, M.; Poulain, P.-M.; Tarasova, R.; Azzopardi, J.; Gauci, A.; Maltese, A.; et al. CALYPSO—An Operational Network of HF Radars for the Malta-Sicily Channel. In Proceedings of the Seventh International Conference on EuroGOOS, Lisbon, Portugal, 28–30 October 2014; Dahlin, H., Fleming, N.C., Petersson, S.E., Eds.; EuroGOOS Publication: Brussels, Belgium, 2015. No. 30. ISBN 978-91-974828-9-9.
29. Capodici, F.; Cosoli, S.; Ciracolo, G.; Nasello, C.; Maltese, A.; Poulain, P.-M.; Drago, A.; Azzopardi, J.; Gauci, A. Validation of HF radar sea surface currents in the Malta-Sicily Channel. *Remote Sens. Environ.* **2019**, *225*, 65–76. [CrossRef]
30. Reyes Suarez, N.C.; Cook, M.S.; Gačić, M.; Paduan, J.D.; Cardin, V. Estimation of sea surface circulation structures in the Malta-Sicily Channel from remote sensing data. *Water* **2019**. under review.
31. Pinardi, N.; Navarra, A. Baroclinic wind adjustment processes in the Mediterranean Sea. *Deep Sea Res. Part II Top. Stud. Oceanogr.* **1993**, *40*, 1299–1326. [CrossRef]

water

MDPI

Article

Deep Flow Variability Offshore South-West Svalbard (Fram Strait)

Manuel Bensi [1,*], Vedrana Kovačević [1], Leonardo Langone [2], Stefano Aliani [2], Laura Ursella [1], Ilona Goszczko [3], Thomas Soltwedel [4], Ragnheid Skogseth [5], Frank Nilsen [5], Davide Deponte [1], Paolo Mansutti [1], Roberto Laterza [1], Michele Rebesco [1], Leonardo Rui [1], Renata Giulia Lucchi [1], Anna Wåhlin [6], Angelo Viola [7], Agnieszka Beszczynska-Möller [3] and Angelo Rubino [8]

[1] OGS—National Institute of Oceanography and Applied Geophysics, 34010 Sgonico, Italy; vkovacevic@inogs.it (V.K.); lursella@inogs.it (L.U.); ddeponte@inogs.it (D.D.); pmansutti@inogs.it (P.M.); rlaterza@inogs.it (R.L.); mrebesco@inogs.it (M.R.); lrui@inogs.it (L.R.); rlucchi@inogs.it (R.G.L.)

[2] CNR–ISMAR—Italian National Research Council, Institute of Marine Sciences, 30122 Venice, Italy; leonardo.langone@bo.ismar.cnr.it (L.L.); stefano.aliani@sp.ismar.cnr.it (S.A.)

[3] IOPAN—Institute of Oceanology Polish Academy of Sciences, 81-712 Sopot, Poland; ilona_g@iopan.gda.pl (I.G.); abesz@iopan.gda.pl (A.B.-M.)

[4] AWI—Alfred Wegener Institute, Helmholtz-Center for Polar and Marine Research, 27570 Bremerhaven, Germany; thomas.soltwedel@awi.de

[5] Arctic Geophysics Department, UNIS—The University Centre in Svalbard, P.O. Box 156, N-9171 Longyearbyen, Norway; Ragnheid.Skogseth@unis.no (R.S.); Frank.Nilsen@unis.no (F.N.)

[6] Department of Marine Sciences, UGOT–University of Gothenburg, 100, SE-405 30 Gothenburg, Sweden; anna.wahlin@marine.gu.se

[7] CNR–ISAC—Italian National Research Council, Institute of Atmospheric Sciences and Climate, Bologna, I-40129, Italy; angelo.viola@artov.isac.cnr.it

[8] Department of Environmental Sciences, Informatics and Statistics, DAIS—University Ca' Foscari of Venice, 30172 Mestre, Italy; rubino@unive.it

* Correspondence: mbensi@inogs.it; Tel.: +39-040-2140431

Received: 22 February 2019; Accepted: 29 March 2019; Published: 2 April 2019

Abstract: Water mass generation and mixing in the eastern Fram Strait are strongly influenced by the interaction between Atlantic and Arctic waters and by the local atmospheric forcing, which produce dense water that substantially contributes to maintaining the global thermohaline circulation. The West Spitsbergen margin is an ideal area to study such processes. Hence, in order to investigate the deep flow variability on short-term, seasonal, and multiannual timescales, two moorings were deployed at ~1040 m depth on the southwest Spitsbergen continental slope. We present and discuss time series data collected between June 2014 and June 2016. They reveal thermohaline and current fluctuations that were largest from October to April, when the deep layer, typically occupied by Norwegian Sea Deep Water, was perturbed by sporadic intrusions of warmer, saltier, and less dense water. Surprisingly, the observed anomalies occurred quasi-simultaneously at both sites, despite their distance (~170 km). We argue that these anomalies may arise mainly by the effect of topographically trapped waves excited and modulated by atmospheric forcing. Propagation of internal waves causes a change in the vertical distribution of the Atlantic water, which can reach deep layers. During such events, strong currents typically precede thermohaline variations without significant changes in turbidity. However, turbidity increases during April–June in concomitance with enhanced downslope currents. Since prolonged injections of warm water within the deep layer could lead to a progressive reduction of the density of the abyssal water moving toward the Arctic Ocean, understanding the interplay between shelf, slope, and deep waters along the west Spitsbergen margin could be crucial for making projections on future changes in the global thermohaline circulation.

Keywords: Fram Strait; deep sea thermohaline variability; slope currents; wind-induced processes; shelf-slope dynamics

1. Introduction

Water masses in the eastern Fram Strait, strongly influenced by the interaction between Atlantic and Arctic waters and by local atmospheric forcing, substantially contribute to drive the global thermohaline circulation [1–4]. There is a remarkable variability in the system due to several forcing mechanisms (e.g., atmospheric, internal, tidal, shelf dynamics) that play an important role, especially in the upper layer [5–10]. On the contrary, it is not completely clear which processes are responsible for the inter-annual and seasonal deep flow variability in the western offshore Spitsbergen region [11,12]. Several studies, using both experimental and numerical modelling approaches, have addressed the role of interactions between Atlantic Water (AW) carried by the West Spitsbergen Current (WSC, [10,11,13–16]), and shelf and fjord waters [2,17–20] in the observed variability. Some of the processes that may be relevant for deep water circulation and variability in the western Spitsbergen region have been summarized in Figure 1.

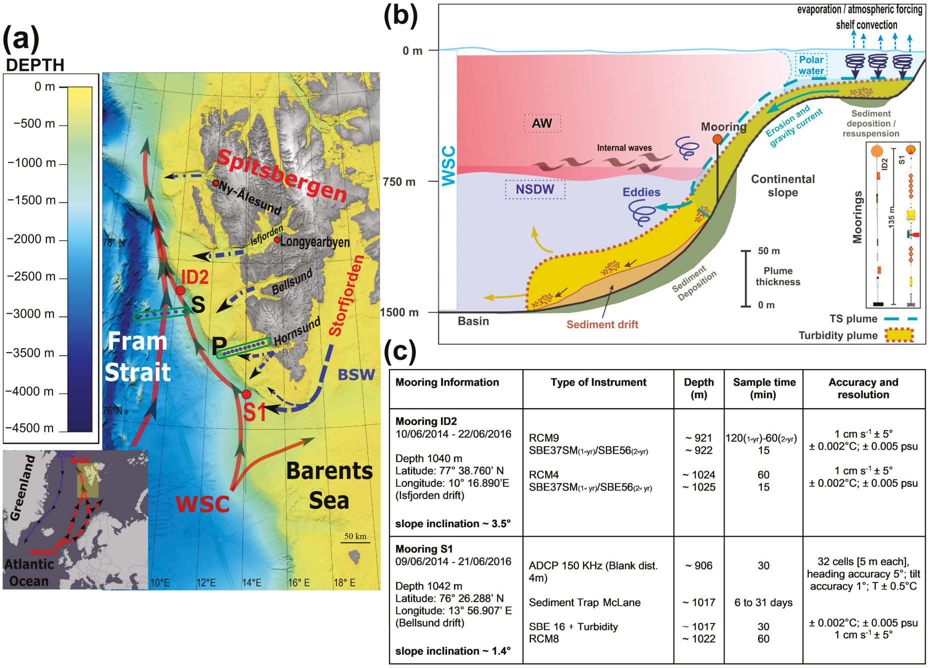

Mooring Information	Type of Instrument	Depth (m)	Sample time (min)	Accuracy and resolution
Mooring ID2 10/06/2014 - 22/06/2016 Depth 1040 m Latitude: 77° 38.760′ N Longitude: 10° 16.890′E (Isfjorden drift) **slope inclination ~ 3.5°**	RCM9 SBE37SM$_{(1^{st}yr)}$/SBE56$_{(2^{nd}yr)}$ RCM4 SBE37SM$_{(1^{st}\,yr)}$/SBE56$_{(2^{nd}\,yr)}$	~ 921 ~ 922 ~ 1024 ~ 1025	120$_{(1^{st}yr)}$-60$_{(2^{nd}yr)}$ 15 60 15	1 cm s^{-1} ± 5° ± 0.002°C; ± 0.005 psu 1 cm s^{-1} ± 5° ± 0.002°C; ± 0.005 psu
Mooring S1 09/06/2014 - 21/06/2016 Depth 1042 m Latitude: 76° 26.288′ N Longitude: 13° 56.907′ E (Bellsund drift) **slope inclination ~ 1.4°**	ADCP 150 KHz (Blank dist. 4m) Sediment Trap McLane SBE 16 + Turbidity RCM8	~ 906 ~ 1017 ~ 1017 ~ 1022	30 6 to 31 days 30 60	32 cells [5 m each], heading accuracy 5°; tilt accuracy 1°; T ± 0.5°C ± 0.002°C; ± 0.005 psu 1 cm s^{-1} ± 5°

Figure 1. (**a**) Map of the study region showing bathymetry and main currents in the Fram Strait and along the west Spitsbergen margin. Red dots indicate the location of moorings S1 and ID2. Blue dots indicate CTD (conductivity-temperature-depth) stations along transects S and P. (**b**) Schematic of the shelf-slope dynamics along the west Spitsbergen slope (figure modified from [6], © American Meteorological Society. Used with permission). (**c**) S1 and ID2 moorings configuration and specification of instruments. (AW = Atlantic Water; NSDW = Norwegian Sea Deep Water; WSC = West Spitsbergen Current; BSW = Brine-enriched Shelf Water; EGC = East Greenland Current; NwAC = Norwegian Atlantic Current).

With this study, we aim at exploring signals observed in time series of temperature, salinity, current velocity, and turbidity, acquired by two near-bottom moorings (S1, ID2; Figure 1) deployed to assess the deep flow variability on short-term, seasonal, and multi-annual time scales in the southwest region offshore the Spitsbergen margin [12]. We also discuss potential links between the local oceanographic and atmospheric forcing in regulating shelf/deep sea interactions, which in turn can trigger baroclinic (internal) waves that stimulate internal mixing in the ocean (Figure 1b). Finally, we put the observed variability in the context of larger-scale circulation changes.

The overall circulation in the eastern Fram Strait (Figure 1) includes the northward flow of the WSC, i.e., the northernmost extension of the Norwegian Atlantic Current [21,22]. Flowing at a steady pace of about 0.25 m s^{-1}, following the 1000-m isobath [23], the WSC transports warm and saline AW into the central Arctic Ocean and, beneath it, colder and fresher Norwegian Sea Deep Water (NSDW, [15,24]) that occupies the deep local layer (Figure 1b). The NSDW is influenced by water contributions from the Greenland Sea (south of Fram Strait) and Eurasian Basin (north of Fram Strait, [15,24]).

Shoreward of the WSC, the Spitsbergen continental shelf is influenced by Arctic waters as well as by drifting sea ice [19]. The northward WSC is compensated by the southward East Greenland Current, which transports cold and fresh Polar Water across the western part of the Fram Strait. The WSC is topographically steered along the continental slope [2,25] with streamlines parallel to contours of constant f/H (Coriolis parameter/water column thickness). It has been traditionally considered as a barotropic flow [13,21]. However, more recent studies have outlined its baroclinic component, together with associated instabilities and eddy formations [14,26]. The AW occupies a large portion of the water column within the WSC (roughly between the surface and 600 m depth; [10]) and its properties undergo a strong interannual variability [27].

Relatively warm and cold periods of AW have been alternating in the last century: cold periods took place during 1900–1920 and 1955–1985, while a warm period occurred in the 1930s–1940s [27]. More recently, two warm AW anomalies passing through the Fram Strait occurred in 1999–2000 and 2005–2007 [22]. Temperature increase (0.06 °C $year^{-1}$, [22]) was accompanied by salinity increase (0.003 $year^{-1}$, [28]). However, based on monthly gridded fields of the meridional current component, no significant trend in the volume transport of AW was observed [22]. A warming of the Arctic Ocean, recorded since 1985 [27,29] became particularly evident in the WSC core after 2004, along with an intensification of the northward propagation of the AW warm signal [30]. Concomitantly with this evolution, the AW influence on temperature and salinity on the West Spitsbergen Shelf and in fjords of the Archipelago (e.g., Hornsund and Kongsfjorden, [20,31]) has become stronger in the last years, probably due to changes in the patterns of the dominating large atmospheric pressure fields [2]. It is not entirely clear to what extent the increased heat transport toward the Arctic is related to a strengthening of the Atlantic Meridional Overturning Circulation [32], to an increase in temperature or in volume of the AW [4,33], or, instead, to the variability of the AW transport along the two preferential pathways (Barents Sea and Fram Strait branches, [33]). Notably, the AW heat transport [29,34] can affect air temperature especially during winter [35], which in turn has direct effects on the dense water formation around the Spitsbergen margin.

In the west Spitsbergen region ocean-atmosphere interactions lead to multiple oceanographic processes, like shelf-slope dynamics, deep water variability through Polar and Atlantic waters interaction, as well as sea ice and dense water formation [1–3,7]. Dense water formation off the southwestern tip of Spitsbergen and in the Fram Strait depends on the rate of cooling (heat loss to the atmosphere) and homogenisation of the upper layers (i.e., water column stratification and mixing depth), sea ice growth, and brine rejection. Brine-enriched Shelf Waters (BSWs) are formed during ice formation in coastal polynyas [36–40]. Within fjords, and in particular in Storfjorden (the largest fjord in the Svalbard Archipelago, see Figure 1a) the accumulated water close to the freezing point has salinity ranging typically between 34.8 and 35.8 [38]. A 120 m deep sill separates this fjord from the shelf edge, and dense water overspills the fjord with strong inter-annual variability [38]. Eventually, it flows northwards along the shelf and the continental slope west of Spitsbergen, at depths where water of similar density is transported by the WSC [41,42]. Numerical models [17,42] simulated the evolution in time and space of the plume in this region, revealing that it can reach velocities as high as 0.6 m s^{-1} over the continental slope.

Dense water spreading is also strongly influenced by tidally induced dispersion [8,9] and by bathymetric constraints [43]. Tides can drive barotropic and baroclinic water exchanges [44], and also generate shelf waves, which propagate as topographically trapped internal waves [13,45] stimulating mixing in the ocean interior. Inall et al. [44] reported about coastal trapped waves in Kongsfjorden, a western Spitsbergen fjord at latitudes (79° N) where the internal Rossby radius is small and the effects of trapped waves become more evident. Increased bottom shear velocities caused by the interaction of semidiurnal internal tides with the sloping bottom can cause sediment resuspension and prevent deposition, shaping thus the continental slope [46]. Topographically induced intrusions are also responsible for the generation of nepheloid layers (i.e., turbid layers with significant amounts of suspended sediment) transported along isopycnals [16,47]. Numerical models support geological observations showing that suspended sediment transported by bottom-arrested gravity plumes may have a role in the slope convection, by increasing the kinetic energy and the bulk density of the water (Figure 1b, [5,6]). Along their routes toward the abyss, offshore southwestern Svalbard, temperature of water plumes increases, while salinity decreases rather slowly due to entrainment of surrounding warm, but relatively saline AW [41,42,48,49]. The mixing and entrainment of these plumes with AW can reduce the maximum reached depth during their cascading [10,17,41,48]. According to Akimova et al. [48], BSW plumes leaving Storfjorden reached the bottom of the Fram Strait only three times, in 1986, 1988, and 2002, over a period from 1984 to 2003. Eddies can also break away from density-driven currents, as demonstrated in laboratory experiments and numerical models [42,50]. Intruding dense water can generate cyclones in the water above and anticyclones in the water below the depth of intrusion [43].

2. Data and Methods

2.1. Oceanographic Moorings

Various instruments attached to two oceanographic moorings (S1, ID2; Figure 1) collected data within a ~150 m thick near-bottom layer along the west Spitsbergen continental slope from June 2014 until June 2016. The payload of mooring S1 included a downward looking ADCP (Acoustic Doppler Current Profiler, Teledyne RD Instruments, Poway, CA, USA) RDI 150 kHz located ~140 m above the sea bottom, a CTD (Conductivity-Temperature-Depth) SBE16 (Sea-Bird Electronics, Bellevue, WA, USA) with Seapoint turbidity meter (Seapoint Sensors, Inc., Exeter, NH, USA) coupled with a sediment trap McLane (PARFLUX Mark 78H-21, McLane Res. Labs, East Falmouth, MA, USA) ~25 m above the sea bottom, and a single point Aanderaa current meter (Aanderaa Data Instruments, Bergen, Norway) RCM8 ~20 m above the sea bottom. Turbidity expressed as Formazin Turbidity Unit (FTU) was calibrated in the laboratory to obtain the corresponding values of suspended sediment concentration (mg L^{-1}). Mooring ID2 was equipped with two Aanderaa current meters (RCM9 and RCM4, ~120 m and ~20 m above the sea bottom, respectively) and two CT SBE37-MicroCAT recorders below each current meter (substituted with T loggers SBE56 in June 2015). A complete scheme of each mooring line (position, bottom depth, instrument type, deployment depth, and sampling time interval) is presented in Figure 1c.

The recorded data were post-processed after each recovery (June 2015, June 2016). Data with different sampling frequencies (15 min, 30 min, or 120 min) were averaged or interpolated to obtain homogenous hourly time series. Temperature, salinity, and turbidity data have been cleaned and despiked according to MyOcean in situ quality control standards and methodology (http://catalogue.myocean.eu.org/static/resources/user_manual/myocean/QUID_INSITU_TS_OBSERVATIONS-v1.0.pdf). Moreover, temperature and salinity time series were checked by comparing them with data from CTD casts performed before and after each mooring deployment. Potential temperature (θ), salinity (S), and potential density anomaly (σ_θ) were calculated from in situ data. Note that only in situ temperature was recorded at ID2 between June 2015 and 2016, when thermistors (without conductivity sensors) were used, hence it was not possible to obtain θ, S, and σ_θ.

Each vertical cell of the ADCP was treated as an individual time series. Current vectors, both from ADCP and RCMs, were decomposed into u (eastward, zonal), v (northward, meridional), and w (vertical) components. Tidal constituents, obtained from harmonic analysis with a signal-to-noise ratio > 1, were subtracted from the original time series, to provide de-tided data [51]. For specific analyses, a low-pass filter with a cut-off period of 33 h was applied to the de-tided time series to remove inertial oscillations and obtain sub-inertial non-tidal flow (i.e., sub-tidal). The principal component analysis was applied to the time series to determine the direction of the major variance of the deep currents. As this direction almost coincided with the along-slope component, the coordinate system was rotated accordingly. The angles of rotation in the trigonometric system were between −34° and −52° at S1, and between −40° and −48° at ID2. By rotating the reference system two new components for the velocity, i.e., *ur* (along-slope) positive towards SE, and *vr* (cross-slope) positive towards NE, were obtained.

Correlation and cross-correlation coefficients calculated between different variables, and reported further in the text, are always within the significance level of 0.05, unless otherwise specified.

2.2. Oceanographic Surveys

CTD measurements during oceanographic cruises provided vertical profiles of temperature (T) and conductivity (C) approaching the seabed within ~ 7–10 m. θ, S, and σ_θ were calculated from in situ data using MATLAB toolbox TEOS-10 (Gibbs SeaWater Oceanographic Toolbox) including thermodynamic equations of seawater (http://www.teos-10.org/software.htm). Oxygen concentrations were measured using a SBE43 sensor mounted on the CTD/Rosette Water Sampler while taking water samples at discrete depths for Winkler titrations [52]. Data were quality checked and averaged every 1 dbar with overall accuracies within ± 0.002 °C for T, ± 0.005 for S, and 2% of saturation for oxygen. Turbidity in the water column was detected by optical sensors mounted on the CTD probe.

CTD data used in this study come from the PREPARED cruise (r/v G.O. Sars, June 2014, PREsent and PAst flow REgime on contourite Drifts west of Spitsbergen), HH cruise (r/v Helmer Hanssen, June 2015), PS99.1 cruise (I/B Polastern, June 2016), and from oceanographic cruises carried out by the University Centre of Svalbard (UNIS) between 2014 and 2016 along section P (Figure 1). Long-term (1997–2017) yearly variability and linear trends were calculated from hydrographic data collected during AREX cruises carried out by the Institute of Oceanology Polish Academy of Sciences (IOPAN, [28]). In our study, we consider data collected along section S (~ 77°30′ N, see Figure 1) in the proximity of mooring ID2, from which we calculated the yearly values of θ, S, and σ_θ averaged in the upper-intermediate (100–800 m depth) and in the deep layers (>800 m depth). Trends have been calculated using a linear regression model (Table 1). Standard error (SE) and Root Mean Squared Error (RMSE) for each statistically significant ($p < 0.05$) trend are also reported in Table 1. In order to focus on the variability of the AW in the upper layer, we only take into consideration CTD measurements that have temperatures compatible with those of the AW (i.e., $\theta > 2°$) in addition to the depth criterion [22]. Furthermore, we use the thickness of the AW layer as the weight while calculating the average θ, S, and σ_θ values. Some figures presented in this paper were elaborated using the Ocean Data View software [53].

Table 1. Linear trends of θ, S and σ_θ in the intermediate (100–800 m) and deep (>800 m) layers from CTD casts collected along section S (see Figure 1 and Figure 3). Data cover the period from 1997 until 2017. Significant linear trends ($p < 0.05$) are reported in red.

	Metrics	Layer 100–800 m and $\theta > 2$ °C Criterion	Layer > 800 m	Layer > 800 m Sub-Period 2009–17
θ	Trend (°C)/year ± SE	0.0314 ± 0.0121	0.009 ± 0.0016	0.0222 ± 0.0033
	RMSE	0.3362	0.0445	0.0254
	p-value	0.01779	0.00002	0.00026
S	Trend /year ± SE	0.0042 ± 0.0007	0.0005 ± 0.0001	0.0007 ± 0.0002
	RMSE	0.0202	0.0035	0.0013
	p-value	0.00001	0.00083	0.00399
σ_θ	Trend (kg m^{-3})/year ± SE	0.0004 ± 0.0010	0 ± 0.0001	−0.0004 ± 0.0001
	RMSE	0.0272	0.0036	0.001
	p-value	0.69369	0.89612	0.01304

2.3. Atmospheric Data

To study atmosphere-ocean interactions between 2014 and 2016 we employed ERA-Interim dataset from the ECMWF (European Center for Medium-Range Weather Forecasts interim reanalysis) regularly spaced at 0.75° (interpolated at 0.25°) of latitude and longitude and available at 6 h time intervals. We initially compared the ECMWF output (e.g., wind speed/direction, air temperature) with data collected at the Amundsen-Nobile Climate Change Tower (CCT, see http://www.isac.cnr.it/~{}radiclim/CCTower/) in Ny-Ålesund. The 34 m high tower is equipped with a large set of instruments along the vertical to investigate physical properties of the atmospheric boundary layer over a long period and to study the turbulent exchange processes of energy and mass at the atmosphere-land interface. The comparison between land observations of wind speed and direction and ECMWF data revealed that both short-term and seasonal variabilities recorded at the CCT are reproduced coherently at S1 and ID2 locations (not shown). Hence, six meteorological parameters were selected from ECMWF dataset to characterize the air-sea interface: air pressure at sea-level, total cloud cover, 10 m zonal (u) and meridional (v) wind components, 2 m air and dew point temperatures, and sea surface skin temperature. The total heat flux (daily and monthly mean values) at the air-sea interface was computed taking into account four heat flux components also downloaded from ECMWF dataset: solar radiation, net longwave radiation, latent and sensible heat. The heat loss and the relative sea water temperature variation occurring during winter months were estimated using the methodological approach described in [54]. To analyse the periodicity and recurrence of intensive events, a Morlet wavelet analysis [55] was applied on the horizontal principal components both of the ECMWF wind data and of the current velocity at moorings S1 and ID2. The obtained results enabled studying non-stationary signals and investigating the dynamic response of the marine currents to the atmospheric forcing.

3. Results

3.1. Thermohaline Patterns on the West Spitsbergen Margin during Oceanographic Cruises between 2014 and 2016

Vertical distribution of hydrographic data along the zonal section P (Figure 1) on the West Spitsbergen Shelf north of Hornsund is shown in Figure 2. It refers to data collected in April 2014, June 2014, May 2015, and August 2016. Thermohaline properties on the shelf, usually occupied by Arctic Water [2,56], show a large seasonal and interannual variability. They depend on the variability of waters transported by the coastal current itself, on the seasonal variability in the contribution of fresh water from the main fjords, and on the variability of the AW inflow from offshore, whose properties and extension vary with large-scale circulation patterns in the area.

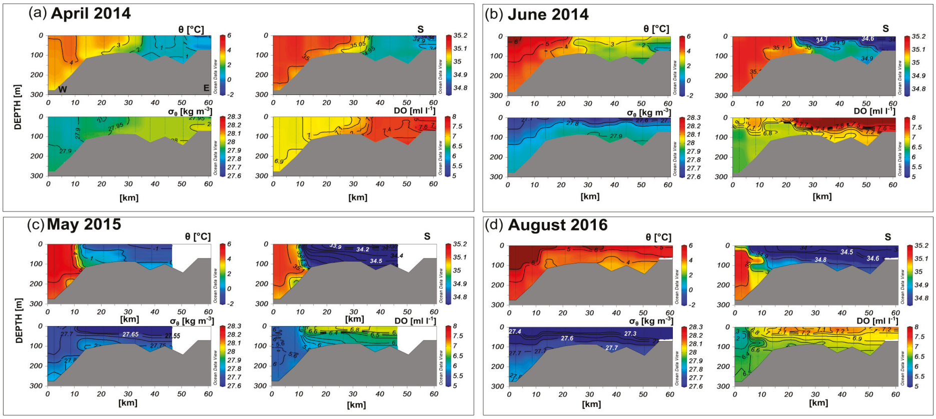

Figure 2. θ (°C), S, σ_θ (kg m^{-3}), DO (mL L^{-1}), along the W–E section P (see Figure 1) in April 2014 (**a**), June 2014 (**b**), May 2015 (**c**), and August 2016 (**d**) on the West Spitsbergen Shelf area. The data are from the PREPARED cruise and from several UNIS cruises.

In April 2014 (Figure 2a), the westernmost part of the section was occupied by warm and saline AW (3°C < θ < 4°C and S > 34.9), while its easternmost part was filled by cool and fresh water (θ < 1 °C and S < 34.9). AW could also be detected by its lower oxygen content with respect to Arctic Water. In June 2014 (Figure 2b), during the PREPARED cruise, a cold and fresh waterfront extended offshore. At that time, the westernmost part of the shelf was occupied by AW. The latter was also present on the continental slope, roughly down to 800 m depth, above the NSDW in the deep layer (>800 m, not shown). At depths between 100 m and 800 m, where AW was present, values of θ ~ 0–4.5°C, S ~ 34.95–35.1, σ_θ ~ 27.85–28.05 kg m^{-3}, and dissolved oxygen (DO) ~ 6.4–6.6 mL L^{-1} were found, while at depths larger than 800 m θ was below 0 °C, S ~ 34.91, σ_θ ~ 28.05–28.08 kg m^{-3}, and DO ~ 6.2–6.4 mL L^{-1}. Light transmission (not shown) decreased when approaching the seabed, revealing high suspended matter concentrations in the bottom layer of the shelf and continental slope. In May 2015, AW retreated offshore (Figure 2c) like in August 2016 (Figure 2d) when, however, θ was everywhere larger than 3 °C and S values were relatively low (<34.85) in the shallow part of the section. In August 2016, the AW was confined in the western part of the section and it was characterized by the highest θ and S values (θ > 6 °C and S > 35.15). Overall, a large variability characterizes the temporal and spatial evolution of the observed parameters along the section [2]. In some cases sharp thermal and saline fronts tend to compensate, and no density structure was found (Figure 2b,c).

3.2. *Multiannual Variability of the Thermohaline Properties along the West Spitsbergen Margin*

CTD casts carried out during annual IOPAN summer cruises aboard the r/v Oceania between 1997 and 2017 help to understand the interannual variability of the thermohaline properties of the along-slope flow (i.e., WSC). Data collected yearly along section S (Figure 1) at latitude ~ 77°30′ N, close to the ID2 mooring, were spatially averaged within two layers: the upper-intermediate layer, between 100 and 800 m, where the AW is detected by the additional θ > 2 °C criterion, and the deep layer (>800 m), mainly occupied by NSDW (Figure 3). Linear trends were calculated for each of the three variables, θ, S and σ_θ (Table 1). They revealed long-term positive trends of θ and S in the upper layer, while no significant trend was found in the σ_θ (Figure 3). However, the upper layer went through relatively warm and saline periods (i.e., 2005–06 and 2011–12) as well as cold and fresher periods (i.e., 2003–04, 2008, and 2013). Noteworthy, starting from 2013 an overall θ increase was not accompanied by S increase. In the deep layer, slightly positive long-term trends in θ and S were also found, and they became more evident between 2009 and 2017, when also a small but significant trend in σ_θ decrease was detected. Years characterized by higher standard deviations for S in the deep layer (i.e., 2000, 2002, 2006, 2008) may indicate the occurrence of advection/intrusion phenomena of different water masses into the layer. No significant correlations ($p < 0.05$) were obtained by comparing detrended time series between the upper and deep layers for each parameter. Observed trends are in agreement with results published by, e.g., Chatterjee et al. [57], where authors point out how changes in the AW properties depend on the strength of the subpolar gyre in the North Atlantic, which in turn is strongly influenced by the wind stress curl. The analysis of the multi-annual variability of the average thermohaline properties gives a general framework in which we undertake a more detailed deep flow variability analysis (including high-frequency signals) presented in the following section. The trends exposed here also provide an indication that the abyssal layer west of Svalbard is slowly becoming warmer and saltier on long temporal scale.

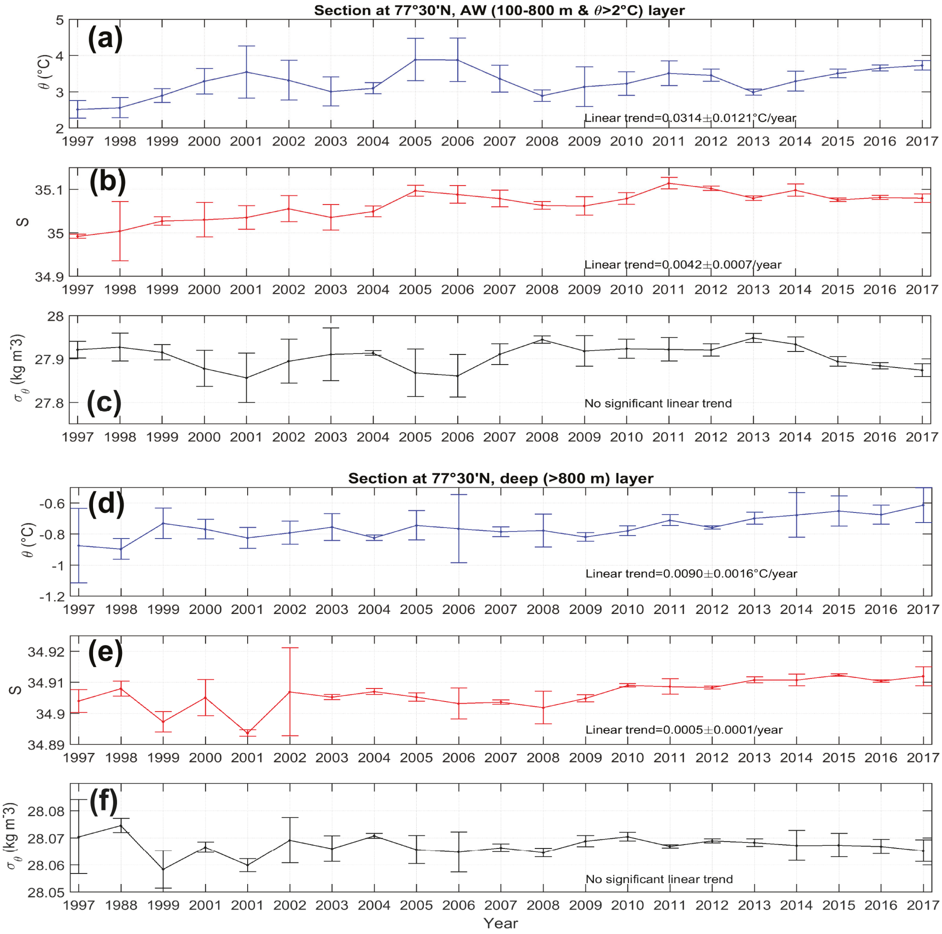

Figure 3. Weighted average of thermohaline properties (θ, S, σ_θ) calculated from CTD stations along the section S at ~ 77°30′ N (between 8 and 10°30′ E, see Figure 1): upper layer (**a**–**c**) (100–800 m with θ > 2 °C) and deep layer (**d**–**f**) (>800 m). Weights are defined by the layer thickness at each station where bottom depth varied between 1000 and 2300 m. Data are from the hydrographic measurements carried out during summer AREX cruises aboard r/v OCEANIA (IOPAN).

3.3. Temporal Variability in Oceanographic Parameters at Moorings S1 and ID2

Time series data recorded at moorings S1 and ID2, at depths >900 m, highlighted the presence of water with properties ($\theta \sim -0.90$ °C, $S \sim 34.91$, and $\sigma_\theta \sim 28.07$ kg m^{-3}) typical of the NSDW [46]. However, perturbations caused by occasional "thermohaline intrusions" of water, which is warmer (up to ~2 °C), saltier (up to ~35), and less dense (down to 27.98 kg m^{-3}), are evident in Figures 4 and 5. Noteworthy, temporal fluctuations of θ, S, and σ_θ were particularly apparent between October and April and occurred almost simultaneously at both moorings, ~170 km apart from each other (see Figure 1a). A larger variability was recorded during winter 2014–15 at both sites. The duration of the observed intrusions of relatively warm and salty water varied from a few hours to several days (up to 10–15 days), during which thermohaline variations oscillated mainly at a diurnal (24 h) frequency.

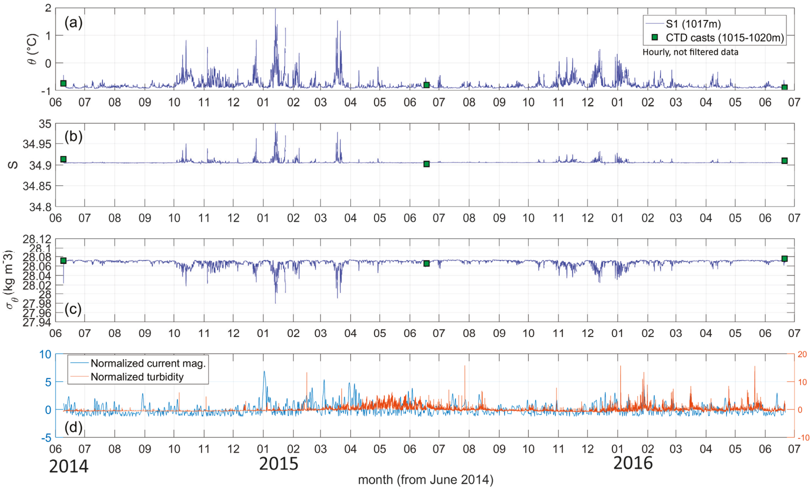

Figure 4. Time series (hourly data) of θ (**a**), S (**b**), and σ_θ (**c**) at S1 (1017 m depth). Green squares show data extracted from CTD casts (θ and S) at depths close to the moored instrument. Panel (**d**) shows normalized values of current magnitude (1022 m) and turbidity (1017 m). Data span from June 2014 to June 2016.

The normalized time series of current magnitude and turbidity at S1 are shown in Figure 4d (normalization was obtained by subtracting the average of each deployment phase and dividing by the corresponding standard deviation). Turbidity peaks were observed generally from December to July. During the first year of measurements, high turbidity values were found around mid-May 2015, while in 2016 several episodes characterized by high turbidity were observed almost each month (Figure 4d).

Overall, data recorded at mooring ID2 show a larger variance with respect to S1 data, except for θ at 1025 m depth (Figure 5). During the first year of measurements, events associated with temperature increase occurred mainly between October and April (Figure 5), while during the second year they were limited to the period October–February (Figure 6).

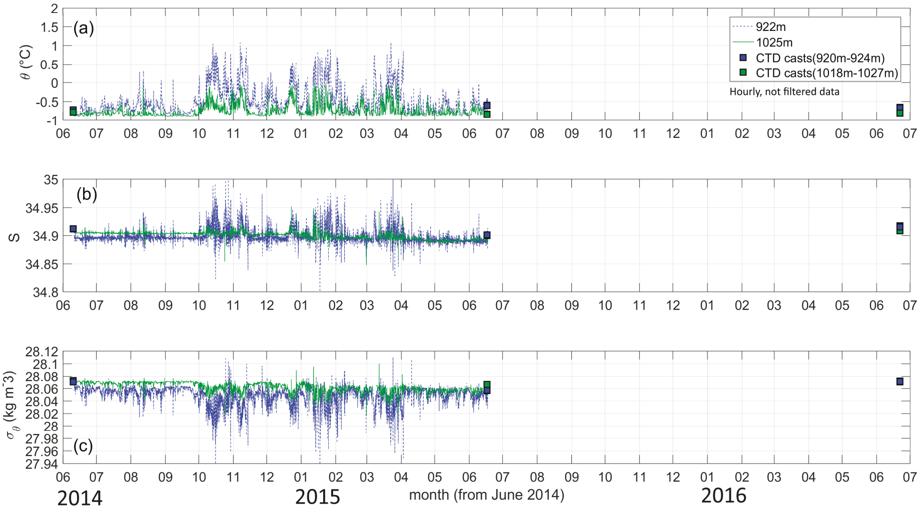

Figure 5. Time series (hourly data) of θ (**a**), S (**b**), and σ_θ (**c**) at ID2 between June 2014 and June 2015 at 922 m and 1025 m depth. Green and blue squares indicate data extracted from CTD casts (θ and S) at depths close to the moored instruments. Note that after June 2015, only temperature sensors were deployed at ID2 (see in situ temperature in Figure 6).

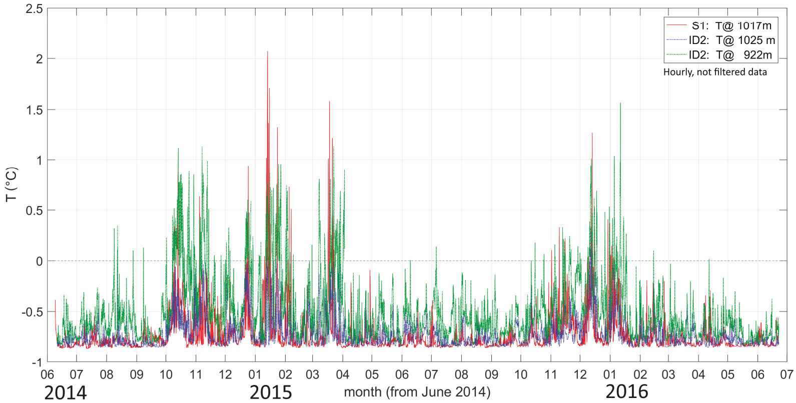

Figure 6. In situ temperature time series at S1 (red) and ID2 (blue and green). Data cover the period from June 2014 to June 2016 (for the position of the moorings refer to Figure 1).

The correlation between θ_{ID2} at two depths (1025 m and 922 m) is rather high (0.75), while the correlation between S_{ID2} at the two depths is smaller, 0.28. Short-term oscillations at 922 m were larger than at 1025 m (Figure 5). Moreover, the difference between S at 1025 m and S at 922 m diminished from ~0.01 to almost zero after one year. Accordingly, the difference in σ_θ progressively diminished as well (Figure 5c). This would be consistent with the effect of mixing in the ~100 m thick near-bottom layer.

A choice to bring together and compare the T (in situ temperature) time series at S1 and ID2 (Figure 6) rises from the fact that only temperature sensors were deployed at ID2 after June 2015. The lack of conductivity sensors prevented calculation of θ, S, and hence, of σ_θ as well. As said, T peaks appeared almost concomitant at the two stations. A significant cross-correlation, ~0.43–0.45, between T recorded at S1 and ID2 was found with the maximum value corresponding to a time lag of

5 h. Similarly, but not shown in Figure 6, S peaks were almost simultaneous at the two stations, despite small cross-correlations (0.06 between S1 and ID2 at 1025 m; 0.17 between S1 and ID2 at 922 m).

In general, large current velocities were observed during the winter period. To study more in detail the possible linkage between the ocean currents and the thermohaline variability in the deep layers at S1 and ID2, we focus on the most energetic period, 1 October 2014–30 April 2015 (Figure 7). A similar variability (but less energetic) was observed also in the period October 2015–April 2016.

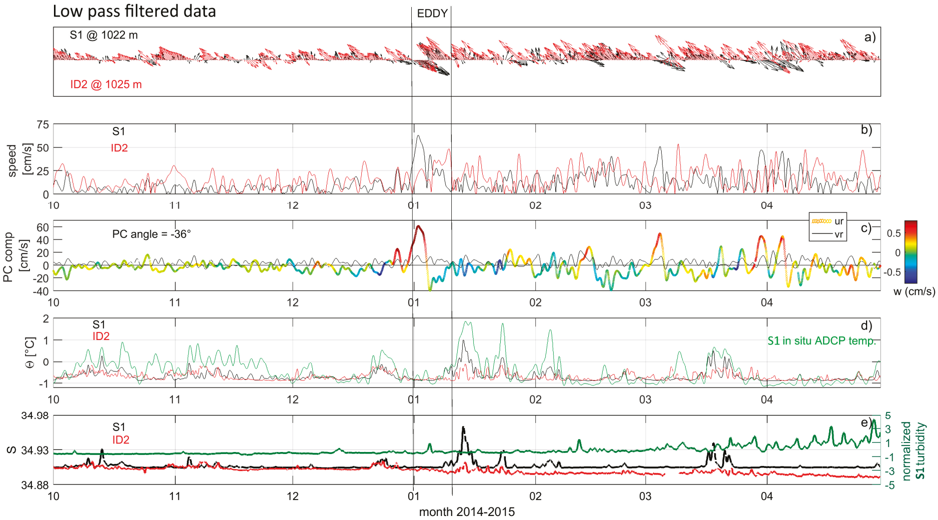

Figure 7. Time series at S1 and ID2. (**a**) Stick diagram of deep currents; (**b**) current magnitude; (**c**) current component along the direction of maximum variance at S1 (1017 m depth, *ur* positive towards SE); the colorbar refers to vertical velocity (w) from the ADCP at the same depth. The angle of maximum variance is referred to the trigonometric system; (**d**,**e**) θ and S at 1017 m (S1) and 1025 m (ID2) depth. Temperature (T) from the ADCP at 909 m and turbidity are also shown (green lines in panels d and e). Data refer to the period 1 October 2014–30 April 2015.

The principal components determined from current data revealed that the main direction of variability was along isobaths. In this frame, the appropriate velocity components are the along-slope (*ur*, positive towards SE) and the cross-slope one (*vr*, positive towards NE, i.e., toward the coast). Major events, mainly associated with anticlockwise (cyclonic) rotations, occurred at the beginning of January, beginning of March, and at the end of March 2015. They could be attributed to the passage of eddies at the mooring location. Sometimes these eddies were detected both at S1 and ID2, but with a certain time delay. This fact was particularly evident at the beginning of January 2015 (Figure 7a), when a cyclonic eddy lasted more than 10 days at S1, and it appeared at ID2 after approximately 30 hours. Strong (>40 cm s^{-1}) positive along-slope currents, and low (<10 cm s^{-1}) positive cross-slope currents (Figure 7c) characterized the first phase of this eddy passage, together with enhanced positive vertical velocities (upward). The second phase of the eddy passage was instead characterized by negative along-slope currents and slightly negative vertical velocities. In general, the eddy was not associated with significant θ and S variations. On the contrary, main episodic events with enhanced θ and S values (Figure 7d,e) were associated with negative vertical velocity (i.e., downward flow, correlation was 0.13), but with relatively small horizontal velocities (Figure 7b–d). Such episodic increases in θ and S seem to occur coherently throughout the 100 m thick bottom layer. The correlation between *ur* (*vr*) and θ was small and around −0.14 (−0.14). However, the cross-correlation between θ and *vr* reached a maximum value (−0.27) with a time lag of 14 h (θ lags *vr*), probably suggesting that θ increases could be associated, to some extent and delayed in time, with enhanced negative cross-slope currents (i.e., directed offshore). It is noteworthy that the correlation between turbidity and *vr* (*ur*) at S1 was not statistically significant considering the period June 2014–June 2015, but it resulted significant, –0.41 (–0.13), by restricting the analysis to the period April–June 2015. These facts suggest that the seasonal increase of turbidity (Figure 4c) was mainly related to a major availability of sediment transported by cross-slope currents from the shelf to the deep sea during spring.

Progressive vector diagrams (Figure 8) show that sub-tidal currents at S1 were directed prevalently northwards, following, as expected, the bathymetric constraints. However, the prevalent current direction slightly changed with increasing depth: it tended to rotate clockwise approaching the seabed (Figure 8a). Periodical current reversals (with the current direction changing from NW to SE) were also evident with a periodicity of about 15 days, usually accompanied by stronger currents, especially during the winter season. Currents, in particular those at 1022 m depth (Figure 8b), were prevalently NE oriented between June 2014 and December 2015 (mean u = 0.5 cm s^{-1}, mean v = 4 cm s^{-1}), while they were prevalently NW oriented between January 2016 and June 2016 (mean u = −0.3 cm s^{-1}, mean v = 3.6 cm s^{-1}). In this last period, the prevalent direction of the flow resulted coherent throughout the deep layer at different depths (not shown) with only a very slight clockwise rotation with increasing depth. Moreover, less current reversals occurred, especially at the deepest measured level. This fact suggests the temporary presence of a more homogeneous deep flow during the last phase of measurements.

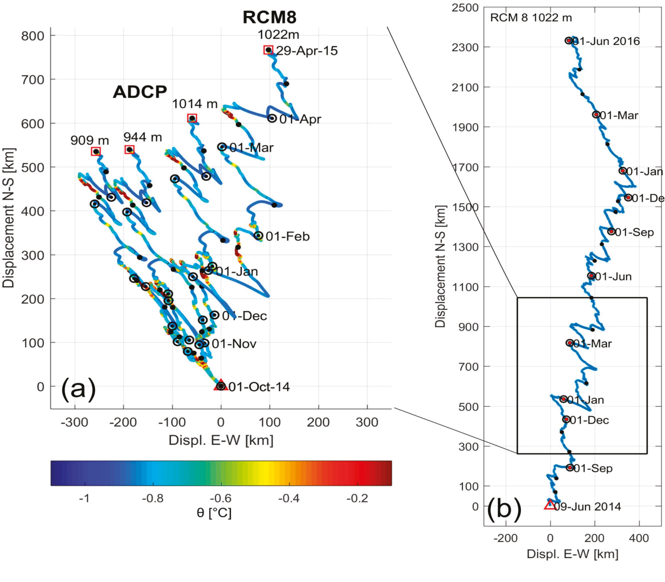

Figure 8. Progressive vector diagram of sub-tidal flow at S1. Panel (**a**): data from ADCP at different depths (909 m, 944 m, and 1014 m) and from current meter RCM8 at 1022 m within the period 1 October 2014–30 April 2015. The colorbar refers to θ at 1017 m depth. Panel (**b**): data from RCM8 at 1022 m within the whole 2-year period (June 2014–June 2016). Black dots correspond to the beginning of each month.

At ID2, the main direction of the sub-tidal currents followed the isobaths (not shown), like those observed at S1. It was prevalently northwestwards (mean u = −6.3 cm s^{-1}, mean v = 7.6 cm s^{-1} at 921 m, and mean u = −9.6 cm s^{-1}, mean v = 7 cm s^{-1} at 1024 m). The direction of the current changed slightly with increasing depth, but in the opposite way than at S1: indeed, while the main flow at 921 m depth was NW, it progressively became W–NW approaching the seabed, hence rotating anti-clockwise.

Moreover, from April 2016 to June 2016, at the deeper level (1024 m) the orientation of the main flow changed from NW to N–NE.

3.4. Local Wind Variability and Dynamic Response of the Ocean

To investigate the relation between atmospheric forcing and dynamic response of the deep layer, we compared the ECMWF time series with oceanographic data recorded at S1 and ID2. In general, in both years of measurements air temperature values decreased below 0 °C starting from September–October (Figure 9), with negative heat fluxes at the air-sea interface (heat loss from the ocean) until April. Maximum daily heat losses around −640 W m^{-2} occurred between December and March during intense storms characterized by strong (>10–15 m s^{-1}) northeasterly winds (not shown). Wintertime (December–March) monthly mean heat losses were between −200 and −260 W m^{-2}. Starting from May, most of the area southwest of Svalbard gained heat from the atmosphere (peak daily net heat flux values up to 200 W m^{-2}). Heat losses were larger during winter 2014–15 when a larger thermohaline and current variability at S1 and ID2 was observed as well, compared to the winter 2015–16. The correlation between ECMWF wind at S1 and ID2, using data smoothed with a daily moving average, is large (>0.84). It confirms the synopticity of meteorological events in the study region. Moreover, the correlation increases up to 0.91 using data smoothed with a seven-days moving average, which still reproduces accurately the features of the strongest events. Overall, by comparing ECMWF wind and currents at S1 and ID2 a coherent variability emerges (Figure 9). Indeed, we observed intensification of the deep currents during winter months when the wind was stronger. Cross-correlations revealed that current peaks lag those of wind by about one day at S1 (0.13), and two days at ID2 (0.08).

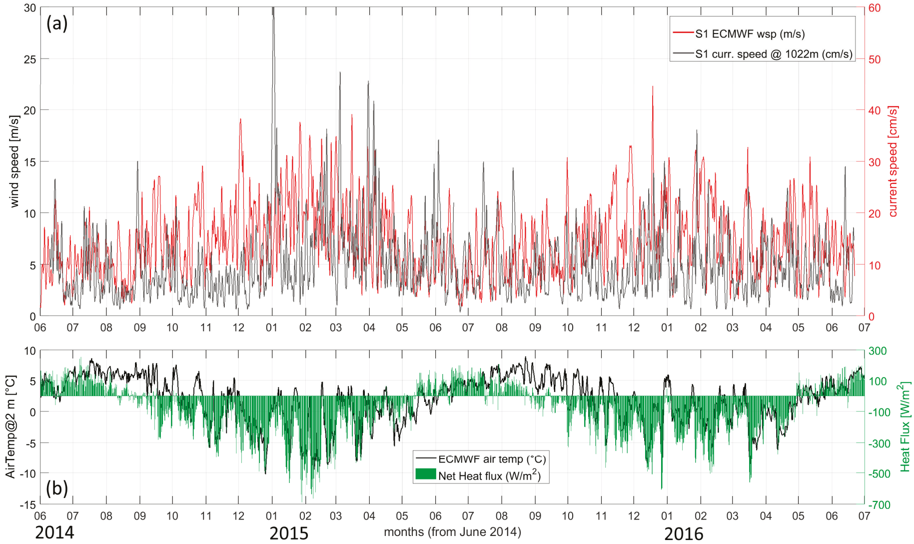

Figure 9. ECMWF wind speed (m s^{-1}) and deep current (cm s^{-1}) time series at S1 (**a**). Data are smoothed with a daily moving average. Air temperature (°C) and net heat fluxes (W m^{-2}) at the air-sea interface obtained from ECMWF ERA-Interim dataset (**b**).

In order to explore the temporal evolution of the energetic events at different time scales, the wavelet analysis was applied on the ECMWF wind and horizontal current decomposed into along-slope and cross-slope principal components. As far as the wind is concerned, there were no prominent differences between outcomes at the two mooring sites, hence, for simplicity, we present only results for S1. We found a pronounced intra-annual variation with the most energetic events occurring during winter months and characterized by periodicities around 500 h (~20 days). In general, the wind in the summer period (i.e., June–August) was more quiescent (Figure 9) and the energy concentrated at a short time scale was much lower with respect to the energy concentrated at longer time scales (Figure 10e,f).

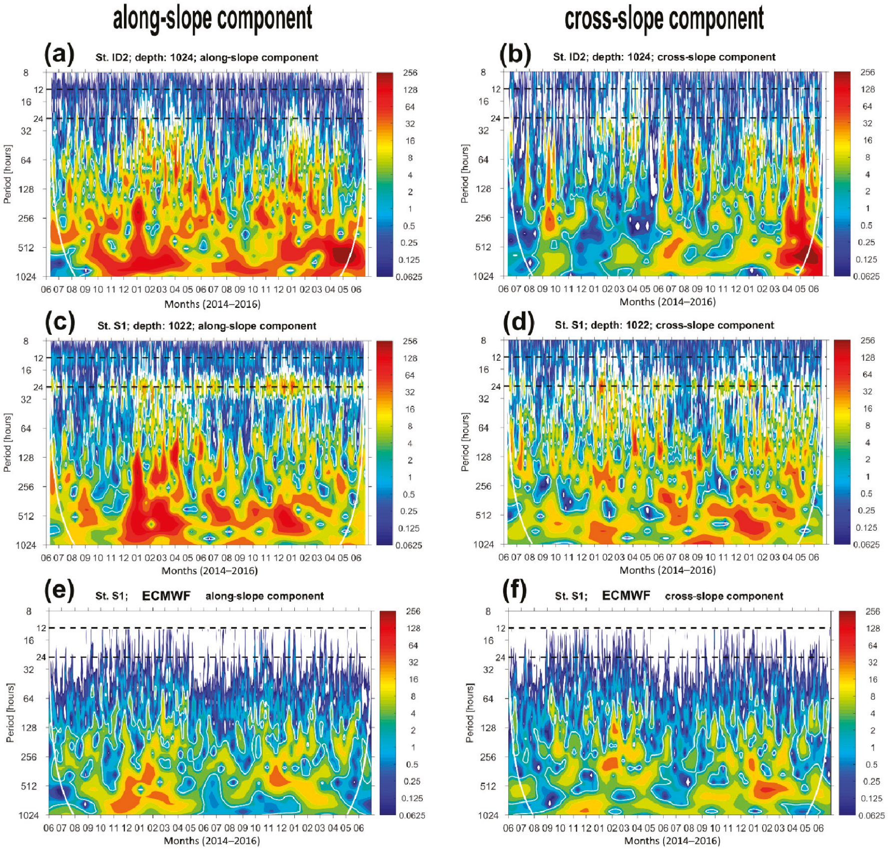

Figure 10. Wavelet power spectrum of the along-slope (**a**,**c**,**e**) and cross-slope (**b**,**d**,**f**) components (obtained from principal component analysis) of deep currents at ID2 and S1, and ECMWF wind data at S1 (not filtered). Periodicities of 12 and 24 h are indicated by black dashed lines.

The wavelet power spectrum of the horizontal currents at S1 and ID2 (Figure 10a–d) shows that the along-slope component was characterized by larger energy than the cross-slope one. However, the time evolution of the energetic events associated with the cross-slope current component (Figure 10b,d) reveals that major events at S1 occurred more or less regularly all over the study period, while at ID2 higher energy was found during the second year, with a peak between April and June 2016.

Referring to both components, most of the variance (i.e., kinetic energy) was concentrated in the low-frequency (long period) domain with typical periodicity centred around 500 h (~20 days) and ranging roughly between 200 and 1000 h (i.e., 1–6 weeks), similarly to what observed for the wind. Part of the energy was also distributed in the time domain between 50 and 200 h (i.e., 2–8 days), as well as in the high-frequency domain (~12, 24 h). As for the energy concentrated in the semidiurnal (12 h) and diurnal (24 h) time scales, which contain tidal signals, we found the former negligible compared to the latter. Noteworthy, the energy concentrated at the diurnal time scale was comparable for both components, although it was larger at S1 than at ID2, where it seems shifted to about 35 h. Moreover, we found that the energy at the diurnal time scale in the cross-slope current component, in addition to being larger at S1 than at ID2, decreased with increasing depth (not shown). Another peculiarity of this signal is that it was not distributed regularly over time, contrary to what we may expect for tidally induced oscillations. In fact, there were periods of the year when the diurnal signal appeared more energetic, mostly during winter, while there were other periods (e.g., August–September 2014) when it was less pronounced or almost absent.

Summarizing, we found a correspondence between wind and current energetic events, especially at longer time scales. The energy induced by the wind and transferred to the water column can trigger fluctuations in the current field at different time scales, even at high frequencies. However, the fact that high energy over broad time scales appear also in periods when the wind is more quiescent, like during summer, suggests that the deep flow is influenced by various concomitant phenomena.

4. Discussion and Conclusions

Our measurements revealed the presence of vigorous deep current activity on the continental slope southwest of the Svalbard region. Several times, at depths of ~1000 m, we observed along-slope jets exceeding 40 cm s^{-1}, with highest values reaching ~60–70 cm s^{-1} (Figures 7 and 9). The prevalent flow was directed northward (from NE to NW), but periodical inversions of the flow were observed (Figure 8). In particular, the period December–March was the most energetic, as it was characterized by current magnitudes almost constantly larger than 30 cm s^{-1}. Thermohaline variations, with large peaks of temperature and salinity, were also observed mainly between October and April. They appeared almost concomitant at the two stations, which are ~170 km apart along the mean pathway of the WSC. In fact, the cross-correlation between temperature at S1 and ID2 revealed a time lag of about 5 h only. However, water parcels travelling with an average velocity of 30 cm s^{-1} would cover the distance between the two moorings in little more than one week. From our analyses, a strong eddy activity at both moorings was also evident. In particular, an energetic eddy that lasted more than 10 days at S1 in January 2015, was observed after about 30 h also at ID2 (Figure 7). Moreover, fluctuations of the thermohaline properties, as well as of the currents, included frequently diurnal time scale. According to these findings, we can exclude that such fluctuations observed at the two sites are part of localized phenomena transported along the west Spitsbergen slope by the WSC. In addition, we can exclude the presence of one large single eddy at both mooring locations since the typical diameter of mesoscale eddies in this polar region is around 10–20 km [58]. On the other hand, eddies may be a manifestation of the mesoscale variability that propagates along the shelf break and along the continental slope, and they are able to induce vertical water displacement. Similarly, the passage of trains of topographically trapped waves, with a predominantly diurnal periodicity, travelling along the continental slope may result in internal oscillations, highlighted by the observed thermohaline variability. This interpretation is in agreement with Nilsen et al. [45], whose findings revealed the presence of both mesoscale variability and topographically trapped waves at shallower depths (shelf break) in a wider zone including our study area, resulting from rotating wind field during passing storms. In particular, beside the mesoscale variability they found internal waves with wavelength $\lambda = 32$ km for periods of 24 h and 35 h. The passage of trains of internal waves would partly explain the thermohaline oscillations observed at the mooring sites since these waves can induce changes in the vertical distribution of the AW along the entire west Svalbard margin. A similar phenomenon was also observed in numerical simulations along the Norwegian continental shelf [59]. Lien et al. [59] found that general intensifications of North Atlantic Oscillation and consequent atmospheric events, are able to amplify the AW depth variability during winter, due to the Ekman cross-shore transport induced by the along-slope (i.e., along-shore) wind component. This fact seems in agreement with the enhanced winter energy found from the wavelet analysis applied to our data. Indeed, we found an overall consistency between the variability of the deep sea currents and the local wind signal (see Figure 9), especially on seasonal and low-frequency scales. In particular, we observed the occurrence of the most energetic events during winter both for the deep current flow and for the wind speed with typical periodicities of ~20 days. Consequently, our interpretation is that the passage of high-low atmospheric pressure systems can explain the origins and amplification of internal oscillations observed along the west Spitsbergen margin at 1000 m depth. Meteorological forcing would hence modulate the current flow, extending its influence from the surface down to deep layers. Von Appen et al. [15] also found variability of deep ocean flows with periodicities of 1–3 weeks in the northern Fram Strait, at depths exceeding 2000 m. They explained such variability by the passage of basin-scale topographic Rossby waves excited by synoptic atmospheric forcing.

Sanchez-Vidal et al. [11] observed similar sporadic intrusions of relatively warm and salty water at their Stations A (close to S1) and B (1500 m depth, slightly deeper on the continental slope) in 2010–11. They suggested that such modifications of the ambient water at large depths were likely related to the influence of shallower AW. Moreover, they also found a 100 m thick bottom layer characterized by relatively high turbidity values, likely associable to a nepheloid layer. Increased turbidity along the west Spitsbergen continental slope can result from resuspension of sediment due to enhanced bottom currents (i.e., passage of trains of internal waves), but also from particles transported during cascading events, for example. According to this, we suppose that observed water intrusions at depths larger than 1000 m have two possible causes: (i) they originate from internal oscillations triggered by the passage of trains of internal waves or eddies, as discussed above; (ii) they occasionally originate from slope currents as a result of dense water formation and vertical mixing events occurring on the shelf, the latter being strongly influenced by the progressive intensification of the AW signal on the shelf and within fjords [20,31].

In support of the second hypothesis, we discuss here a combined analysis of meteorological and oceanographic data. Air-sea interaction and strong vorticity in the wind field lead to Ekman pumping and vertical convection over the West Spitsbergen Shelf [1,23,60]. Nilsen et al. [2] demonstrated that in the period autumn–winter (between September and May) low-pressure atmospheric systems influence the West Spitsbergen Shelf area. They also found a negative correlation with a zero time lag between along-shore wind stress and ocean temperature at their mooring I1, at the mouth of Isfjorden on the shelf, at 50 m and 190 m depths. Subsequently, northerly wind events (and associated positive wind stress curl field) could cause upwelling of AW that can be cooled after reaching the surface and become denser. The wintertime heat fluxes in our study had daily peak heat loss from the ocean to the atmosphere reaching -640 W m^{-2}, while average monthly in the period December–March had values around -200 W m^{-2}. Such heat losses could cool down by 2–3 °C the intruding warm and saline AW all the way to the bottom on the ~200 m deep continental shelf, in agreement with findings by Hakkinen and Cavalieri [61]. Cooling of this magnitude would increase the density of the AW ($\theta > 2$ °C, $S > 34.92$, $27.70 < \sigma_\theta < 27.97$ kg m^{-3}) on the shelf by reaching values of ~28.04 kg m^{-3}, triggering the sinking of shelf water downslope to depths > 900 m (Figure 1b). Consequently, thermohaline and current variability observed in the deep layer at S1 and ID2 could also be sporadically caused by the arrival of gravity currents driven by dense water plumes formed over the shelf during intense meteorological events (i.e., those producing shelf convection) or formed after sea ice formation within fjords (i.e., BSW). Dense plumes descending as bottom-arrested currents follow preferential routes constrained by bathymetry, undergo a strong entrainment of AW that occupies the intermediate and upper layers of the WSC [41]. These dense plumes can collect sediments (Figure 1b) that increase their kinetic energy and bulk density [6,62,63]. In this regard, Fohrmann et al. [6] pointed out how a volumetric concentration of 1000 mg L^{-1} of suspended quartz particles increases the bulk water density of 0.6 kg m^{-3}. They also demonstrated how turbidity plumes in the Svalbard region are 10 times faster and can reach deeper layers with respect to mere temperature-salinity plumes. However, at S1, we found turbidity values up to 6 FTU in late winter season, corresponding to a concentration of suspended sediment of about 16–18 mg L^{-1}, which would not be sufficient to compensate the low density deriving solely from temperature and salinity. Hence, an input of sediments from the shelf/slope that would stimulate water cascading is plausible, but not so explicit from our data. In any case, at S1 we found a larger correlation between the cross-slope velocity component directed offshore and turbidity during spring. This fact may indicate cross-slope currents transporting more sediments toward the deep layers. Since slope currents can affect ocean stratification through baroclinic instabilities, they can themselves generate oscillatory signals in the deep layer [64] and induce current reversals, which in turn, cause vertical displacements of the water as well as sediment resuspension, interacting with the continental slope. Hence, the two phenomena, i.e., internal oscillations and gravity currents, can coexist although hardly discernible from our data.

Finally, our study shows that the West Spitsbergen Shelf experiences high seasonal and interannual thermohaline variability associated with the inflows of AW and outflows of cold and fresh water from fjords. A large thermohaline variability can strongly influence the generation of dense water plumes on the shelf, as well as their properties. At the same time, a warming trend of AW emerges in agreement with previous studies [22,28,65]. Similarly, a slightly positive temperature trend appear also in the deep layer, which is consistent with the observed continuous warming of the deep waters in all sub-regions of the Nordic Seas [65].

In conclusion, our observations suggest that shelf-slope dynamics modulated by synoptic atmospheric forcing can increase the mixing rate between upper and deep layers along the west Spitsbergen continental slope, contributing to the slow modification of the deep layer (>800 m depth) along the west Svalbard margin, which is experiencing a slight tendency to become warmer and saltier. Further analyses are required to understand if prolonged injections of relatively warm water within the deep layer along the west Spitsbergen margin could potentially be responsible for future modifications of the abyssal waters in the Arctic Ocean.

Author Contributions: M.B. set the leading hypotheses of the work, performed data analysis, and wrote the main manuscript text. V.K., L.L., S.A. co-designed the research, participated in data analyses and interpretation and contributed to writing the text. A.R., L.U., I.G., T.S., R.S., F.N., contributed to data analyses and writing the manuscript. D.D., P.M., R.L., M.R., L.R., R.G.L., A.V., A.W., and A.B.-M. participated in data acquisition and interpretation. All authors reviewed the manuscript.

Funding: This research was funded by the FP7-EU/Eurofleets2 initiative through the PREPARED (PREsent and PAst flow REgime on contourite Drifts west of Spitsbergen) project and by the Italian Ministry of University and Research through the National Programme of Research in Antarctic (PNRA), project DEFROST (DEep Flow Regime Off SpiTsbergen). This study was partially supported by the Svalbard Integrated Arctic Earth Observing System (SIOS) through the first SESS report pilot call (SOA project, contract n°2017_0007).

Acknowledgments: We acknowledge Matthias Forwick (UiT), as well as Captains and Crews of the r/v Helmer Hanssen, r/v G.O. Sars, I/B Polastern, and r/v Alliance (Italian Hydrographic Institute, “High-North” programme) for moorings maintenance and assistance in the field works. We thank Daniela Accettella (OGS) for preparing the bathymetry map shown in Figure 1a. We also acknowledge the anonymous reviewers for their valuable comments.

Conflicts of Interest: The authors declare no competing interests.

References

1. Skogseth, R.; Sandvik, A.D.; Asplin, L. Wind and tidal forcing on the meso-scale circulation in Storfjorden, Svalbard. *Cont. Shelf Res.* **2007**, *27*, 208–227. [CrossRef]
2. Nilsen, F.; Skogseth, R.; Vaardal-Lunde, J.; Inall, M. A Simple Shelf Circulation Model: Intrusion of Atlantic Water on the West Spitsbergen Shelf. *J. Phys. Oceanogr.* **2016**, *46*, 1209–1230. [CrossRef]
3. Onarheim, I.H.; Årthun, M. Toward an ice-free Barents Sea. *Geophys. Res. Lett.* **2017**, *44*, 8387–8395. [CrossRef]
4. Polyakov, I.V.; Pnyushkov, A.V.; Alkire, M.B.; Ashik, I.M.; Baumann, T.M.; Carmack, E.C.; Goszczko, I.; Guthrie, J.; Ivanov, V.V.; Kanzow, T.; et al. Greater role for Atlantic inflows on sea-ice loss in the Eurasian Basin of the Arctic Ocean. *Science* **2017**, *356*, 285–291. [CrossRef]
5. Backhaus, J. Formation and export of water masses produced in Arctic shelf polynyas—Process studies of oceanic convection. *ICES J. Mar. Sci.* **1997**, *54*, 366–382. [CrossRef]
6. Fohrmann, H.; Backhaus, J.O.; Blaume, F.; Rumohr, J. Sediments in Bottom-Arrested Gravity Plumes: Numerical Case Studies. *J. Phys. Oceanogr.* **1998**, *28*, 2250–2274. [CrossRef]

7. Rudels, B.; Björk, G.; Nilsson, J.; Winsor, P.; Lake, I.; Nohr, C. The interaction between waters from the Arctic Ocean and the Nordic Seas north of Fram Strait and along the East Greenland Current: Results from the Arctic Ocean-02 Oden expedition. *J. Mar. Syst.* **2005**, *55*, 1–30. [CrossRef]
8. Postlethwaite, C.F.; Morales Maqueda, M.A.; le Fouest, V.; Tattersall, G.R.; Holt, J.; Willmott, A.J. The effect of tides on dense water formation in Arctic shelf seas. *Ocean Sci.* **2011**, *7*, 203–217. [CrossRef]
9. Wobus, F.; Shapiro, G.I.; Huthnance, J.M.; Maqueda, M.A.M.; Aksenov, Y. Tidally induced lateral dispersion of the Storfjorden overflow plume. *Ocean Sci.* **2013**, *9*, 885–899. [CrossRef]
10. Wobus, F.; Shapiro, G.I.; Huthnance, J.M.; Maqueda, M.A.M. The piercing of the Atlantic Layer by an Arctic shelf water cascade in an idealised study inspired by the Storfjorden overflow in Svalbard. *Ocean Model.* **2013**, *71*, 54–65. [CrossRef]
11. Sanchez-Vidal, A.; Veres, O.; Langone, L.; Ferré, B.; Calafat, A.; Canals, M.; Durrieu de Madron, X.; Heussner, S.; Mienert, J.; Grimalt, J.O.; et al. Particle sources and downward fluxes in the eastern Fram strait under the influence of the west Spitsbergen current. *Deep Sea Res. Part Oceanogr. Res. Pap.* **2015**, *103*, 49–63. [CrossRef]
12. Bensi, M.; Kovačević, V.; Ursella, L.; Rebesco, M.; Langone, L.; Viola, A.; Mazzola, M.; Beszczynska-Möller, A.; Goszczko, I.; Soltwedel, T.; et al. Spitsbergen Oceanic and Atmospheric interactions—SOA. In *SESS Report 2018 The State of Environmental Science in Svalbard—An Annual Report*; Orr, E., Hansen, G., Lappalainen, H., Hübner, C., Lihavainen, H., Eds.; Longyearbyen, Svalbard Integrated Arctic Earth Observing System (SIOS): Longyearbyen, Norway, 2019; ISBN 978-82-691528-0-7.
13. Teigen, S.H.; Nilsen, F.; Gjevik, B. Barotropic instability in the West Spitsbergen Current. *J. Geophys. Res.* **2010**, *115*. [CrossRef]
14. Teigen, S.H.; Nilsen, F.; Skogseth, R.; Gjevik, B.; Beszczynska-Möller, A. Baroclinic instability in the West Spitsbergen Current. *J. Geophys. Res. Oceans* **2011**, *116*. [CrossRef]
15. Von Appen, W.-J.; Schauer, U.; Somavilla, R.; Bauerfeind, E.; Beszczynska-Möller, A. Exchange of warming deep waters across Fram Strait. *Deep Sea Res. Part Oceanogr. Res. Pap.* **2015**, *103*, 86–100. [CrossRef]
16. Van Haren, H.; Greinert, J. Turbulent high-latitude oceanic intrusions—Details of non-smooth apparent isopycnal transport West of Svalbard. *Ocean Dyn.* **2016**, *66*, 785–794. [CrossRef]
17. Fer, I.; Ådlandsvik, B. Descent and mixing of the overflow plume from Storfjord in Svalbard: An idealized numerical model study. *Ocean Sci.* **2008**, *4*, 115–132. [CrossRef]
18. Nilsen, F.; Cottier, F.; Skogseth, R.; Mattsson, S. Fjord–shelf exchanges controlled by ice and brine production: The interannual variation of Atlantic Water in Isfjorden, Svalbard. *Cont. Shelf Res.* **2008**, *28*, 1838–1853. [CrossRef]
19. Tverberg, V.; Nøst, O.A.; Lydersen, C.; Kovacs, K.M. Winter sea ice melting in the Atlantic Water subduction area, Svalbard Norway. *J. Geophys. Res. Oceans* **2014**, *119*, 5945–5967. [CrossRef]
20. Tverberg, V.; Skogseth, R.; Cottier, F.; Sundfjord, A.; Walczowski, W.; Inall, M.; Falck, E.; Pavlova, O.; Nilsen, F. The Kongsfjorden Transect: Seasonal and inter-annual variability in hydrography. In *The Ecosystem Kongsfjorden, Svalbard*; Hop, H., Wiencke, C., Eds.; Adv. Polar Ecol.; Springer: Cham, Switzerland, 2019; p. 562. ISBN 978-3-319-46423-7.
21. Aagaard, K.; Foldvik, A.; Hillman, S.R. The West Spitsbergen Current: Disposition and water mass transformation. *J. Geophys. Res. Oceans* **1987**, *92*, 3778–3784. [CrossRef]
22. Beszczynska-Möller, A.; Fahrbach, E.; Schauer, U.; Hansen, E. Variability in Atlantic water temperature and transport at the entrance to the Arctic Ocean, 1997–2010. *ICES J. Mar. Sci.* **2012**, *69*, 852–863. [CrossRef]
23. Boyd, T.J.; D'Asaro, E.A. Cooling of the West Spitsbergen Current: Wintertime observations west of Svalbard. *J. Geophys. Res. Oceans* **1994**, *99*, 22597–22618. [CrossRef]
24. Swift, J.H.; Koltermann, K.P. The origin of Norwegian Sea deep water. *J. Geophys. Res. Oceans* **1988**, *93*, 3563–3569. [CrossRef]
25. Sternal, B.; Szczuciski, W.; Forwick, M.; Zajączkowski, M.; Lorenc, S.; Przytarska, J. Postglacial variability in near-bottom current speed on the continental shelf off south-west Spitsbergen. *J. Quat. Sci.* **2014**, *29*, 767–777. [CrossRef]
26. Menze, S.; Ingvaldsen, R.B.; Haugan, P.; Fer, I.; Sundfjord, A.; Beszczynska-Moeller, A.; Falk-Petersen, S. Atlantic Water Pathways along the North-Western Svalbard Shelf Mapped Using Vessel-Mounted Current Profilers. *J. Geophys. Res. Oceans* **2019**, *124*. [CrossRef]

27. Polyakov, I.V.; Alekseev, G.V.; Timokhov, L.A.; Bhatt, U.S.; Colony, R.L.; Simmons, H.L.; Walsh, D.; Walsh, J.E.; Zakharov, V.F. Variability of the Intermediate Atlantic Water of the Arctic Ocean over the Last 100 Years. *J. Clim.* **2004**, *17*, 4485–4497. [CrossRef]
28. Walczowski, W.; Beszczynska-Möller, A.; Wieczorek, P.; Merchel, M.; Grynczel, A. Oceanographic observations in the Nordic Sea and Fram Strait in 2016 under the IO PAN long-term monitoring program AREX. *Oceanologia* **2017**, *59*, 187–194. [CrossRef]
29. Polyakov, I.V.; Bhatt, U.S.; Walsh, J.E.; Abrahamsen, E.P.; Pnyushkov, A.V.; Wassmann, P.F. Recent oceanic changes in the Arctic in the context of long-term observations. *Ecol. Appl.* **2013**, *23*, 1745–1764. [CrossRef] [PubMed]
30. Walczowski, W.; Piechura, J. Pathways of the Greenland Sea warming. *Geophys. Res. Lett.* **2007**, *34*, L10608. [CrossRef]
31. Promińska, A.; Cisek, M.; Walczowski, W. Kongsfjorden and Hornsund hydrography–comparative study based on a multiyear survey in fjords of west Spitsbergen. *Oceanologia* **2017**, *59*, 397–412. [CrossRef]
32. Oldenburg, D.; Armour, K.C.; Thompson, L.; Bitz, C.M. Distinct Mechanisms of Ocean Heat Transport into the Arctic Under Internal Variability and Climate Change. *Geophys. Res. Lett.* **2018**, *45*, 7692–7700. [CrossRef]
33. Lien, V.S.; Vikebø, F.B.; Skagseth, Ø. One mechanism contributing to co-variability of the Atlantic inflow branches to the Arctic. *Nat. Commun.* **2013**, *4*, 1488. [CrossRef] [PubMed]
34. Polyakov, I.V.; Beszczynska, A.; Carmack, E.C.; Dmitrenko, I.A.; Fahrbach, E.; Frolov, I.E.; Gerdes, R.; Hansen, E.; Holfort, J.; Ivanov, V.V.; et al. One more step toward a warmer Arctic. *Geophys. Res. Lett.* **2005**, *32*. [CrossRef]
35. Walczowski, W.; Piechura, J.; Goszczko, I.; Wieczorek, P. Changes in Atlantic water properties: An important factor in the European Arctic marine climate. *ICES J. Mar. Sci.* **2012**, *69*, 864–869. [CrossRef]
36. Haarpaintner, J. The Storfjorden polynya: ERS-2 SAR observations and overview. *Polar Res.* **1999**, *18*, 175–182. [CrossRef]
37. Haarpaintner, J.; Gascard, J.-C.; Haugan, P.M. Ice production and brine formation in Storfjorden, Svalbard. *J. Geophys. Res. Oceans* **2001**, *106*, 14001–14013. [CrossRef]
38. Skogseth, R.; Haugan, P.M.; Jakobsson, M. Watermass transformations in Storfjorden. *Cont. Shelf Res.* **2005**, *25*, 667–695. [CrossRef]
39. Jardon, F.P.; Vivier, F.; Bouruet-Aubertot, P.; Lourenço, A.; Cuypers, Y.; Willmes, S. Ice production in Storfjorden (Svalbard) estimated from a model based on AMSR-E observations: Impact on water mass properties. *J. Geophys. Res. Oceans* **2014**, *119*, 377–393. [CrossRef]
40. Preußer, A.; Willmes, S.; Heinemann, G.; Paul, S. Thin-ice dynamics and ice production in the Storfjorden polynya for winter-seasons 2002/2003–2013/2014 using MODIS thermal infrared imagery. *Cryosphere* **2015**, *9*, 1063–1073. [CrossRef]
41. Quadfasel, D.; Rudels, B.; Kurz, K. Outflow of dense water from a Svalbard fjord into the Fram Strait. *Deep Sea Res. Part Oceanogr. Res. Pap.* **1988**, *35*, 1143–1150. [CrossRef]
42. Jungclaus, J.H.; Backhaus, J.O.; Fohrmann, H. Outflow of dense water from the Storfjord in Svalbard: A numerical model study. *J. Geophys. Res.* **1995**, *100*, 24719. [CrossRef]
43. Shaw, P.-T.; Chao, S.-Y. Effects of a baroclinic current on a sinking dense water plume from a submarine canyon and heton shedding. *Deep Sea Res. Part Oceanogr. Res. Pap.* **2003**, *50*, 357–370. [CrossRef]
44. Inall, M.E.; Nilsen, F.; Cottier, F.R.; Daae, R. Shelf/fjord exchange driven by coastal-trapped waves in the A rctic. *J. Geophys. Res. Oceans* **2015**, *120*, 8283–8303. [CrossRef]
45. Nilsen, F.; Gjevik, B.; Schauer, U. Cooling of the West Spitsbergen Current: Isopycnal diffusion by topographic vorticity waves. *J. Geophys. Res.* **2006**, *111*, C08012. [CrossRef]
46. Cacchione, D.A.; Pratson, L.F.; Ogston, A.S. The shaping of continental slopes by internal tides. *Science* **2002**, *296*, 724–727. [CrossRef]
47. Cacchione, D.A.; Drake, D.E. Nepheloid layers and internal waves over continental shelves and slopes. *Geo-Mar. Lett.* **1986**, *6*, 147–152. [CrossRef]
48. Akimova, A.; Schauer, U.; Danilov, S.; Núñez-Riboni, I. The role of the deep mixing in the Storfjorden shelf water plume. *Deep Sea Res. Part Oceanogr. Res. Pap.* **2011**, *58*, 403–414. [CrossRef]
49. Rebesco, M.; Wåhlin, A.; Laberg, J.S.; Schauer, U.; Beszczynska-Möller, A.; Lucchi, R.G.; Noormets, R.; Accettella, D.; Zarayskaya, Y.; Diviacco, P. Quaternary contourite drifts of the Western Spitsbergen margin. *Deep Sea Res. Part Oceanogr. Res. Pap.* **2013**, *79*, 156–168. [CrossRef]

50. Etling, D.; Gelhardt, F.; Schrader, U.; Brennecke, F.; Kühn, G.; d'Hieres, G.C.; Didelle, H. Experiments with density currents on a sloping bottom in a rotating fluid. *Dyn. Atmos. Oceans* **2000**, *31*, 139–164. [CrossRef]
51. Pawlowicz, R.; Beardsley, B.; Lentz, S. Classical tidal harmonic analysis including error estimates in MATLAB using T_TIDE. *Comput. Geosci.* **2002**, *28*, 929–937. [CrossRef]
52. Carpenter, J.H. The Accuracy of the Winkler Method for Dissolved Oxygen Analysis1. *Limnol. Oceanogr.* **1965**, *10*, 135–140. [CrossRef]
53. Schlitzer, R. Ocean Data View. 2018. Available online: http://odv.awi.de/ (accessed on 1 October 2018).
54. Artegiani, A.; Paschini, E.; Russo, A.; Bregant, D.; Raicich, F.; Pinardi, N. The Adriatic Sea General Circulation. Part I: Air–Sea Interactions and Water Mass Structure. *J. Phys. Oceanogr.* **1997**, *27*, 1492–1514. [CrossRef]
55. Torrence, C.; Compo, G.P. A practical guide to wavelet analysis. *Bull. Am. Meteorol. Soc.* **1998**, *79*, 61–78. [CrossRef]
56. Saloranta, T.M.; Svendsen, H. Across the Arctic front west of Spitsbergen: High-resolution CTD sections from 1998–2000. *Polar Res.* **2001**, *20*, 177–184.
57. Chatterjee, S.; Raj, R.P.; Bertino, L.; Skagseth, Ø.; Ravichandran, M.; Johannessen, O.M. Role of Greenland Sea Gyre Circulation on Atlantic Water Temperature Variability in the Fram Strait. *Geophys. Res. Lett.* **2018**, *45*, 8399–8406. [CrossRef]
58. Zhao, M.; Timmermans, M.-L.; Cole, S.; Krishfield, R.; Proshutinsky, A.; Toole, J. Characterizing the eddy field in the Arctic Ocean halocline. *J. Geophys. Res. Oceans* **2014**, *119*, 8800–8817. [CrossRef]
59. Lien, V.S.; Gusdal, Y.; Vikebø, F.B. Along-shelf hydrographic anomalies in the Nordic Seas (1960–2011): Locally generated or advective signals? *Ocean Dyn.* **2014**, *64*, 1047–1059. [CrossRef]
60. Skeie, P.; Gronaas, S. Strongly stratified easterly flows across Spitsbergen. *Tellus A* **2000**, *52*, 473–486. [CrossRef]
61. Häkkinen, S.; Cavalieri, D.J. A study of oceanic surface heat fluxes in the Greenland, Norwegian, and Barents Seas. *J. Geophys. Res. Oceans* **1989**, *94*, 6145–6157. [CrossRef]
62. Akiyama, J.; Stefan, H. Turbidity Current with Erosion and Deposition. *J. Hydraul. Eng.* **1985**, *111*, 1473–1496. [CrossRef]
63. Kämpf, J.; Backhaus, J.O.; Fohrmann, H. Sediment-induced slope convection: Two-dimensional numerical case studies. *J. Geophys. Res. Oceans* **1999**, *104*, 20509–20522. [CrossRef]
64. Gill, A. *Atmosphere-Ocean Dynamics*, 1st ed.; Academic Press: San Diego, CA, USA, 1982; Volume 30, ISBN 978-0-08-057052-5.
65. González-Pola, C.; Larsen, K.M.; Fratantoni, P.; Beszczynska-Möller, A.; Hughes, S.L. *ICES Report on Ocean Climate 2016*; ICES Cooperative Research Report No. 339; International Council for the Exploration of the Sea (ICES), Conseil International pour l'Exploration de la Mer (CIEM): Copenhagen, Denmark, 2018; p. 110.

water

Article

A Census of the 1993–2016 Complex Mesoscale Eddy Processes in the South China Sea

Huimeng Wang [1,2], Yunyan Du [1,2,*], Fuyuan Liang [3], Yong Sun [4] and Jiawei Yi [1,2]

[1] State Key Laboratory of Resources and Environmental Information System, Institute of Geographic Science and Natural Resources Research, Chinese Academy of Sciences, Beijing 100101, China; wanghm@lreis.ac.cn (H.W.); yijw@lreis.ac.cn (J.Y.)
[2] University of Chinese Academy of Sciences, Beijing 100101, China
[3] Department of Earth, Atmospheric, and Geographic Information Sciences, Western Illinois University, Macomb, IL 61455, USA; F-Liang@wiu.edu
[4] Shandong University of Science and Technology, Qingdao 266000, China; ttsunyong@163.com
* Correspondence: duyy@lreis.ac.cn; Tel.: +86-010-64888973

Received: 16 March 2019; Accepted: 5 June 2019; Published: 10 June 2019

Abstract: Mesoscale eddy process with at least one splitting and/or merging event can be defined as either a complex process or a simple process. Investigation of the difference between these two categories could provide new insights into how different factors, such as the seabed topography, Kuroshio intrusion, and winds, affect the origin, migration, and decay of the mesoscale eddies. This study compared the characteristics of the complex against the simple eddy processes in the South China Sea (SCS) from 1993 to 2016. We comprehensively analyzed the eddy processes with regards to their characteristic points, trajectories, and networks. The simple and complex processes share many similarities but do show significantly different behaviors. Both the simple and complex processes mainly start from the eastern SCS. However, the complex processes mainly vanish in the western SCS whereas the simple processes disappear almost everywhere across the SCS. The complex processes last longer and migrate more than the simple processes. Lastly, the complex processes mainly move westward within the community. The complex processes can be further categorized into complex anticyclonic and cyclonic eddy processes. Spatially, the splitting and merging events mainly occur in the southwest of Taiwan, northwest of the Luzon Island, and the southeast of Vietnam. Temporally, the merging and splitting events mainly occur in the fall. The interaction among the communities reveals the different migration patterns of the complex anticyclonic and cyclonic eddy processes in the SCS.

Keywords: complex processes; eddies; mobility indicators; splitting and merging; community division; South China Sea

---

1. Introduction

Mesoscale eddies are a common dynamic phenomenon in the ocean, which is constantly moving around and changing with respect to their geometric and thematic characteristics. Previous studies have shown that mesoscale eddies migration facilitates transport and exchange of energy and substance in the oceans, and thus plays a significant role in the marine ecosystem, atmospheric environment, and surface ocean circulation [1–5]. Mesoscale eddies even show their effects on the migration and biogeochemical processes of the deep-ocean biological communities [3–5]. The heat exchange between the eddies and the atmosphere also affects the local wind field, clouds, and precipitation [6].

Many studies have been done on mesoscale eddies in different sea areas (such as the Pacific Ocean, the Indian Ocean, the Mediterranean Sea, Peru, etc.) to develop methods for identifying and tracking eddies [7–9], to examine eddies statistical characteristics [10–15] and the driving mechanisms behind them [16–19], and to study the influences of eddies on current circulation [2,20,21], oceanic ecology, and biogeochemical processes [5,22]. As in other waters, mesoscale eddies are also very common and active in the South China Sea (SCS), which is a marginal sea of the Pacific Ocean and also the largest semi-enclosed sea in the tropics. Different methods and multiple-source data sets have been used to examine the eddies in the SCS. For example, Yang et al. [23] and Yuan et al. [24] discovered a seasonal cyclonic (CE) and an anticyclonic eddy (AE) in the northern SCS from the climatological Levitus data and satellite altimeter data. From the Argo float data, Chow et al. [25] found perennial cold eddies in the south of the Dongsha Islands, mainly in winter or spring. Observational studies in the east of Vietnam [26] show that during the summer monsoon season, more anticyclonic eddies are found in the southern SCS whereas more cyclonic eddies are found in the northern SCS. Chen et al. [27] used in situ hydrographic data, 375 Argo profiles, and sea level anomaly (SLA) data to find relatively large current heat exchange both along the parallel and the meridian directions. Polar eddy current heat transfer was found in summer in the east of Vietnam. In the west of Luzon Island, polar heat exchange was found in winter. In the western Luzon Strait, a large equatorial heat transfer was found in winter.

Statistics has been widely used to depict the overall characteristics and movement patterns of the mesoscale eddies in different regions, from which efforts have been made to infer the driving mechanism and provide support for numerical simulation of the eddies [11–14,26]. Statistical analysis of the eddies in the SCS has been conducted from different perspectives by using the satellite altimeter data and observational data. Many studies focused on statistically analyzing the total number of eddies over a certain period and their lifespans, propagation directions, movement speeds, emerging and vanishing locales, spatiotemporal distribution patterns of their attributes, and even the correlation with the El Nino or La Nina events. For example, Wang et al. [11] examined the 1993 to 2000 sea surface height anomaly data and delineated the SCS into four regions based on the statistical analysis results of emerging locales of the eddies. By using the 1993 to 2001 TOPEX/Poseidon merged ERS-1/2 altimeter data, Lin et al. [26] showed that about 80% of eddies moved westward from the southwest of Taiwan to the east of southern Vietnam. Xiu et al. [12] conducted an eddy census in terms of the number, size, and lifespan from 1993 to 2007 and showed that the radius of the eddies ranged from 46.5 km to 223.5 km, with an average of 87.4 km. More than 70% of the eddies have a radius smaller than 100 km. They also found that the eddy activities in the SCS are not directly related to the El Niño–Southern Oscillation events. Chen et al. [13] examined the 1992 to 2009 SLA data and statistically summarized the seasonal and inter-annual variability of the eddies. They found that the eddies in the SCS mainly develop in an elongated northeast–southwest zone in the southwest of the Luzon Strait, and argued that eddy activity is sensitive to the wind stress curl in the northern SCS. Du et al. [14] investigated the general characteristics of the eddies in the SCS, particularly the spatial distribution patterns of eddy disappearing, reappearing, splitting, and merging activities.

Nowadays, mesoscale eddies are observed splitting and merging frequently thanks to the availability of high-quality spatial data, including satellite observation data, in situ observation data and the emergence of various model data [28–32]. In this study, we define a mesoscale eddy evolution process with at least one or without any splitting and merging event as a complex or simple process, respectively. It is valuable to study complex eddy processes as the splitting and merging events tend to impact seawater interaction and marine ecosystems more than the simple eddy processes [29,30]. For example, eddy splitting can cause eddy deformation, substance dispersion, and subsequent energy attenuation, affecting the temperature, salinity, water mass and microorganisms in the marine ecosystems [31]. Eddy merging may strengthen seawater interaction and the energy and entropy transfer across multiple scales in turbulent flows [29,32]. In fact, some studies have examined the complex processes and already recognized the great value of comparing simple against complex processes [28–32]. For example, Li et al. [31] argued that an eddy merging event may trigger a tropical storm, whereas a splitting event can initiate and enhance energy and material exchange among different regions. Not much statistical analysis has been conducted on the complex eddy processes in the SCS, and it remains unclear how the spatiotemporal characteristics are different between the simple and complex eddy processes.

Various factors, such as Kuroshio intrusion, wind stress, and coastal jet have been frequently cited to explain the origin, migration, and extinction of the eddies in the SCS. Unfortunately, the driving mechanism is still pretty vague. For example, the northern SCS is where eddies mainly start. It has been attributed to the shedding of the Kuroshio intrusion [24,33], wind stress [11,34] or influence of other eddies that invaded from the Pacific Ocean through the Luzon Strait [35]. In the east of Vietnam, the unstable strong currents along the coast may trigger more births of eddies [36]. A comprehensive statistical census of the complex eddies processes, in comparison with the simple processes, is thus needed and the results may shed new light on the mechanisms that drive the splitting, merging, and even the migration patterns of the eddies in the SCS.

This paper reports a comprehensive census of the complex eddy processes in the SCS from 1993 to 2016. The aim of this study is to examine the spatiotemporal characteristics of the complex eddy processes in the SCS to better understand their spatial distribution and mobility patterns in comparison with those of the simple processes. The movement patterns of eddy processes not only reflect their evolution characteristics but also imply the spatial interaction between the different geographic locations where the eddies pass. In this study, we used a variety of Geographic Information System (GIS)-based methods and network data mining method, including kernel density, hot spot analysis, and community detection, to examine the complex eddy processes.

The kernel density analysis calculates the density of point or linear features within a neighborhood around those features. The hot spot analysis identifies where features with either high or low values cluster spatially. Both kernel density and hot spot analysis are widely used in crime, utility, disease, rainfall, disasters, and wildlife mapping [37–39]. We applied these two methods to the SCS eddies to identify where the starting, demising, splitting, and merging locales are most clustered. Identifying the clustered locales would help us understand why certain locales are clustered at certain places. Community detection is an important method of network data mining, which is widely used to analyze the regional and mobile characteristics of objects such as mobile phone users and web graph in space [40,41]. The community detection method is used to delineate the SCS into different communities. We then examine the activities of the eddies within a community and between two adjacent communities to identify interaction among different communities (regions) in the SCS.

The paper is organized as follows. Section 2 introduces the data sets and methods used in this study. Section 3 focuses on the analysis results and we also compare and discuss the characteristics of the complex and simple eddy processes in the SCS. Section 4 focuses on the influence of topography on the splitting and merging of the complex eddy processes. Finally, we summarize this study and outline our future work in Section 4.2.

2. Data and Methods

2.1. Data

This study used the SLA data from January 1993 to December 2016. The SLA dataset is widely used in studying eddies [38] and has a temporal resolution of 1 day and a spatial resolution of ¼ degree [42]. We developed and improved the eddy identification and tracking methods and built a spatiotemporal database, from which every eddy in the SCS could be queried and studied for different purposes. In our dataset, there were 5773 eddy processes (3452 simple and 2321 complex processes). We provided a brief description of the data processing and data accuracy assessment results below. More details are available in Yi et al. [9,43–45].

The eddies in our database were identified using a hybrid detection (HD) method [43], which takes the advantages of the two widely-used eddy identification methods: the Okubo–Weiss (OW) [46,47] and the Sea Surface Height (SSH) [8] methods. An eddy truly exists only if it meets the OW criterion ($W < -0.2\sigma w$, where σw is the spatial standard deviation of W, and W is computed from the horizontal velocity field as $W = Sn^2 + Ss^2 - \omega$, where Sn, Ss, and ω are the straining deformation rate, the shearing deformation rate, and the vorticity, respectively) and includes either a local maximum or minimum SLA value. The identification results derived from the HD, OW, and SSH methods were compared, showing success rates of 96.6%, 96.6%, 100% and failure rates of 14.2%, 70.3%, 36.8%, respectively. Overall, the HD method outperformed the other two methods in correctly identifying eddies in the SCS [43].

The eddies identified were then concatenated using the method proposed by Yi et al. [44]. It is very common that an eddy is concatenated to a wrong predecessor or successor, particularly when an eddy splits, merges, disappears, and reappears. A global nearest neighbor filter (GNNF) approach [44], which combines the Kalman filter and optimal data association technologies to recursively recover the predecessor and successor of a specific eddy. The GNNF tracking results of the eddies in the SCS were compared with those derived from the distance-based search [48] and the overlap-based search [49] methods. The mismatching rates were 0.19%, 0.30% and 1.17% for these three methods respectively. The three methods were also used to track synthetic eddy trajectories with mismatching rates 0.2%, 0.4% and 0.5%, respectively. The comparison shows that the GNNF approach had its advantages in concatenating eddies.

2.2. Methods

In this study, an eddy process is represented as a trajectory with multiple points in chronological order (p1, p2, p3 . . . . . . pn). Every point along the trajectory was defined with its longitude, latitude, and a timestamp (pi = (xi, yi, ti)). The trajectory could bear with or without branches. A structure containing no branches would represent a simple eddy process and otherwise a complex process (Figure 1). Any branch along the trajectory would represent either a splitting or a merging event.

The complexity of a trajectory was first quantitatively measured by a complexity index η ($0 < \eta \leq 1$), which is the ratio between the number of the points along the branch(es) and all points on the trajectory. Figure 1a illustrates a complex trajectory. At a specific time-stamp, the eddy represented by point p3 splits into two eddies p4 and p5, which then merge into eddy p7. At another time-stamp, eddies p8 and p9 merge into eddy p10, which then splits into eddies p11 and p12. The total number of points along this trajectory is 13 and nine of them are on the branches. Therefore, the η is 0.69. A simple eddy trajectory (Figure 1b) is a linear structure without any branches thus has a complexity index 0 ($\eta = 0$).

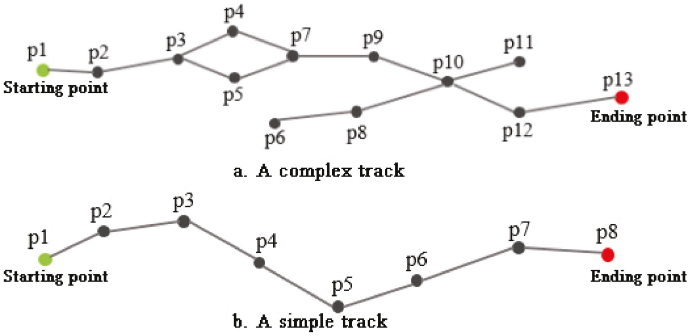

Figure 1. A complex trajectory (**a**) and a simple trajectory (**b**).

In this study, conceptually the eddy trajectories could be represented as different objects: feature points, lines, and then networks. A variety of methods were used to statistically examine these objects (Figure 2). We first conducted kernel density and hot spot analysis on the feature points. Then we used a series of activity parameters to describe the movement characteristics of the feature points. The networks, formed by the points and lines, were examined using the fast folder community detection method [41]. The sections to follow provide more details about these methods.

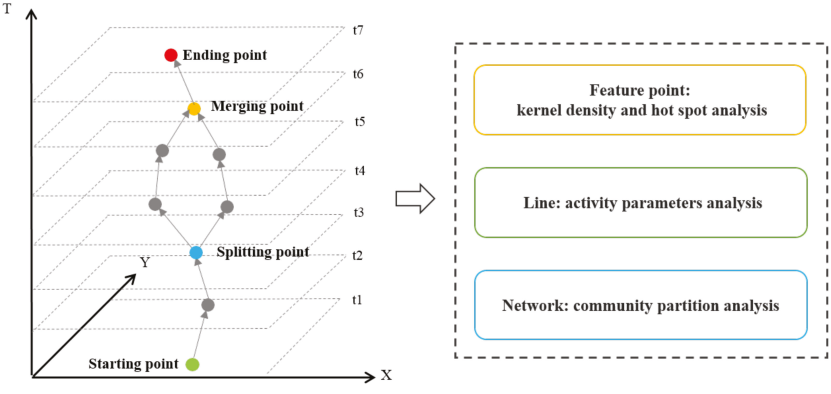

a. A complex eddy process **b. Methods**

Figure 2. A diagram showing the structure of an eddy trajectory, which is represented as different objects (points, lines, and networks) (**a**), which were then examined using different methods (**b**).

2.2.1. Kernel Density and Hot Spot Analysis

We first conducted spatial kernel density and hot spot analysis on the feature points, which include the starting, ending, splitting, and merging points along the trajectories of cyclonic and anticyclonic eddies. Kernel density shows the concentration of points over an interpolated and smooth surface. In the places where points are clustered, the surface would have a higher density, which then gradually diminishes with increasing distance from the point clusters. The kernel density of the starting and ending points showed the places where eddies mainly originated and disappeared. By contrast, the kernel density of the splitting and merging points revealed the locales where the eddies tended to split and merge, probably due to the influence of different ocean environmental and climatic factors.

The Gi* method [50] was used to identify the hot and cold spots of the feature points by examining the z-score and *p*-value. A hot spot is a place where high-value features are surrounded by other high-value features. By contrast, a cold spot is a place where low-value features are clustered together. First, a 1° × 1° square fishnet was generated to cover the whole study area. We chose the 1° × 1° grid (about 108 km × 108 km in the SCS) as the radii of most eddies in the SCS are between 100 km and 200 km, and the average moving distance is 74 km [12,14]. Secondly, we counted the total number of every type of feature points in each grid. The counts and the Euclidean distance among the points were then used to calculate the Gi* values. Lastly, statistical significance was evaluated by looking at the z-score, *p*-value, and confidence level. A hot spot was identified when a z-score was greater than 1.65 and a *p*-value less than 0.10. In contrast, a low negative z-score (<-1.65) and a small *p*-value (<0.10) indicated a cold spot clustering, i.e., few eddies nearby.

2.2.2. Eddy Mobility Index

Activity space in geography is mainly used to examine human activities within a space [51,52]. We employed the same idea and computed four indexes, namely the complexity, activity duration, activity scope, and the number of activity points, to study how an eddy migrates within an activity space. The complexity, as discussed in Section 2.2, showed how complex an eddy trajectory is. The activity duration referred to the lifespan of an eddy, indicating how long an eddy process lasted. The activity scope was defined as the maximum distance between any two points along a specific track, indicating the maximum span within which an eddy was moving around. The number of activity points was the number of different positions that an eddy may occupy over its life span. More activity points suggested a more active eddy process.

2.2.3. Community Detection

A geographic area could be delineated into a set of communities, each of which has similar attributes and/or functions in a network graph [53]. Many partitioning methods have been developed for community detection. This study used the fast unfolding method [54]. Eddy movement essentially is inhomogeneous as eddies are more active in certain regions across the SCS [13]. From a GIS perspective, any movement from one position to another could be represented as a connection (i.e., an edge). Movements of a large number of eddies could be translated and represented as a complex network consisting of nodes and edges. The network could then be delineated into different communities (Figure 3). Within a specific community, the eddies were similar in terms of their characteristics. The eddies' characteristics showed homogeneity within a community but heterogeneity among communities.

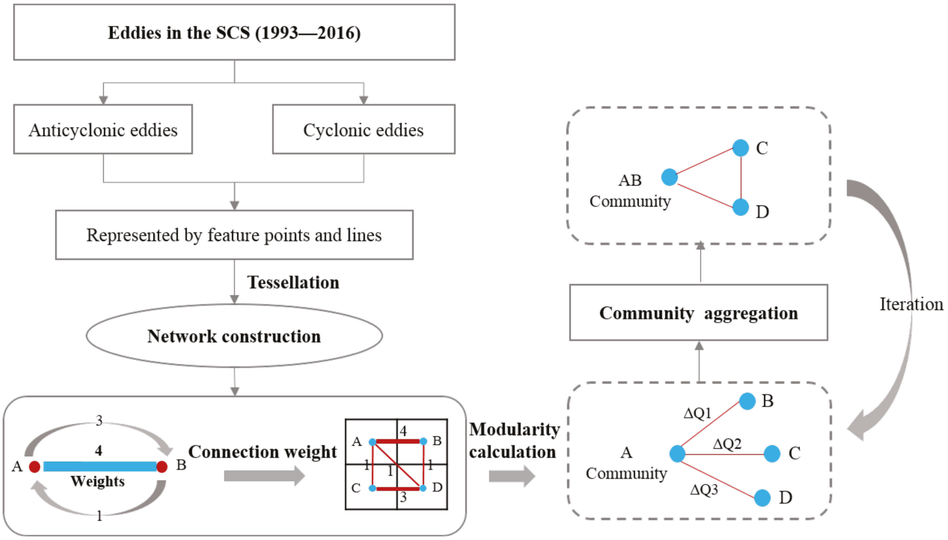

Figure 3. Community partition workflow.

The fast unfolding method includes two major steps in a sequence (Figure 3). The first step is to construct the movement network. We generated tessellated square grids of 1° × 1° to cover the whole study area and the center of each grid was represented as a node. We then counted the total number of eddies within each grid (node), respectively. The connections between any two adjacent grid nodes in the network were weighted using the total number of eddies that crossed their boundary. A network thus was constructed with the nodes representing the grids and edges the total number of eddies that crossed the boundary of two adjacent grids.

The second step was to partition the communities. Each node was regarded as a community and would be grouped with its neighboring nodes (communities) one by one. A modularity gain ΔQ was calculated as below [41].

$$\Delta Q = \left[\frac{\sum_{in} + k_{i,in}}{2m} - \left[\frac{\sum_{tot} + k_i}{2m}\right]^2\right] - \left[\frac{\sum_{in}}{2m} - \left[\frac{\sum_{tot}}{2m}\right]^2 - \left[\frac{k_i}{2m}\right]^2\right] \quad (1)$$

where m represents the total connection weights across the entire network, $\sum_{in}$ is the total connection weights within a specific community, $\sum_{tot}$ is the sum of all connection weights associated with nodes within the specific community, k_i is the sum of the weights of all the connections to node i, $k_{i,\,in}$ denotes the sum of the connection weights between nodes i and all the other nodes in the community. If the maximum ΔQ was greater than 0, the node would be grouped with its neighboring node. Otherwise, it stayed as it was. If a node was grouped into another community, a new network was constructed and the afore-mentioned procedure was repeated until no more nodes shifted to another community.

3. Results and Analysis

Over the study period from 1993 to 2016, 5773 tracks were identified and stored in our database. Among them, 2321 and 3452 were complex and simple eddy processes, respectively. The 2321 complex processes included 1120 and 1201 anticyclonic eddies (CPAEs) and cyclonic eddies (CPCEs), respectively. By contrast, 1682 and 1770 out of the 3452 simple processes were anticyclonic eddies (SPAEs) and cyclonic eddies (SPCEs), respectively.

3.1. Feature Points Analysis

3.1.1. Kernel Density Analysis of the Simple and Complex Eddy Processes

The kernel density difference of the starting and ending points of the SPAEs (Figure 4a) and SPCEs (Figure 4b) showed that the eastern SCS witnesses more births than deaths of SPAEs and SPCEs, respectively. The death places of SPAEs and SPCEs were scattered across the whole SCS.

The kernel density difference of the starting and ending points of the CPAEs (Figure 4c) and CPCEs (Figure 4d) showed that more CPAEs and CPCEs were born in the eastern SCS and disappeared mainly in the western SCS. Such a finding is consistent with previous studies conducted by Wang et al. [11], Xiu et al. [12], and Chen et al. [13], in which the simple and complex eddy processes were not differentiated and studied as a whole. In this study, we examined the simple and complex eddy processes separately and found that the complex processes mainly disappeared in the western SCS whereas the simple processes disappeared almost everywhere across the SCS.

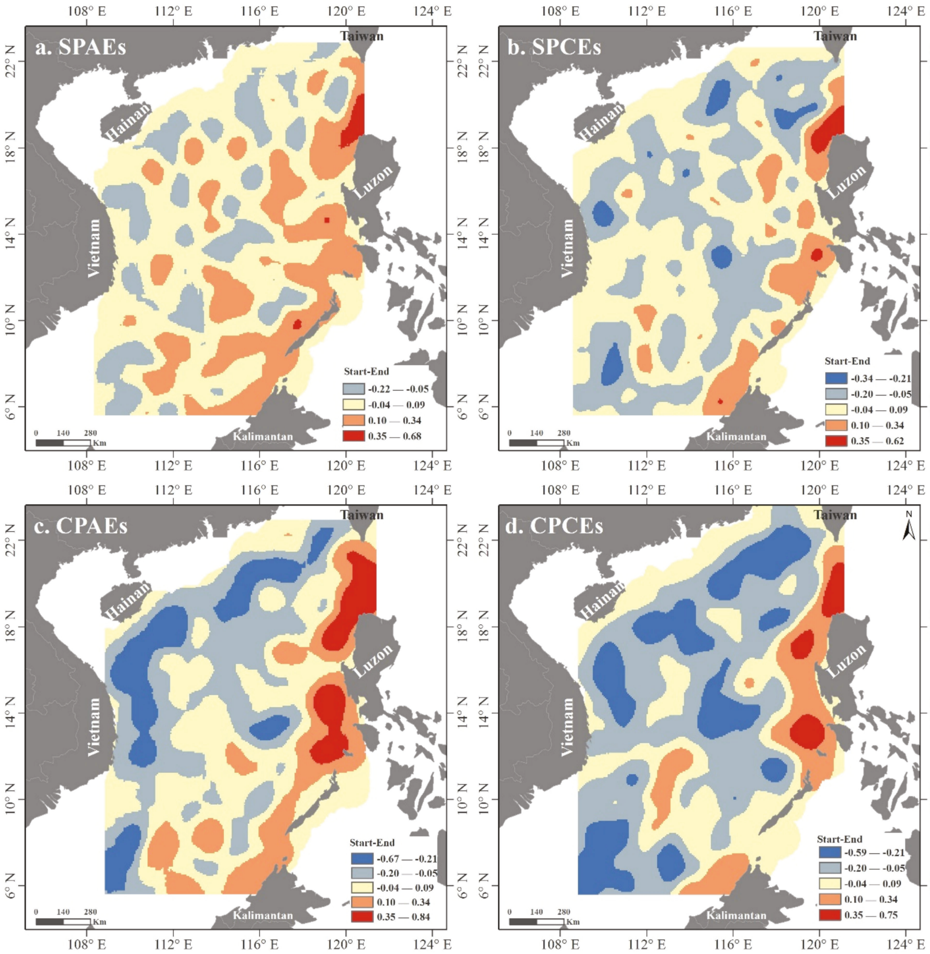

Figure 4. The difference of the kernel density of the starting and ending points of simple processes of anticyclonic eddies (SPAEs) (**a**), simple processes of cyclonic eddies (SPCEs) (**b**), complex processes of anticyclonic eddies (CPAEs) (**c**), and complex processes of cyclonic eddies CPCEs (**d**).

3.1.2. Hot Spot Analysis of Simple and Complex Eddy Processes

Figure 5 shows the hot and cold spots of where the simple and complex eddy processes originated, respectively. The hot spots were mainly located in the eastern SCS whereas the cold spots were mainly located in the western SCS. Such a pattern indicates that the eastern SCS was where most eddies start from. However, the hot spots of the complex eddy processes were more extensive and continuous in the eastern SCS, covering the area from the southwest of Taiwan, west of Luzon Strait and Luzon, Huangyan Island, Nansha Islands, northwest of the Kalimantan. By contrast, the hot spots of simple eddy processes were more isolated in the eastern SCS and could only be found in the southwest and northwest of Luzon and Palawan, southwest of Nansha Islands (7° N–9° N, 110° E–113° E). The same pattern was also found for the cold spots. Extensive cold spots were found for the complex eddy processes in the northwestern SCS. The cold spots of simple eddy processes were isolated and found in only a couple of grids in the east of Hainan Island and the southwestern SCS.

The difference between the hot and cold spots of the simple and complex eddy processes indicates that the complex processes originated from an extensive area in the eastern SCS. Very few complex eddy processes started from a quite extensive area in the northwestern SCS. By contrast, the simple processes mainly originated from three concentrated regions in the eastern SCS as shown in Figure 5a. There are only a couple of places in the western SCS that few simple processes originated from.

Both the kernel density and hot spot analysis indicated that the southwest of Taiwan Island, the west of Luzon Strait (Luzon strait between Taiwan Island and the Luzon Island) and the northwest of Luzon Island were where significant numbers of simple and complex processes started. Previous studies have shown that the local wind stress curl and Kuroshio intrusion contributed to the generation of both cyclonic and anticyclonic eddies in this area [33,55]. This study shows that origination of complex processes in this region could also be attributed to the local wind stress curl and Kuroshio intrusion. In Section 4.1.1, we discussed and analyzed how wind stress curl and Kuroshio intrusion affect the eddy evolution processes.

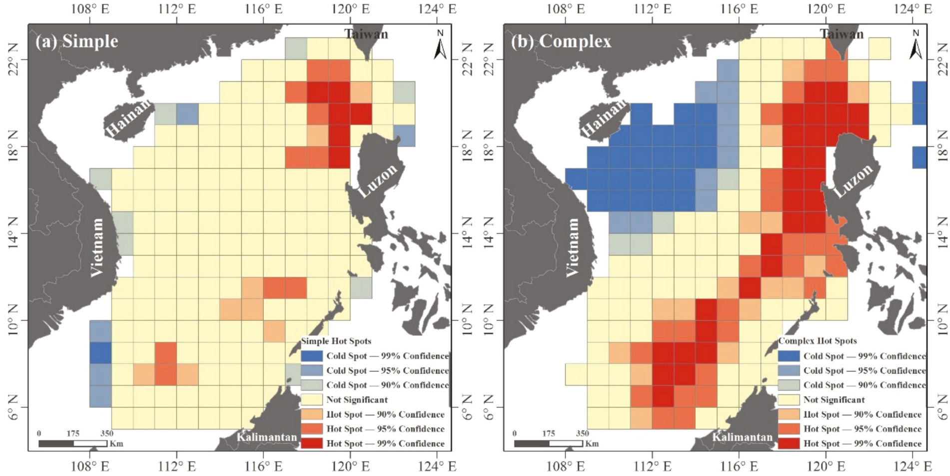

Figure 5. The hot and cold spots of the simple (**a**) and complex eddy processes (**b**).

3.1.3. Splitting and Merging of Complex Eddy Processes

Unlike the simple eddy processes, the complex eddy processes split and merge. On average, the complex eddy processes split and merged 75 and 45 times every year in the SCS (Figure 6a). The CPAEs and CPCEs showed no significant difference between the numbers of merging and splitting events (Figure 6a). However, the numbers of splitting and merging events varied significantly in different seasons, with 908 (542), 898 (539), 1013 (612), and 809 (495) splitting (merging) events occurring in the spring, summer, fall, and winter, respectively (Figure 6b). Fall was the most favorable season that the complex eddy processes tended to split and merge.

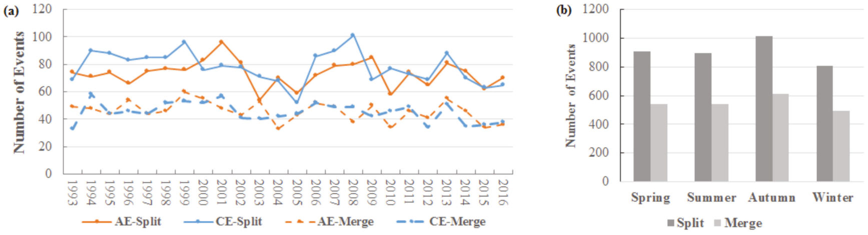

Figure 6. The statistics of splitting and merging events of CPAE and CPCE by year (**a**) and season (**b**).

The kernel density difference between the splitting and merging feature points shows that CPAEs merged more in the southwest of the Taiwan Island and the east of Vietnam, whereas they split more in the southeastern SCS (Figure 7a). By contrast, the CPCEs split more in the east of Luzon Island and the southwest of Taiwan Island (Figure 7b). In the southern SCS, the CPCEs split more except southeast of Vietnam. These regions were also where the eddies were concentrated, the differences in splitting/merging events between different areas will be discussed in Section 4.1.2.

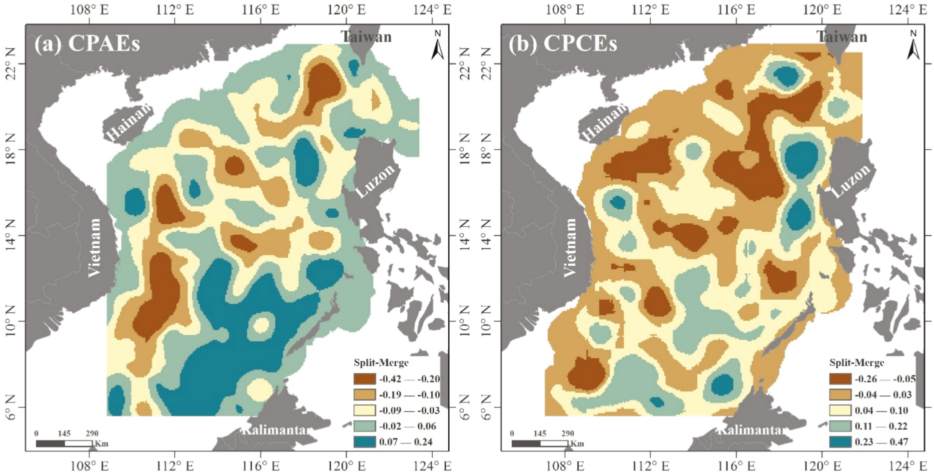

Figure 7. The kernel density difference between the splitting and merging feature points of CPAEs (**a**) and CPCEs (**b**).

3.2. Line Analysis

Figure 8 shows the trajectory density of all (a), complex (b), and simple eddy processes (c) in the SCS, respectively. There was no significant difference between the trajectory distribution of all and complex processes, with higher density in the southwest of Taiwan and northwest of Luzon, west of Mindoro, and east and south of Vietnam. The trajectories of simple processes also concentrated in the southwest of Taiwan and northwest of Luzon. However, more trajectories of simple processes were found across an extensive region in the southwestern SCS.

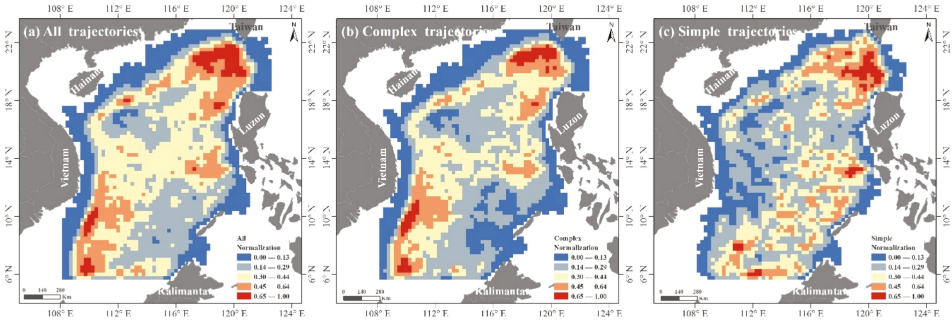

Figure 8. The grid-based trajectory density for all (**a**), complex (**b**), and simple (**c**) eddy processes.

The simple and complex eddy processes were also different in terms of the mobility indexes, including the activity duration, activity scope, and the number of activity points (Table 1). The complex eddy processes had a much longer activity duration (33.5 days) than that of the simple eddy processes

(8 days). Both the activity scope and the number of activity points were over three times more extensive than those of the simple eddy processes. About 90% of the simple eddy processes have less than 10 active points and the travel range was less than 150 km in a lifespan less than 28 days (Figure 9). By contrast, about 90% of complex eddy processes had less than 43 active points and the travel range was less than 503 km in a lifespan less than 123 days. More than 80% of the complex eddy processes had a complexity index between 0.3 and 0.8 and the complexity index of the simple eddy processes, of course, was 0. All the differences between the means of all three mobility indexes were statistically significant (Table 1). However, there was no significant difference between the mobility indexes of the SPAEs and SPCEs. There were significantly more CPCEs than CPAEs with a complex index of 0.5 (Figure 9).

Table 1. Comparison of the means between the simple and complex eddy processes. The last column shows the significance test results of the Mann–Whitney U test for the mobility indexes.

Mobility Indexes	Simple Processes	Complex Processes	Sig.
Activity duration (days)	8	35	0.000
Scope of activity (km)	71.36	224.3	0.000
Number of activity points	5	16	0.000

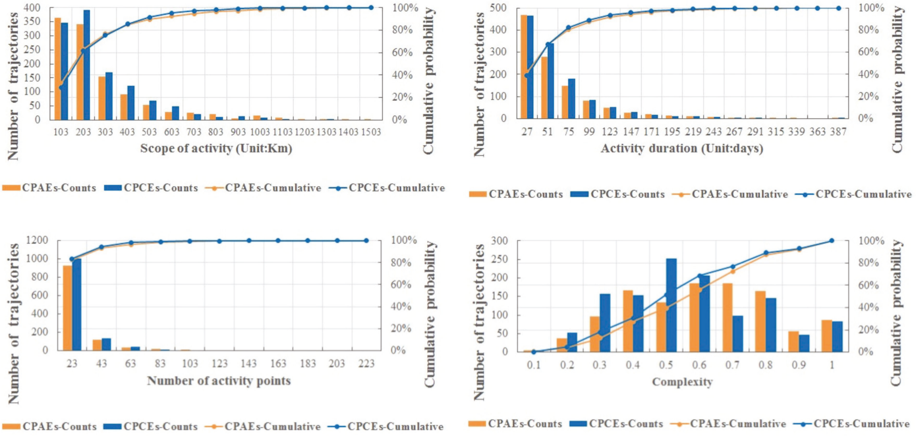

Figure 9. Statistics of the mobility indexes of CPAEs and CPCEs.

3.3. Network Analysis

The SCS beyond the 200-m bathymetry contour line could be divided into eight communities based on the networks built from all, simple, and complex eddy processes, respectively (Figure 10). The communities were roughly similar. Particularly, the community delineation results based on the complex- and all-eddy networks were very similar (Figure 10a,c). Roughly, the northern, central, and southern SCS could be divided into three, two, and three communities, respectively. However, difference does exist. For example, only one community was partitioned from the all-eddy networks in the southern part of the southern SCS (C8 in Figure 10a), whereas this region was divided into two simple- and complex-eddy communities, separately. A community was identified in the east of Hainan Island and Vietnam based on the simple-eddy networks (C3 in Figure 10c). This region was divided into two communities based on the complex- and all-eddy networks.

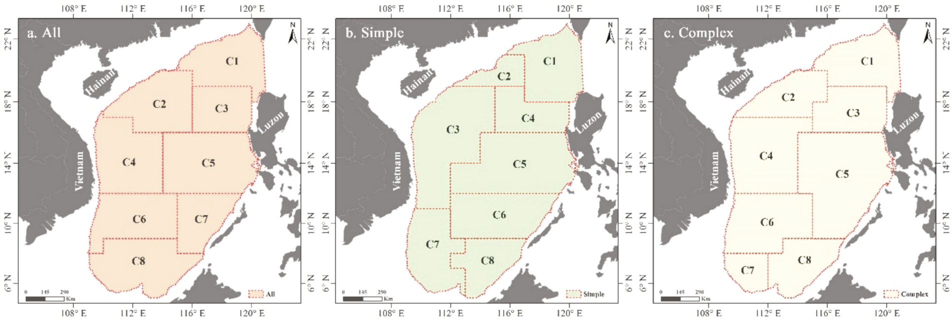

Figure 10. The community delineation results based on the all- (**a**), simple- (**b**), complex-eddy processes (**c**).

We then mainly focused on discussing how the SCS could be divided into different communities based on the networks constructed with the CPAEs (complex processes of anticyclonic eddies) and CPCEs (complex processes of cyclonic eddies) separately. The delineation results were very similar for the northern and southern SCS (Figure 11) but not for the central SCS. For example, the communities could be delineated for the central SCS based on the complex anticyclonic eddy networks (C4–C6 in the Figure 11a). However, no such communities were identified in the central SCS based on the networks of complex cyclonic eddy processes (Figure 11b). The complex cyclonic eddy processes-derived communities (C6–C7 in Figure 11b) in the central SCS tended to extend into either the northern or the southern SCS.

Eddy processes frequently migrated between adjacent communities. The interaction patterns of the complex anticyclonic and cyclonic eddy processes shared many similarities yet also with a significant difference. The CPAEs and CPCEs moved more frequently in the southwest of Taiwan Island (CPAEs-C1, CPCEs-C1), northwest of Luzon Island (CPAEs-C3, CPCEs-C3) and southeast of Vietnam (CPAEs-C7, C8, CPCEs-C6, C8) and much less in the southeastern SCS (CPAEs-C9, CPCEs-C7).

In the northern SCS, the CPAEs mainly migrated from C3 to C2 along the 18° N parallel from the northwest of the Luzon Island to the east of the Hainan Island. The CPAEs processes also frequently flowed from communities C1 to C2 along the shelf slope of the northern SCS from the southwest of Taiwan to the southeast of Hainan [56,57].

In the central SCS, the CPAEs mainly migrated westward from communities C6 to C4 between the 12° N and 16° N parallels (from the southwest of the Luzon Island to the northeastern Vietnam). In the southern SCS, there were strong interactions of CPAEs between communities C7 and C8, and from C9 to C7. In general, CPAEs showed strong interactions along the parallels between communities in the northern (C3 and C2), central (C6, C5 and C4), and southern (C8 and C7) SCS. Stronger regional interaction in the southeastern Vietnam Sea and the dominant westward migration across the central SCS are consistent with what was reported in previous studies [12–14].

The CPCEs in the northern SCS (Figure 11b) showed a strong interaction between the communities in the west of the Luzon Strait (C1) and the northwest of Luzon (C3). In the central SCS (C4, C5, C6, C7), interaction was more notable between C5 and C7 in the southwest of Luzon. In the southern SCS, interaction was more prominent in southeastern Vietnam between communities C6 and C8, C9 and C8.

Compared to the CPAEs, the CPCEs also showed significant interactions among communities along the meridian direction in the eastern SCS (C1, C3, C5, C7), which accounted for about 36% of the total CPCEs interaction in the SCS. Modeling results about how an island/seamount splits eddies showed that, after splitting, CPAEs tended to propagate southwestward while CPCEs did so toward the northwest [32]. The same patterns were not only observed in the splitting but also the merging processes in this study.

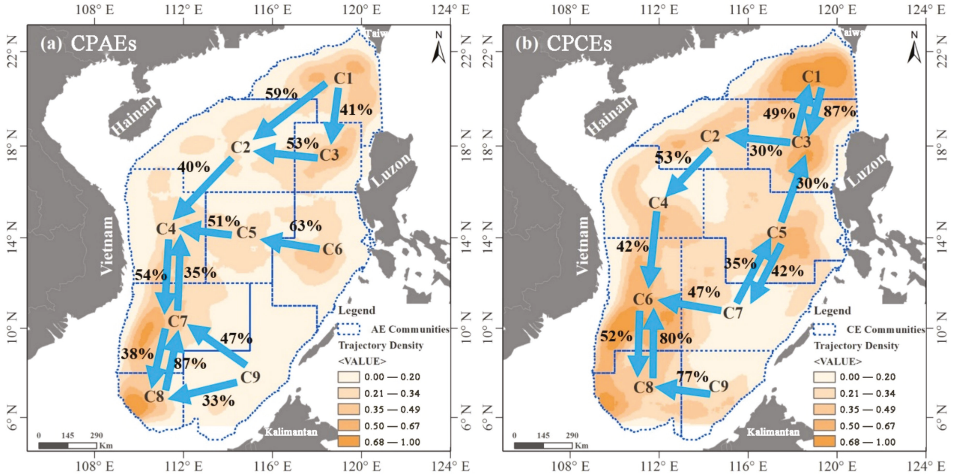

Figure 11. The community division results of CPAEs (**a**) and CPCEs (**b**). The numbers show the percentages of the eddies that migrate along with the dominate flow directions, which are shown by the blue arrows.

Within the community (Figure 12), both the CPAEs (a) and CPCEs (b) showed a dominant westward propagation direction, mainly due to the beta effect [55]. In the northwest of Luzon, quite large portions of the CPAEs and CPCEs (CPAEs-C3, CPCEs-C3) moved northward. In the southeast of Vietnam offshore, there were slightly more north–south than east–west eddy migration, probably because of the uneven Coriolis force [36].

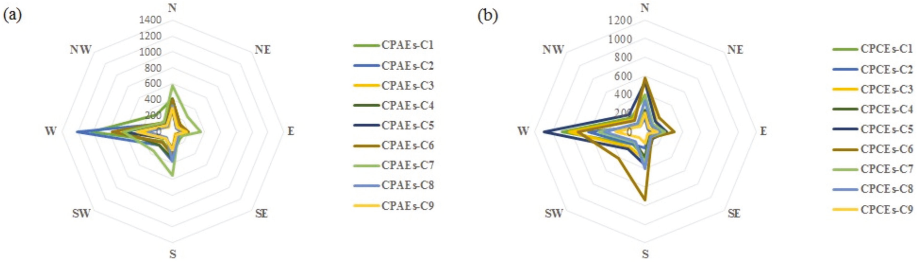

Figure 12. The inter-community movement directions of CPAEs (**a**) and CPCEs (**b**).

4. Discussion and Summary

4.1. Discussion

4.1.1. The Generation and Extinction of Simple and Complex Eddy Processes

Our results show that both complex and simple eddy processes are mainly born in the eastern SCS, including the southwest of Taiwan Island, the west of Luzon Strait, the northwest of Luzon Island. This is mainly due to the strong wind stress curl variations and the intrusion of the Kuroshio in these areas [33–55].

The local wind stress curl is mainly controlled by the Asian monsoon, which can be divided into the winter (November to April) and summer (mid-May to mid-September) monsoon. Due to the topographic and narrow tube effects, the winds in the southwest of Taiwan, west of Luzon Strait and northwest of the Luzon Island are stronger than those in other regions in the SCS, especially during the winter monsoon period [34]. Under such a constraint, the surface water tends to move as a fast jet at the place with stronger wind shear potential. The jet flow would be blocked once it reaches the edge of the water and the water would reverse and move along the regions with weaker wind shear potential. Such an unstable water flow field make this region an active place of eddy formation [11,13,26]. The local wind stress curl may cause Ekman effect in this region [34]. The Ekman downwelling prevents the deep cold water from advecting upward and is favorable for the formation of anticyclonic eddies. By contrast, the Ekman upwelling is favorable for the formation of cyclonic eddies.

In addition to the local wind stress curl, the Kuroshio intrusion [33,58] is another significant contributor to eddy generation in the Luzon Strait. Previous studies have shown that Kuroshio intrusion can cause baroclinic instability and subsequently a horizontal density gradient. A large enough horizontal density gradient would provide enough energy and mass for the generation of mesoscale eddies in the SCS [33]. In the Luzon Strait, the Kuroshio may form a "current jacket", which could shear mesoscale eddies [58,59].

For the extinction of eddy processes, both simple and complex eddy processes mainly migrate toward the west because of the beta effect [55]. The complex eddy processes, with a longer life span than the simple eddy processes tend to travel longer toward the west (Table 1). As a result, they mainly disappear in the western SCS. However, the simple eddy processes travel a shorter distance due to their shorter life spans and smaller ranges of activity (Table 1) and consequently show no concentrated extinction zones in the SCS.

4.1.2. Variations in Splitting and Merging Events in Different Regions in the SCS

Interactions among eddies through splitting and merging could be another factor that leads to new eddy formation. Our study shows that the regions in the SCS with significant splitting and merging events also witness the significant formation of eddies. The regions with significant eddy splitting and merging tend to be packed with more eddies and therefore more frequent or even stronger interactions among the eddies. Such interactions may form more new-born eddies.

Spatial distribution in eddy splitting and merging events probably indicate how the factors locally impact the eddy evolution processes. More splitting in the western Luzon Island may be attributed to the seabed topography, which is more complex in the west of Luzon Island [33]. Results from this study are consistent with previous studies [31], showing that topography is the major factor the triggers eddy splitting and merging events. This study also shows the west of Luzon Island probably is an ideal place for scientists to model the relationship between the eddy splitting activities and the topography, which, however, obviously is not the only factor leading to eddy splitting and merging.

We also found that, in the southwest of Taiwan, CPAEs tend to merge whereas CPCEs tend to split more. It is likely that this phenomenon could also be attributed to wind stress and the Kuroshio intrusion, which significantly affect the oceanic environment of this area [56]. Our knowledge about the SCS is not enough to elaborate on why CPAEs and CPCEs are prone to merging and splitting in this area, respectively. In fact, dense observation stations have been deployed in this area, providing enough data for physical oceanographers to investigate the mechanism behind this phenomenon. A more thorough discussion about the effects of topography and wind stress curl on eddy splitting and merging is available in the discussion Section 4.1.3.

In the southeast of Vietnam, both CPAEs and CPCEs tend to merge more, though they both also split. The strong eastward jet shooting away from the coast in this region pushes anticyclones to move southward and cyclones move northward [27]. It also significantly disturbs the water masses in this region, which forces CPAEs and CPCEs to either merge or split.

4.1.3. Topography and Wind Stress Curl Effects

Previous studies have shown that, in other oceans, seabed topography may cause an eddy to split or merge and thus significantly affects the evolution and structure of eddies [28,29]. To understand how the seabed topography in the SCS affects the eddy evolution, we used GIS spatial analysis tools to calculate the slope of the seabed topography in the SCS. Here the slope refers to the maximum rate of change in elevation from a cell to its immediate neighbors. In this study, the cell was defined as a grid of 1° × 1° (about 108 km × 108 km in the SCS). We chose this resolution as the radii of most eddies in the SCS are between 100 km and 200 km, and the average moving distance is 74 km [12,14]. The slope was calculated for each cell from the seabed topographic data that was obtained from National Centers for Environmental Information. We then calculated the number of splitting and merging events within each grid. The calculation results, including the total number of grids and the number of grids that splitting and merging events occurred at least four times, were summarized by slope ranges (Table 2).

Table 2. The percentage of splitting and merging events in different slope ranges.

Slope Range	Number of Grids	CPAEs		CPCEs	
		Splitting	Merging	Splitting	Merging
(0–10)	17	41.18%	47.06%	41.18%	41.18%
(10–20)	28	71.43%	71.43%	75.00%	78.57%
(20–30)	48	77.08%	64.58%	81.25%	65.75%
(30–40)	51	76.47%	58.82%	76.47%	52.94%
(40–50)	20	90.00%	75.00%	85.00%	75.00%
(50–60)	7	100.00%	100.00%	100.00%	100.00%

The eddies were more prone to splitting or merging in areas with a steeper slope. The percentages of the CPAEs and CPCEs that merged or split increased four times and more significantly increased with the increased seabed slopes, indicating the rugged seabed tends to disturb the eddies more significantly (Table 2). All (100%) of the CPAEs and CPCEs passing through the grids with a slope over 50 degrees either split or merge at least four times over our study time period. By contrast, roughly half (41%–47%) of the CPAEs and CPCEs merge or split four times within the cells with a seabed slope less than 10 degrees. Eddies in the southwest of Taiwan and the west of Luzon Island were also prone to splitting and merging as these two areas have an average slope of 37 and 39 degrees, respectively.

In addition to the topography, other factors such as wind stress, background currents, and Kuroshio invasion may also influence eddy splitting and merging. Wang et al. [11] pointed out that the wind stress curl formed by the interaction between wind and topography may be one of the important mechanisms for the formation of mesoscale eddies in the SCS. The southwest of Taiwan and the northwest of Luzon are the active areas of eddy formation, splitting, and merging. This study also showed that the eddy splitting and merging events in the SCS more frequently occurred in autumn. This is the reason when summer monsoon starts to weaken and winter monsoon starts to strengthen. Under such an unstable wind field, multi-eddy structures frequently appear in the upper circulation. The multi-eddy structure generally is a transitional state before eddy splitting, and/or merging. Once the winter monsoon dominates the northern SCS, wind stress significantly increases in the southeast of Taiwan and the west of Luzon Island due to the narrow tube effect [34]. The interaction between the wind stress and the topography probably further enhances eddy splitting and merging in these areas. However, further studies are needed to clearly illustrate how the topography and wind combine to drive the eddies to split or merge.

4.1.4. The Interaction of Complex Eddy Processes among Communities in the SCS

In the northern and central SCS, both the CPAEs and CPCEs processes mainly propagate westward and the CPCEs also northward and southward in the west of Luzon. The remarkable westward migration trend is mainly due to the beta effect [55]. In the southern SCS, CPAEs and CPCEs show no uniform propagation direction but the north–south interactions are more frequent in the regions next to southeastern Vietnam. The strong eastward jet shooting away from the Vietnam coast pushes anticyclones to move southward and cyclones move northward in the southeastern of Vietnam [27].

Previous studies have also shown that significant poleward heat transfer occurs in the east of Vietnam in summer and the west of Luzon Island in winter, whereas large equatorward heat transfer occurs in Western Luzon Strait in winter [60]. However, it is not clear whether the same patterns of heat transfer could be found in other areas in the SCS due to the limitation of time scale and space range of the observation data [27,60]. Our results show that the interactions among communities show very similar heat transfer patterns across the whole SCS, as reflected by the eddy migration patterns (Figures 11 and 12). Further studies are needed to use the observation data, when they become available, to confirm the heat transfer patterns in the other SCS regions except for the east of Vietnam, west of Luzon Island, and Western Luzon Strait. Once the heat transfer patterns are identified for the whole SCS, we may better unravel the underlying physical mechanisms that drive the eddy-induced heat transfer in the SCS.

4.2. Summary

This study examined the mesoscale eddies in the SCS from a GIS perspective. As a real-world phenomenon, eddies could be represented either as a point, a line, or a polygon. The point and line then form a network, showing the connection and interactions among the eddies. In this study, we translated the eddies in the SCS into points, lines, and networks. Different GIS analysis methods were used to examine these three types of objects and unravel the kernel density and hotspots of the starting, ending, splitting and merging points, eddy migration patterns, eddy exchange, and interactions among communities in the SCS. We studied the difference of all the afore-mentioned aspects between the simple and the complex eddy processes, as well as between the anticyclonic and cyclonic eddies in the SCS.

Our results show that both the complex and simple eddy processes are mainly born in the eastern SCS, including the west of Luzon Strait, the northwest and southwest of Luzon Island. This is mainly due to the strong wind stress curl variations and the intrusion of the Kuroshio in these areas [33,55]. Both simple and eddy processes mainly migrate toward the west due to the beta effect [55]. The complex processes mainly disappear in the western SCS whereas the simple processes disappear almost everywhere across the SCS because of the different life span and scope of activity.

The CPAEs show more merging than splitting events in the southwest of Taiwan Island and the east of Vietnam. By contrast, the CPCEs mainly split in the southwest of Taiwan Island and the west of Luzon. Merging also frequently occurs in the southeastern SCS for both CPAEs and CPCEs. More rugged topography tends to trigger more splitting and merging events, particularly when the slope is more than 50 degrees (Table 2). However, it is not clear why the eddies merge or split more in some specific regions and less in other regions. Temporally, most splitting and merging events occur in the fall, when the wind direction starts to reverse in the SCS.

The SCS could be divided into the different number of communities based on the networks built from all-, simple-, and complex-eddy processes, separately. The community delineation results, as well as the eddy interaction and exchange among the communities share similarities but difference does exist. The most active inter-community interactions are mainly found in the southwest of Taiwan Island, the west of Luzon Island and the southeast of Vietnam. These are the regions where most eddies were born and then start to travel westward. The interactions between adjacent communities reveal the dominant migration pattern of both CPAEs and CPCEs from a totally different perspective. In the northern and central SCS, both the CPAEs and CPCEs processes mainly propagate westward. In the southern SCS, CPAEs and CPCEs show no uniform propagation direction but the north–south interactions are more frequent in the regions next to southeastern Vietnam due to the strong eastward jet shooting away from the Vietnam coast [27].

In short, multiple factors including the Kuroshio intrusion, local wind stress, topography, and the beta effect could all affect the behaviors of complex eddy processes in the SCS. Contributions of these factors tend to vary in different regions in the SCS. More comprehensive studies are needed to better reveal their different contributions in different regions.

Author Contributions: Conceptualization, H.W. and Y.D.; methodology, H.W.; software, Y.S.; validation, H.W., Y.D. and F.L.; formal analysis, H.W.; investigation, H.W.; resources, J.Y.; data curation, J.Y.; writing—original draft preparation, H.W.; writing—review and editing, F.L.; visualization, Y.S.; supervision, Y.D.; project administration, Y.D.; funding acquisition, Y.D.

Funding: This work was supported in part by a grant from the National Science Foundation of China (41671445), National Key R&D Program of China (2017YFB0503605).

Conflicts of Interest: The authors declare no conflict of interest.

References

1. Holland, W.R.; Lin, L.B. On the origin of mesoscale eddies and their contribution to the general circulation of the ocean. I. A preliminary numerical experiment. *J. Phys. Oceanogr.* **1975**, *5*, 642–657. [CrossRef]
2. Holland, W. The role of mesoscale eddies in the general circulation of the ocean—Numerical experiments using a wind-driven quasigeo-strophic model. *J. Phys. Oceanogr.* **1978**, *8*, 363–392. [CrossRef]
3. Adams, D.K.; Mullineaux, L.S. Surface-Generated Mesoscale Eddies Transport Deep-Sea Products from Hydrothermal Vents. *Science* **2011**, *332*, 580–583. [CrossRef] [PubMed]
4. Cotroneo, Y.; Aulicino, G.; Simón, R. Glider and satellite high resolution monitoring of a mesoscale eddy in the algerian basin: Effects on the mixed layer depth and biochemistry. *J. Mar. Syst.* **2016**, *162*, 73–88. [CrossRef]
5. McGillicuddy, D.J., Jr. Mechanisms of Physical-Biological-Biogeochemical Interaction at the Oceanic Mesoscale. *Annu. Rev. Mar. Sci.* **2016**, *8*, 125–159. [CrossRef] [PubMed]
6. Keffer, T.; Holloway, G. Estimating Southern Ocean eddy flux of heat and salt from satellite altimetry. *Nature* **1988**, *332*, 624–626. [CrossRef]
7. Font, J.; Isern-Fontanet, J.; Salas, J.J. Tracking a big anticyclonic eddy in theWestern Mediterranean Sea. *Sci. Mar.* **2004**, *68*, 331–342. [CrossRef]
8. Chelton, D.B.; Schlax, M.G.; Samelson, R.M. Global observations of nonlinear mesoscale eddies. *Progr. Oceanogr.* **2011**, *91*, 167–216. [CrossRef]
9. Yi, J.; Du, Y.; Zhou, C. Automatic Identification of Oceanic Multieddy Structures from Satellite Altimeter Datasets. *IEEE J. Sel. Top. Appl. Earth Obs. Remote Sens.* **2015**, *8*, 1555–1563. [CrossRef]
10. Chaigneau, A.; Gizolme, A.; Grados, C. Mesoscale eddies off Peru in altimeter records: Identification algorithms and eddy spatio-temporal patterns. *Prog. Oceanogr.* **2008**, *79*, 106–119. [CrossRef]
11. Wang, G.; Su, J.; Chu, P.C. Mesoscale eddies in the South China Sea observed with altimeter data. *Geophys. Res. Lett.* **2003**, *30*, 2121. [CrossRef]
12. Xiu, P.; Chai, F.; Shi, L. A Census of Eddy Activities in the South China Sea during 1993–2007. *J. Geophys. Rese.-Oceans* **2010**, *115*. [CrossRef]
13. Chen, G.; Hou, Y.; Chu, X. Mesoscale eddies in the South China Sea: Mean properties, spatiotemporal variability, and impact on thermohaline structure. *J. Geophys. Res.* **2011**, *116*, 1–20. [CrossRef]
14. Du, Y.; Yi, J.; Di, W. Mesoscale oceanic eddies in the South China Sea from 1992 to 2012: Evolution processes and statistical analysis. *Acta Oceanol. Sin.* **2014**, *33*, 36–47. [CrossRef]
15. Cheng, Y.H.; Ho, C.R.; Zheng, Q. Statistical features of eddies approaching the Kuroshio east of Taiwan Island and Luzon Island. *J. Oceanogr.* **2017**, *73*, 427–438. [CrossRef]
16. Pujol, M.I.; Larnicol, G. Mediterranean sea eddy kinetic energy variability from 11 years of altimetric data. *J. Mar. Syst.* **2005**, *58*, 121–142. [CrossRef]
17. Cotroneo, Y.; Budillon, G.; Fusco, G.; Spezie, G. Cold core eddies and fronts of the Antarctic Circumpolar Current south of New Zealand from in situ and satellite data. *J. Geophys. Res.* **2013**, *118*, 2653–2666. [CrossRef]
18. Ansorge, I.J.; Jackson, J.M.; Reid, K. Evidence of a southward eddy corridor in the south-west Indian ocean. *Deep Sea Res. Part II Top. Stud. Oceanogr.* **2015**, *119*, 69–76. [CrossRef]
19. Pessini, F.; Olita, A.; Cotroneo, Y.; Perilli, A. Mesoscale eddies in the Algerian Basin: Do they differ as a function of their formation site? *Ocean Sci.* **2018**, *14*, 669–688. [CrossRef]
20. Aulicino, G.; Cotroneo, Y.; Ruiz, S.; Sanchez Roman, A.; Pascual, A.; Fusco, G.; Tintore, J.; Budillon, G. Monitoring the Algerian Basin through glider observations, satellitealtimetry and numerical simulations along a SARAL/AltiKa track. *J. Mar. Syst.* **2018**, *179*, 55–71. [CrossRef]

21. Cotroneo, Y.; Aulicino, G.; Ruiz, S.; Sánchez Román, A.; Torner Tomàs, M.; Pascual, A.; Fusco, G.; Heslop, E.; Tintoré, J.; Budillon, G. Glider data collected during the Algerian Basin Circulation Unmanned Survey. *Earth Syst. Sci. Data* **2019**, *11*, 147–161. [CrossRef]
22. Olita, A.; Ribotti, A.; Sorgente, R.; Fazioli, L.; Perilli, A. SLA-chlorophyll-a variability and covariability in the Algero-Provençal Basin (1997–2007) through combined use of EOF and wavelet analysis of satellite data. *Ocean Dyn.* **2011**, *61*, 89–102. [CrossRef]
23. Yang, H.J.; Liu, Q.Y. The seasonal features of temperature distributions in the upper layer of the South China Sea (in Chinese with English abstract). *Oceanol. Limnol. Sin.* **1998**, *29*, 385–393.
24. Yuan, D.; Han, W.; Hu, D. Surface Kuroshio path in the Luzon Strait area derived from satellite remote sensing data. *J. Geophys. Res. Oceans* **2006**, 111. [CrossRef]
25. Chow, C.H.; Hu, J.H.; Centurioni, L.R.; Niiler, P.P. Mesoscale Dongsha Cyclonic Eddy in the northern South China Sea by drifter and satellite observations. *J. Geophys. Res. Oceans* **2008**, 113. [CrossRef]
26. Lin, P.F.; Fan, W.; Chen, Y.L. Temporal and spatial variation characteristics on eddies in the South China Sea I. Statistical analyses. *Acta Oceanol. Sin.* **2007**, *29*, 14–22.
27. Chen, G.; Hou, Y.; Zhang, Q.; Chu, X. The eddy pair off eastern Vietnam: Interannual variability and impact on thermohaline structure. *Cont. Shelf Res.* **2010**, *30*, 715–723. [CrossRef]
28. Fang, F.; Morrow, R. Evolution, movement and decay of warm-core Leeuwin Current eddies. *Deep Sea Res. Part II Top. Stud. Oceanogr.* **2003**, *50*, 2245–261. [CrossRef]
29. Rodríguez, R.; Viudez, A.; Ruiz, S. Vortex Merger in Oceanic Tripoles. *J. Phys. Oceanogr.* **2011**, *41*, 1239–1251. [CrossRef]
30. Nan, F.; He, Z.; Zhou, H. Three long-lived anticyclonic eddies in the northern South China Sea. *J. Geophys. Res. Oceans* **2011**, 116. [CrossRef]
31. Li, Q.Y.; Sun, L.; Lin, S.F. GEM: A dynamic tracking model for mesoscale eddies in the ocean. *Ocean Sci. Discuss.* **2016**, *12*, 1249–1267. [CrossRef]
32. Yang, S.; Xing, J.; Chen, D. A modelling study of eddy-splitting by an Island/Seamount. *Ocean Sci.* **2017**, *13*, 1–25. [CrossRef]
33. Nan, F.; Xue, H.; Yu, F. Kuroshio intrusion into the South China Sea: A review. *Prog. Oceanogr.* **2015**, *137*, 314–333. [CrossRef]
34. Chi, P.C.; Chen, Y.; Lu, S. Wind-driven South China Sea deep basin warm-core/cool-core eddies. *J. Oceanogr.* **1998**, *54*, 347–360. [CrossRef]
35. Xie, L.; Zheng, Q.; Tian, J. Cruise observation of Rossby waves with finite wavelengths propagating from the Pacific to the South China Sea. *J. Phys. Oceanogr.* **2016**, *46*, 2897–2913. [CrossRef]
36. Gan, J.; Qu, T. Coastal jet separation and associated flow variability in the southwest South China Sea. *Deep Sea Res. Part I Oceanogr. Res. Pap.* **2008**, *55*, 1–19. [CrossRef]
37. Ord, J.K.; Getis, A. Local Spatial Autocorrelation Statistics: Distributional Issues and an Application. *Geogr. Anal.* **1995**, *27*, 286–306. [CrossRef]
38. Liu, J.K.; Shih, P.T.Y. Topographic Correction of Wind-Driven Rainfall for Landslide Analysis in Central Taiwan with Validation from Aerial and Satellite Optical Images. *Remote Sens.* **2013**, *5*, 2571–2589. [CrossRef]
39. Noce, S.; Collalti, A.; Valentini, R.; Santini, M. Hot spot maps of forest presence in the Mediterranean basin. *Inforest-Biogeosci. For.* **2016**, *9*, 766–774. [CrossRef]
40. Javed, M.A.; Younis, M.S.; Latif, S. Community detection in networks: A multidisciplinary review. *J. Netw. Comput. Appl.* **2018**, *108*, 87–111. [CrossRef]
41. Blondel, V.D.; Guillaume, J.L.; Lambiotte, R. Fast unfolding of communities in large networks. *J. Stat. Mech. Theory Exp.* **2008**, *10*, P10008. [CrossRef]
42. Pujol, M.I.; Faugère, Y.; Taburet, G.; Dupuy, S.; Pelloquin, C.; Ablain, M.; Picot, N. DUACS DT2014: The new multi-mission altimeter data set reprocessed over 20 years. *Ocean Sci.* **2016**, *12*, 1067–1090. [CrossRef]
43. Yi, J.; Du, Y.; He, Z. Enhancing the accuracy of automatic eddy detection and the capability of recognizing the multi-core structures from maps of sea level anomaly. *Ocean Sci.* **2014**, *10*, 39–48. [CrossRef]
44. Yi, J.; Du, Y.; Liang, F. An auto-tracking algorithm for mesoscale eddies using global nearest neighbor filter. *Limnol. Oceanogr. Methods* **2017**, *15*, 276–290. [CrossRef]
45. Yi, J.; Du, Y.; Liang, F. A representation framework for studying spatiotemporal changes and interactions of dynamic geographic phenomena. *Int. J. Geogr. Inf. Sci.* **2014**, *28*, 1010–1027. [CrossRef]

46. Okubo, A. Horizontal dispersion of floatable particles in the vicinity of velocity singularities such as convergences. *Deep Sea Res. Oceanogr. Abstr.* **1970**, *17*, 445–454. [CrossRef]
47. Weiss, J. The dynamics of enstrophy transfer in two-dimensional hydrodynamics. *Physica D* **1991**, *48*, 273–294. [CrossRef]
48. Morrow, R. Divergent pathways of cyclonic and anticyclonic ocean eddies. *Geophys. Res. Lett.* **2004**, *31*, L24311. [CrossRef]
49. Henson, S.A.; Thomas, A.C. A census of oceanic anticyclonic eddies in the Gulf of Alaska. *Deep Sea Res. Part I Oceanogr. Res. Pap.* **2008**, *55*, 163–176. [CrossRef]
50. Getis, A.; Ord, J.K. The Analysis of Spatial Association by Use of Distance Statistics. *Geogr. Anal.* **1992**, *24*, 189–206. [CrossRef]
51. Shoval, N.; Isaacson, M. Sequence Alignment as a Method for Human Activity Analysis in Space and Time. *Ann. Assoc. Am. Geogr.* **2007**, *97*, 282–297. [CrossRef]
52. Xu, Y.; Shaw, S.L.; Zhao, Z. Another Tale of Two Cities: Understanding Human Activity Space Using Actively Tracked Cellphone Location Data. *Ann. Am. Assoc. Geogr.* **2016**, *106*, 489–502.
53. Girvan, M.; Newman, M.E. Community structure in social and biological networks. *Proc. Natl. Acad. Sci. USA* **2002**, *99*, 7821–7826. [CrossRef] [PubMed]
54. Fortuanto, S. Community detection in graphs. *Phys. Rep.* **2010**, *486*, 75–174. [CrossRef]
55. Zhang, Z.; Zhao, W.; Tian, J. A mesoscale eddy pair southwest of Taiwan and its influence on deep circulation. *J. Geophys. Res. Oceans* **2013**, *118*, 6479–6494. [CrossRef]
56. Chen, G.; Hu, P.; Hou, Y. Intrusion of the Kuroshio into the South China Sea, in September 2008. *J. Oceanogr.* **2011**, *67*, 439–448. [CrossRef]
57. Li, J.X.; Zhang, R.; Jin, B. Eddy characteristics in the Northern South China Sea as inferred from Lagrangian drifter data. *Ocean Sci.* **2011**, *7*, 1575–1599. [CrossRef]
58. Zhang, Z.; Zhao, W.; Qiu, B. Anticyclonic eddy sheddings from Kuroshio loop and the accompanying cyclonic eddy in the northeastern South China Sea. *J. Phys. Oceanogr.* **2017**, *47*, 1243–1259. [CrossRef]
59. Cai, Z.; Gan, J. Formation and dynamics of a long-lived eddy-train in the South China Sea: A modeling study. *J. Phys. Oceanogr.* **2017**, *47*, 2793–2810. [CrossRef]
60. Chen, G.; Gan, J.; Xie, Q. Eddy heat and salt transports in the South China Sea and their seasonal modulations. *J. Geophys. Res. Oceans.* **2012**, *117*, C05021. [CrossRef]

water

MDPI

Article

The Four Patterns of the East Branch of the Kuroshio Bifurcation in the Luzon Strait

Ruili Sun [1,*], Fangguo Zhai [2] and Yanzhen Gu [2]

[1] College of Environmental Science and Engineering, Zhejiang Gongshang University, Hangzhou 310018, China
[2] College of Oceanic and Atmospheric Sciences, Ocean University of China, Qingdao 266100, China; gfzhai@ouc.edu.cn (F.Z.); guyanzhen@ouc.edu.cn (Y.G.)
* Correspondence: sunruili2007@126.com; Tel.: 188-5711-9795; Fax: 0571-2800-8214

Received: 17 November 2018; Accepted: 6 December 2018; Published: 10 December 2018

Abstract: Based on the self-organizing map (SOM) method, a suite of satellite measurement data, and Hybrid Coordinate Ocean Model (HYCOM) reanalysis data, the east branch of the Kuroshio bifurcation is found to have four coherent patterns associated with mesoscale eddies in the Pacific Ocean: anomalous southward, anomalous eastward, anomalous northward, and anomalous westward. The robust clockwise cycle of the four patterns causes significant intraseasonal variation of 62.2 days for the east branch. Furthermore, the study shows that the four patterns of the east branch of the Kuroshio bifurcation can influence the horizontal and vertical distribution of local sea temperature.

Keywords: Kuroshio bifurcation; Luzon Strait; SOM; temporal and spatial variation; sea surface temperature; mesoscale eddy

1. Introduction

The Kuroshio, which is the strongest western boundary current in the Northwest Pacific (NWP), originates from the North Equatorial Current (NEC). Encountering Luzon Island, the NEC bifurcates into the northward Kuroshio Current and the southward Mindanao Current. Then the Kuroshio passes to the east of the Luzon Strait (LS), flows northward along the Taiwan Island into the East China Sea, and returns to the Pacific Ocean through the Tokara Strait. Because the Kuroshio transports a lot of heat and matter from low latitudes to mid-latitudes, it plays an important role in regional and global climate, and the marine ecosystem [1–5]. Meanwhile, the Kuroshio carries enormous amounts of momentum and kinetic energy, so it strongly interacts with mesoscale eddies and influences regional circulation such as the one in the LS [6–11].

The LS, located between Taiwan Island and Luzon Island, is an important gap in the NWP (as shown in Figure 1). Affected by the Kuroshio, monsoon, mesoscale eddies, and topography, the circulation in the LS is very complicated, and has been studied extensively in previous literatures [8,9,12]. These studies have specifically discussed the interaction between the Kuroshio and mesoscale eddies: (1) the Kuroshio can generate mesoscale eddies by its own variation [11,13]; (2) the Kuroshio can affect mesoscale eddies in the NWP into the South China Sea [7,9]; (3) mesoscale eddies can alter the Kuroshio current field [8,10,14]; (4) interaction between the Kuroshio and mesoscale eddies can influence the local marine environment [14,15]. Although there are many related studies, some questions involving small and moderate ocean phenomena in the LS remain unclear.

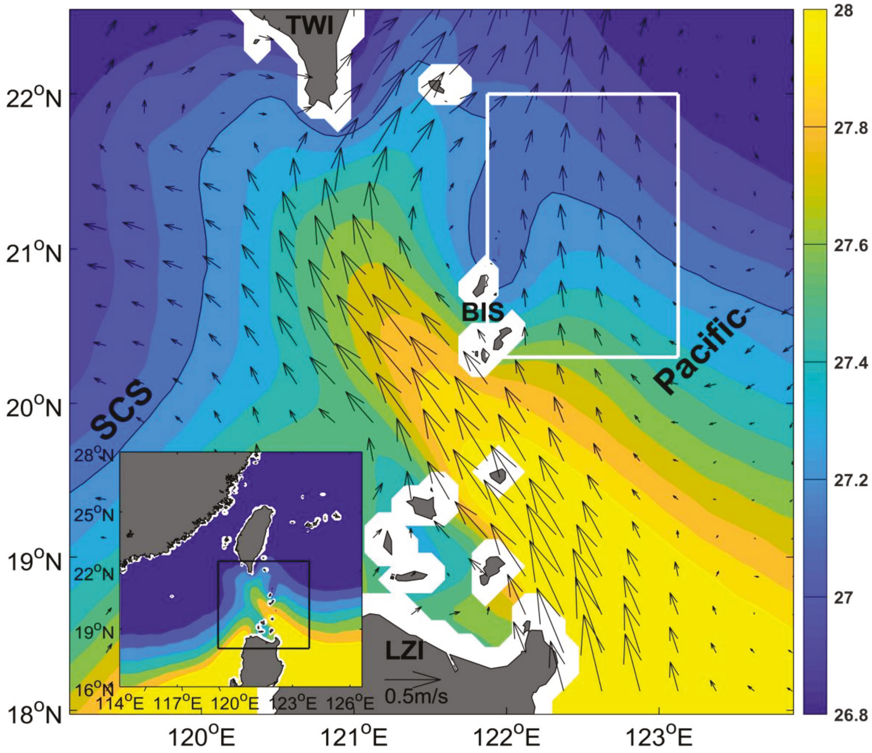

Figure 1. Climatology of geostrophic current and sea surface temperature (SST) around the LS. The black line represents 27.2 °C, in order to emphasize the spatial patterns of two warm tongues. The white box covers 20.3° N–22° N, 121.875 °E–123.125 °E. Geostrophic current (m/s, in vector); SST (°C, in color); TWI: Taiwan Island; BIS: Batanes Islands; LZI: Luzon Island; SCS: South China Sea. The extent of the main map is shown as a black box in the inset.

The accumulation of high-resolution satellite remote sensing data enables us to better study small and moderate ocean phenomena. Based on high-resolution satellite remote sensing data and hydrological data along with numerical model simulations, the Kuroshio bifurcation phenomena in the LS has been put forward: The Kuroshio in the LS bifurcates into two branches located on the western and eastern sides of the Batanes Islands, and produces two warm tongues east of the LS [14]. The western branch is the main part of the Kuroshio, and its temporal and spatial variability has been widely studied [16–19]. However, the temporal and spatial variability of the eastern branch has hardly been studied and remains unclear, although its intensity is related to mesoscale eddies in the NWP [14]. The Kuroshio transports warm water from low latitudes to middle latitudes, so it can cause temporal and spatial variability of local sea temperature in most cases [14,16]. The east branch of the Kuroshio bifurcation, as a part of the Kuroshio, can produce a warm tongue [1] (Figure 1). However, it is unclear whether and how local sea temperature patterns are related to the patterns of the east branch. The purpose of the present study is to assess the variability of the east branch of the Kuroshio bifurcation and its effect on the local sea temperature. The rest of the paper is organized as follows: Section 2 briefly introduces the data and methods. Section 3 shows the temporal and spatial variability of the four patterns of the east branch and their effect on local sea temperature. Section 4 is a summary of this paper.

2. Data and Method

2.1. Data

Absolute dynamic topography (ADT) data and geostrophic current anomalies data were processed by Ssalto multimission ground segment (SSALTO)/Data unification and Altimeter combination system (DUACS) (AVISO, Ramonville Saint-Agne, France) and distributed by Archiving Validation and Interpretation of Satellite Data in Oceanography (AVISO) with support from CNES (Centre National d'Etudes Spatiales). The product is merged from Jason-1/2, Topex/Poseidon, Envisat, Geosat, and other altimeter missions. The raw satellite measurements have applied atmospheric corrections and a sea-land transition. The product is computed on a Cartesian 1/4° × 1/4° spatial resolution and provides daily data from 1 January 1993 to the present [20,21].

Sea surface temperature (SST) is provided by Remote Sensing Systems (RSS, Santa Rosa, CA, USA). The product combines the through-cloud capabilities of the microwave SST data with the high spatial resolution and near-coastal capability of the infrared SST data. The microwave SST data is merged from Advanced Microwave Scanning Radiometer for Earth Observing System, WindSat, Tropical Rainfall Measuring Mission Microwave Images and Giant magnetoimpedance. The infrared SST data is merged from Moderate Resolution Imaging Spectroradiometer and Visible Infrared Imaging Radiometer Suite. The product has applied atmospheric corrections. It provides daily data from 1 July 2002 to present and its spatial resolution is 9 km × 9 km.

Hybrid Coordinate Ocean Model (HYCOM) reanalysis data is provided by HYCOM organization, which provides access to near-real-time global data-based ocean prediction system output. The HYCOM organization provides four HYCOM data-assimilation product, and we choose the product with the longest time span, which is from 2 October 1992 to 31 December 2012. The product has uniform 0.08 degree latitude/longitude grid between 80.48 °S and 80.48 °N and is interpolated to 40 standard z-levels. It provides sea surface height (SSH), temperature, salinity, meridional flow, and zonal flow.

2.2. Method

SOM can be classified as a type of clustering technique [22], and is an effective method for feature extraction and pattern classification [22,23]. A best-matching unit (SST), which records the category of each pattern and can reflect the evolution of each pattern, is obtained based on the minimum Euclidean distance from the input data. Previous studies have demonstrated that the SOM is more useful than conventional EOF (Empirical Orthogonal Function) to extract nonlinear information [24–27], and showed that the SOM has been applied in oceanography and atmosphere science [15,26,28–31]. It needs to be pointed out that the SOM can give the occurrence time of the patterns, which can be used to calculate the period of the patterns [15,32].

Tunable parameters need to be specified in the process of SOM training. The parameters such as training method, lattice, initialized weights, and map shape are chosen according to Liu et al. [27], who gave a practical method for choosing parameters. The parameter of map size defines the number of patterns and should be specified subjectively according to the variability of the shift and strength of the east branch in the LS. The shift of the east branch can generally be classified into two types: westerly or easterly, and the strength of the east branch can also be classified into two types: strong or weak. Thus, a map size of 2 × 2 is chosen. The method we use to choose the map size is similar to the one described in Jin et al. [22]. We run a series of tests with different map sizes such as 2 × 3, 3 × 3, 3 × 4 and 4 × 4. The east branch patterns with these larger map sizes are very similar to the ones with the map size of 2 × 2 although the patterns in the larger SOM provide more details about the east branch variability.

3. Results

3.1. The Four Patterns of the East Branch of the Kuroshio Bifurcation

Applying the SOM method to the corresponding AVISO ADT data in the white box of Figure 1, we can obtain the dominant variation patterns of the east branch. Figure 2 shows that the east branch has four coherent patterns: anomalous southward (P1), anomalous eastward (P2), anomalous northward (P3), and anomalous westward (P4), which correspond to a cyclonic eddy (CE), CE-anticyclonic eddy (AE), an AE, and AE-CE to the east of the LS, respectively. Briefly, the four patterns of the east branch are dominated by single and dipole eddy structure, which is very similar to the SSH variability east of the Taiwan Island [33,34]. To the authors' knowledge, the four patterns of the east branch in the LS have not been previously reported. P1 shows significantly southward velocity anomaly, which is caused by a CE to the east of LS. P2 shows significantly eastward velocity anomaly, which is accompanied by an eddy pair consisting of a CE on the north side of 21.2 °N and an AE on the south side of 21.2 °N. P3 is the opposite of P1, and is caused by an AE to the east of the LS. P4 is the opposite of P2, and is accompanied by an AE on the north side of 21.2 °N and a CE on the south side of 21.2 °N. The four patterns of the east branch also are identified in the HYCOM SSH data. Figure 3 shows that, P1 (P3) corresponds to a CE (an AE), and P2 (P4) corresponds to a CE (an AE) on the north side of 21.2 °N and an AE (a CE) on the south side of 21.2 °N, which corresponds well to the ones in Figure 2, although the occurrence rate of corresponding pattern of Figures 2 and 3 is not exactly the same, which may be related to HYCOM model bias.

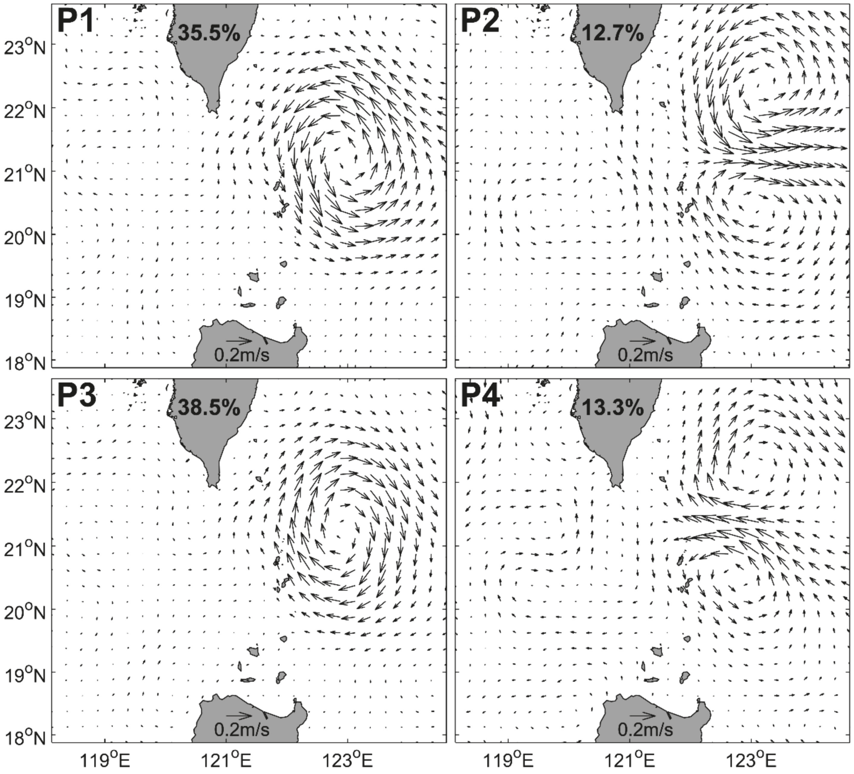

Figure 2. The 2 × 2 SOM patterns derived from the AVISO ADT fields for the east branch. Geostrophic current anomaly (m/s, in vector). The number on each panel represents the occurrence rate of corresponding pattern.

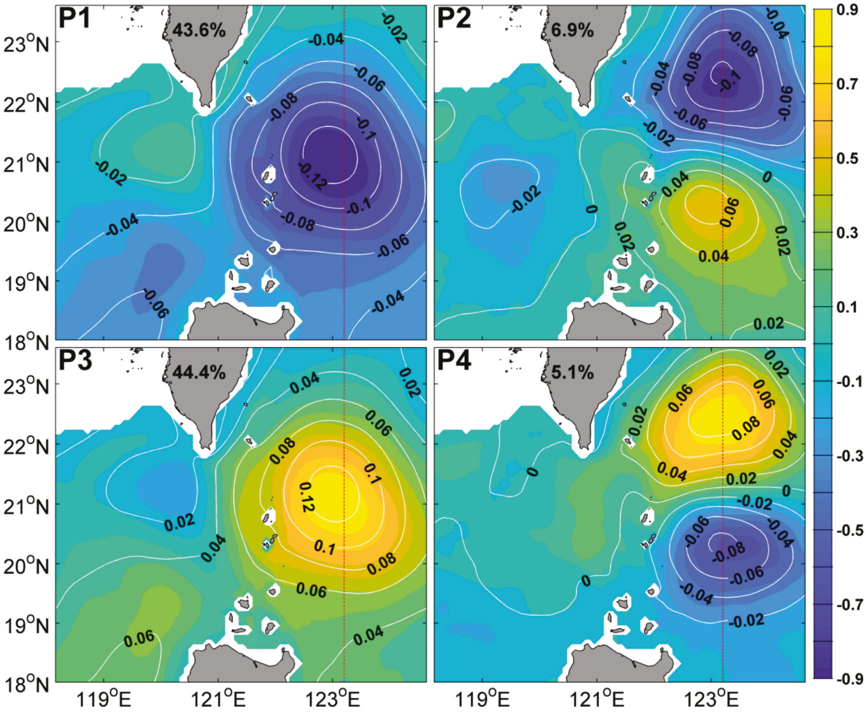

Figure 3. The 2 × 2 SOM patterns derived from the HYCOM SSH fields for the east branch, and corresponding sea temperature anomaly in 300 meters deep. Sea Surface Height Anomaly (SSHA) (m, in contour); Sea temperature (°C, in color). The number on each panel represents the occurrence rate of corresponding pattern. The red dotted line represents meridional section of sea temperature, and its longitude is 123.2 °E.

The temporal evolution of the four patterns can be seen from the time series of the BMU (Figure 4). The cycle characterized as a clockwise trajectory in the SOM space is very noteworthy, which has been marked by red lines in Figure 4. We take the cycle of P1, P2, P3, P4 and P1 as an example. First, a CE approaches from the east and weakens the east branch (P1). Second, as the CE flows northward and gradually weakens, an AE begins to form in the south (P2). Third, with the AE eddy strengthening, it approaches and enhances the east branch (P3). Finally, as the AE moves northward and gradually weakens, a CE in the south begins to form (P4). Note P1 as the initial pattern in the sequence is arbitrary. We define the occurrence of the preferred cycle by counting occurrences of clockwise trajectories that pass through all four patterns at least once. The percentage of time that follows the preferred cycle (red lines) to the total time analyzed is 39.2%.

Power spectrum analysis shows that the most significant cycle of the BMU is 62.2 days (Figure 5), which is consistent with the significant cycle of upper-layer and intermediate-layer transports based on observation data in the LS [35], and Zhang et al. pointed out that the ~60 days of variability might be attributed to the impinging mesoscale eddies from the Pacific [35]. The average consecutive days are 19.2, 6.0, 18.8, and 6.5 for P1, P2, P3, and P4, respectively, causing the total time length of a cycle of P1, P2, P3, and P4 to be between 56.5 days and 69.7 days, which is very close to 62.2 days. Therefore, we think that the cycle of the 62.2 days of the BMU is mainly caused by the cycle of P1, P2, P3, and P4.

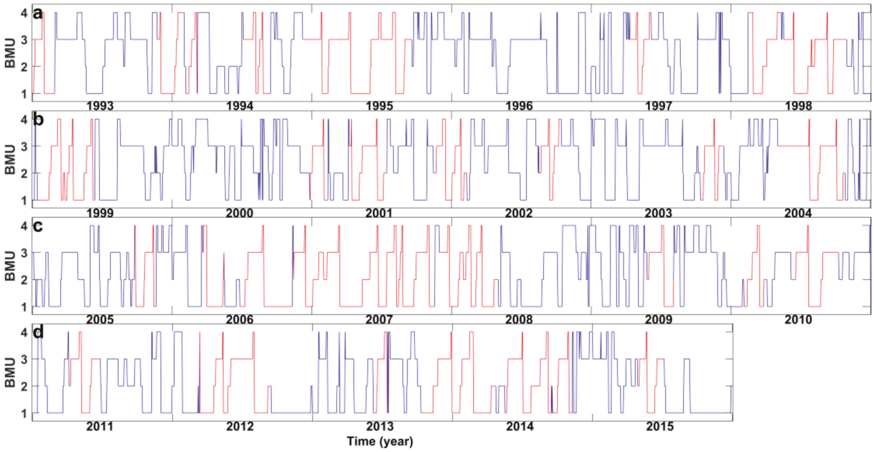

Figure 4. Time series of the BMU for the four patterns, as shown in Figure 2. On the y axis, 1, 2, 3 and 4 correspond to P1, P2, P3, and P4, respectively. The subgraphs (**a**), (**b**), (**c**), and (**d**) correspond to the period from 1993 to 1998, from 1999 to 2004, from 2005 to 2010, and from 2011 to 2015, respectively.

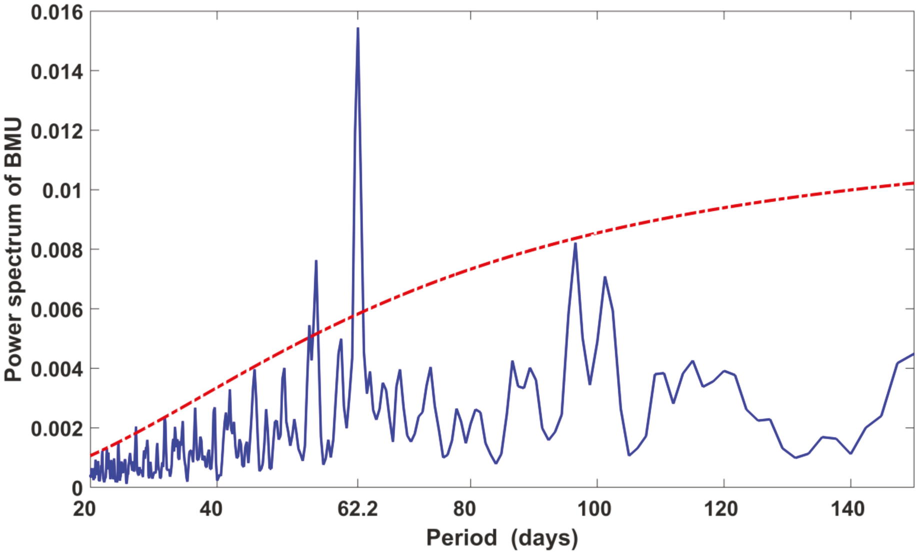

Figure 5. Power spectrum analysis of time series of the BMU for the four patterns. The red dotted line represents the 95% significant level.

3.2. The Effect of the Four Patterns on the Local Sea Temperature

SST around the LS has obvious seasonal variability. Figure 6 shows that there is a good correspondence between the Kuroshio and warm tongues in most months, especially in winter, However, the Kuroshio fails to correspond well with warm tongues in some months such as in June and August. The high temperature in June and August is not conducive to the formation of warm tongue around the LS [32].

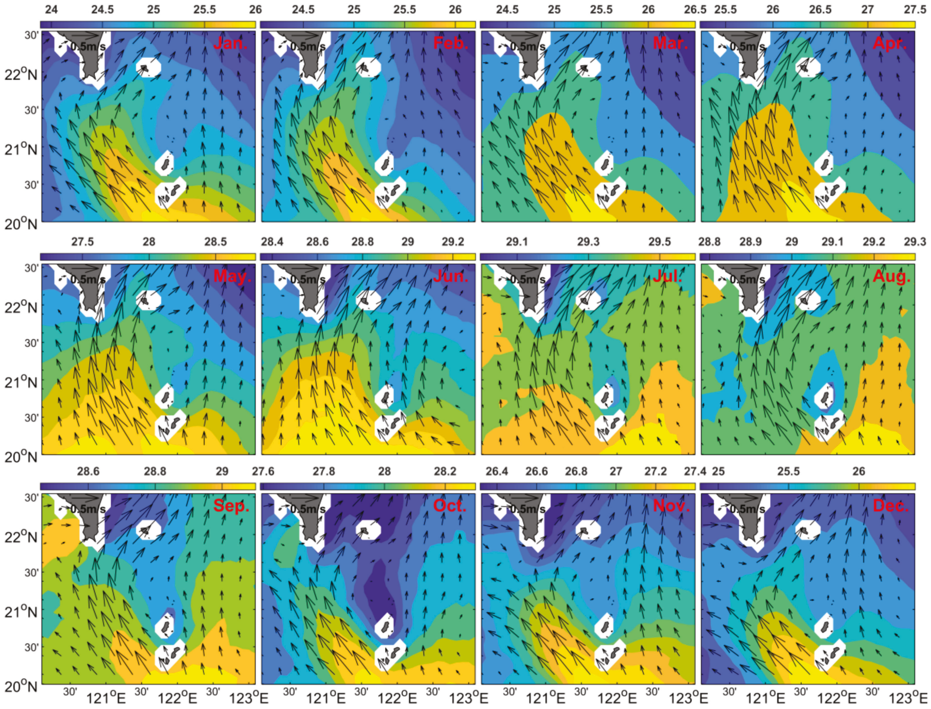

Figure 6. Seasonal variability of SST and geostrophic current around the LS. SST (°C, in color); Geostrophic current (m/s, in vector).

We apply a 4° moving average for RSS SST field for the purpose of removing the background state to highlight the effect of mesoscale process. Figure 7 shows that the four patterns of the east branch have a significant effect on SST around the LS. Sun et al. used a mixed-layer model based on temperature equation to demonstrate that the Kuroshio affects SST mainly through geostrophic thermal advection in the LS [14]. Through thermal advection, the east branch of the anomalous southward causes SST reduction in the location of the east branch (P1); the east branch of the anomalous eastward causes an eastward warm tongue (P2); P3 is the opposite of the P1, and SST increases in the location of the east branch (P3); P4 shows that the east branch of the anomalous westward causes a westward cold tongue. Figure 7 embodies that mesoscale eddies can influence sea temperature distribution by modulating the east branch of the Kuroshio of the western boundary current.

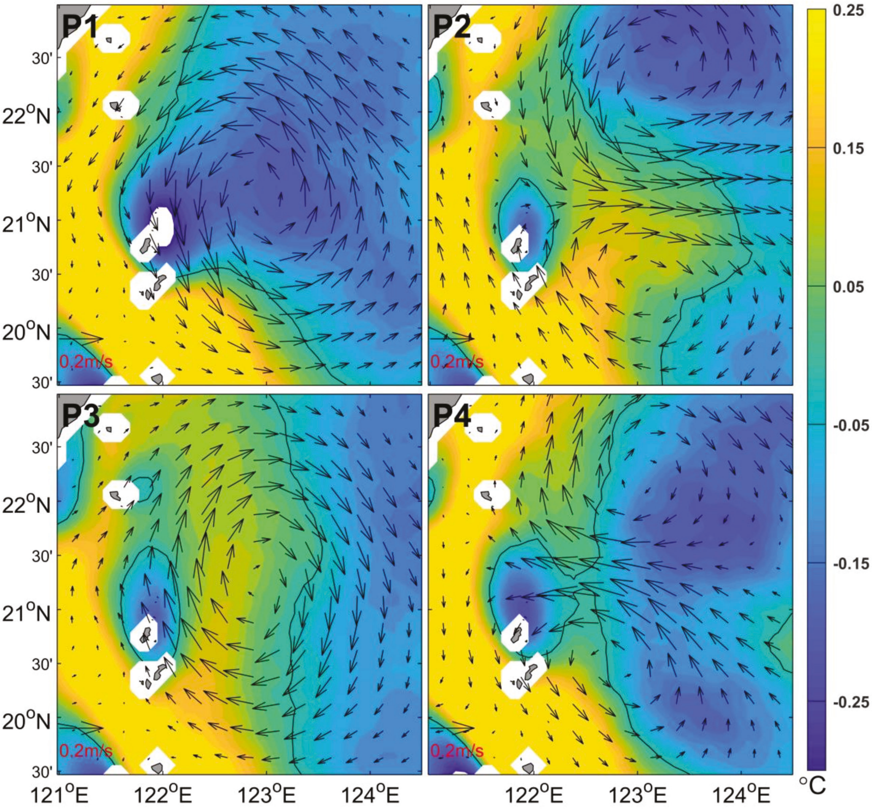

Figure 7. The spatial pattern of high-pass-filtered RSS SST corresponding to 2 × 2 SOM patterns derived from the AVISO ADT fields for the east branch. Geostrophic current anomaly (m/s, in vector); SST (°C, in color). The spatial filtering is done by subtracting a 4° moving average from the original RSS SST data to remove the large-scale background state. The black line represents a zero contour line.

Besides affecting SST, the four patterns of the east branch can also affect deep sea temperature. Figure 3 shows that there is a good correspondence between sea temperature in 300 meters depth and the four patterns of the east branch: the CE (AE) corresponds to a cold (warm) center of sea temperature anomaly because of the following reasons. When the CE (AE) exists, SSHA is negative (positive) and upwelling (downwelling) occurs, and then the temperature in the deep ocean correspondingly decreases (increases) [36], which indicates that the four patterns of the east branch can affect the vertical distribution of sea temperature. Figure 8 gives vertical profile of sea temperature anomaly along the 123.2°E, which is marked as a red dotted line in Figure 3, and shows negative (positive) temperature anomaly corresponding to a CE (an AE) can reach 5000 meters deep. Based on Conductivity Temperature Depth (CTD) data, Zhang et al. found that mesoscale eddies can affect sea temperature in 2530 meters depth [36], and the conclusion in this paper is consistent with it in magnitude. However, based on HYCOM data in this paper, we found that the effect of the four patterns of the east branch on sea temperature can reach 5000 meters in depth, or even deeper [37].

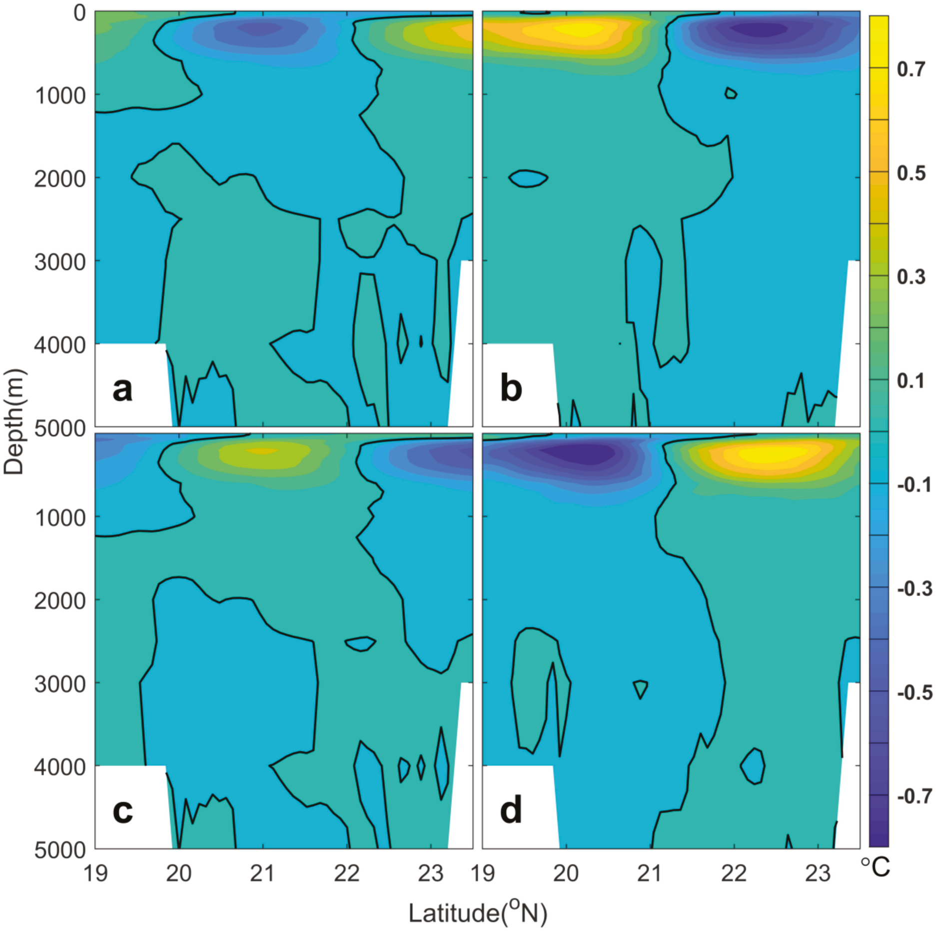

Figure 8. The profile of HYCOM temperature anomaly corresponding to the four patterns of the east branch. Subgraphs (**a**), (**b**), (**c**), and (**d**) correspond to P1, P2, P3 and P4 of the east branch patterns, respectively. The black line represents the zero contour line. It is noted that the zonal mean has been removed. Sea temperature (°C, in color).

4. Summary

Spatial patterns of the east branch of the Kuroshio bifurcation in the LS are extracted from the AVISO data and HYCOM data using the method of SOM. Four coherent patterns are used to summarize the variation of the east branch: anomalous southward, anomalous eastward, anomalous northward, and anomalous westward, which corresponds to a CE, CE-AE, an AE, and AE-CE to the east of the LS, respectively. The robust clockwise cycle of the four patterns causes a 62.2 days cycle of the east branch.

The four patterns of the east branch modulated by mesoscale eddies can influence horizontal and vertical distribution of local sea temperature. East branch of anomalous southward (northward) causes SST reduction (increase) in the location of east branch. East branch of anomalous eastward causes an eastward warm tongue while east branch of anomalous westward causes a westward cold tongue. The effect of the four patterns of the east branch on sea temperature can reach 5000 meters deep.

The patterns of the east branch of the Kuroshio bifurcation and their temporal evolution, as revealed by the SOM, provide new insights into the variability of the Kuroshio and their effect on the local sea temperature. Detailed dynamic mechanism studies with numerical models and more in situ observations are warranted as part of future work.

Author Contributions: Conceptualization, R.S.; Methodology, R.S.; Software, R.S.; Validation, R.S., and F.Z.; Formal Analysis, R.S.; Investigation, R.S.; Resources, R.S.; Data Curation, R.S.; Writing-Original Draft Preparation, R.S.; Writing-Review & Editing, R.S., F.Z. and Y.Z.; Visualization, R.S.; Supervision, R.S., F.Z. and Y.Z.; Project Administration, R.S.; Funding Acquisition, R.S.

Funding: This research was funded by National Natural Science Foundation of China grant number (41806019), Natural Science Foundation of Zhejiang Province grant number (LY18D060004), Foundation of Department of Education of Zhejiang Province grant number (1260KZ0417982), National Natural Science Foundation of China grant number (41506008), Open Fund of the Key Laboratory of Ocean Circulation and Waves, Chinese Academy of Sciences grant number (KLOCW1503), Talent Start Foundation of Zhejiang Gongshang University grant number (1260XJ2317015 and 1260XJ2117015), and The APC was funded by National Natural Science Foundation of China grant number (41806019).

Acknowledgments: The authors thank AVISO (Archiving Validation and Interpretation of Satellite Data in Oceanography, available for download at: ftp://ftp.aviso.oceanobs.com/), RSS (Remote Sensing System, available for download at: ftp://ftp.remss.com), and HYCOM (Hybrid Coordinate Ocean Model, available for download at: https://hycom.org/dataserver/) for providing the data used in this paper.

Conflicts of Interest: The authors declare no conflict of interest. The funders had no role in the design of the study; in the collection, analyses, or interpretation of data; in the writing of the manuscript, and in the decision to publish the results.

References

1. Tokinaga, H.; Tanimoto, Y.; Xie, S.; Sampe, T.; Tomita, H.; Ichikawa, H. Ocean frontal effects on the vertical development of clouds over the Western North Pacific: In situ and satellite observations. *J. Clim.* **2009**, *22*, 4241–4260. [CrossRef]
2. Kelly, K.A.; Small, R.J.; Samelson, R.M.; Qiu, B.; Joyce, T.M.; Kwon, Y.-O.; Meghan, F.C. Western boundary currents and frontal air-sea interaction: Gulf stream and Kuroshio extension. *J. Clim.* **2010**, *23*, 5644–5667. [CrossRef]
3. Qiu, B.; Chen, S.; Schneider, N.; Taguchi, B. A coupled decadal prediction of the dynamic state of the Kuroshio extension system. *J. Clim.* **2014**, *27*, 1751–1764. [CrossRef]
4. Guo, L.; Xiu, P.; Chai, F.; Xue, H.; Wang, D.; Sun, J. Enhanced chlorophyll concentrations induced by Kuroshio intrusion fronts in the northern South China Sea. *Geophys. Res. Lett.* **2017**, *44*, 11565–11572. [CrossRef]
5. Zhou, P.; Song, X.; Yuan, Y.; Wang, W.; Cao, X.; Yu, Z. Intrusion pattern of the Kuroshio Subsurface Water onto the East China Sea continental shelf traced by dissolved inorganic iodine species during the spring and autumn of 2014. *Mar. Chem.* **2017**, *196*, 24–34. [CrossRef]
6. Waseda, T. On the Eddy-Kuroshio interaction: Meander formation process. *J. Geophys. Res.* **2003**, *108*, 3220. [CrossRef]
7. Sheu, W.; Wu, C.; Oey, L. Blocking and westward passage of eddies in the Luzon Strait. *Deep. Sea. Res.* **2010**, *57*, 1783–1791. [CrossRef]
8. Zheng, Q.; Tai, C.; Hu, J.; Lin, H.; Zhang, R.-H.; Su, F.-C.; Yang, X. Satellite altimeter observations of nonlinear Rossby Eddy-Kuroshio interaction at the Luzon Strait. *J. Oceanogr.* **2011**, *67*, 365–376. [CrossRef]
9. Lu, J.; Liu, Q. Gap-leaping Kuroshio and blocking westward-propagating Rossby wave and eddy in the Luzon Strait. *J. Geophys. Res.* **2013**, *118*, 1170–1181. [CrossRef]
10. Cheng, Y.; Ho, C.; Zheng, Q.; Qiu, B.; Hu, J.; Kuo, N.-J. Statistical features of eddies approaching the Kuroshio east of Taiwan Island and Luzon Island. *J. Oceanogr.* **2017**, *73*, 1–12. [CrossRef]
11. Zhang, Z.; Zhao, W.; Qiu, B.; Tian, J. Anticyclonic eddy sheddings from Kuroshio Loop and the accompanying cyclonic eddy in the northeastern South China Sea. *J. Phys. Oceanogr.* **2017**, *47*, 1243–1259. [CrossRef]
12. Wang, G.; Wang, D.; Zhou, T. Upper layer circulation in the Luzon Strait. *Aquat. Ecosyst. Health* **2012**, *15*, 39–45. [CrossRef]
13. Jia, Y.; Liu, Q. Eddy shedding from the Kuroshio Bend at Luzon Strait. *J. Oceanogr.* **2004**, *60*, 1063–1069. [CrossRef]
14. Sun, R.; Wang, G.; Chen, C. The Kuroshio bifurcation associated with islands at the Luzon Strait. *Geophys. Res. Lett.* **2016**, *43*, 5768–5774. [CrossRef]

15. Sun, R.; Gu, Y.; Li, P.; Li, L.; Zhai, F.; Gao, G. Statistical characteristics and formation mechanism of the Lanyu cold eddy. *J. Oceanogr.* **2016**, *72*, 641–649. [CrossRef]
16. Ho, C.-R.; Zheng, Q.; Kuo, N.-J.; Tsai, C.-H.; Huang, N.E. Observation of the Kuroshio intrusion region in the South China Sea from AVHRR data. *Int. J Remote. Sens.* **2004**, *25*, 4583–4591. [CrossRef]
17. Caruso, M.J.; Gawarkiewicz, G.G.; Beardsley, R.C. Interannual variability of the Kuroshio intrusion in the South China Sea. *J. Oceanogr.* **2006**, *62*, 559–575. [CrossRef]
18. Nan, F.; Xue, H.; Chai, F.; Shi, L.; Shi, M.; Guo, P. Indentification of different types of Kuroshio intrusion into the South China Sea. *Ocean. Dynam.* **2011**, *61*, 1291–1304. [CrossRef]
19. Nan, F.; Xue, H.; Yu, F. Kuroshio intrusion into the South China Sea: A review. *Prog. Oceanogr.* **2015**, *137*, 314–333. [CrossRef]
20. Ducet, N.; Traon, P.Y.; Reverdin, G. Global high-resolution mapping of ocean circulation from TOPEX/Poseidon and ERS-1 and-2. *J. Geophys Res.* **2000**, *105*, 19477–19498. [CrossRef]
21. Duacs. *A New Version of SSALTO/Duacs Products Available in April 2014*; Duacs: Toulouse, France, 2014.
22. Jin, B.; Wang, G.; Liu, Y.; Zhang, R. Interaction between the East China Sea Kuroshio and the Ryukyu Current as revealed by the self-organizing map. *J. Geophys. Res.* **2010**, *115*. [CrossRef]
23. Kohonen, T. *Self-Organizing Maps*; Vol. of 30 Springer Series in Information Sciences, 3rd ed. Springer: Berlin, Germany, 2001; p. 501.
24. Hsieh, W.W. Non-linear principal component analysis by neural networks. *Tellus A* **2001**, *53*, 599–615. [CrossRef]
25. Hsieh, W.W. Nonlinear multivariate and time series analysis by neural network methods. *Rev. Geophys.* **2004**, *42*. [CrossRef]
26. Liu, Y.; Weisberg, R.H. Patterns of ocean current variability on the West Florida Shelf using the self-organizing map. *J. Geophys. Res.* **2005**, *110*. [CrossRef]
27. Liu, Y.; Weisberg, R.H.; Mooers, C.N. Performance evaluation of the self-organizing map for feature extraction. *J. Geophys. Res.* **2006**, *111*, 1–14. [CrossRef]
28. Cavazos, T. Using self-organizing maps to investigate extreme climate events: An application to wintertime precipitation in the Balkans. *J. Clim.* **2000**, *13*, 1718–1732. [CrossRef]
29. Iskandar, I.; Tozuka, T.; Masumoto, Y.; Yamagata, T. Impact of Indian Ocean Dipole on intraseasonal zonal currents at 90° E on the equator as revealed by self-organizing map. *Geophys. Res. Lett.* **2008**, *35*. [CrossRef]
30. Johnson, N.C. How many ENSO flavors can we distinguish? *J. Clim.* **2013**, *26*, 4816–4827. [CrossRef]
31. Yin, Y.; Lin, X.; Li, Y. Seasonal variability of Kuroshio intrusion northeast of Taiwan Island as revealed by self-organizing map. *Chin. J. Oceanol. Limnol.* **2014**. [CrossRef]
32. Sun, R. The Ocean Dynamics and Its effect on the sea temperature near the Luzon Strait. Ph.D. Thesis, Ocean University of China, Qingdao, China, December 2015. (In Chinese)
33. Hsin, Y.; Qiu, B.; Chiang, T.; Wu, C.-R. Seasonal to interannual variations in the intensity and central position of the surface Kuroshio east of Taiwan. *J. Geophys. Res.* **2013**, *118*, 4305–4316. [CrossRef]
34. Yan, X.; Zhu, X.; Pang, C.; Zhang, L. Effects of mesoscale eddies on the volume transport and branch pattern of the Kuroshio east of Taiwan. *J. Geophys. Res.* **2016**, *121*, 7683–7700. [CrossRef]
35. Zhang, Z.; Zhao, W.; Tian, J.; Yang, Q.; Qu, T. Spatial structure and temporal variability of the zonal flow in the Luzon Strait. *J. Geophys. Res.* **2015**, *120*, 759–776. [CrossRef]
36. Zhang, Z.; Zhao, W.; Tian, J.; Liang, X. A mesoscale eddy pair southwest of Taiwan and its influence on deep circulation. *J. Geophys. Res.* **2013**, *118*, 6479–6494. [CrossRef]
37. Zhang, Z.; Tian, J.; Qiu, B.; Zhao, W. Observed 3D structure, generation, and dissipation of oceanic mesoscale eddies in the South China Sea. *Sci. Rep.* **2016**, *6*, 24349. [CrossRef] [PubMed]

water

MDPI

Article

Picoplankton Distribution and Activity in the Deep Waters of the Southern Adriatic Sea

Danijela Šantić [1,*], Vedrana Kovačević [2], Manuel Bensi [2], Michele Giani [2], Ana Vrdoljak Tomaš [1], Marin Ordulj [3], Chiara Santinelli [2], Stefanija Šestanović [1], Mladen Šolić [1] and Branka Grbec [1]

[1] Institute of Oceanography and Fisheries, Šetalište Ivana Meštrovića 63, POB 500, 21000 Split, Croatia
[2] National Institute of Oceanography and Applied Geophysics, Borgo Grotta Gigante 42/c, 34010 Sgonico (Ts), Italy
[3] University of Split, University Department of Marine Studies, Ruđera Boškovića 37, 21000 Split, Croatia
[*] Correspondence: segvic@izor.hr; Tel.: +385-21-408-006; Fax: +385-21-358-650

Received: 19 July 2019; Accepted: 8 August 2019; Published: 10 August 2019

Abstract: Southern Adriatic (Eastern Mediterranean Sea) is a region strongly dominated by large-scale oceanographic processes and local open-ocean dense water formation. In this study, picoplankton biomass, distribution, and activity were examined during two oceanographic cruises and analyzed in relation to environmental parameters and hydrographic conditions comparing pre and post-winter phases (December 2015, April 2016). Picoplankton density with the domination of autotrophic biomasses was higher in the pre-winter phase when significant amounts of picoaoutotrophs were also found in the meso-and bathy-pelagic layers, while *Synechococcus* dominated the picoautotrophic group. Higher values of bacterial production and domination of High Nucleic Acid content bacteria (HNA bacteria) were found in deep waters, especially during the post-winter phase, suggesting that bacteria can have an active role in the deep-sea environment. Aerobic anoxygenic phototrophic bacteria accounted for a small proportion of total heterotrophic bacteria but contributed up to 4% of bacterial carbon content. Changes in the picoplankton community were mainly driven by nutrient availability, heterotrophic nanoflagellates abundance, and water mass movements and mixing. Our results suggest that autotrophic and heterotrophic members of the picoplankton community are an important carbon source in the food web in the deep-sea, as well as in the epipelagic layer. Besides, viral lysis may affect the activity of the picoplankton community and enrich the water column with dissolved organic carbon.

Keywords: picoplankton community; deep-sea; Southern Adriatic; Mediterranean Sea

1. Introduction

Autotrophic members of the picoplankton community are important primary producers, while bacteria are consumers of the dissolved organic matter that can originate from primary production, thus transferring carbon towards higher trophic levels. Bacteria represent the main component of plankton, which is involved in the degradation of organic matter and in transforming inorganic compounds into the shapes adequate for primary producers. The role of the picoplankton community has become more important in oligotrophic and phosphorus-limited (P-limited) areas, such as the open sea area of the Adriatic Sea (Mediterranean Sea), where bacteria, *Synechococcus*, *Prochlorococcus*, and picoeukaryotes play an important role in the production and flow of biomass and energy [1–3] than in eutrophic areas. However, previous studies on picoplankton communities were mostly focused on investigating the epipelagic layer (i.e., depths less than 200 m). The deep-sea is characterized by the absence of light, i.e., conditions that are unfavorable for the primary production. Tanaka and Rassoulzadegan [4] pointed out the importance of bacteria and their biomass in carbon flux in the deep-sea. Moreover, Arístegui et al. [5] have highlighted that the deep ocean represents a key site for remineralization of organic matter and long-term carbon storage. The discovery of cyanobacteria *Synechococcus* in the deep part of the Adriatic Sea revealed that they could be used to gain a better understanding of the effects of deep-ocean convection, such as ventilation and renewal of deep waters [6]. Hence, the vertical distribution of the picoplankton in the open southern Adriatic Sea, below the euphotic zone, has recently started to be investigated more intensively [7–10]. Aerobic anoxygenic phototrophs (AAPs), a bacterial group recently discovered in the Adriatic Sea [11,12] and primarily unknown in the investigated area, are up to 3 × bigger than other bacterial cells [13,14], and hence they could represent a remarkable source of carbon in the marine environment. These photoheterotrophic microorganisms can harvest light energy using pigment bacteriochlorophyll *a* to supplement their primarily organotrophic metabolism only in the presence of oxygen [15].

The Adriatic Sea is an elongated semi-enclosed basin of the Eastern Mediterranean Sea. According to its morphology and bathymetry, it can be divided into three sub-basins (northern, middle, and southern). The Southern Adriatic Pit (hereafter SAP) is the deepest area, with a depth reaching ~1250 m. Adriatic is characterized by a cyclonic basin-scale circulation. Through the Strait of Otranto at its southern end (~80 km wide, with a sill depth of ~800 m) [16,17], the Adriatic exchanges water and mass with the adjacent Ionian Sea. The Eastern Adriatic Current (EAC) brings northward warm and saline waters from the Ionian Sea and the Western Adriatic Current (WAC), transporting southward colder and fresher waters [18]. Waters from the Ionian Sea enrich the P-limited Adriatic Sea [19,20] with nutrients and organic substances, causing changes in the food web [21] and the distribution of organisms [6,8,10,22]. The prevalent heat and salt import from the Ionian involve the surface and intermediate layers of the Adriatic Sea, between the surface and 800 m depth. According to Gačić et al. [23], periodical changes in the sense of the rotation between cyclonic and anticyclonic phases of the North Ionian Gyre (NIG) deviate the branch of the Atlantic water, entering the Eastern Mediterranean through the Strait of Sicily, towards the Adriatic (during anticyclonic phase) or towards the Cretan and Levantine basins (during cyclonic phase). Under these two opposite conditions, changes in the heat and salt content of the SAP may occur out of phase compared to those observed in the Levantine basin [24]. Moreover, water masses flowing into the Adriatic along its eastern flank have important ecological implications. Indeed, the pool of available nutrients in the SAP changes according to the phases of the NIG [25–27]. The deep part of the SAP occasionally receives the North Adriatic Dense Water (NAdDW), that ventilates the deepest layers after winter cooling [28,29]. Locally, the open-sea winter convection triggers vertical mixing and produces dense water (Adriatic Deep Water, AdDW) that reaches depths between 300 and 1000 m [30–32]. Subsequently, AdDW outflows across the Strait of Otranto sinks into the Ionian Sea abyss and ventilates the deep layers of the eastern Mediterranean [33].

The picoplankton community is exposed to sudden physical-chemical changes in a dynamic environment. The ability of certain members to acclimate physiologically determine their presence and activity or absence in the water column. Hence, environmental conditions (vertical convection, lateral exchanges, long-term trends, and multiannual oscillatory signals) make the Southern Adriatic an ideal laboratory to study vertical distribution and activity of picoplankton members in the deep zones (below epipelagic layer), where they can represent a significant source of carbon through their biomass.

The primary goal of the ESAW (evolution and spreading of the Southern Adriatic Waters) cruise was to assess and compare the pre-and post-winter hydrographic and environmental (physical, biogeochemical) conditions in the middle and southern Adriatic basins. The objective of the present study was to evaluate for the first time, the abundance of aerobic anoxygenic phototrophs (AAPs) in the deep waters of the Southern Adriatic Pit (hereafter SAP). Beside the AAPs, we determined the distribution of *Synechococcus*, *Prochlorococcus*, picoeukaryotes, and heterotrophic bacteria and estimated their contribution to carbon budget from epipelagic to deep waters. Our study shows and discusses results obtained from the analysis of picoplankton biomasses and their activity concerning environmental parameters and hydrographic conditions and the effect of grazing and viral lysis.

2. Material and Methods

2.1. Physical and Biochemical Sampling

In this study, we used data collected during the two ESAW cruises (Evolution and spreading of the Southern Adriatic Waters), supported by the EUROFLEETS2 program. The first one was conducted in December 2015 (10–15 December). The second one was conducted in April 2016 (5–10 April), when the hydrographic and environmental conditions were supposed to be changed after the wintertime occurrence of vertical convection, and consequent dense water formation. The intention was to measure the signals of a possible spread of dense water from the middle to the southern Adriatic, because the former may be both an accumulation site and an occasional formation site for dense waters [34]. Here, we focused only on data collected in the SAP, at hydrological stations regularly spaced along a transect between Bari (Ba; Italy) and Dubrovnik (Du; Croatia, Figure 1). A conductivity-temperature-depth (CTD) SBE 911plus probe (Sea-Bird Electronics, Bellevue, WA, USA) measured vertical profiles of temperature (T), conductivity (C), dissolved oxygen (DO), fluorescence, and turbidity. The sampling rate was set to 24 Hz. The T-C sensors were controlled and calibrated before and after the cruise at the Calibration facility center at OGS (Trieste, Italy). For water sampling purposes, the CTD probe was coupled with a rosette sampler, holding 12 Niskin bottles (8-L capacity). Salinity (S), potential temperature (θ), and potential density anomaly (σ_θ) were calculated using the MATLAB toolbox TEOS-10 (http://www.teos-10.org/software.htm) and Ocean Data View software [35]. The reference pressure for θ and σ_θ was 0 dbar. Data were processed and quality checked according to MyOcean in situ quality control standards and methodology. The final vertical profiles consisted of the data averaged every 1 dbar, with overall accuracies ±0.005 °C for T, and ±0.005 for S, and 2% of DO saturation. Due to the malfunctioning of the SBE43 sensor for DO detection, these data were missing at stations 8 and 9 during the April cruise. The missing profiles were substituted by the data from the closest stations, namely, 7 and 10 (Figure 1), assuming that the main pattern of the vertical structure was similar in the deep SAP region (as compared in Figure 2). Sampling depths for the nutrients and dissolved organic compounds were 2, 45 (56 m in April), 84 (100 m in April), 220 (204 m in April), 400, 500, 662 (600 m in April), 800, 940 (900 m in April), 1000, 1100, 1140 m at station 8; 2, 50 (62 m in April), 96 (100 m in April), 193 (201 m in April), 400 (350 m in April), 520 (missing in April), 700, 800, 900, 1000, 1100, 1208 m at station 9. Dissolved organic carbon (DOC) samples were occasionally sampled at a smaller rate. During sampling, there were no pieces of evidence on neither water leakage from the Niskin bottles nor some other possible source of contamination of the water samples. Moreover, there were no striking patterns among measured parameters which could have indicated such kind of a problem. Therefore, we are confident that the samples were taken correctly.

Water samples for measuring dissolved inorganic nutrient concentrations (nitrite, NO_2, nitrate, NO_3, ammonium, NH_4, phosphate, PO_4, and silicic acid, H_4SiO_4) were prefiltered through glass-fiber filters (Whatman GF/F) immediately after sampling and stored at −20 °C in polyethylene vials until performing analysis in the on-shore laboratory. The samples were defrosted and analyzed colorimetrically with a QuAAtro Seal Analytical continuous segmented flow analyzer, according to Hansen and Koroleff [36]. Detection limits for the procedure were 0.003 µM, 0.01 µM, 0.04 µM, 0.02 µM, and 0.02 µM for NO_2, NO_3, NH_4, PO_4, and H_4SiO_4, respectively. The accuracy and precision of the analytical procedures at low concentrations were checked periodically through the quality assurance program QUASIMEME, and the relative coefficient of variation for five replicates was less than 5%. Internal quality control samples were used during each analysis. As in the case of inorganic nutrients, samples for dissolved organic nitrogen and phosphorus analysis were filtered through Whatman GF/F glass fiber filters, collected in acid-washed polyethylene vials rinsed with seawater, and frozen immediately (−20 °C) until laboratory analysis. Total dissolved inorganic nitrogen (TDN) and phosphorus (TDP) were determined after quantitative conversion to inorganic N and P by persulfate oxidation [36] and subsequent analyses of nitrate + nitrites and phosphates. Dissolved organic nitrogen (DON) and phosphorus (DOP) were computed from the relationship DON = TDN

– ($N\text{-}NH_4$ + $N\text{-}NO_2$ + $N\text{-}NO_3$) and DOP = TDP − $P\text{-}PO_4$. DOC samples were filtered immediately after collection through 0.2 µm membrane filters (Sartorius, Minisart, SM 16534, Goettingen, Germany) and stored at 4 °C in the dark until analysis (within 3 months). DOC samples were analyzed using a Shimadzu TOC-VCSN. Samples were acidified with 2N HCl and sparged for 3 min with CO_2-free pure air, to remove inorganic carbon before high-temperature catalytic oxidation. One hundred microliters of the sample were injected into the furnace after a four-fold syringe washing. From 3 to 5, replicate injections were performed until the analytical precision was within <2% (±1 µM). The calibration curve was determined by using four different solutions of potassium phthalate, in the same concentration range as the samples. The reliability of the measurements was checked daily using consensus reference materials (CRM) kindly supplied by Prof. D. A. Hansell, University of Miami. At least two CRM and two low carbon water (LCW) analyses were performed for each analytical day (measured value = nominal value ± 0.5 µM).

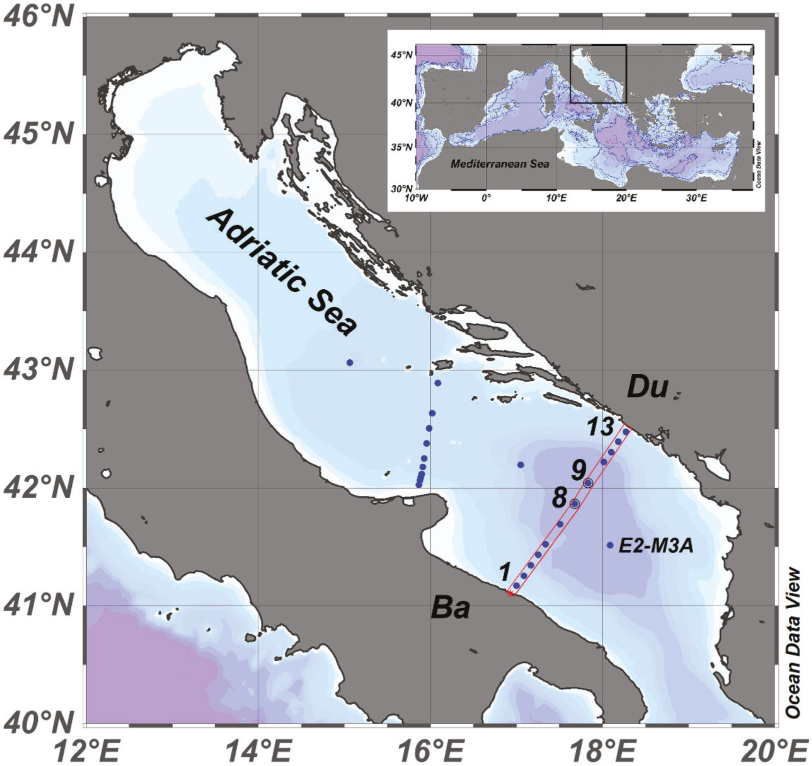

Figure 1. The Adriatic Sea. Blue dots indicate CTD (conductivity-temperature-depth) stations of the ESAW (Evolution and spreading of the Southern Adriatic Waters) cruises. Red line indicates the SAP (Southern Adriatic Pit) transect. Biological sampling concerns stations 8 and 9.

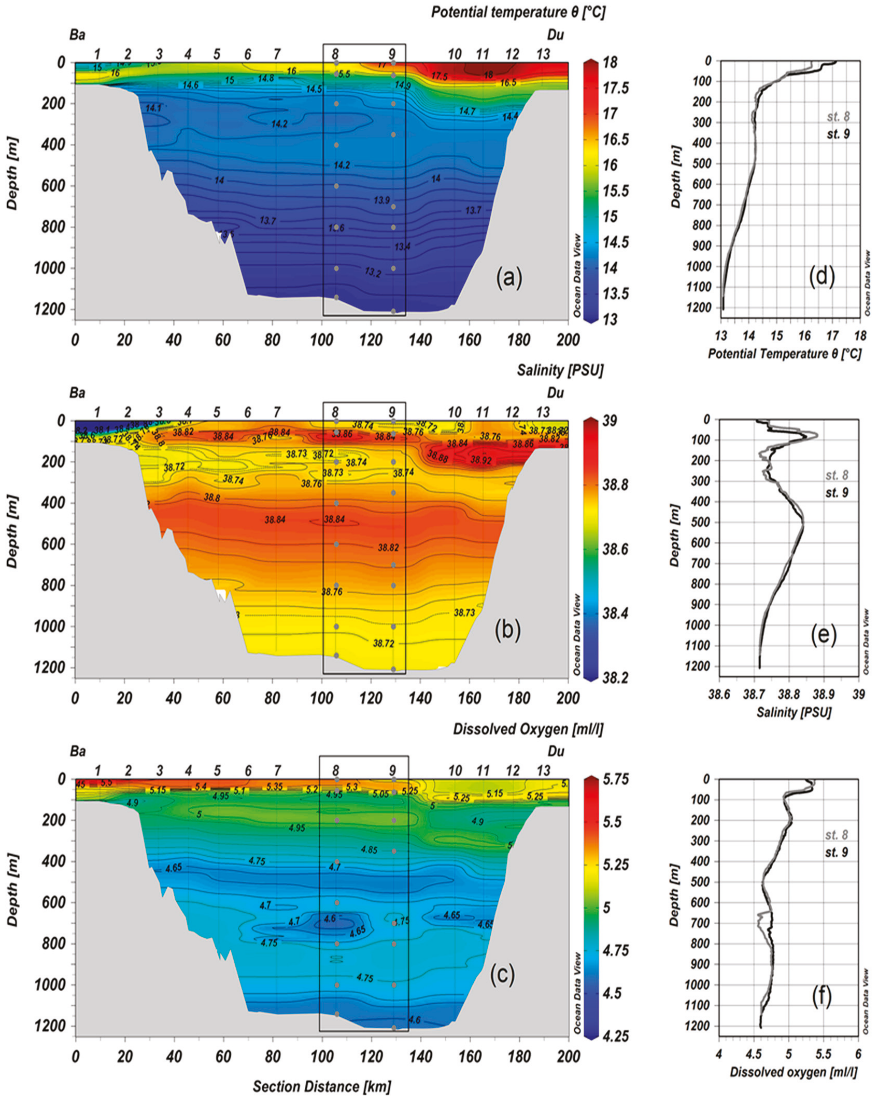

Figure 2. Vertical distribution of (**a**) potential temperature, (**b**) salinity, (**c**) dissolved oxygen, along the Bari-Dubrovnik (Ba-Du) section during the ESAW1 cruise in December 2015. Grey dots indicate locations of picoplankton sampling. Panels (**d**–**f**) show the vertical profiles of the same properties at stations 8 and 9.

2.2. Picoplankton Analysis

Sampling depths for the picoplankton analysis were 2, 45 (56 m in April), 220 (204 m in April), 400, 662 (600 m in April), 800, 1000, 1140 m at station 8; 2, 50 (62 in April), 96 (100 m in April), 193 (201 m in April), 400 (350 in April), 520 (missing in April), 700, 800, 1000, 1208 m at station 9. Flow cytometry was used to determine the abundances of *Synechococcus*, *Prochlorococcus*, picoeukaryotes, and heterotrophic bacteria [37]. Samples for autotrophic cells analysis (2 mL) were preserved in 0.5% glutaraldehyde, frozen at −80 °C, and stored until analysis (5–10 days). Samples for analysis of bacteria were preserved in 2% formaldehyde and frozen until analysis (5–10 days). Autotrophic cells were divided into two groups: cyanobacteria (*Synechococcus* and *Prochlorococcus*) and picoeukaryotes, distinguished according to light scattering, cellular chlorophyll content, and phycoerythrin-rich cells signals, respectively. Bacterial abundance was determined in scatter plots of particle side scatter versus Sybr Green I fluorescence related to cellular nucleic acid content, to discriminate bacteria from other particles. According to the cellular nucleic acid content, the bacterial population is divided into two sub-groups, HNA (High Nucleic Acid content) and LNA (Low Nucleic Acid content) bacteria. Abundances of Sybr Green-I-stained heterotrophic nanoflagellates (HNF) were also determined by cytometry [38]. For obtaining abundances, samples were processed on a Beckman Coulter EPICS XL-MCL with a high flow rate from 1 to 1.2 µL s^{-1}. AAPs were sampled only in April and were determined using the protocol described by Mašìn et al. [39]. Cells were collected on 0.2-µm polycarbonate (PC) filters by filtration and dyed with 4′,6-diamidino-2-phenylindole (DAPI) using 3:1 mixture of Citifluor™ AF1 and Vectashield® after drying. AAP bacteria were enumerated using an Olympus BX51 microscope equipped with an Olympus UPlanSApo 100×/1.40 OIL, IR objective, and software for image analysis (CellSens, Münster, Germany). The microscope was equipped with a Hg Lamp U-RFL-T, Olympus, for excitation. Fluorescent images were taken using an XM10-IR camera. Three epifluorescent filter sets were used, DAPI, IR, and chlorophyll, to create the composite image. These images were afterward used for distinguishing between organisms that contain bacteriochlorophyll *a* and chlorophyll *a*, but also for determining the number of heterotrophic bacteria, cyanobacteria, and AAP bacteria in each sample. The abundance of virus-like particles (VLP) was determined, as described in Noble and Fuhrman [40]. Collected samples were preserved in formaldehyde (2%, final concentration), flash-frozen in liquid nitrogen, and stored at −80 °C until analysis, which was performed in the laboratory immediately after the end of the cruise. Preserved samples (2 mL) were filtered through 0.02-µm pore-size filters (Anodisc; diameter: 25 mm; Al_2O_3, Whatman, Maidstone, UK) and stained with Sybr Green I (stock solution diluted 1:300). Filters were incubated in the dark for 20 min and mounted on glass slides with a drop of 50% phosphate buffer (6.7 mM, pH 7.8) and 50% glycerol, containing 0.5% ascorbic acid. Slides were stored at a temperature of −20 °C until analysis. Viral counts were obtained by epifluorescence microscopy (Olympus BX 51, 1250× magnification, equipped with a blue excitation filter, Tokyo, Japan) and were expressed as the number of virus-like particles (VLP).

Bacterial cell production was estimated by measuring the incorporation of ^{3}H-thymidine into bacterial DNA [41]. Methyl-^{3}H-thymidine was added to 10 mL samples at a final concentration of 10 nmol (specific activity: 86 Ci $mmol^{-1}$). Triplicate samples, together with a formaldehyde-killed adsorption control (final concentration: 0.5%), were incubated for one hour. The incubations were stopped with formaldehyde (final concentration: 0.5%). The thymidine samples were extracted with ice-cold trichloroacetic acid (TCA), according to Fuhrman and Azam [41]. Finally, the TCA-insoluble fraction was collected by filtering the samples through 0.2 µm pore size polycarbonate filters.

The biomass of studied picoplankton groups was estimated using the following cell-to-carbon conversion factors: 20 fgC $cell^{-1}$ for heterotrophic bacteria [42,43], 36 fgC $cell^{-1}$ for *Prochlorococcus* [44], 255 fgC $cell^{-1}$ for *Synechococcus* [44], and 2590 fgC $cell^{-1}$ for picoeukatyotes [44] and for AAPs [45].

An empirical model was used to examine the regulation of bacteria by predation [46]. Information about coupling between the abundance of bacteria and heterotrophic nanoflagellates (HNF) would be analyzed using a log-log graph. In particular, this graph included Maximum Attainable Abundance (MAA) and Mean Realized Abundance (MRA) lines. The MAA line described the HNF abundance reached at a given bacterial abundance (max log HNF = −2.47 + 1.07 log bacterial abundance). Data close to the MAA line, thus, suggested a strong coupling between the bacteria and HNF abundance, likely interpreted as strong predation on the bacteria [46]. Data positioned below the MRA line instead, suggested that bacterial abundance was not controlled by HNF grazing.

2.3. Statistical Analysis

Pearson's correlation analysis was carried out to examine the relationship between picoplankton community members and environmental variables. The response of the picoplankton community to environmental conditions was analyzed using multivariate statistical analyses. Principal component analysis (PCA) was performed using CANOCO software (http://www.canoco5.com/), v5 [47]. PCA is a multivariate statistical method mainly used for data reduction. Analysis attempts were made to identify a few components that explain the major variation within data. In our study, PCA was used to better understand the relationships in multivariate data set between environmental and biological parameters in the SAP. The data were centered and standardized to remove the large differences in abundances between groups. Model results were reproduced in ordination biplots, summarizing the main trends in the data.

3. Results

3.1. Environmental Parameters

The main physical characteristics observed throughout the water column in December 2015 (Figure 2) and April 2016 (Figure 3) were depicted from the distribution of θ, S, and DO concentration along the transect crossing the SAP (roughly from Bari, Italy toward Dubrovnik, Croatia), and from the vertical profiles of the stations 8 and 9, where picoplankton was sampled. Hereafter, we have referred to the upper layer considering the water column between the surface and 100 m depth, to the intermediate layer considering depths between 100 m and 800 m, and to the deep layer considering depths between 800 m and the bottom (~1250 m depth).

In December 2015, the upper layer along the Ba-Du section was quite heterogeneous, which might be due to the contrasting water masses transported into the SAP by the EAC along its eastern side [18], and by the WAC along its western side (Figure 2). In particular, relatively warm and saline waters moving along the eastern margin of the SAP protruded offshore, reaching the central zone of the pit (Figure 2a,b) due to local cyclonic circulation. There, complex features, such as mesoscale eddies, determine large thermohaline differences among close stations, especially between stations 8 and 9. DO distribution (Figure 2c) in the upper layer showed a marked horizontal gradient, with values diminishing from west to east. The upper intermediate layer, between 100 and 400 m, although more homogeneous, was characterized by the presence of water with properties ($\theta > 14.30$ °C and S up to 38.95) typical of the Ionian surface water and the LIWs/CIWs (Levantine/Cretan Intermediate Waters). In the central zone of the SAP, θ gradually decreased with increasing depth, while S had a structure with alternating fresher and saltier layers. Moreover, between 200 and 300 m depth, a branch of fresher water with local S minimum ~38.70 extended from the western flank towards the center of the pit (Figure 2b). In the lower intermediate layer, between 400 and 800 m, instead, S increased up to 38.84, while θ slightly decreased down to 13.60 °C. Overall, layers characterized by high S values were also characterized by reduced DO values (Figure 2c). Notably, two relative oxygen minima were found around 100 m and 500 m depth, in correspondence of relative S maxima (Figure 2e,f). However, there were some differences between stations 8 and 9, concerning mostly S and DO. At station 8 between 100 and 300 m, S values were lower than at station 9 in the same layer. The origin of that fresher layer might be attributable to a detachment of the western-coast vein of freshwater originating from the northern/middle Adriatic, as hinted from the S transect. At station 8, there was a DO minimum at 700 m depth, which was not so evident at the nearby station 9. This seems to be connected with the small scale recirculation of the "old" intermediate layers, associated with the LIW/CIW. The deep layer (>800 m) of the SAP was occupied by relatively cold, less saline, and dense waters likely formed during previous winters in the northern Adriatic. These waters would have been trapped in the deepest part of the SAP, which lies below the depth of the Otranto sill [32,34]. Dense waters coming from the northern Adriatic usually sink to the deep part of the SAP following bathymetric constraints over the slope [48] and they reach their equilibrium depths according to their densities. At the time of the cruise

(December 2015), θ and S in the deep layer had values of 13.10 °C and 38.71, respectively (Figure 2d,e). As far as the oxygen content is concerned, higher values were found between 800 m and 1000 m depth (Figure 2f), and lower values were found below 1000 m depth. This was a sign of water stagnation and lack of ventilation of the deepest part of the SAP during winters before the oceanographic survey, while, likely, relatively dense waters founded their equilibrium depths between 800 and 1000 m.

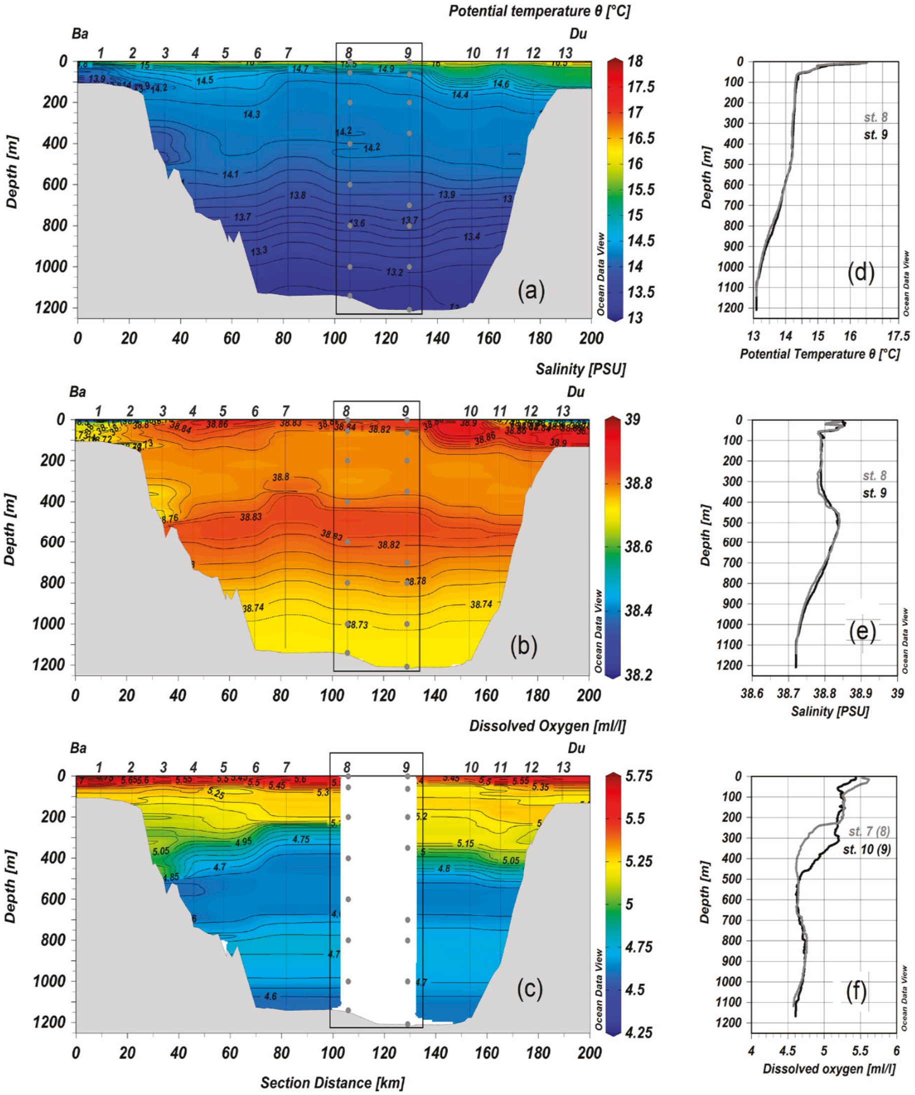

Figure 3. Vertical distribution of (**a**) potential temperature, (**b**) salinity, (**c**) dissolved oxygen, along the Bari-Dubrovnik (Ba-Du) section during the ESAW2 cruise in April 2016. Grey dots indicate locations of picoplankton sampling. Panels (**d**–**f**) show the vertical profiles of the same properties at stations 8 and 9, except the oxygen data, which were taken from stations 7 and 10 (data from station 8 and 9 are missing, due to technical problems).

In April 2016 (Figure 3), the largest differences with respect to the pre-winter conditions in December 2015 (Figure 2) were found mainly in the upper layer temperature, due to the season signal. The temperature differences between the western and eastern flanks, as well as between the surface and bottom layers over the western shelf, diminished with respect to December 2015 (Figure 3a). On the western slope, at depths between 300 and 500 m (stations 3 and 4), a branch of relatively cold, fresh, and ventilated water (θ ~14.10 °C, S ~38.74, DO ~4.9–5.1 mL/L) pointed to a possible intrusion of northern and/or middle Adriatic waters. However, data collected in the deepest layers revealed that θ and DO did not change significantly with respect to the pre-winter period, while S values slightly increased from 38.72 to 38.74 (Figure 3d–f). At the two nearby stations, 8 and 9, the thermohaline properties were almost uniform. From the DO profiles at the stations 7 and 10 (close to 8 and 9, where DO values were not recorded due to technical problems), we might guess that the vertical convection and mixing, resulting in a homogenous vertical distribution of DO, reached 350 m at station 9, and 250 m at station 8. In any case, the vertical distribution of the physical parameters and DO (Figure 3) suggested that a weak vertical convection occurred during winter 2015–2016, and it probably did not exceed 400 m in depth, as confirmed by time-series data recorded at E2-M3A (http://nettuno.ogs.trieste.it/e2-m3a/), also located in the SAP (Figure 1). The highest S values (~38.94) measured in April 2016, associated with the LIW influence, were slightly lower than those observed in December 2015 (~38.95). From the physical parameters, we inferred that the doming structure, typical of the cyclonic circulation in the SAP, was much more enhanced in April than in December. Moreover, it was centered near station 7. This means that the sub-basin-scale cyclonic gyre was probably stronger in April than in December, favoring lateral exchanges along the perimeter of the SAP. The lateral exchange between both coastal flanks and the middle of the transect seemed less active with respect to December 2015. Biogeochemical properties were obtained through chemical analyses performed on water samples collected from discrete depths along the SAP transect. Here we reported the data from stations 8 and 9, relevant for the biological sampling (Figure 1). The vertical distribution of nutrients was similar at the two stations 8 and 9 (Figure 4), for both cruises. Nitrate, phosphates, and silicates were depleted in the upper layer and increased with increasing depth. Highest values of nitrates and phosphates were found between 400 and 600 m, whereas silicates increased almost uniformly until 800 m, and then more rapidly between 1000 m and 1100 m, reaching the highest values in the bottom waters, where turbidity (proportional to the suspended particle concentration) was also high (Figure S1a,c). Ammonia concentrations were higher in December 2015 than in April 2016. Nitrites were low, but local maxima were observed at depths between 50 and 100 m in both December and April, corresponding to fluorescence maxima (Figure S1b,d). The DON and DOP concentrations throughout the water column were higher in December 2015 than in April 2016 (Figure 5). On the contrary, DOC concentrations were higher in April 2016 than in December 2015 (Figure 5a,b). High concentrations of DOC, DON, and DOP were found in the upper layer, between the surface and 100 m. In the upper layer, at 100 m depth, turbidity was relatively high in both periods, with apparently higher values in April 2016 (Figure S1a,c). Turbidity slightly increased also between 200 m and 600 m, where a prominent LIW signal was found.

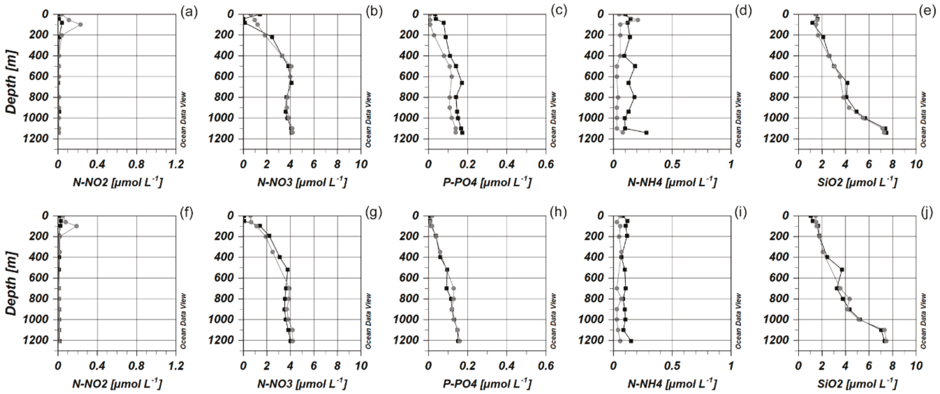

Figure 4. Vertical profiles of nutrients. Station 8: panels (**a**–**e**) and Station 9: panels (**f**–**j**). Periods: December 2015 ESAW1 (black line) and April 2016 ESAW2 (grey line). Symbols indicate sample locations.

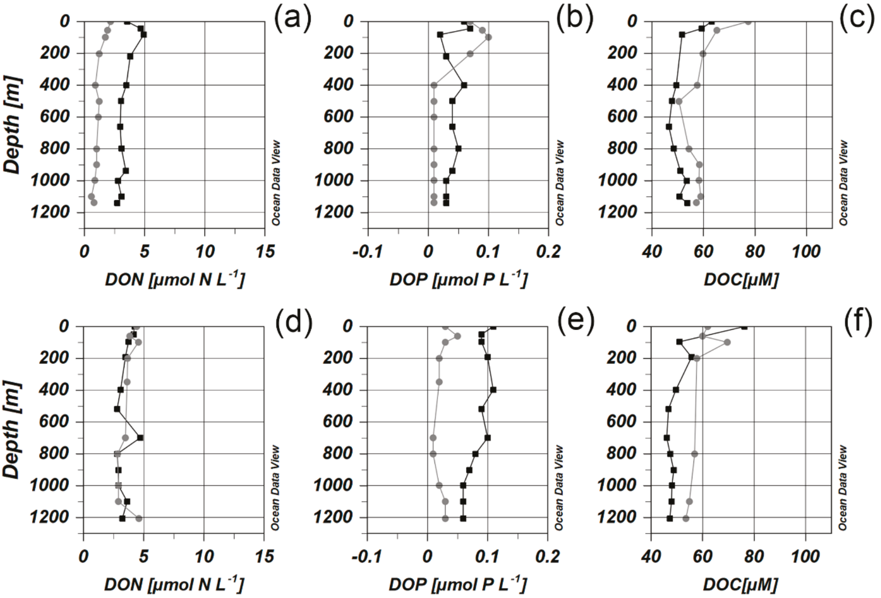

Figure 5. Vertical profiles of dissolved organic nitrogen (DON), dissolved organic phosphorus (DOP), and dissolved organic carbon (DOC). Station 8: panels (**a**–**c**). Station 9: panels (**d**–**f**). Periods: December 2015 ESAW1 (black line) and April 2016 ESAW2 (grey line). Symbols indicate sample locations.

3.2. Picoplankton Community

In both surveys, among the measured microbial community (heterotrophic bacteria, *Synechococcus*, *Prochlorococcus*, picoeukaryotes), *Synechococcus* abundances (Table S1) were the highest in the autotrophic fraction and reached values up to 93.93×10^3 cells ML^{-1}. *Prochlorococcus* and picoeukaryotes abundances were up to 47.09×10^3 cells mL^{-1} and 2.96×10^3 cells mL^{-1}, respectively. Bacterial abundance ranged from 0.03×10^6 to 0.24×10^6 cell mL^{-1} with the highest values found above 100 m depth.

In December, the autotrophic biomass (an average of 13.6 μgCL^{-1}) was almost six times higher than heterotrophic (an average of 2.29 μgCL^{-1}), with the domination of *Synechococcus*. Vertical distribution revealed the prevalence of autotrophic biomass over heterotrophic in the epipelagic layer but also deep waters (Figure 6a,b). In April, the heterotrophic biomass was similar to that in December (on average 2.90 μgCL^{-1}) and slightly higher than the autotrophic biomass (on average 2.47 μgCL^{-1}). The autotrophic biomass, mainly composed by picoeukaryotes, was slightly higher than the heterotrophic biomass in the epipelagic layer, while in the deep waters, the heterotrophic biomass dominated among the observed communities (Figure 6c,d).

Bacterial production ranged from 0.01×10^4 to 0.09×10^4 cells h^{-1} mL^{-1}. The highest values were found at the surface, but surprisingly high values were recorded at 800 m and 1200 m depth, during April 2016 (Figure 7a). The ratio of nucleic acid content showed the domination of LNA cells in all samples within the bacterial community throughout the euphotic zone (up to 200 m) and the prevalence of HNA cells in the deeper layers (Figure 7b). The abundance of viruses ranged from 0.39×10^6 VLP mL^{-1} to 5.37×10^6 VLP mL^{-1} (Figure 7c). Overall, their vertical distribution revealed a large abundance in the euphotic zone and low abundance below 300 m depth, at both sampling sites. However, at both stations, values of VLP slightly increased in the layers below 800 m in December, while at station 8, also increased in the deep layer in April. The average virus to bacteria ratio (VBR) was higher in December (19 ± 10 at station 8 and 29 ± 12 at station 9) compared to April (8 ± 2 at station 8 and 8 ± 4 at station 9).

AAPs were observed in all samples during April, with abundance ranging from 0.04×10^4 to 0.61×10^4 cells mL^{-1}. In general, their vertical distribution showed similar patterns at both stations 8 and 9. Below 200 m, in correspondence of the nutricline and the minimum fluorescence layer (Figure S1b,d) the abundances of AAPs started decreasing steeply (Figure 7d). The proportion of AAPs abundances in total prokaryotes ranged from 0.65% to 2.48%, while the proportion of the AAPs biomass ranged from 0.37% to 4.09%, respectively.

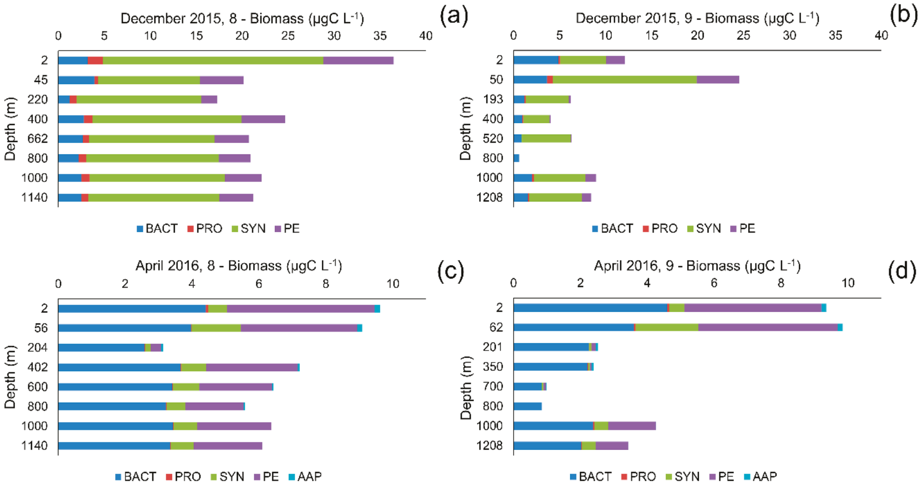

Figure 6. Vertical profiles of biomass for heterotrophic bacteria (BACT), *Prochlorococcus* (PRO), *Synechococcus* (SYN), picoeukaryotes (PE), aerobic anoxygenic phototrophs (AAP) at stations 8 (**a**) and 9 (**b**) in December 2015 (ESAW1) and at stations 8 (**c**) and 9 (**d**) in April 2016 (ESAW2).

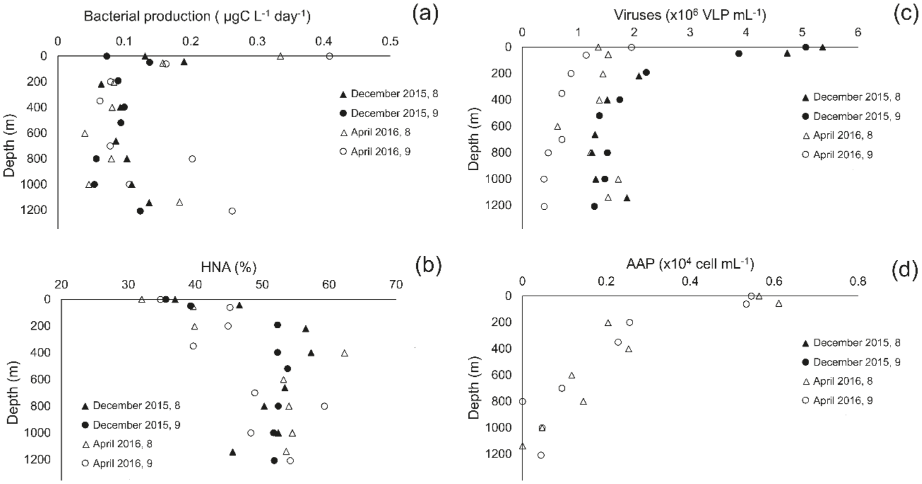

Figure 7. Vertical profile of bacterial production (**a**), HNA % (High Nucleic Acid content) (**b**), viruses (VLP) (**c**), and AAPs (**d**) at the station 8 and 9 in December 2015 (ESAW1) and in April 2016 (ESAW2).

3.3. Distribution of Picoplankton Community Members Concerning Environmental Variables

Relationship between environmental parameters and picoplankton was tested by Pearson's correlation analysis (Table S2). DOC, HNF, and temperature seemed to be the most important environmental factors for bacterial abundance and production, exhibiting significant positive correlations. Ammonium ion displayed a significant positive correlation with *Prochlorococcus* and *Synechococcus.* During the investigation period, VLP significantly correlated with autotrophic members of the picoplankton community.

Positive correlations of AAPs were found for temperature (r = 0.83; $p < 0.05$), for fluorescence (r = 0.76; $p < 0.05$), and for nitrites, nitrates, phosphates, and total dissolved phosphates (r = 0.85; r = −0.94; r = −0.90; r = −0.69; $n = 14$; $p < 0.05$). Furthermore, AAPs were also positively correlated with picoeukaryotes and HNF (r = 0.74; r = 0.91; $n = 14$; $p < 0.05$).

PCA ordination of picoplankton groups concerning environmental variables was used to analyze main factors affecting the abundances of the picoplankton groups (Figure 8a). PCA clustered the samples corresponding to depth (E-epipelagic layer; D-deep layer) and period (Figure 8b). The first principal component explained 44.83% of the variance and correlated positively with HNF and temperature, negatively with a concentration of nitrates and phosphates. The second principal component explained 17.75% of the variance and correlated positively with picoautotrophs and abundance of VLP (Table S3). Picoplankton community members were distributed in two groups, based on the correlation between them. On the one hand, bacteria, bacterial production, and LNA bacteria were closely related, while on the other hand, this was also the case for *Synechococcus* and *Prochlorococcus*. Bacterial cluster showed the strongest correlation with DOC, HNF, and temperature, as indicated by the perpendicular projection of bacterial arrow-tips on the line overlapping the DOC, HNF, and temperature arrow. Cyanobacteria were more related to ammonium, while HNA bacteria showed a positive relationship with nitrates and picoeukaryotes with VLP.

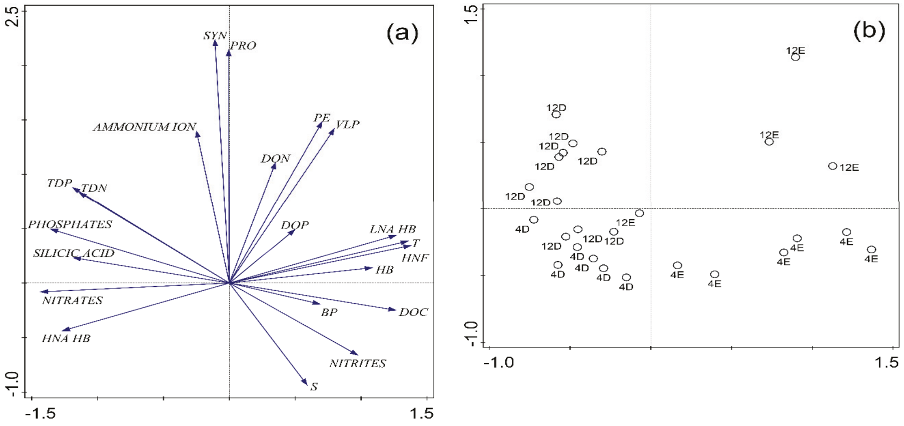

Figure 8. PCA (principal component analysis) of (**a**) biological (*Synechococcus*-SYN, *Prochlorococcus*-PRO, picoeukaryotes-PE, total bacteria—HB, HNA HB, LNA HB, VLP, HNF, bacterial production BP) and environmental parameters (Salinity—S, Temperature—T, nutrients). The arrow direction points out to the steepest increase of the variable. The angle between arrows indicates correlations between variables (an angle < 90° between two arrows of interest implies positive correlation), whereas the length of an arrow depicts the strength of association between a variable and the ordination axes shown in the biplot. (**b**) PCA clustering of the samples corresponding to depth (E-epipelagic layer; D-deep layer) and period. LNA: Low Nucleic Acid; VLP: virus-like particle; HNF: heterotrophic nanoflagellates.

The relationship between HNF as the main predator of bacteria and the bacteria was described by the Gasol model [46], which we used for our dataset. Most samples from the epipelagic layer were placed above the MRA line, whereas most samples from deep waters were below MRA. This pattern suggested a stronger coupling between bacteria and HNF in the epipelagic layer. In the deep waters layer, HNF predation pressure on bacteria was lower, suggesting larger importance for bottom-up control of bacteria and top-down control of HNF (Figure 9).

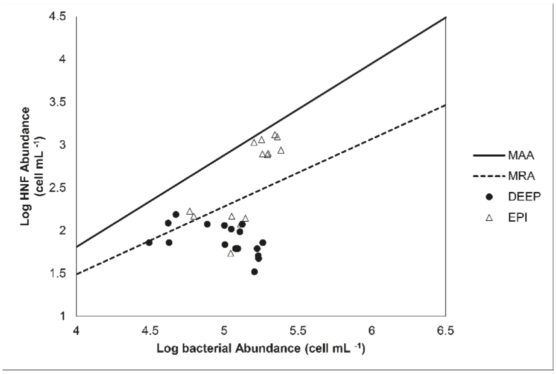

Figure 9. Relationship between bacterial and HNF abundance at study stations, plotted in a theoretical model (Gasol, 1994) (MAA-maximum attainable abundance: max log HNF = −2.47 + 1.07 log bacterial abundance; MRA-mean realized abundance: mean log HNF = −1.67 + 0.79 log bacterial abundance) in epipelagic (epi-) and deep (deep-) water layers.

4. Discussion

One of the main findings in this survey was the unusually high biomass of picoautotrophs found in the epipelagic and deep layers in December 2015. *Synechococcus* dominated the picoplankton community with a maximum value of 23.95 μgCL^{-1}. Observed high value of *Synechococcus* biomass agrees with those measured in the Levantine basin during the late summer-autumn period [49]. It is well known that picophytoplankton tends to dominate autotrophic biomass and primary production in oligotrophic waters, like those of the Mediterranean Sea [50–52]. Furthermore, picoeukaryotes contributed significantly to the autotrophic biomass due to their larger size and carbon content, compared to cyanobacteria.

Physical and biogeochemical measurements performed in December 2015 revealed the presence of LIW in the intermediate layer and NAdDW at depths > 800 m. Our results also revealed the presence, in the deep layers of the SAP, of *Synechococcus*, *Prochlorococcus,* and picoeukaryotic cells coming from the Eastern Mediterranean and the North Adriatic Sea. Our findings agree well with previous studies [6,53], which associated the high abundances of *Synechococcus* and bacterial cells in the deep layers with water mass movement.

The results of this research showed the remarkably high autotrophic biomass in the deep waters, which is not characteristic of that environment. We suggest that picoautotrophs, aside from their important role in primary production, could be a significant carbon source for higher trophic levels in the form of dead or live prey, or as sinking particles in upper [54–58] and deep ocean waters [59]. In this study, physical and biogeochemical measurements performed in the Southern Adriatic revealed that weak vertical convection occurred during winter 2015–2016, which probably did not exceed 400 m depth. Moreover, a strong heterogeneity of the physical properties distribution, both horizontally and vertically, suggested the large influence of lateral exchanges due to the cyclonic circulation and mesoscale activity, apparently stronger during spring.

In April 2016, the picoplankton community throughout the water column was dominated by heterotrophic biomass (contrary to the December case), which is consistent with previous research for the open Adriatic area [3]. *Synechococcus*, *Prochlorococcus,* and picoeukaryotes abundances fluctuate in a range typical for the euphotic zone in the open Adriatic Sea [3,60,61]. In this survey, *Synechococcus* was the most abundant autotroph. *Synechococcus* hold the advantage over genus *Prochlorococcus* and thrive in P-depleted environments due to the high affinity for inorganic phosphorus and higher phosphate uptake rates as reported recently [62,63]. Furthermore, both genera of cyanobacteria showed a positive relationship with the concentration of ammonium, which is supported by the fact that *Synechococcus* can exploit both the reduced and the oxidized forms of nitrogen. In oligotrophic environments, ammonium represents the major nitrogen compound for primary production [64], and *Prochlorococcus* are effective in consuming the same [65,66].

Our findings clearly showed that bacterial production and biomass values measured in the deep waters were similar to the values for the epipelagic layer. La Ferla et al. [67] also found similar vertical patterns of bacterial density and bacterial production in the Western and the Eastern Mediterranean Sea. Additionally, we determined the dominance of HNA bacterial group in the deep-sea, while the LNA bacterial group prevailed in the epipelagic layer. Recent research from the Adriatic Sea pointed out the increase of HNA bacteria with depth, and together with LNA bacteria, they participated in the bacterial activity [10,68]. It is well known that HNA bacterial cells are larger than LNA cells and that the proportion of HNA bacteria increases with depth [69,70]. Larger cell size is reflected in a higher-level cell-specific activity or higher metabolic versatility in the mesopelagic ocean [5,70,71]. So, we argue that similar values of bacterial production measured in the deep water and epipelagic layer, together with the dominance of HNA bacteria in deep water, showed bacterial activity in the deep waters of SAP. We can conclude that the results of bacterial production as the measure of activity in this study support the idea that deep ocean prokaryotes are active as those living in the epipelagic waters [4,72–75]. Beside the domination of HNA cells in the bacterial community, our data showed increased values of DOC, phosphates, and bacterial production below 800 m during the post-winter period. This suggests that the bacterial activity increases with the supply of organic carbon, as Nagata et al. [76] previously described for the deep-sea environment.

Bacterial abundance throughout the water column was approximately 10^5 cells mL^{-1}, which is per the recent data reported for the SAP [8,10] and with previous studies carried out in the Mediterranean Sea [67,72,77–79]. Heterotrophic bacteria contribute at a high percentage in total picoplankton biomass, acting as decomposers of organic matter and important producers of new biomass. Through grazing by HNF or larger zooplankton, their biomass becomes available to higher trophic levels, in both the epipelagic and deep waters of the Mediterranean Sea [5,46,59]. During our surveys, bacterial abundance and productivity showed positive relationships with DOC concentration and HNF abundance. Our results showed that the increase in bacterial abundance and cell production supported the increase in the number of HNF, especially in the epipelagic layer. It revealed that bacteria constitute a potential food resource for the nanoflagellate community and suggest a strong top-down control of bacteria. These results confirm previous findings showing [2,80] that predators prefer active bacteria and remove bacterial production, and that they can control the abundance of the bacterial community in surface waters [46]. Some studies [21,81] suggested strong bottom-up control of bacteria, which is in accordance with our results, showing a positive relationship between bacterial parameters and DOC concentration through the water column.

Little is known about the role and distribution of AAPs in the Adriatic Sea, especially in its deepest part. Šantić et al. [12] investigated AAPs abundances along the eastern Adriatic, in coastal and transitional waters, and found that their proportion in total prokaryotes was 7.3% (±4.3%). Celussi et al. [11] pointed out that the concentration of bacteriochlorophyll *a*, the main pigment of AAPs, could be converted into abundance. Therefore, AAPs might represent up to 10% of total prokaryotes in the open Adriatic Sea. In recent research of AAPs, the abundance, the proportion in total prokaryotes, and biomass decreased along the trophic gradient [45]. Furthermore, these counts were substantially low at the oligotrophic open sea station, especially under 70 m depth. Similar vertical distribution was already noted [13,82–86] since these organisms inhabit the euphotic zone because of their phototrophic nature. The results of this study are consistent with previous reports, which also found lower abundances in the more oligotrophic area when compared to the more productive regions or shelf seas [13,39,82,85–89].

The main environmental parameters that influenced the picoplankton community according to the research conducted by Šantić et al. [12] were chlorophyll, followed by nitrates and temperature.

In this research, fluorescence, as a proxy of chlorophyll, nitrates, nitrites, phosphates, and total dissolved phosphates, influenced the abundance of AAPs. Besides, the correlation found between bacteria and AAPs, which has also been reported by Celussi et al. [11], could be explained by the fact that both AAPs and heterotrophic bacteria rely on labile DOC, part of which is released by phytoplankton. Secondly, AAPs and phytoplankton have a similar dependence on light [90], and this relationship may reflect the same dependence on limiting nutrients, such as phosphorus or nitrogen [15]. The majority of AAP surveys have shown that temperature, salinity, chlorophyll concentration, and carbon and nitrogen compounds affect the dynamics and distribution of the AAP population [39,85–87,89]. The high positive correlation between AAPs and HNF found during our study suggest that AAPs represent an important prey for flagellates in the open Adriatic Sea, as documented in the Mediterranean Sea [91,92]. It is a well-known fact that AAPs are larger than the average heterotrophic bacteria [13,14,86,93] and that, consequently, their biomass contribution to total bacterial biomass is also high (up to 11% in this survey). Cell size is an important parameter in feeding ecology, which provides a valuable insight into the trophic significance of AAPs. It was previously observed that nanoflagellates preferentially ingest the larger bacterial cells [94–96].

The number of viruses ranged between 0.39×10^6 VLP Ml^{-1} and 5.37×10^6 VLP mL^{-1}, which is in accordance with other studies for the Adriatic and Mediterranean Sea [97–101]. Their average abundance was 16 ± 12× higher than the abundance of prokaryotes, as well as in previous studies on oligotrophic deep waters [99]. Relatively high VBR determined in the deep waters could be a result of higher lytic activity caused by lysogenic viruses. Water mass sinking to the SAP could cause the induction of lysogenic viruses and thus keep the viral abundance stable. Winter et al. [102] recently pointed out that mixing in the deeper waters led to the induction of lysogenic viruses. Viruses positively correlated with the members of the picoplankton community at the sampling sites, indicating their involvement in shaping the picoplankton abundances in the oligotrophic waters of the SAP. The PCA analysis revealed a close relationship between viruses and the picoautotrophic group. It is known that viruses can be an important mortality factor for picoeukaryotes in oligotrophic oceanic waters [103]. Our results suggest that viruses are an important component of the microbial food web, but this topic should be addressed in further studies.

5. Conclusions

The present study points out the importance of *Synechococcus*, *Prochlorococcus*, picoeukaryotes, heterotrophic bacteria, AAPs, heterotrophic nanoflagellates, and viruses altogether in the carbon flux through the microbial food web in the SAP for the first time, which depended largely on water mass movements and mixing.

A significant amount of picoautotropic biomass was found in the epipelagic, as well as in the deep layers, during the period under the influence of LIW inflow and NAdDW sinking, respectively. After weak vertical convection during winter, heterotrophic bacteria dominated picoplankton biomass throughout the water column. Furthermore, bacterial activity values in the deep layer were similar to the ones obtained in the epipelagic layer. Besides the physical pump, the changes in the picoplankton community in the SAP were mainly driven by nutrient availability, more specifically bacteria by DOC and cyanobacteria by ammonium ion. Our results also reveal that bacteria represent an important prey for nanoflagellates, especially in the epipelagic layer. Moreover, autotrophic and heterotrophic members of the picoplankton community could be available prey and a source of carbon for the food web below the epipelagic layer. Finally, AAPs contributed up to 4% of bacterial biomass, which can be transferred through higher trophic levels by grazing. Viral lysis may affect the activity of the picoplankton community and serve as an important source of DOC in the deep-sea.

Supplementary Materials: The following are available online at http://www.mdpi.com/2073-4441/11/8/1655/s1, Figure S1:Vertical profiles of optical backscattering and fluorescence. Station 8: panels (a) and (b). Station 9: panels (c) and (d). Periods: December 2015 ESAW1 (black line) and April 2016 ESAW2 (grey line), Table S1: Summary of the picoplankton community abundances, Table S2. Summary of the correlations between picoplankton community (Synechococcus-SYN, Prochlorococcus-PRO, picoeukaryotes-PE, total bacteria HB, HNA HB, LNA HB, VLP, HNF, bacterial production BP) and environmental variables (Temperature-T, nutrients). Acronym n.s. stands for not significant, Table S3. Summary of the principal component analysis (PCA) of the picoplankton groups and environmental variables.

Author Contributions: Conceptualization, M.B.; Data curation, V.K.; Formal analysis, D.Š. and A.V.T.; Funding acquisition, V.K.; Investigation, D.Š.; Methodology, D.Š., M.G., A.V.T., M.O., C.S., S.Š. and B.G.; Project administration, V.K.; Supervision, M.Š.; Writing—original draft, D.Š.; Writing—review and editing, V.K., M.B., M.G., A.V.T. and M.O.

Funding: The study was carried out within the framework of the EUROFLEETS2 research infrastructures project under the 7th Framework Program of the European Commission (grant agreement 312762). It was partially funded by the Italian national project RITMARE (Ricerca Italiana per il Mare, grant numbers: SP3-WP3-AZ1; SP4-LI4-WP1; SP5-WP3-AZ3) and by the Croatian Science Foundation as a part of research projects: IP-2014-09-4143 "Marine microbial food web processes in global warming perspective" (MICROGLOB).

Acknowledgments: We thank L.U. for nutrients, TDN and TDP analyses, H.M. and S.M. for their help with sampling, and the crew of R/V BIOS DVA.

Conflicts of Interest: The authors declare no conflict of interest.

References

1. Ninčević Gladan, Ž.; Marasović, I.; Kušpilić, G.; Krstulović, N.; Šolić, M.; Šestanović, S. Abundance and composition of picoplankton in the mid Adriatic Sea. *Acta Adriat.* **2006**, *47*, 127–140.
2. Šolić, M.; Grbec, B.; Matić, F.; Šantić, D.; Šestanović, S.; Gladan, Ž.N.; Bojanić, N.; Ordulj, M.; Jozić, S.; Vrdoljak, A. Spatio-temporal reproducibility of the microbial food web structure associated with the change in temperature: Long-term observations in the Adriatic Sea. *Prog. Oceanogr.* **2018**, *161*, 87–101. [CrossRef]
3. Šantić, D.; Krstulović, N.; Šolić, M.; Ordulj, M.; Kušpilić, G. Dynamics of prokaryotic picoplankton community in the central and southern Adriatic Sea (Croatia). *Helgoland Mar. Res.* **2013**, *67*, 471–481. [CrossRef]
4. Tanaka, T.; Rassoulzadegan, F. Full-depth profile (0–2000m) of bacteria, heterotrophic nanoflagellates and ciliates in the NW Mediterranean Sea: Vertical partitioning of microbial trophic structures. *Deep Sea Res. Part II Top. Stud. Oceanogr.* **2002**, *49*, 2093–2107. [CrossRef]
5. Arístegui, J.; Gasol, J.M.; Duarte, C.M.; Herndl, G.J. Microbial oceanography of the dark ocean's pelagic realm. *Limnol. Oceanogr.* **2009**, *54*, 1501–1529. [CrossRef]
6. Vilibić, I.; Šantić, D. Deep water ventilation traced by *Synechococcus* cyanobacteria. *Ocean Dyn.* **2008**, *58*, 119–125. [CrossRef]
7. Azzaro, M.; La Ferla, R.; Maimone, G.; Monticelli, L.S.; Zaccone, R.; Civitarese, G. Prokaryotic dynamics and heterotrophic metabolism in a deep convection site of Eastern Mediterranean Sea (the Southern Adriatic Pit). *Cont. Shelf Res.* **2012**, *44*, 106–118. [CrossRef]
8. Batistić, M.; Jasprica, N.; Carić, M.; Čalić, M.; Kovačević, V.; Garić, R.; Njire, J.; Mikuš, J.; Bobanović-Ćolić, S. Biological evidence of a winter convection event in the South Adriatic: A phytoplankton maximum in the aphotic zone. *Cont. Shelf Res.* **2012**, *44*, 57–71. [CrossRef]
9. Cerino, F.; Aubry, F.B.; Coppola, J.; La Ferla, R.; Maimone, G.; Socal, G.; Totti, C. Spatial and temporal variability of pico-, nano-and microphytoplankton in the offshore waters of the southern Adriatic Sea (Mediterranean Sea). *Cont. Shelf Res.* **2012**, *44*, 94–105. [CrossRef]
10. Šilović, T.; Mihanović, H.; Batistić, M.; Radić, I.D.; Hrustić, E.; Najdek, M. Picoplankton distribution influenced by thermohaline circulation in the southern Adriatic. *Cont. Shelf Res.* **2018**, *155*, 21–33. [CrossRef]
11. Celussi, M.; Gallina, A.A.; Ras, J.; Giani, M.; Del Negro, P. Effect of sunlight on prokaryotic organic carbon uptake and dynamics of photoheterotrophy in the Adriatic Sea. *Aquat. Microb. Ecol.* **2015**, *74*, 235–249. [CrossRef]
12. Šantić, D.; Šestanović, S.; Vrdoljak, A.; Šolić, M.; Kušpilić, G.; Ninčević Gladan, Ž.; Koblížek, M. Distribution of aerobic anoxygenic phototrophs in the Eastern Adriatic Sea. *Mar. Environ. Res.* **2017**, *130*, 134–141. [CrossRef] [PubMed]
13. Sieracki, M.E.; Gilg, I.C.; Thier, E.C.; Poulton, N.J.; Goericke, R. Distribution of planktonic aerobic anoxygenic photoheterotrophic bacteria in the northwest Atlantic. *Limnol. Oceanogr.* **2006**, *51*, 38–46. [CrossRef]
14. Stegman, M.R.; Cottrell, M.T.; Kirchman, D.L. Leucine incorporation by aerobic anoxygenic phototrophic bacteria in the Delaware estuary. *ISME J.* **2014**, *8*, 2339–2348. [CrossRef] [PubMed]
15. Koblížek, M. Ecology of aerobic anoxygenic phototrophs in aquatic environments. *FEMS Microbiol. Rev.* **2015**, *39*, 854–870. [CrossRef]
16. Kovačević, V.; Gačić, M.; Poulain, P.M. Eulerian current measurements in the Strait of Otranto and in the Southern Adriatic. *J. Mar. Syst.* **1999**, *20*, 255–278. [CrossRef]
17. Yari, S.; Kovačević, V.; Cardin, V.; Gačić, M.; Bryden, H.L. Direct estimate of water, heat, and salt transport through the Strait of Otranto. *J. Geophys. Res. Oceans* **2012**, *117*. [CrossRef]
18. Artegiani, A.; Paschini, E.; Russo, A.; Bregant, D.; Raicich, F.; Pinardi, N. The Adriatic Sea General Circulation. Part I: Air-Sea Interactions and Water Mass Structure. *J. Phys. Oceanogr.* **1997**, *27*, 1492–1514. [CrossRef]
19. Buljan, M. Oceanographical properties of the Adriatic Sea. *Oceanogr. Mar. Biol. Ann. Rev.* **1976**, *14*, 11–98.
20. Vukadin, I.; Stojanoski, L. Phosphorus versus nitrogen limitation in the middle Adriatic Sea. In Proceedings of the Rapport du 36e Congrès de la Commission Internationale pour l'Exploration Scientifique de la mer Mediterranee, Monaco, 1 October 2001.
21. Šolić, M.; Krstulović, N.; Vilibić, I.; Kušpilić, G.; Šestanović, S.; Šantić, D.; Ordulj, M. The role of water mass dynamics in controlling bacterial abundance and production in the middle Adriatic Sea. *Mar. Environ. Res.* **2008**, *65*, 388–404. [CrossRef]

22. Skejić, S.; Arapov, J.; Kovačević, V.; Bužančić, M.; Bensi, M.; Giani, M.; Bakrač, A.; Mihanović, H.; Ninčević Gladan, Ž.; Urbini, L.; et al. Coccolithophore diversity in open waters of the middle Adriatic Sea in pre-and post-winter periods. *Mar. Micropaleontol.* **2018**, *43*, 30–45. [CrossRef]
23. Gačić, M.; Borzelli, G.L.E.; Civitarese, G.; Cardin, V.; Yari, S. Can internal processes sustain reversals of the ocean upper circulation? The Ionian Sea example. *Geophys. Res. Lett.* **2010**, *37*, L09608. [CrossRef]
24. Bensi, M.; Velaoras, D.; Meccia, L.V.; Cardin, V. Effects of the Eastern Mediterranean Sea circulation on the thermohaline properties as recorded by fixed deep-ocean observatories. *Deep Sea Res. Part I Oceanogr. Res. Pap.* **2016**, *112*, 1–13. [CrossRef]
25. Civitarese, G.; Gačić, M.; Lipizer, M.; Eusebi Borzelli, G.L. On the impact of the Bimodal Oscillating System (BiOS) on the biogeochemistry and biology of the Adriatic and Ionian Seas (Eastern Mediterranean). *Biogeosciences* **2010**, *7*, 3987–3997. [CrossRef]
26. Batistić, M.; Garić, R.; Molinero, J.C. Interannual variations in Adriatic Sea zooplankton mirror shifts in circulation regimes in the Ionian Sea. *Clim. Res.* **2014**, *61*, 231–240. [CrossRef]
27. Matić, F.; Kovač, Ž.; Vilibić, I.; Mihanović, H.; Morović, M.; Grbec, B.; Leder, N.; Džoić, T. Oscillating Adriatic temperature and salinity regimes mapped using the Self-Organizing Maps method. *Cont. Shelf Res.* **2017**, *132*, 11–18. [CrossRef]
28. Vilibić, I.; Orlić, M. Adriatic water masses, their rates of formation and transport through the Otranto Strait. *Deep Sea Res. Part I Oceanogr. Res. Pap.* **2002**, *49*, 1321–1340. [CrossRef]
29. Querin, S.; Bensi, M.; Cardin, V.; Solidoro, C.; Bacer, S.; Mariotti, L.; Stel, F.; Malačič, V. Saw-tooth modulation of the deep-water thermohaline properties in the southern Adriatic Sea. *J. Geophys. Res. Oceans* **2016**, *121*, 4585–4600. [CrossRef]
30. Vilibić, I.; Orlić, M. Least-squares tracer analysis of water masses in the South Adriatic (1967–1990). *Deep Sea Res. Part I Oceanogr. Res. Pap.* **2001**, *48*, 2297–2330. [CrossRef]
31. Cardin, V.; Bensi, M.; Pacciaroni, M. Variability of water mass properties in the last two decades in the Southern Adriatic Sea with emphasis on the period 2006–2009. *Cont. Shelf Res.* **2011**, *31*, 951–965. [CrossRef]
32. Bensi, M.; Cardin, V.; Rubino, A.; Notarstefano, G.; Poulain, P.M. Effects of winter convection on the deep layer of the Southern Adriatic Sea in 2012. *J. Geophys. Res. Oceans* **2013**, *118*, 6064–6075. [CrossRef]
33. Schlitzer, R.; Roether, W.; Oster, H.; Junghans, H.; Hausmann, M.; Johannsen, H.; Michelato, A. Chlorofluoromethane and oxygen in the Eastern Mediterranean. *Deep Sea Res. Part A Oceanogr. Res. Pap.* **1991**, *38*, 1531–1535. [CrossRef]
34. Mihanović, H.; Vilibić, I.; Carniel, S.; Tudor, M.; Russo, A.; Bergamasco, A.; Bubić, N.; Ljubešić, Z.; Viličić, D.; Boldrin, A.; et al. Exceptional dense water formation on the Adriatic shelf in the winter of 2012. *Ocean Sci.* **2013**, *9*, 561–572. [CrossRef]
35. Schlitzer, R. Ocean Data View. 2018. Available online: http://odv.awi.de/ (accessed on 1 February 2019).
36. Hansen, H.P.; Koroleff, F. Determination of nutrients. *Methods Seawater Anal.* **1999**, *27*, 159–228.
37. Marie, D.; Partensky, F.; Jacquet, S.; Vaulot, D. Enumeration and cell cycle analysis of natural populations of marine picoplankton by flow cytometry using the nucleic acid stain SYBR Green I. *Appl. Environ. Microbiol.* **1997**, *63*, 186–193. [PubMed]
38. Christaki, U.; Courties, C.; Massana, R.; Catala, P.; Lebaron, P.; Gasol, J.M.; Zubkov, M.V. Optimized routine flow cytometric enumeration of heterotrophic flagellates using SYBR Green I. *Limnol. Oceanogr. Methods* **2011**, *9*, 329–339. [CrossRef]
39. Mašín, M.; Zdun, A.; Ston-Egiert, J.; Nausch, M.; Labrenz, M.; Moulisová, V.; Koblížek, M. Seasonal changes and diversity of aerobic anoxygenic phototrophs in the Baltic Sea. *Aquat. Microb. Ecol.* **2006**, *45*, 247–254. [CrossRef]
40. Noble, R.T.; Fuhrman, J.A. Use of SYBR Green I for rapid epifluorescence counts of marine viruses and bacteria. *Aquat. Microb. Ecol.* **1998**, *14*, 113–118. [CrossRef]
41. Fuhrman, J.A.; Azam, F. Thymidine incorporation as a measure of heterotrophic bacterioplankton production in marine surface waters: Evaluation and field results. *Mar. Biol.* **1982**, *66*, 109–120. [CrossRef]
42. Lee, S.; Fuhrman, J.A. Relationships between biovolume and biomass of naturally derived marine bacterioplankton. *Appl. Environ. Microbiol.* **1987**, *53*, 1298–1303.
43. Kirchman, D.L. *Handbook of Methods in Aquatic Microbial Ecology*; Lewis Publishers: Boca Raton, FL, USA, 1993; pp. 509–512.

44. Buitenhuis, E.T.; Li, W.K.W.; Vaulot, D.; Lomas, M.W.; Landry, M.R.; Partensky, F.; McManus, G.B. Picophytoplankton biomass distribution in the global ocean. *Earth Syst. Sci. Data* **2012**, *4*, 37–46. [CrossRef]
45. Vrdoljak Tomaš, A.; Šantić, D.; Šolić, M.; Ordulj, M.; Jozić, S.; Šestanović, S.; Matić, F.; Kušpilić, G.; Ninčević Gladan, Ž. Dynamics of Aerobic Anoxygenic Phototrophs along the trophic gradient in the central Adriatic Sea. *Deep Sea Res. Part II Top. Stud. Oceanogr.* **2019**. [CrossRef]
46. Gasol, J.M. A framework for the assessment of top-down vs bottom-up control of heterotrophic nanoflagellate abundance. *Mar. Ecol. Prog. Ser.* **1994**, *113*, 291–300. [CrossRef]
47. ter Braak, C.J.; Šmilauer, P. *Canoco Reference Manual and User's Guide: Software for Ordination*, version 5.0; Microcomputer Power: Ithaca, NY, USA, 2012.
48. Rubino, A.; Romanenkov, D.; Zanchettin, D.; Cardin, V.; Hainbucher, D.; Bensi, M.; Boldrin, A.; Langone, L.; Miserocchi, S.; Turchetto, M. On the descent of dense water on a complex canyon system in the southern Adriatic basin. *Cont. Shelf Res.* **2012**, *44*, 20–29. [CrossRef]
49. Bayindirli, C.; Ulysal, Z. Monthly changes in the abundance and biomass of cyanobacteria Synechococcus in the Cilician Basin. *Rapp. Comm. Int. Mer. Médit.* **2007**, *38*, 347.
50. Li, W.K. Annual average abundance of heterotrophic bacteria and *Synechococcus* in surface ocean waters. *Limnol. Oceanogr.* **1998**, *43*, 1746–1753. [CrossRef]
51. Zubkov, M.V.; Sleigh, M.A.; Burkill, P.H.; Leakey, R.J. Picoplankton community structure on the Atlantic Meridional Transect: A comparison between seasons. *Prog. Oceanogr.* **2000**, *45*, 369–386. [CrossRef]
52. Li, W.K.W.; Harrison, W.G. Chlorophyll, bacteria and picophytoplankton in ecological provinces of the North Atlantic. *Deep Sea Res. Part II Top. Stud. Oceanogr.* **2001**, *48*, 2271–2293. [CrossRef]
53. Carlucci, A.F.; Craven, D.B.; Robertson, K.J.; Henrichs, S.M. Microheterotrophic utilization of dissolved free amino-acids in depth profiles of southern-California borderland basin waters. *Oceanol. Acta* **1986**, *9*, 89–96.
54. DeLong, E.F.; Yayanos, A.A. Biochemical function and ecological significance of novel bacterial lipids in deep-sea prokaryotes. *Appl. Environ. Microbiol.* **1986**, *51*, 730–737.
55. Li, W.K. Primary production of prochlorophytes, cyanobacteria, and eukaryotic ultraphytoplankton: Measurements from flow cytometric sorting. *Limnol. Oceanogr.* **1994**, *39*, 169–175. [CrossRef]
56. Partensky, F.; Blanchot, J.; Lantoine, F.; Neveux, J.; Marie, D. Vertical structure of picophytoplankton at different trophic sites of the tropical northeastern Atlantic Ocean. *Deep Sea Res. Part I Oceanogr. Res. Pap.* **1996**, *43*, 1191–1213. [CrossRef]
57. Blanchot, J.; André, J.M.; Navarette, C.; Neveux, J.; Radenac, M.H. Picophytoplankton in the equatorial Pacific: Vertical distributions in the warm pool and in the high nutrient low chlorophyll conditions. *Deep Sea Res. Part I Oceanogr. Res. Pap.* **2001**, *48*, 297–314. [CrossRef]
58. Buesseler, K.O.; Lamborg, C.H.; Boyd, P.W.; Lam, P.J.; Trull, T.W.; Bidigare, R.R.; Bishop, J.K.; Casciotti, K.L.; Dehairs, F.; Elskens, M.; et al. Revisiting carbon flux through the ocean's twilight zone. *Science* **2007**, *316*, 567–570. [CrossRef] [PubMed]
59. Zhang, Y.; Jiao, N.; Hong, N. Comparative study of picoplankton biomass and community structure in different provinces from subarctic to subtropical oceans. *Deep Sea Res. Part II Top. Stud. Oceanogr.* **2008**, *55*, 1605–1614. [CrossRef]
60. Šilović, T.; Balagué, V.; Orlić, S.; Pedrós-Alió, C. Picoplankton seasonal variation and community structure in the northeast Adriatic coastal zone. *FEMS Microbiol. Ecol.* **2012**, *82*, 678–691. [CrossRef] [PubMed]
61. Najdek, M.; Paliaga, P.; Šilović, T.; Batistić, M.; Garić, R.; Supić, N.; Ivančić, I.; Ljubimir, S.; Korlević, M.; Jasprica, N.; et al. Picoplankton community structure before, during and after convection event in the offshore waters of the Southern Adriatic Sea. *Biogeosciences* **2014**, *11*, 2645–2659. [CrossRef]
62. Moutin, T.; Thingstad, T.F.; Van Wambeke, F.; Marie, D.; Slawyk, G.; Raimbault, P.; Claustre, H. Does competition for nanomolar phosphate supply explain the predominance of the cyanobacterium *Synechococcus*? *Limnol. Oceanogr.* **2002**, *47*, 1562–1567. [CrossRef]
63. Martiny, A.C.; Kathuria, S.; Berube, P.M. Widespread metabolic potential for nitrite and nitrate assimilation among Prochlorococcus ecotypes. *Proc. Natl. Acad. Sci. USA* **2009**, *106*, 10787–10792. [CrossRef]
64. Raven, J.A.; Wollenweber, B.; Handley, L.L. A comparison of ammonium and nitrate as nitrogen sources for photolithotrophs. *New Phytol.* **1992**, *121*, 19–32. [CrossRef]
65. Partensky, F.; Hess, W.R.; Vaulot, D. *Prochlorococcus*, a marine photosynthetic prokaryote of global significance. *Microbiol. Mol. Biol. Rev.* **1999**, *63*, 106–127. [PubMed]

66. Wyman, M.; Bird, C. Lack of control of nitrite assimilation by ammonium in an oceanic picocyanobacterium, *Synechococcus* sp. strain WH 8103. *Appl. Environ. Microbiol.* **2007**, *73*, 3028–3033. [CrossRef] [PubMed]
67. La Ferla, R.; Azzaro, M.; Budillon, G.; Caroppo, C.; Decembrini, F.; Maimone, G. Distribution of the prokaryotic biomass and community respiration in the main water masses of the Southern Tyrrhenian Sea (June and December 2005). *Adv. Ocean. Limnol.* **2010**, *1*, 235–257. [CrossRef]
68. Šantić, D.; Krstulović, N.; Šolić, M.; Kušpilić, G. HNA and LNA bacteria in relation to the activity of heterotrophic bacteria. *Acta Adriat.* **2012**, *53*, 25–40.
69. Andrade, L.; Gonzalez, A.M.; Araujo, F.V.; Paranhos, R. Flow cytometry assessment of bacterioplankton in tropical marine environments. *J. Microbiol. Methods* **2003**, *55*, 841–850. [CrossRef] [PubMed]
70. Corzo, A.; Rodríguez-Gálvez, S.; Lubian, L.; Sobrino, C.; Sangrá, P.; Martínez, A. Antarctic marine bacterioplankton subpopulations discriminated by their apparent content of nucleic acids differ in their response to ecological factors. *Polar Biol.* **2005**, *29*, 27–39. [CrossRef]
71. Reinthaler, T.; Van Aken, H.; Veth, C.; Arístegui, J.; Robinson, C.; Williams, P.J.L.B.; Lebaron, P.; Herndl, G.J. Prokaryotic respiration and production in the meso-and bathypelagic realm of the eastern and western North Atlantic basin. *Limnol. Oceanogr.* **2006**, *51*, 1262–1273. [CrossRef]
72. Tanaka, T.; Rassoulzadegan, F. Vertical and seasonal variations of bacterial abundance and production in the mesopelagic layer of the NW Mediterranean Sea: bottom-up and top-down controls. *Deep Sea Res. Part I Oceanogr. Res. Pap.* **2004**, *51*, 531–544. [CrossRef]
73. Herndl, G.J.; Reinthaler, T.; Teira, E.; van Aken, H.; Veth, C.; Pernthaler, A.; Pernthaler, J. Contribution of Archaea to total prokaryotic production in the deep Atlantic Ocean. *Appl. Environ. Microb.* **2005**, *71*, 2303–2309. [CrossRef]
74. Teira, E.; Van Aken, H.; Veth, C.; Herndl, G.J. Archaeal uptake of enantiomeric amino acids in the meso-and bathypelagic waters of the North Atlantic. *Limnol. Oceanogr.* **2006**, *51*, 60–69. [CrossRef]
75. Del Giorgio, P.A.; Gasol, J.M. Physiological structure and single-cell activity in marine bacterioplankton. In *Microbial Ecology of the Oceans*, 2nd ed.; Kirchman, D.L., Ed.; John Wiley & Sons, Inc.: New York, NY, USA, 2008; pp. 243–285.
76. Nagata, T.; Fukuda, H.; Fukuda, R.; Koike, I. Bacterioplankton distribution and production in deep Pacific waters: Large-scale geographic variations and possible coupling with sinking particle fluxes. *Limnol. Oceanogr.* **2000**, *45*, 426–435. [CrossRef]
77. Tholosan, O.; Garcin, J.; Bianchi, A. Effects of hydrostatic pressure on microbial activity through a 2000 m deep water column in the NW Mediterranean Sea. *Mar. Ecol. Prog. Ser.* **1999**, *183*, 49–57. [CrossRef]
78. La Ferla, R.; Azzaro, M.; Caruso, G.; Monticelli, L.S.; Maimone, G.; Zaccone, R.; Packard, T.T. Prokaryotic abundance and heterotrophic metabolism in the deep Mediterranean Sea. *Adv. Oceanogr. Limnol.* **2010**, *1*, 143–166. [CrossRef]
79. Yokokawa, T.; De Corte, D.; Sintes, E.; Herndl, G.J. Spatial patterns of bacterial abundance, activity and community composition in relation to water masses in the eastern Mediterranean Sea. *Aquat. Microb. Ecol.* **2010**, *59*, 185–195. [CrossRef]
80. Del Giorgio, P.A.; Gasol, J.M.; Vaqué, D.; Mura, P.; Agustí, S.; Duarte, C.M. Bacterioplankton community structure: Protists control net production and the proportion of active bacteria in a coastal marine community. *Limnol. Oceanogr.* **1996**, *41*, 1169–1179. [CrossRef]
81. Šolić, M.; Krstulović, N.; Kušpilić, G.; Gladan, Ž.N.; Bojanić, N.; Šestanović, S.; Šantić, D.; Ordulj, M. Changes in microbial food web structure in response to changed environmental trophic status: A case study of the Vranjic Basin (Adriatic Sea). *Mar. Environ. Res.* **2010**, *70*, 239–249. [CrossRef] [PubMed]
82. Cottrell, M.T.M.; Mannino, A.; Kirchman, D.L. Aerobic anoxygenic phototrophic bacteria in the Mid-Atlantic Bight and the North Pacific Gyre. *Appl. Environ. Microbiol.* **2006**, *72*, 557–564. [CrossRef] [PubMed]
83. Lami, R.; Cottrell, M.; Ras, J.; Ulloa, O.; Obernosterer, I.; Claustre, H.; Kirchman, D.L.; Lebaron, P. High abundances of aerobic anoxygenic photosynthetic bacteria in the South Pacific Ocean. *Appl. Environ. Microbiol.* **2007**, *73*, 4198–4205. [CrossRef] [PubMed]
84. Lami, R.; Čuperová, Z.; Ras, J.; Lebaron, P.; Koblížek, M. Distribution of free-living and particle-attached aerobic anoxygenic phototrophic bacteria in marine environments. *Aquat. Microb. Ecol.* **2009**, *55*, 31–38. [CrossRef]
85. Hojerová, E.; Mašín, M.; Brunet, C.; Ferrera, I.; Gasol, J.M.; Koblížek, M. Distribution and growth of aerobic anoxygenic phototrophs in the Mediterranean Sea. *Environ. Microbiol.* **2011**, *13*, 2717–2725. [CrossRef] [PubMed]

86. Lamy, D.; Jeanthon, C.; Cottrell, M.T.; Kirchman, D.L.; Wambeke, F.V.; Ras, J.; Dahan, O.; Pujo-Pay, M.; Oriol, L.; Bariat, L.; et al. Ecology of aerobic anoxygenic phototrophic bacteria along an oligotrophic gradient in the Mediterranean Sea. *Biogeosciences* **2011**, *8*, 973–985. [CrossRef]
87. Jiao, N.; Zhang, Y.; Zeng, Y.; Hong, N.; Liu, R.; Chen, F.; Wang, P. Distinct distribution pattern of abundance and diversity of aerobic anoxygenic phototrophic bacteria in the global ocean. *Environ. Microbiol.* **2007**, *9*, 3091–3099. [CrossRef]
88. Ritchie, A.E.; Johnson, Z.I. Abundance and genetic diversity of aerobic anoxygenic phototrophic bacteria of coastal regions of the Pacific Ocean. *Appl. Environ. Microbiol.* **2012**, *78*, 2858–2866. [CrossRef]
89. Ferrera, I.; Borrego, C.M.; Salazar, G.; Gasol, J.M. Marked seasonality of aerobic anoxygenic phototrophic bacteria in the coastal NW Mediterranean Sea as revealed by cell abundance, pigment concentration and pyrosequencing of pufM gene. *Environ. Microbiol.* **2014**, *16*, 2953–2965. [CrossRef]
90. Yutin, N.; Suzuki, M.T.; Teeling, H.; Weber, M.; Venter, J.C.; Rusch, D.B.; Béjà, O. Assessing diversity and biogeography of aerobic anoxygenic phototrophic bacteria in surface waters of the Atlantic and Pacific Oceans using the Global Ocean Sampling expedition metagenomes. *Environ. Microbiol.* **2007**, *9*, 1464–1475. [CrossRef]
91. Ferrera, I.; Gasol, J.M.; Sebastián, M.; Hojerová, E.; Koblížek, M. Growth rates of aerobic anoxygenic phototrophic bacteria as compared to other bacterioplankton groups in coastal Mediterranean waters. *Appl. Environ. Microbiol.* **2011**, *77*, 7451–7458. [CrossRef]
92. Ferrera, I.; Sarmento, H.; Priscu, J.C.; Chiuchiolo, A.; González, J.M.; Grossart, H.P. Diversity and distribution of freshwater aerobic anoxygenic phototrophic bacteria across a wide latitudinal gradient. *Front. Microbiol.* **2017**, *8*, 175. [CrossRef]
93. Kirchman, D.L.; Stegman, M.R.; Nikrad, M.P.; Cottrell, M.T. Abundance, size, and activity of aerobic anoxygenic phototrophic bacteria in coastal waters of the West Antarctic Peninsula. *Aquat. Microb. Ecol.* **2014**, *73*, 41–49. [CrossRef]
94. Andersen, P.; Sorensen, H.M. Population dynamics and trophic coupling in pelagic microorganisms in eutrophic coastal waters. *Mar. Ecol. Prog. Ser.* **1986**, *33*, 99–109. [CrossRef]
95. Gonzalez, J.M.; Sherr, E.B.; Sherr, B.F. Size-selective grazing on bacteria by natural assemblages of estuarine flagellates and ciliates. *Appl. Environ. Microb.* **1990**, *56*, 583–589.
96. Šimek, K.; Chrzanowski, T.H. Direct and indirect evidence of size-selective grazing on pelagic bacteria by freshwater nanoflagellates. *Appl. Environ. Microbiol.* **1992**, *58*, 3715–3720.
97. Corinaldesi, C.; Crevatin, E.; Del Negro, P.; Marini, M.; Russo, A.; Fonda-Umani, S.; Danovaro, R. Large-scale spatial distribution of virioplankton in the Adriatic Sea: Testing the trophic state control hypothesis. *Appl. Environ. Microbiol.* **2003**, *69*, 2664–2673. [CrossRef]
98. Weinbauer, M.G.; Brettar, I.; Höfle, M.G. Lysogeny and virus-induced mortality of bacterioplankton in surface, deep, and anoxic marine waters. *Limnol. Oceanogr.* **2003**, *48*, 1457–1465. [CrossRef]
99. Magagnini, M.; Corinaldesi, C.; Monticelli, L.S.; De Domenico, E.; Danovaro, R. Viral abundance and distribution in mesopelagic and bathypelagic waters of the Mediterranean Sea. *Deep Sea Res. Part I Oceanogr. Res. Pap.* **2007**, *54*, 1209–1220. [CrossRef]
100. Magiopoulos, I.; Pitta, P. Viruses in a deep oligotrophic sea: Seasonal distribution of marine viruses in the epi-, meso-and bathypelagic waters of the Eastern Mediterranean Sea. *Deep Sea Res. Part I Oceanogr. Res. Pap.* **2012**, *66*, 1–10. [CrossRef]
101. Ordulj, M.; Krstulović, N.; Šantić, D.; Jozić, S.; Šolić, M. Distribution of marine viruses in the Central and South Adriatic Sea. *Mediterr. Mar. Sci.* **2015**, *16*, 65–72. [CrossRef]
102. Winter, C.; Köstner, N.; Kruspe, C.P.; Urban, D.; Muck, S.; Reinthaler, T.; Herndl, G.J. Mixing alters the lytic activity of viruses in the dark ocean. *Ecology* **2018**, *99*, 700–713. [CrossRef]
103. Baudoux, A.C.; Veldhuis, M.J.; Witte, H.J.; Brussaard, C.P. Viruses as mortality agents of picophytoplankton in the deep chlorophyll maximum layer during IRONAGES III. *Limnol. Oceanogr.* **2007**, *52*, 2519–2529. [CrossRef]

Article

Numerical Investigations of Tsunami Run-Up and Flow Structure on Coastal Vegetated Beaches

Hongxing Zhang [1], Mingliang Zhang [1,*], Tianping Xu [1] and Jun Tang [2]

[1] School of Ocean Science and Environment, Dalian Ocean University, Dalian 116023, China; zhxing611@163.com (H.Z.); xtpptx@outlook.com (T.X.)

[2] State Key Laboratory of Coastal and Offshore Engineering, Dalian University of Technology, Dalian 116023, China; jtang@dlut.edu.cn

* Correspondence: mlzhang@dlou.edu.cn

Received: 23 October 2018; Accepted: 29 November 2018; Published: 3 December 2018

Abstract: Tsunami waves become hazardous when they reach the coast. In South and Southeast Asian countries, coastal forest is widely utilized as a natural approach to mitigate tsunami damage. In this study, a depth-integrated numerical model was established to simulate wave propagation in a coastal region with and without forest cover. This numerical model was based on a finite volume Roe-type scheme, and was developed to solve the governing equations with the option of treating either a wet or dry wave front boundary. The governing equations were modified by adding a drag force term caused by vegetation. First, the model was validated for the case of solitary wave (breaking and non-breaking) run-up and run-down on a sloping beach, and long periodic wave propagation was investigated on a partially vegetated beach. The simulated results agree well with the measured data. Further, tsunami wave propagation on an actual-scale slope covered by coastal forest *Pandanus odoratissimus* (*P. odoratissimus*) and *Casuarina equisetifolia* (*C. equisetifolia*) was simulated to elucidate the influence of vegetation on tsunami mitigation with a different forest open gap. The numerical results revealed that coastal vegetation on sloping beach has significant potential to mitigate the impacts from tsunami waves by acting as a buffer zone. Coastal vegetation with open gaps causes the peak flow velocity at the exit of the gap to increase, and reduces the peak flow velocity behind the forest. Compared to a forest with open gaps in a linear arrangement, specific arrangements of gaps in the forest can increase the energy attenuation from tsunami wave. The results also showed that different cost-effective natural strategies in varying forest parameters including vegetation collocations, densities, and growth stages had significant impacts in reducing the severity of tsunami damage.

Keywords: tsunami waves; numerical simulation; wave run-up; flow structure; coastal vegetation

1. Introduction

Tsunamis are generated by marine earthquakes, underwater volcanic eruptions, or submerged landsides. Recent tsunami disasters (e.g., in the Indian Ocean in 2004, Samoa in 2009, Chile in 2010, Tohoku in 2011, and Indonesia in 2018) have caused vast losses of life and property, destruction of critical infrastructure in low-lying coastal areas, and massive damage to the coastal ecosystem [1–4]. These great threats demonstrate the need to mitigate tsunamis by using artificial obstacles including wave-dissipating blocks, rock breakwaters, and large embankments. Recent studies investigated tsunami waves in both laboratory experiments [5–8] and field investigations [9,10] with the ultimate goal of mitigating their impacts and reducing natural disasters in coastal regions. Considering the advantages of flexibility and repeatability in numerical models, many numerical simulations have been carried out using different models to investigate the run-up heights and velocity processes of tsunamis [11–16]. Typical models that were considered included depth-integrated Boussinesq-type models and depth-integrated non-linear shallow water models (NSWMs), with results showing that NSWMs are more robust and efficient for tsunami predictions in real-scale basins.

Generally, coastal forests which act as natural obstacles are widely distributed in coastal areas. They also effectively mitigate tsunami damage from economic, environmental, and aesthetically pleasing points of view in concert with hard structures [17,18]. Currently, there is some literature on the capability of coastal vegetation to attenuate wave energy in short-period waves [19,20]. While tsunamis are categorically different from short-period waves, there have been an increasing number of studies that address the role of vegetation in mitigating coastal natural disasters, which can include the strategy of planting coastal vegetation as a bio-shield [21–23]. Recent research has calculated the friction and drag force of vegetation in a tsunami, using mathematical equations. Real-scale simulations of tsunami were performed to investigate the effectiveness of forests as a bio-shield for tsunami protection, with results indicating that a forest with two layers in the vertical direction including *P. odoratissimus* and *C. equisetifolia* was effective for attenuating the wave energy [24]. Based on two dimensional nonlinear long-wave equations, Thuy et al. developed a numerical model to estimate tree-breaking, the drag forces, and turbulence-induced shear force due to the presence of vegetation (*P. odoratissimus* and *C. equisetifolia*) [25]. Considering the effects of the porosity of vegetation, a one-dimensional numerical model using Boussinesq-type equations was developed to evaluate the effects of the forest density distribution on tsunami-force reduction, including the drag and inertia forces caused by vegetation [26]. Numerical investigations were conducted to study the impact of patchy vegetation on tsunami dynamics based on Boussinesq model, and the results demonstrated that patchy vegetation, with appropriate configuration, can be effective in mitigating tsunami hazards [27]. Based on a nonlinear long wave equation model that included the breaking or washout of trees, numerical simulations were carried out to estimate the effects of coastal forest and sea embankments on reducing the washout area and the tsunami mitigation function of the coastal forest [28].

Roads are perpendicular to the coast function as pathways that form gaps in the vegetation of the coastal forest. Gaps in the coastal forest can increase risks and potential damage, as the water flow from the tsunami accelerates as it moves through the gap into the densely populated block [29]. Tanimoto et al. studied it by changing the width of open gap and found that a specific gap with 15 m width causes the highest flow velocity in their simulated conditions [30]. Thuy et al. numerically simulated the effect of an open gap in coastal forests on tsunami run-up, and found that maximum flow velocity greatly increased at the open gap exit, meaning that an open gap (like a road) in a coastal forest had a negative effect on tsunami run-up behind the forest [31]. Nandasena et al. investigated hydrodynamic parameters (flow velocity and depth) of tsunami waves and bending moment of vegetation on Misawa, a site covered by pine forest with two gaps [32]. However, no studies have discussed the effects of different open gaps in existing forests via the analysis of maximum tsunami run-up and variations of velocity through the gaps using a model with shock capture capability.

In this paper, we numerically investigate the hydrodynamic processes on a vegetated sloping beach and quantify the effects of a gap in forest vegetation on the run-up by solving the depth-averaged 2D model. The proposed model was tested for breaking and non-breaking solitary waves propagating on a bare sloping beach, and long periodic wave propagation on a partially-vegetated sloping beach to examine the accuracy of the numerical model. Then, the model was used to simulate tsunami waves propagating on actual-scale forest-covered beach, and to study the mitigation effects of gap arrangements and different vegetation parameters on tsunami waves.

2. Numerical Method

2.1. Governing Equations

The depth-averaged 2D shallow water equations are formed by integrating the Navier–Stokes equations which include continuity and momentum equations for depth-averaged free surface flows. These are expressed as Equations (1)–(3):

$$\frac{\partial h}{\partial t} + \frac{\partial uh}{\partial x} + \frac{\partial vh}{\partial y} = 0 \tag{1}$$

$$\frac{\partial hu}{\partial t} + \frac{\partial (huu)}{\partial x} + \frac{\partial (hu\mathrm{v})}{\partial y} - \frac{\partial}{\partial x}(v_t h\frac{\partial u}{\partial x}) - \frac{\partial}{\partial y}(v_t h\frac{\partial u}{\partial y}) = -gh\frac{\partial \eta}{\partial x} - \tau_{bx} + f_c hv - f_x \tag{2}$$

$$\frac{\partial hv}{\partial t} + \frac{\partial (huv)}{\partial x} + \frac{\partial (hvv)}{\partial y} - \frac{\partial}{\partial x}(v_t h\frac{\partial v}{\partial x}) - \frac{\partial}{\partial y}(v_t h\frac{\partial v}{\partial y}) = -gh\frac{\partial \eta}{\partial y} - \tau_{by} - f_c hu - f_y \tag{3}$$

In the above equations, t is time, h indicates the local water depth, u and v stand for the depth-averaged flow velocities in the x and y directions, respectively, η stands for the water surface elevation from a reference datum, v_t is defined as the eddy viscosity coefficient calculated by $\nu_t = \alpha u_* h$ where α is empirical constant and ranges from 0.3 to 1.0, u_* means the bed shear velocity, τ_{bx} and τ_{by} denote friction in the x and y directions, respectively, $\tau_{bx} = \mathrm{g}\frac{n^2 u\sqrt{u^2 + v^2}}{h^{\frac{1}{3}}}$, $\tau_{by} = \mathrm{g}\frac{n^2 v\sqrt{u^2 + v^2}}{h^{\frac{1}{3}}}$, where n stands for Manning's roughness coefficient, f_c indicates the Coriolis parameter, and f_x and f_{y} stand for the drag force caused by vegetation.

The conservative and vector form of 2D shallow water equations with vegetation effects are expressed as follows:

$$\frac{\partial \mathbf{U}}{\partial t} + \frac{\partial \mathbf{F}}{\partial x} + \frac{\partial \mathbf{G}}{\partial y} = \frac{\partial \mathbf{F}_d}{\partial x} + \frac{\partial \mathbf{G}_d}{\partial y} + \mathbf{S} \tag{4}$$

The definitions of **U**, **F**, **G**, $\mathbf{F}_d$ and $\mathbf{G}_d$ are shown as follows:

$$\mathbf{U} = \begin{bmatrix} h \\ hu \\ hv \end{bmatrix}, \mathbf{F} = \begin{bmatrix} hu \\ huu \\ huv \end{bmatrix}, \mathbf{G} = \begin{bmatrix} hv \\ huv \\ hvv \end{bmatrix}, \mathbf{F}_d = \begin{bmatrix} 0 \\ \nu_t \frac{\partial uh}{\partial x} \\ \nu_t \frac{\partial vh}{\partial x} \end{bmatrix}, \mathbf{G}_d = \begin{bmatrix} 0 \\ \nu_t \frac{\partial uh}{\partial y} \\ \nu_t \frac{\partial vh}{\partial y} \end{bmatrix}, \mathbf{S} = \begin{bmatrix} 0 \\ -gh\frac{\partial \eta}{\partial x} - \tau_{bx} + f_c hv - f_x \\ -gh\frac{\partial \eta}{\partial y} - \tau_{by} - f_c hu - f_y \end{bmatrix} \tag{5}$$

For notational convenience, Equation (4) is often rewritten as:

$$\frac{\partial \mathbf{U}}{\partial t} + \nabla \cdot \mathbf{E}_w^{adv} = \nabla \cdot \mathbf{E}_w^{dif} + \mathbf{S} \tag{6}$$

where $\mathbf{E}_w^{adv} = \mathbf{F}i + \mathbf{G}j$ and $\mathbf{E}_w^{dif} = \mathbf{F}_d i + \mathbf{G}_d j$.

2.2. Vegetation Drag Force

The resistance effects of vegetation on flow are added into the momentum equations as an internal source of resistant force per unit fluid mass. The drag force exerted by vegetation per unit volume is expressed as [33]:

$$f_x = \frac{1}{2} N C_D(h) bv \min(h_v, h) u\sqrt{u^2 + v^2}, f_y = \frac{1}{2} N C_D(\mathrm{h}) b_v \min(h_v, h) v\sqrt{u^2 + v^2} \tag{7}$$

Here, N stands for the vegetation density defined as the number of plants per square meter, b_v indicates the diameter, and h_v indicates the height of the vegetation. C_D *(h)* indicates the depth-averaged equivalent drag coefficient which considers the vertical stand structures of a tree, defined by Tanaka et al. [1] as follows:

$$C_D(h) = C_{D-ref}\frac{1}{h}\int_0^{\mathrm{h}} \alpha(z_g)\beta(z_g)dz_g \tag{8}$$

$$\alpha(z_g) = \frac{b(z_g)}{b_{ref}} \tag{9}$$

$$\beta(z_g) = \frac{C_D(z_g)}{C_{D\text{-}ref}} \tag{10}$$

where $C_{D\text{-}ref}$ is the reference drag coefficient of the trunk at z_g (equal to 1.2 m in principle), $\alpha(\mathrm{z}_g)$ is considered as an additional coefficient to express the effects of cumulative width on drag force at each height z_g, $b(z_g)$ means the projected width, and b_{ref} indicates the reference projected width. $\beta(z_g)$ is expressed as an additional coefficient representing the effect of leaves or aerial roots on drag force, and $C_D(z_g)$ is drag coefficient of a tree at the height z_g above the ground surface.

2.3. Finite Volume Method

The discretization of the governing equations is based on the finite volume method using an unstructured triangular mesh. The conserved variables are defined at the cell centers and represent the average value of each cell. The integral form of Equation (10) over the ith control volume can be expressed as:

$$\int_{V_i} \frac{\partial \mathbf{U}}{\partial t} d_V + \int_{V_i} \nabla \cdot \mathbf{E}_w^{adv} d_V = \int_{V_i} \nabla \cdot \mathbf{E}_w^{dif} d_V + \int_{V_i} \mathbf{S} d_V \tag{11}$$

In this expression, subscript i and j denote the element and the element side, respectively, while V_i stands for the domain of the ith. Basing Green's theorem. Equation (11) can be rewritten as:

$$\frac{\Delta \mathbf{U}_i}{\Delta t} A_i = -\oint_{L_i} \mathbf{E}_w^{adv} \cdot \mathbf{n} dl + \oint_{L_i} \mathbf{E}_w^{dif} \cdot \mathbf{n} dl + \int_{V_i} \mathbf{S} d_V \tag{12}$$

where U_i stands for the average value of the conserved variables over the ith cell, and U_i is stored at the center of the ith cell, with $\mathbf{U}_i = \frac{1}{A_i}\int_{V_i} \mathbf{U} d_V$. L_i means the boundary of the V_i. A_i denotes the area of the ith cell, $\mathbf{n}$ is the outward surface normal vector of L_i, with $\mathbf{n} = (n_x, n_y) = (\cos\phi, \sin\phi)$, and ϕ is the angle included between the x direction and the outward normal vector.

In the 2D triangular grid system, the line integral term in the Equation (12) can be further approximated and assessed as follows:

$$\Delta \mathbf{U}_i = -\frac{\Delta t}{A_i}\sum_{j=1}^{m}\left(\mathbf{E}_w^{adv} \cdot \mathbf{n}_{ij}\right) l_{ij} + \frac{\Delta t}{A_i}\sum_{j=1}^{m}\left(\mathbf{E}_w^{dif} \cdot \mathbf{n}_{ij}\right) l_{ij} + \frac{\Delta t}{A_i}\int_{V_i} \mathbf{S} d_V \tag{13}$$

where m denotes the number of total edges of the triangular cell (three in this model), the subscript j means the index of the edge of a triangular mesh, $\mathbf{n}_{ij}$ stands for the outward normal flux vector, and l_{ij} means the length of the arc.

2.4. Evaluation of Numerical Fluxes

Variables are usually approximated as constant states within each control volume. Riemann problems at the interface of the cell can be solved using various Riemann approximations for evaluating the interface fluxes. The interface fluxes of Roe's solver are expressed as follows:

$$\mathbf{E}_w^{adv} \cdot \mathbf{n} = \frac{1}{2}\left[(\mathbf{F},\mathbf{G})_R \cdot \mathbf{n} + (\mathbf{F},\mathbf{G})_L \cdot \mathbf{n} - |J|(\mathbf{U}_R - \mathbf{U}_L)\right] \tag{14}$$

where $\mathbf{U}_R$ and $\mathbf{U}_L$ are reconstructed Riemann state variables on the right and left sides of the cell interface, respectively. The flux Jacobian matrix A can be assessed as:

$$|J| = \frac{\partial\left(\mathbf{E}_w^{adv}\cdot\mathbf{n}\right)}{\partial \mathbf{U}} = \frac{\partial \mathbf{F}}{\partial \mathbf{U}} n_x + \frac{\partial \mathbf{G}}{\partial \mathbf{U}} n_y = \begin{bmatrix} 0 & n_x & n_y \\ (c^2 - u^2)n_x - uvn_y & 2un_x + vn_y & un_y \\ -uvn_x + (c^2 - v^2)n_y & vn_x & un_x + 2vn_y \end{bmatrix} \tag{15}$$

where n_x and n_y denote the components of the outward surface normal vector in the x- and y- directions, respectively, and c indicates the wave velocity, with

$$c = \sqrt{gh}$$

where $|J| = R|\Lambda|L$, R and L stand for the right and left eigenvector matrices, and $|\Lambda|$ denotes the diagonal matrix of the absolute values of the eigenvalues of A.

Where $|\Lambda|$ is defined as:

$$|\Lambda| = \begin{pmatrix} \Lambda^1 & 0 & 0 \\ 0 & \Lambda^2 & 0 \\ 0 & 0 & \Lambda^3 \end{pmatrix}$$

where

$$\lambda^1 = un_x + vn_y,\ \lambda^2 = un_x + vn_y - c,\ \lambda^3 = un_x + vn_y + c \tag{16}$$

The right and left eigenvector matrices are expressed as follows:

$$R = \begin{pmatrix} 0 & 1 & 1 \\ n_y & u - cn_x & u + cn_x \\ -n_x & v - cn_y & v - cn_y \end{pmatrix},\ L = \begin{pmatrix} -(un_y - vn_x) & n_y & -n_x \\ \frac{un_x + vn_y}{2c} + \frac{1}{2} & \frac{-n_x}{2c} & \frac{-n_y}{2c} \\ -\frac{un_x + vn_y}{2c} + \frac{1}{2} & \frac{n_x}{2c} & \frac{n_y}{2c} \end{pmatrix} \tag{17}$$

where the Riemann state variables u, v, and c on the cell interface are necessary to deal with the fluxes as calculated by Roe's average:

$$u = \frac{\sqrt{h_+}u_+ + \sqrt{h_-}u_-}{\sqrt{h_+} + \sqrt{h_-}},\ v = \frac{\sqrt{h_+}v_+ + \sqrt{h_-}v_-}{\sqrt{h_+} + \sqrt{h_-}},\ c = \sqrt{\frac{g(h_+ + h_-)}{2}} \tag{18}$$

The subscripts $+$ and $-$ indicate the right and left sides of the cell edge, respectively. When the drying-wetting interfaces exist in the computational domain, Roe's average can be calculated by: $u = \frac{u_+ + u_-}{2}$, $v = \frac{v_+ + v_-}{2}$.

2.5. Treatment of Wetting and Drying Fronts

A technique to treat both wet and dry boundaries was introduced to achieve zero mass error [34,35]. A criterion, ε, was adopted to define and classify the following four types of edges:

1. Wet edge (see Figure 1a): two adjacent cells are wet, in which water depth of left cell $h_{\mathrm{L}} > \varepsilon$ and water depth of right cell $h_{\mathrm{R}} > \varepsilon$.
2. Partially wet edge (with flux), as presented in Figure 1b: a wet cell (left) links to a dry cell on the right, and the water level of the wet cell is higher than that of the dry cell, where $h_{\mathrm{L}} > \varepsilon$, $h_{\mathrm{R}} \leq \varepsilon$ and water level of left cell $\eta_{\mathrm{L}} >$ water level of left cell η_{R}.
3. Partially wet edge (no flux), as shown in Figure 1c: a wet cell (left) links to a dry cell on the right, and the water level of the wet cell is lower than that of the dry cell, where $h_{\mathrm{L}} > \varepsilon$, $h_{\mathrm{R}} \leq \varepsilon$, and $\eta_{\mathrm{L}} < \eta_{\mathrm{R}}$. To eliminate the non-physical flux problem produced in the interface, the water level η_{R} and bed level Z_{bR} for the dry cell were temporarily replaced by a value which equaled to the water level η_{L} in the wet cell.
4. Dry edge, as presented in Figure 1d: two adjacent cells are dry, where $h_{\mathrm{L}} \leq \varepsilon$ and $h_{\mathrm{R}} \leq \varepsilon$.

According to these four types of edges, cells were correspondingly divided into three types:

1. Wet cell: all the edges of this cell consisted of a wet or partially wet edges (with flux) and all the nodes of the cell are flooded.
2. Dry cell: all the edges of this cell consist of dry or partially wet edges (no flux).
3. Partially wet cell: all other cells do not satisfy the criteria of either a wet or dry cell, as defined above.

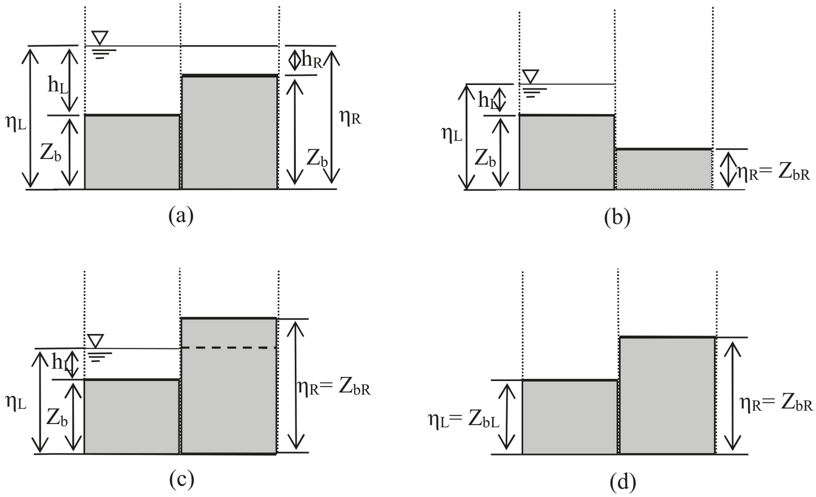

(a) (b)

(c) (d)

Figure 1. Schematic diagram of wet-dry edges.

3. Numerical Simulation and Experimental Validation

3.1. Solitary Wave Run-up on a Bare Sloping Beach

The depth-integrated shallow water model was run for experiment cases of breaking and non-breaking solitary waves on a bare sloping beach conducted by Synolakis to validate the accuracy of the numerical scheme for modeling wave run-up and run-down [36]. The topography consists of a 1:19.85 sloping beach adjacent to a constant depth region, as illustrated in Figure 2. A solitary wave propagates from left to right in a wave flume; and according to first-order solitary wave theory, the water surface elevation and velocity in initial time are defined as follows:

$$\eta(x) = H_W \sec h^2\left(\sqrt{\frac{3HW}{4{h_0}^3}}(x - X_0)\right) \tag{19}$$

$$u(x) = \eta(\mathrm{x})\sqrt{\frac{g}{h_0}} \tag{20}$$

where H_w means wave height, h_0 denotes initial water depth with a value of 1 m, X_0 stands for the position of initial wave crest and is located a half wave length from the toe of the sloping beach in the computing domain, and u is wave velocity.

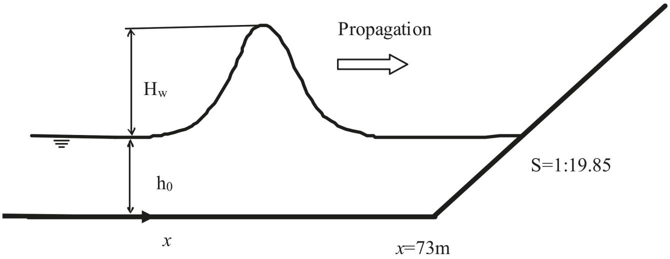

Figure 2. Sketch of the solitary wave propagation on a sloping beach.

In this case study, the numerical model used uniform triangular cells with a grid spacing of 0.02 m and a time step of 0.001 s. The minimum water depth to define a "dry bed" was set as 0.0001 m, and the Manning's bed roughness coefficient was calibrated as 0.01 for the glassed flume in the present model. The solitary wave was defined as non-breaking in this case, as H_W/h_0 = 0.0185. For convenience, the results are presented in non-dimensional forms: $\mathrm{x}^* = \frac{x}{h_0}$, $\eta^* = \frac{\eta}{h_0}$ and $\mathrm{t}^* = t\sqrt{\frac{g}{h_0}}$. Comparisons of the simulated and experimental free-surface evolutions are presented in Figure 3. As illustrated, the incident wave propagates on the sloping beach at the early stage (t^* = 25, 30, 35, 40, 45, and 50), and reaches maximum run-up height at about t^* = 55, at which point backwash occurs. The maximum run-down happens at around t^* = 70. Simulated free surface profiles show good agreement with experimental data. Figure 4 shows the comparison of simulated and experimental water surface processes from a breaking solitary wave with H_w/h_0 = 0.3. In Figure 4, wave breaking is not well reproduced by the depth-averaged shallow model and the computed wave fronts are steeper and slightly earlier than the experimental results at t^* = 15 and t^* = 20, as the model does not consider a wave dispersion term [37,38]. However, the wave breaking is only in a small portion of the domain. At the next step (t^* = 25), wave breaking is reasonably simulated by the model as a collapse of the wave near the shoreline approximately which can be explained that the wave breaking may be weakened and become smaller portion of the domain. The breaking solitary wave reaches a maximum height around t^* = 45, and approaches the lowest position where a hydraulic jump is formed near the shoreline around t^* = 55. The simulated results agree with experimental data very well, which indicate that the proposed model can accurately predict the propagation of breaking and non-breaking solitary waves on a bare sloping beach.

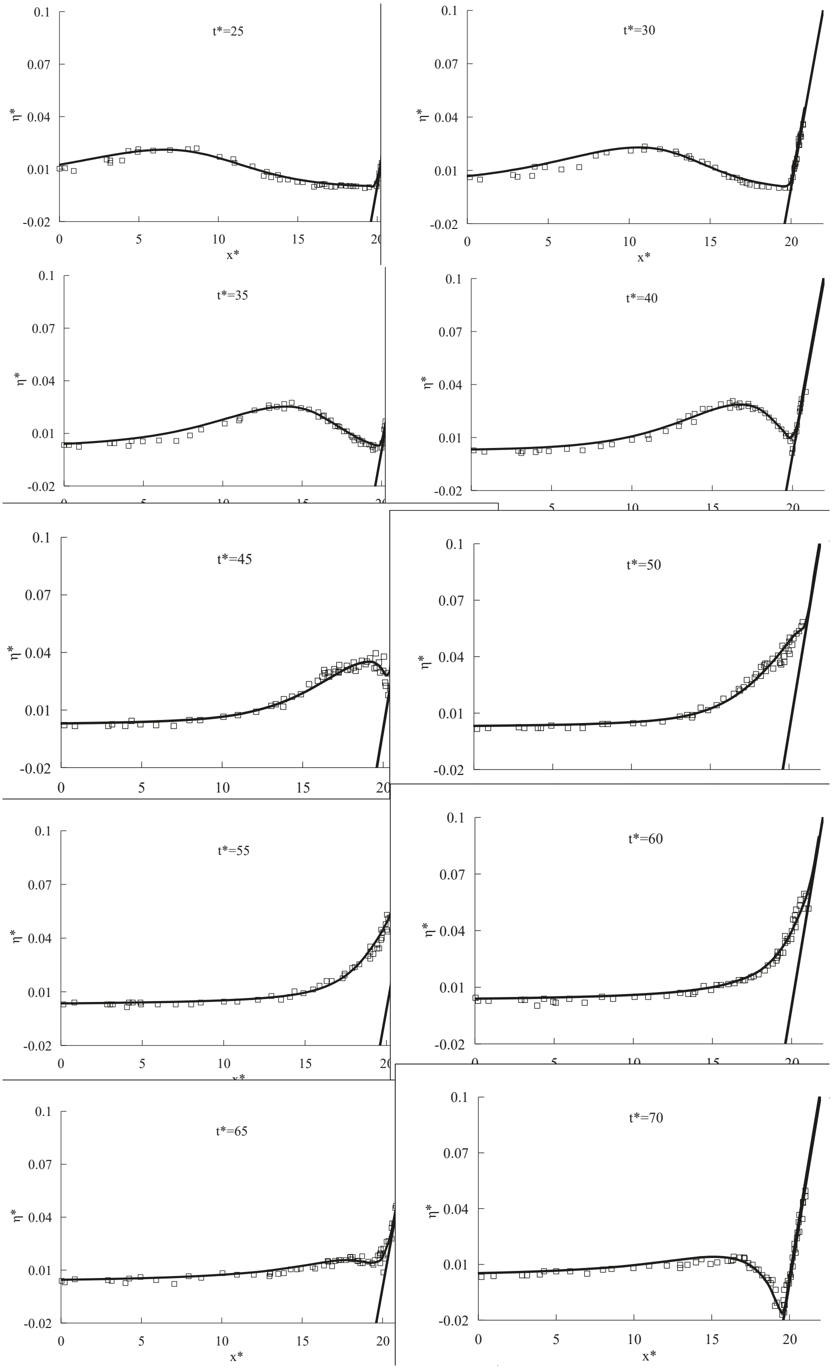

Figure 3. Run-up and run-down of H_w/h_0 = 0.0185 non-breaking solitary wave on a 1:19.85 sloping beach.

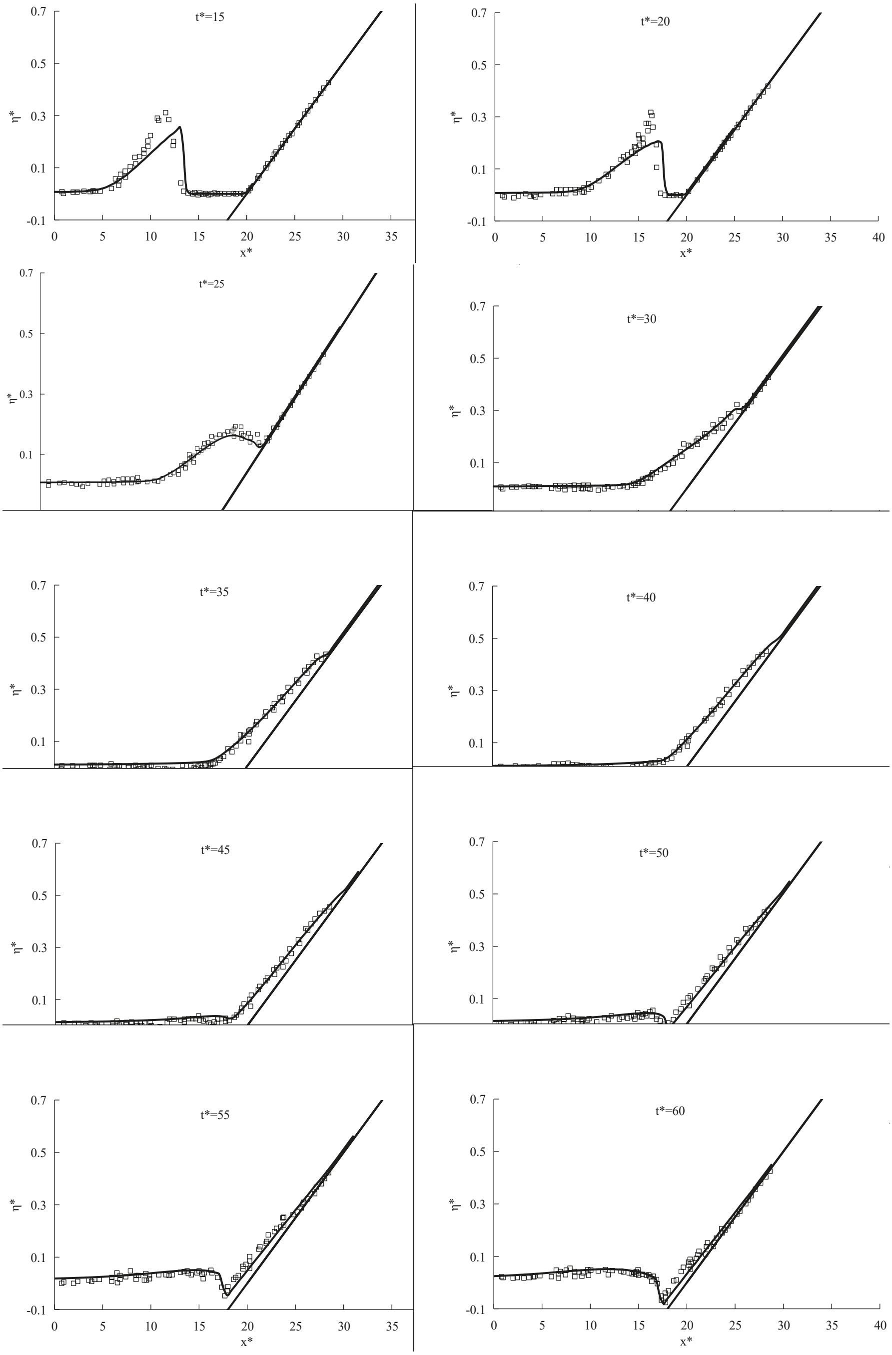

Figure 4. Run-up and run-down of $H_w/h_0 = 0.3$ breaking solitary wave on a 1:19.85 sloping beach.

3.2. Propagation of Long Periodic Waves on a Partially Vegetated Sloping Beach

A laboratory experiment exploring the propagation of long periodic waves in a wave channel with a partially-vegetated sloping beach was conducted in Saitama University [31,32]. In this experiment, the wave tank was 15 m long and 0.4 m wide for propagation, and the bed profile of the beach consisted of several sections with various slopes (Figure 5a). The vegetation was modelled using wooden cylinders with a diameter of 0.005 m at a still water depth of 0.44 m. The vegetation domain was from x = 10.36 to 11.36 m, with different vegetation gap widths (B_g = 0, 0.07, and 0.4 m), while the vegetation density was set as 2200 stem/m^{-2}, and the drag coefficient C_D of wooden cylinders was calibrated as 2.5 in the present study. An incident sinusoidal wave with a period of T = 20 s and wave height of 0.16 cm was propagated from a 0.52 m long constant bottom segment to a sloping beach. In the current case, water surface elevations were measured using capacitance wave gauges at six positions (G1–G6) along the center of the flume in cases of B_g = 0 and 0.4 m, and the flow velocities were measured using electromagnetic current meters at locations in the cross section passing behind vegetation domain G6 (see Figure 5b) in case of B_g = 0.07 m. The run-up height above still water surface was measured by tracing the moving of water front by eyes with a scale on the slope. The computational domain was represented by uniform triangular cells with a grid spacing of 0.01 m and a time step of 0.002 s for the numerical model. The minimum depth criterion for a dry and wet bed was considered as 0.001 m, and the Manning coefficient was set as 0.012.

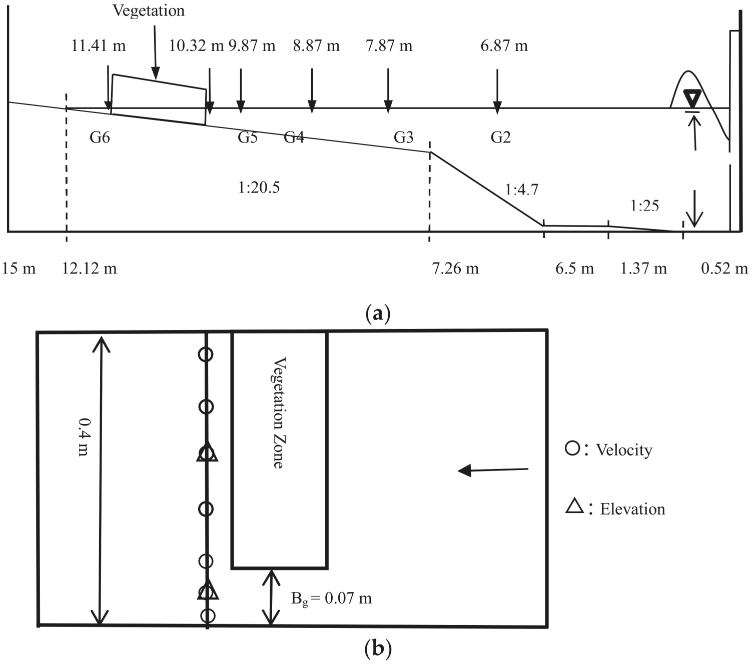

Figure 5. Experimental setup of wave flume. (**a**) Longitudinal section, (**b**) plan view of vegetation zone and measurement points.

A comparison of wave crests, heights, and troughs in Figure 6a,b demonstrates that for the case of non-vegetated areas, wave heights increased due to shoaling as the long waves approached shallow water, however, the increased amplitudes of wave heights were attenuated by the resistance effects of vegetation at the sloping zone, with the attenuated rate reaching 38.96% at G6 (at the center behind vegetation). The wave height at the front of the vegetated zone was also affected by the reflection of waves caused by the vegetation. Figure 7 shows the comparison of time series of velocities at the center of the gap exit and the center of the end of the vegetation when $B_g = 0.07$ m, indicating that the peak flow velocity at the center of the gap exit can reach 0.42 m/s and is 3.07 times more than the peak flow velocity at behind the center of the vegetation zone. Figure 8 shows the distribution of the peak velocities averaged from five wave periods at steady state in a cross-section of Gage 6, indicating that vegetation plays an important role in the distribution of flow velocities. The results demonstrate that the present model is an effective tool to predict long periodic wave propagation on a partially vegetated sloping beach. Vegetation can effectively attenuate the wave propagation; however, an open gap in vegetation zone generates large flow and adverse effect at gap exit.

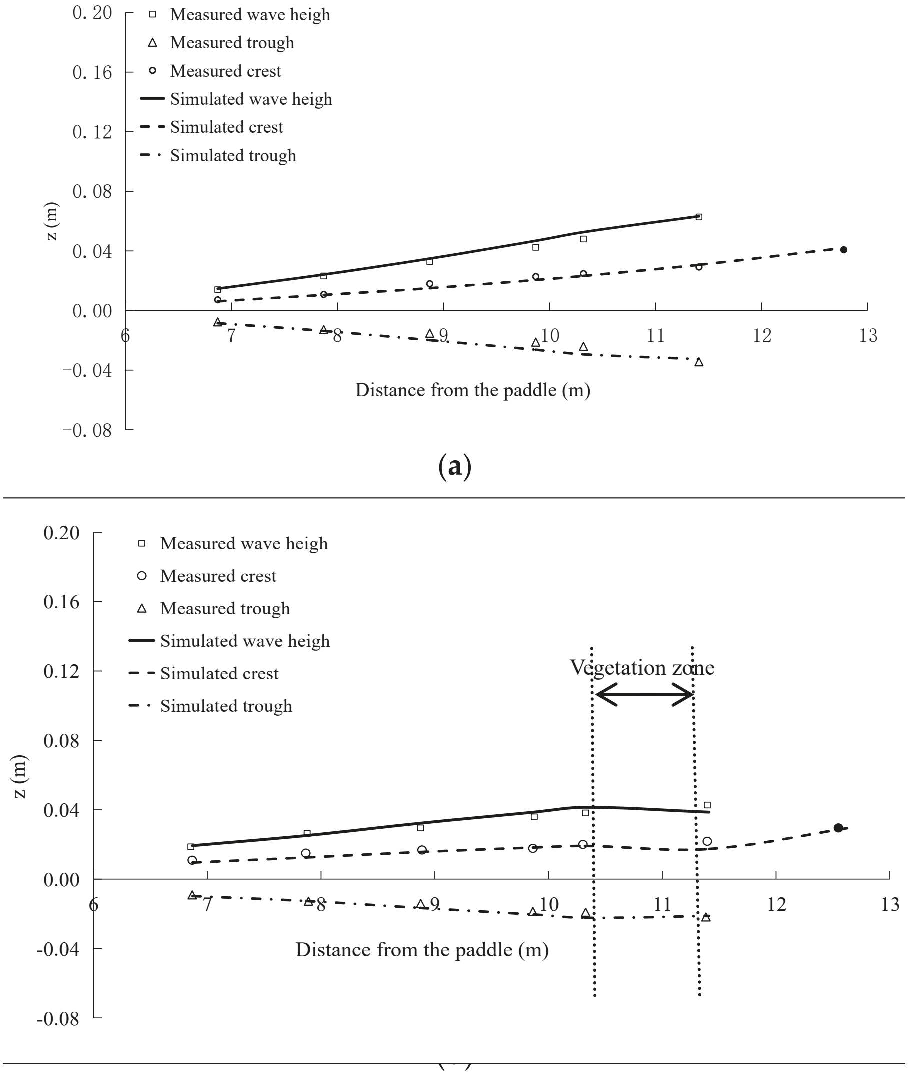

Figure 6. Comparison of measured and calculated wave crests, heights, and troughs. (**a**) Case without vegetation, (**b**) Case with full vegetation.

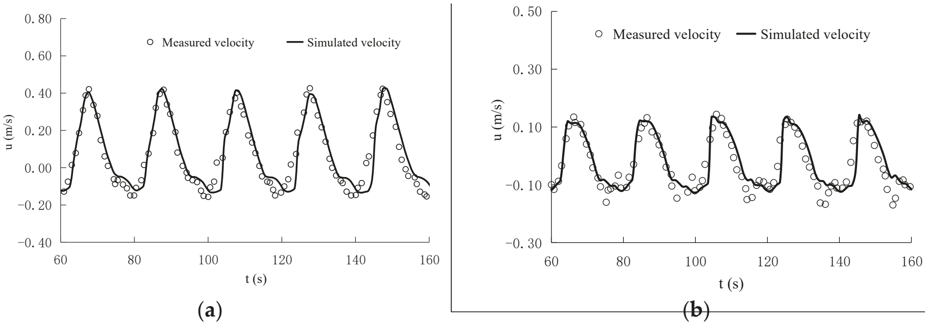

(**a**) (**b**)

Figure 7. Time series of velocities, (**a**) at the center of the gap exit, (**b**) at the center of the end of the vegetation.

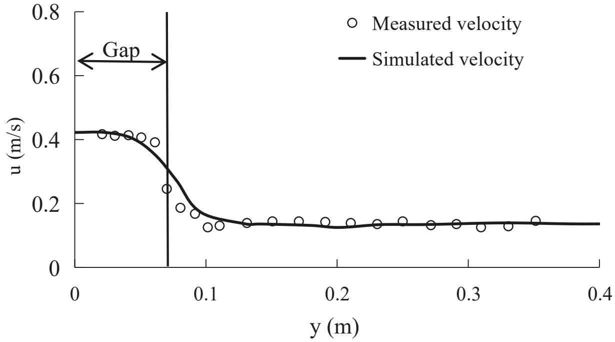

Figure 8. Transverse profiles of maximum velocity in a cross-section of Gage 6 (B_g = 0.07 m).

3.3. Effects of Forest on Tsunami Run-up at Actual Scale

3.3.1. Coastal Topography and Forest Conditions

Coastal forests are widely considered to mitigate tsunami damage on coastal beaches in some countries and regions. In this case study, a numerical simulation was performed to investigate the run-up of tsunami and the effects of forest vegetation on tsunami mitigation. A coastal topography adopted for tsunami simulation is presented in Figure 9 [25,31]. The bed profile of the computed domain consisted of four slopes: S = 1/10, 1/100, 1/50, and 1/500, while the offshore water depth with a horizontal bed was 102 m below the still water level, all parameters for a tsunami wave simulation can be seen in references [25,31].

P. odoratissimus is a representative tree of South and Southeast Asia with a complex aerial root structure growing in coastal beach. In addition, *C. equisetifolia* is another representative species that grows densely on sandy beaches. These two species are discussed in evaluating the resistance of vegetation on tsunami propagation. The tree heights h_v of *P. odoratissimus* and *C. equisetifolia* are considered as 8 m and 11 m, respectively; the reference diameters b_{ref} of *P. odoratissimus* and *C. equisetifolia* are set as 0.2 m and 0.15 m, respectively; and the density values N of *P. odoratissimus* and *C. equisetifolia* are 0.22 trees/m^2 and 0.4 trees/m^2, respectively. The depth-averaged equivalent drag coefficient $C_D(h)$ are variable with vegetation parameters and inundation depth h, and they are modified by Tanaka et al. and Thuy et al. [22,26]. The coastal forest starts at a slope of 1/500 (see Figure 9).

In this numerical simulation, the computational domain is discretized into 38,010 triangular meshes, in which the coarsest grid spacing at the sea-side is 20 m, and the finest grid spacing is 2.5 m at the nearshore area. The Manning's roughness coefficient is set as 0.02 for the computational domain.

By comparing the maximum water surface elevations in Figure 10, there is good agreement between the simulated and Thuy's results [31].

In non-vegetated areas, as the wave crest approaches a 1/50 slope, its energy compresses and the maximum water surface elevations increase slightly because of shoaling. When the wave crest approaches a slope of 1/500, the maximum water surface elevations decrease due to the accelerated flow velocity on a mild slope. For fully vegetated areas, the maximum water surface elevations increase significantly at the front of the forest due to the reflection of the waves caused by the vegetation. In the forest zone, the maximum water surface elevations decrease drastically. The run-up height above the still water level is 5.10 m with full vegetation, which is lower than the 6.86 m for non-vegetation areas. The results indicate that *P. odoratissimus* effectively protects coastal communities from the destruction by a tsunami wave by reducing wave energy.

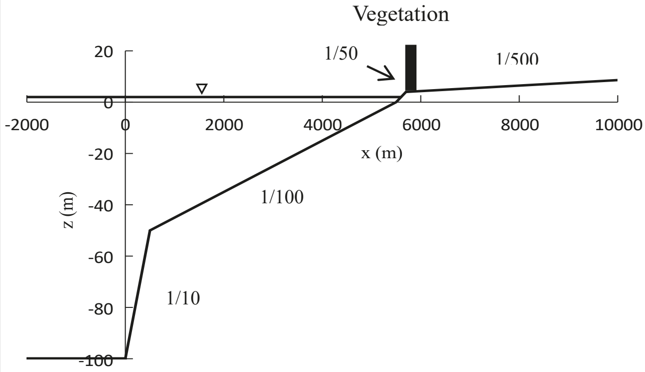

Figure 9. Schematic topography of a tsunami flume with vegetation effects.

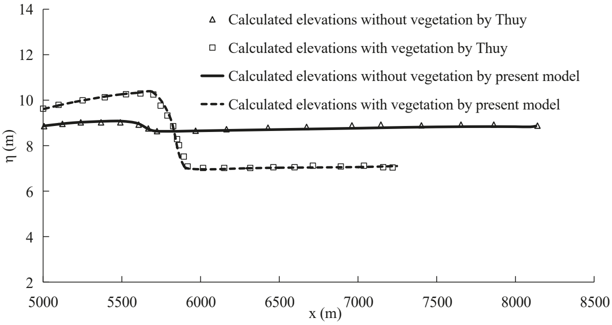

Figure 10. Maximum water surface elevations of the first wave without vegetation and with *P. odoratissimus* vegetation [26].

3.3.2. Effects of Forest with a Straight Open Gap on Tsunami Run-up

Figure 11 shows four types of gap arrangements (Cases 1, 2, 3, and 4) in *P. odoratissimus* forest with the simulation conditions of L_F = 200 m, B_F = 200 m, and B_G = 15 m. In this section, tsunami run-up on the sloping beach is considered using a straight gap (Case 1) to investigate the effect on tsunami run-up.

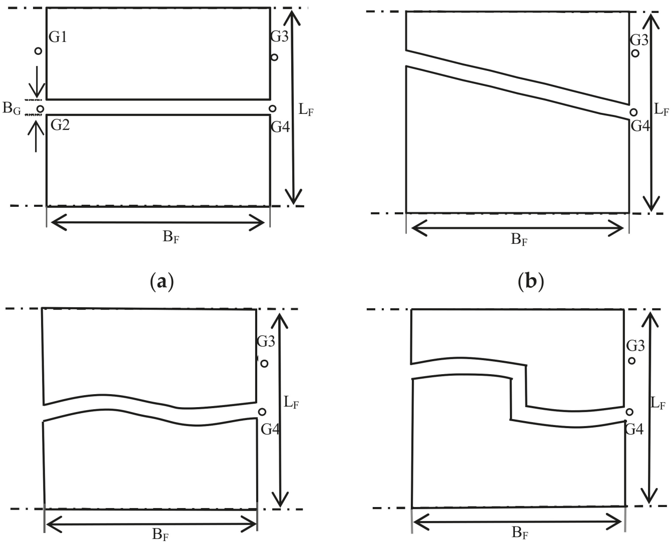

(**a**) (**b**)

(**c**) (**d**)

Figure 11. Sketch of gap arrangements, (**a**) Case 1, (**b**) Case 2, (**c**) Case 3, (**d**) Case 4.

Figure 12a–c presents the predicted flow structure in Case 1 at different times (600, 660 and 700 s). The flow velocity of the first wave is fast in an open gap zone, while the wave moves slowly in the forest domain due to the resistance from vegetation. The first wave front quickly passes the open gap and spreads out from the exit, and the flow behind the forest gradually becomes uniform, with the exception of the areas close to the gap exit. Figure 13 shows the temporal variation of water surface elevations and flow velocities at four predicted stations (G1, G2, G3, and G4) for Case 1. In this case, the maximum water surface elevations in the presence of vegetation are higher at G1 (the middle of the open gap) and G2 (the middle before the vegetation) than those in the absence of vegetation due the reflection of tsunami waves caused by *P. odoratissimus* forest.

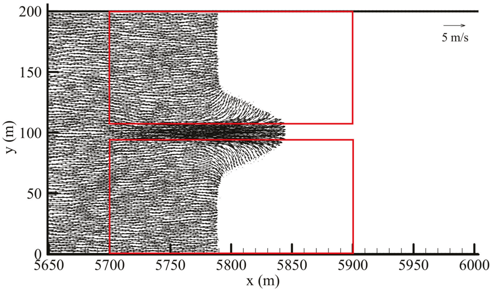

(**a**) T = 600 s

Figure 12. *Cont.*

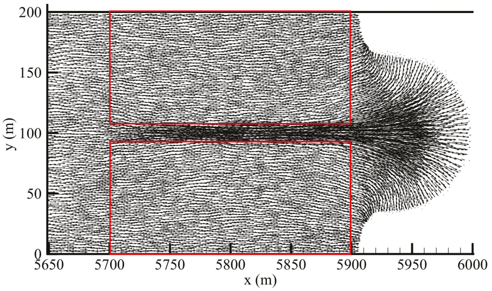

(**b**) T = 660 s

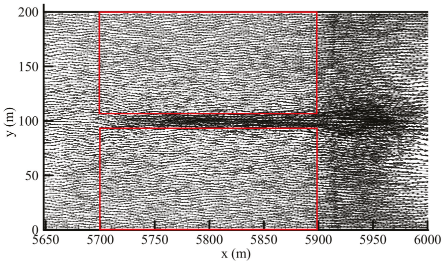

(**c**) T = 700 s

Figure 12. Flow structure in Case 1 at different times ((**a**) T = 600 s, (**b**) T = 660 s, (**c**) T = 700 s).

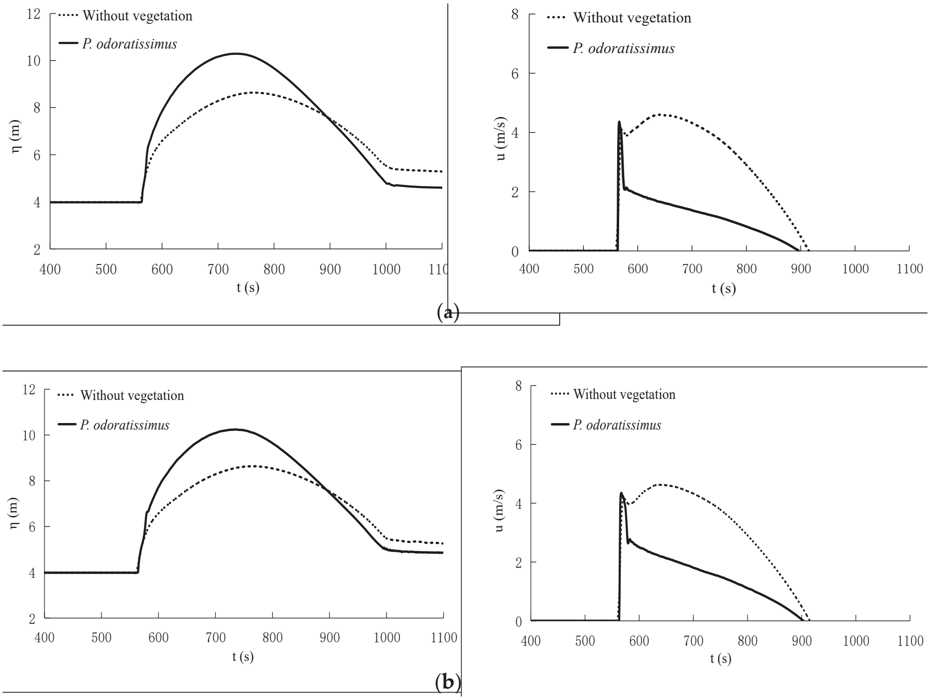

Figure 13. *Cont.*

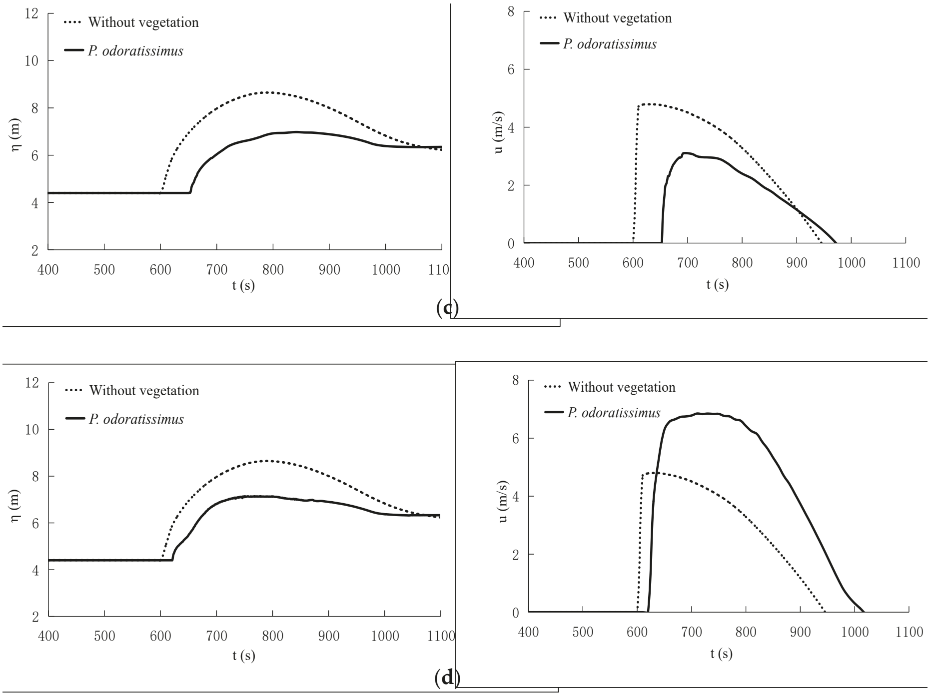

Figure 13. Temporal variation of water surface elevations and flow velocities at four predicted stations of Case 1, (**a**) G1, (**b**) G2, (**c**) G3, (**d**) G4.

As the flow passes the forest, the maximum water surface elevations drastically decrease. The maximum water surface elevation values at G3 (the middle behind the forest) and G4 (the middle at the end of the open gap) in the presence of vegetation with an open gap decrease to 80.72% and 82.52% of that for the case of non-vegetation, respectively. The time delays in a tsunami arriving at G3 and G4 are about 45 and 14 s, respectively, when the wave passes through forest with an open gap compared to that of non-vegetated case. The *P. odoratissimus* forests slightly impact the peak velocities at G1 and G2, which reach 4.36 and 4.35 m/s, respectively. Due the resistance effects of *P. odoratissimus*, the flow velocities at G1 and G2 decrease dramatically after reaching their peak. The peak velocity at G3 is decreased by 35.13% and the peak velocity at G4 is increased by 44.04%. The open gap in forest vegetation amplifies negative effects on tsunami propagation even more than in the non-vegetated case.

3.3.3. Effects of Arrangements of Vegetation Patches and Open Gaps

Four types of gap structures are discussed to investigate their potential to increase the energy attenuation of tsunami waves on a vegetated beach. Figure 14 illustrates the structures of a flow field at 660 s for three cases with different gap arrangements, and shows that the flow velocities are larger in open gaps than those in vegetated zones, and the front of the first wave quickly passes the open gap, and the maximum peak flow velocities appear around the gap exit. The furthest distance that tsunami waves reach is variable, but there are differences in flow where structures occur. As presented in Figure 15, the effects of the gap arrangements on the water surface elevations at G3 and G4 are insignificant for four cases, while the different gap arrangements have important effects on flow velocities of tsunami waves.

Compared to Case 1, the peak flow velocities at the G3 station are increased by about 0.15 m/s (4.92%) and 0.21 m/s (6.71%) for Case 2 and Case 4, respectively, and the peak flow velocity is attenuated slightly by about 0.05 m/s (−1.46%) for Case 3. Compared to Case 1, the peak flow velocities at G4 are decreased by about 0.47 m/s (−6.77%), 0.34 m/s (−4.87%) and 0.89 m/s (−12.88%) for Case 2, 3, and 4, respectively. Figure 16 shows the comparisons of the run-up heights of the first tsunami wave for different cases including fully vegetated, non-vegetated, and four types of vegetation arrangements with different gaps. The results indicate that the slight differences of run-up heights occur for different gap arrangements, however, the presence of vegetation significantly attenuates the energy of tsunami waves compared to non-vegetated case. Therefore, it is reasonable to reduce the disadvantages from open gaps by changing gap arrangements.

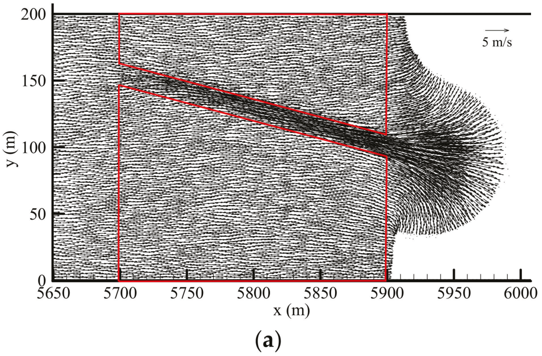

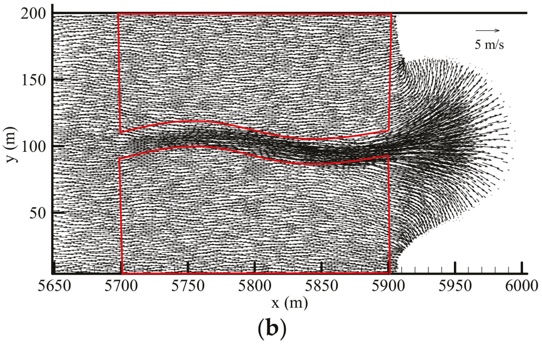

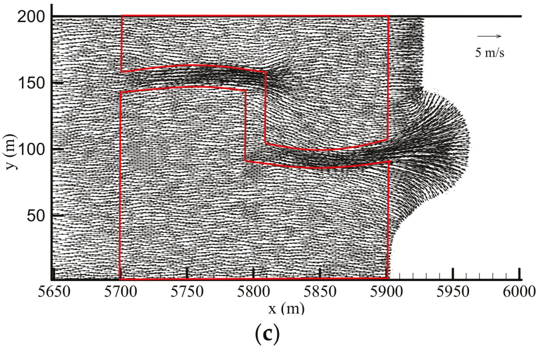

Figure 14. Flow structures at 660 s: (**a**) Case 2, (**b**) Case 3, and (**c**) Case 4.

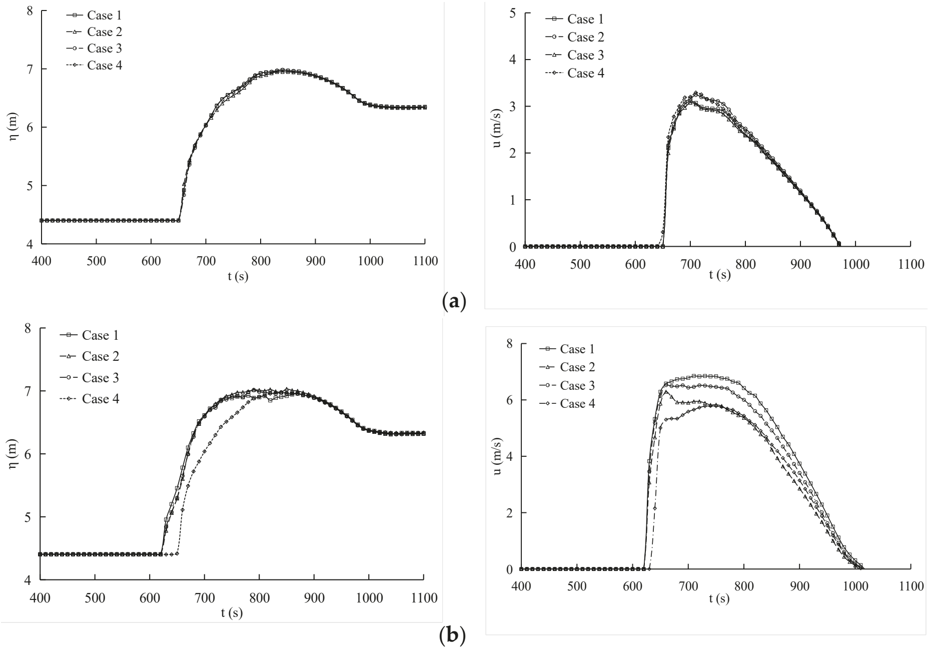

Figure 15. Temporal variation of surface water elevations and current velocities at (**a**) = G3 and (**b**) = G4.

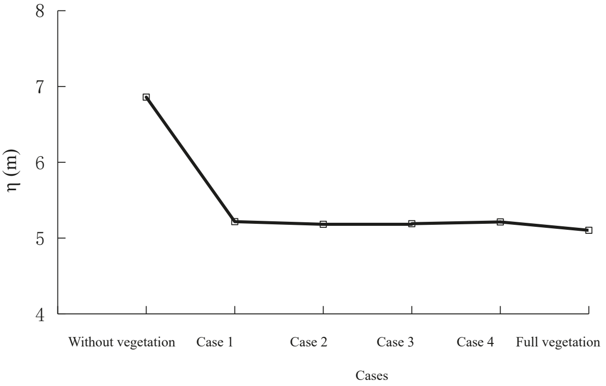

Figure 16. The comparison of maximum run-up heights.

3.3.4. Effects of Forest Parameters on Tsunami Run-up

To investigate the effects of coastal forest parameters on tsunami run-up, a sensitivity analysis of different tree configurations, densities, and growth stages was examined in the gap arrangement of Case 4. In this section, Collocation 1 (pure *P. odoratissimus*), Collocation 2 (pure *C. equisetifolia*), Collocation 3 (*C. equisetifolia* as the back vegetation layer of *P. odoratissimus*), and Collocation 4 (*C. equisetifolia* as the front vegetation layer of *P. odoratissimus*) are considered to analyze effects of tree configuration on tsunami propagation. Figure 17 shows the variation of normalized run-up heights (η/η_0) and normalized peak flow velocities (V/V_0) at simulated gauges (G3 and G4) with different tree arrangements, respectively, where η_0 and V_0 denote the run-up height and the peak flow velocity in the absence of vegetation. The results indicate that *C. equisetifolia* as a new vegetation layer at the back of existing *P. odoratissimus* (Collocation 3) can minimize the amplification of the peak flow velocity through the open gap, while generating a slightly larger peak flow velocity at the G3 station. The run-up height is higher than that of Collocation 1 (pure *P. odoratissimus*) and smaller than that of Collocation 2. This is because the peak flow velocity is reduced significantly due greater resistance of *P. odoratissimus* when it passes the *P. odoratissimus* vegetation layer, and in back zone of *C. equisetifolia* vegetation with smaller drag force, the velocity increment in open gap is smaller compared to that of other tree configurations.In Collocation 1 (pure *P. odoratissimus*), Figure 18 indicates that normalized run-up height and normalized peak flow velocity at G3 decreased monotonously with increased densities, while the normalized peak flow velocity of G4 first increased (vegetation density $\leq$ 0.15 tree/m^2) and then presented adverse variation. Figure 19 indicates that the increased vegetation height and diameter at different growth stages of *P. odoratissimus* generate positively correlated effects on normalized peak flow velocity at G4, and significant attenuation effects on normalized run-up height and normalized peak flow velocity at G3. Generally, changing forest parameters (e.g. vegetation collocations, densities and growth stages) could be a more cost-effective way to mitigate tsunami damage.

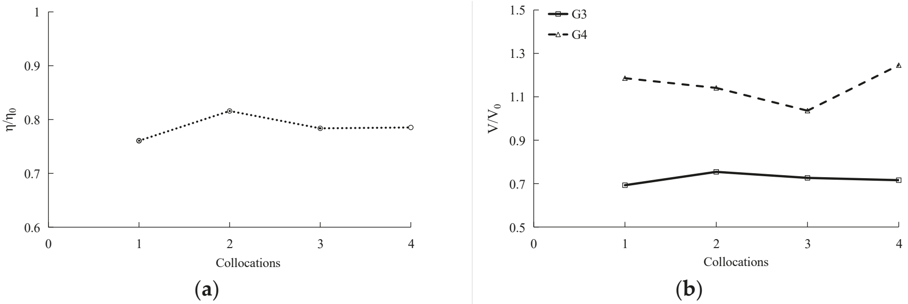

(**a**) (**b**)

Figure 17. Variation of normalized run-up heights and normalized peak flow velocities at G3 and G4 with different tree collocations, (**a**) The normalized run-up heights, (**b**) The normalized peak flow velocities.

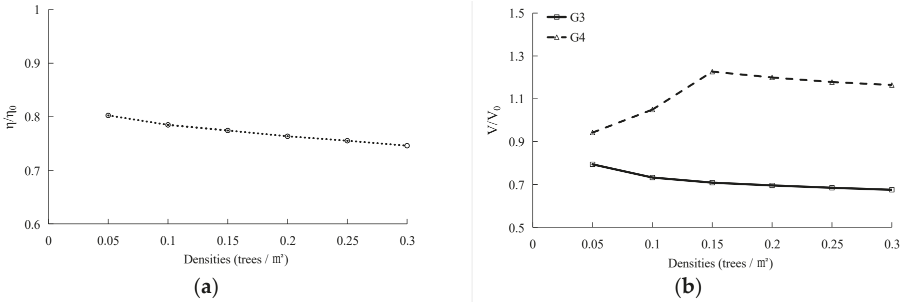

(**a**) (**b**)

Figure 18. Variation of normalized run-up heights and normalized peak flow velocities at G3 and G4 with different densities of pure *P. odoratissimus.* (**a**) The normalized run-up heights, (**b**) The normalized peak flow velocities.

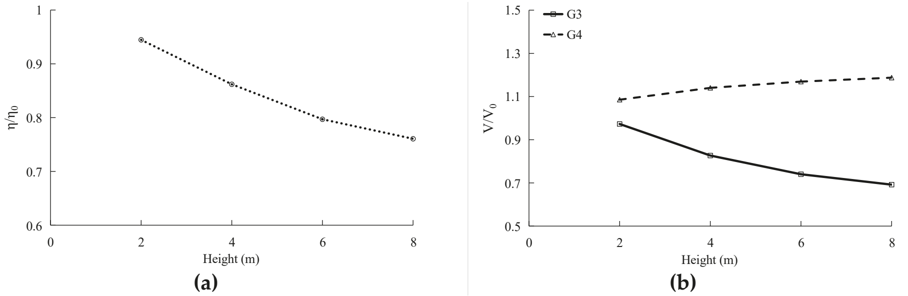

(a) **(b)**

Figure 19. Variation of normalized run-up heights and normalized peak flow velocities at G3 and G4 with different heights of pure *P. odoratissimus*; (**a**) The normalized run-up heights, (**b**) The normalized peak flow velocities.

4. Conclusions

Based on the shallow water equations of mass and momentum, an explicit depth-averaged 2D numerical model was developed to simulate wave attenuation and tsunami wave mitigation in a vegetated coastal region. The finite volume method was used to keep conservation of mass in this model. The proposed model was well verified for both breaking and non-breaking solitary wave propagations on a bare sloping beach, and long periodic wave propagation on a partially-vegetated sloping beach, as shown by comparison of experimental data. Overall, the present numerical model has been shown to accurately account for wave propagation and transformation in vegetated and non-vegetated sloping beaches.

In the case of full *P. odoratissimus* forest on an actual-scale beach, the water surface elevations at the front of the forest belt increased due to the effect of reflected waves caused by vegetation. Here, *P. odoratissimus* forest played a positive role in reducing maximum water surface elevations through the vegetated zone, and as such the maximum wave run-up height of the tsunami was effectively reduced. When a forest has an open gap, the negative effects can be reduced by choosing a beneficial arrangement of vegetation and open gaps. Sensitivity analysis was also carried out by changing tree collocation, tree densities, and growth stage, with results showing that they had important impacts in reducing the peak flow velocity of the tsunami wave at the open gap exit.

Overall, these study findings provide cost-effective natural strategies to improve the effectiveness of *P. odoratissimus* forests with an open gap by changing vegetation arrangements and vegetation parameters (collocations, tree densities, and growth stage), which are important in the design and establishment of vegetated bioshields against tsunami hazards.

Author Contributions: H.Z. contributed to the establishment of model, significantly to analysis and manuscript preparation. M.Z. contributed to the conception of the study and the final editing. T.X. and J.T. contributed to the collection of experimental data.

Funding: This work was supported by the National Nature Science Foundation of China (51779039, 51879028), the Wetland Degradation and Ecological Restoration Program of Panjin Pink Beach (PHL-XZ-2017013-002), the Fund of Liaoning Marine Fishery Department (201725).

Conflicts of Interest: The authors declare no conflict of interest.

References

1. Gopinath, G.; Løvholt, F.; Kaiser, G.; Harbitz, C.B.; Srinivasa, R.K.; Ramalingam, M.; Singh, B. Impact of the 2004 Indian ocean tsunami along the Tamil Nadu coastline: field survey review and numerical simulations. *Nat. Hazards* **2014**, *72*, 743–769. [CrossRef]
2. Gelfenbaum, G.; Apotsos, A.; Stevens, A.W.; Jaffe, B. Effects of fringing reefs on tsunami inundation American Samoa. *Earth Sci. Rev.* **2011**, *107*, 12–22. [CrossRef]

3. Liu, H.; Shimozono, T.; Takagawa, T.; Okayasu, A.; Fritz, H.; Sato, S.; Tajima, Y. The 11 March 2011 Tohoku tsunami survey in rikuzentakata and comparison with historical event. *Pure Appl. Geophys.* **2013**, *170*, 1033–1046. [CrossRef]
4. Sarfaraz, M.; Pak, A. SPH numerical simulation of tsunami wave forces impinged on bridge superstructures. *Coast. Eng.* **2017**, *121*, 145–157. [CrossRef]
5. Touhami, H.E.; Khellaf, M.C. Laboratory study on effects of submerged obstacles on tsunami wave and run-up. *Nat. Hazards* **2017**, *87*, 757–771. [CrossRef]
6. Hsiao, S.C.; Lin, T.C. Tsunami-like solitary waves impinging and overtopping an impermeable seawall: experiment and RANS modeling. *Coast. Eng.* **2010**, *57*, 1–18. [CrossRef]
7. Irish, J.L.; Weiss, R.; Yang, Y.; Yang, Y.; Song, Y.; Zainali, A.; Marivela-Colmenarejo, R. Laboratory experiments of tsunami run-up and withdrawal in patchy coastal forest on a steep beach. *Nat. Hazards* **2014**, *74*, 1933–1949. [CrossRef]
8. Ko, H.T.S.; Yeh, H. On the splash-up of tsunami bore impact. *Coast. Eng.* **2018**, *131*, 1–11. [CrossRef]
9. Witt, D.L.; Yin, L.Y.; Yim, S.C. Field investigation of tsunami impact on coral reefs and coastal sandy slopes. *Mar. Geol.* **2011**, *289*, 159–163. [CrossRef]
10. Fritz, H.M.; Petroff, C.M.; Catalán, P.A.; Cienfuegos, R.; Winckler, P.; Kalligeris, N.; Weiss, R.; Barrientos, S.E.; Meneses, G.; Valderas-Bermejo, C.; et al. Field Survey of the 27 February 2010 Chile Tsunami. *Pure Appl. Geophys.* **2011**, *168*, 1989–2010. [CrossRef]
11. Shuto, N. Numerical simulation of tsunamis-Its present and near future. *Nat. Hazards* **1991**, *4*, 171–191. [CrossRef]
12. Li, L.; Qiu, Q.; Huang, Z. Numerical modeling of the morphological change in Lhok Nga, west banda aceh, during the 2004 Indian ocean tsunami: Understanding tsunami deposits using a forward modeling method. *Nat. Hazards* **2012**, *64*, 1549–1574. [CrossRef]
13. Suppasri, A.; Imamura, F.; Koshimura, S. Effects of the rupture velocity of fault motion, ocean current and initial sea level on the transoceanic propagation of tsunami. *Coast. Eng. J.* **2010**, *52*, 107–132. [CrossRef]
14. Ryan, K.J.; Geist, E.L.; Barall, M.; Oglesby, D.D. Dynamic models of an earthquake and tsunami offshore Ventura, California. *Geophys. Res. Lett.* **2015**, *42*, 6599–6606. [CrossRef]
15. Maris, F.; Kitikidou, K. Tsunami hazard assessment in Greece-Review of numerical modeling (numerical simulations) from twelve different studies. *Renew. Sust. Energ. Rev.* **2016**, *59*, 1563–1569. [CrossRef]
16. Qu, K.; Ren, X.; Kraatz, S. Numerical investigation of tsunami-like wave hydrodynamic characteristics and its comparison with solitary wave. *Appl. Ocean Res.* **2017**, *63*, 36–48. [CrossRef]
17. Kerr, A.M.; Baird, H.B. Natural barriers to natural disasters. *Bioscience* **2017**, *57*, 102–103. [CrossRef]
18. Okal, E.; Fritz, H.M.; Synolakis, C.E.; Borrero, J.C. Field survey of the Samoa tsunami of 29 September. *Seismol. Res. Lett.* **2010**, *81*, 577–591. [CrossRef]
19. Augustin, L.N.; Irish, J.L.; Lynett, P. Laboratory and numerical studies of wave damping by emergent and near-emergent wetland vegetation. *Coast. Eng.* **2009**, *5*, 332–340. [CrossRef]
20. Yang, Z.; Tang, J.; Shen, Y. Numerical study for vegetation effects on coastal wave propagation by using nonlinear Boussinesq model. *Appl. Ocean Res.* **2018**, *70*, 32–40. [CrossRef]
21. Tanaka, N.; Ogino, K. Comparison of reduction of tsunami fluid force and additional force due to impact and accumulation after collision of tsunami-produced driftwood from a coastal forest with houses during the Great East Japan tsunami. *Landsc. Ecol. Eng.* **2017**, *13*, 287–304. [CrossRef]
22. Feagin, R.A.; Mukherjee, N.; Shanker, S.; Baird, A.H.; Cinner, J.; Kerr, A.M.; Koedam, N.; Sridhar, A.; Arthur, R.; Jayatissa, L.P.; et al. Shelter from the storm? Use and misuse of coastal vegetation bioshields for managing natural disasters. *Conserv. Lett.* **2010**, *3*, 1–11. [CrossRef]
23. Bayas, J.C.L.; Marohn, C.; Dercon, G.; Dewi, S.; Piepho, H.P.; Joshi, L.; Noordwijk, M.V.; Cadisch, G. Influence of coastal vegetation on the 2004 tsunami wave impact in west Aceh. *Proc. Natl. Acad. Sci. USA* **2011**, *108*, 18612–18617. [CrossRef] [PubMed]
24. Tanaka, N.; Nandasena, N.A.K.; Jinadasa, K.S.B.N.; Sasaki, Y.; Tanimoto, K.; Mowjood, M.I.M. Developing effective vegetation bioshield for tsunami protection. *J. Civ. Environ. Eng. Syst.* **2009**, *26*, 163–180. [CrossRef]
25. Thuy, N.B.; Tanaka, N.; Tanimoto, K. Tsunami mitigation by coastal vegetation considering the effect of tree breaking. *J. Coast. Conserv.* **2012**, *16*, 111–121. [CrossRef]
26. Iimura, K.; Tanaka, N. Numerical simulation estimating effects of tree density distribution in coastal forest on tsunami mitigation. *Ocean Eng.* **2012**, *54*, 223–232. [CrossRef]

27. Yang, Y.Q.; Irish, J.L.; Weiss, R. Impact of patchy vegetation on tsunami dynamics. *Waterw. Port Coast. Ocean Eng.* **2017**, *143*, 04017005. [CrossRef]
28. Tanaka, N.; Yasuda, S.; Iimura, K.; Yagisawa, J. Combined effects of coastal forest and sea embankment on reducing the washout region of houses in the Great East Japan tsunami. *J. Hydro-Environ. Res.* **2014**, *8*, 270–280. [CrossRef]
29. Mascarenhas, A.; Jayakumar, S. An environmental perspective of the post-tsunami scenario along the coast of Tamil Nadu, India: Role of sand dunes and forests. *J. Environ. Manag.* **2008**, *89*, 24–34. [CrossRef]
30. Tanimoto, K.; Tanaka, N.; Thuy, N.B.; Nandasena, N.A.K.; Iimura, K. Effect of open gap in coastal forest on tsunami run-up—Investigation by 2-dimensional numerical simulation. *Ocean Eng.* **2008**, *24*, 87–92. (In Japanese)
31. Thuy, N.B.; Tanimoto, K.; Tanaka, N.; Harada, K.; Iimura, K. Effect of open gap in coastal forest on tsunami run-up-investigations by experiment and numerical simulation. *Ocean Eng.* **2009**, *36*, 1258–1269. [CrossRef]
32. Nandasena, N.A.K.; Sasaki, Y.; Tanaka, N. Modeling field observations of the 2011 Great East Japan tsunami: Efficacy of artificial and natural structures on tsunami mitigation. *Coast. Eng.* **2012**, *67*, 1–13. [CrossRef]
33. Zhang, M.; Li, C.; Shen, Y. Depth-averaged modeling of free surface flow in open channels with emerged and submerged vegetation. *Appl. Math. Model.* **2013**, *37*, 540–553. [CrossRef]
34. Liang, Q.; Borthwick, A.G.L. Adaptive quadtree simulation of shallow flows with wet-dry fronts over complex topography. *Comput. Fluids* **2009**, *38*, 221–234. [CrossRef]
35. Brufau, P.; García-Navarro, P.; Vázquez-Cendón, M.E. Zero mass error using unsteady wetting-drying conditions in shallow flows over dry irregular topography. *Int. J. Numer. Methods Fluids* **2004**, *45*, 1047–1082. [CrossRef]
36. Synolakis, C.E. The run-up of long waves. Ph D Thesis, California Institute of Technology, Pasadena, CA, USA, January 1986.
37. Wu, W.; Marsooli, R. A depth-averaged 2D shallow water model for breaking and non-breaking long waves affected by rigid vegetation. *J. Hydraul. Res.* **2012**, *50*, 558–575. [CrossRef]
38. Tang, J.; Causon, D.; Mingham, C.; Qian, L. Numerical study of vegetation damping effects on solitary wave run-up using the nonlinear shallow water equations. *Coast. Eng.* **2013**, *75*, 21–28. [CrossRef]

MDPI
St. Alban-Anlage 66
4052 Basel
Switzerland
Tel. +41 61 683 77 34
Fax +41 61 302 89 18
www.mdpi.com

Water Editorial Office
E-mail: water@mdpi.com
www.mdpi.com/journal/water

MDPI
St. Alban-Anlage 66
4052 Basel
Switzerland

Tel: +41 61 683 77 34
Fax: +41 61 302 89 18

www.mdpi.com

ISBN 978-3-03936-153-3